UNIVERSITÄTSKLINIKUM HAMBURG-EPPENDORF

Institut für Entwicklungsneurowissenschaften

Prof. Dr. Ileana L. Hanganu-Opatz

Olfactory Modulation of Cognitive Development

Dissertation

zur Erlangung des Doktorgrades PhD an der

Medizinischen Fakultät der Universität Hamburg.

vorgelegt von:

Yu-Nan Chen (陈裕楠)

aus Swatow, Volksrepublik China

Hamburg 2024

Angenommen von der
Medizinischen Fakultät der Universität Hamburg am: 27.06.2025

Veröffentlicht mit Genehmigung der
Medizinischen Fakultät der Universität Hamburg.

Prüfungsausschuss, der/die Vorsitzende: Prof. Dr. Ileana L. Hanganu-Opatz

Prüfungsausschuss, zweite/r Gutachter/in: Prof. Dr. Thomas Oertner

Prüfungsausschuss, dritte/r Gutachter/in: Prof. Dr. Ivan Manzini

OLFACTORY MODULATION OF COGNITIVE DEVELOPMENT

"In me the tiger sniffs the rose."
Siegfried Sassoon, 1918

Contents

1 Introduction

The sensory system is mainly composed of the sensory periphery, main sensory neuronal pathways and accessory sensory structures. As one of the two chemosensory perceptions, olfaction starts once the odor binds to a receptor within the nasal cavity.

1.1 Overview of the olfactory system

1.1.1 Structure of the olfactory system

The mammalian olfactory system consists of the olfactory epithelium (OE), the olfactory bulb (OB) and the olfactory cortex. The bipolar olfactory sensory neurons (OSNs) are located in the middle layer of the OE, which extend their axons to glomeruli in the OB to preprocess a variety of odors. Excitatory mitral and tufted cells (M/TCs) in the OB stretch the dendrite branches into glomeruli to form synaptic connections with the OSNs which receive odor information (Sakano, 2010; Nishizumi et al., 2019). This is considered a major procedure of odor coding, which is responsible for transferring the received olfactory information to the olfactory cortex for further processing (Igarashi et al., 2012) that bypasses the sensory thalamus (Cleland & Linster, 2003; Neville & Haberly, 2004). Unlike the other sensory modalities, this unique relay enables the OB as a "bottleneck" to modulate the information flow of peripheral olfactory inputs (Kay & Sherman, 2007).

Long-range axonal projections of M/TCs directly target the piriform cortex (PIR), lateral entorhinal cortex (LEC), anterior olfactory nucleus (AON) and cortical amygdaloid nucleus (COA) through the lateral olfactory tract (LOT), where the bundle of afferent fibers converges. As the largest portion of the olfactory cortex, PIR, also known as the "primary olfactory cortex", receives major afferent projections from M/TCs (Igarashi et al., 2012). Subsequently, the projection neurons in PIR connect to higher-order cortical areas, including the prefrontal cortex (PFC) and orbitofrontal cortex (OFC). The secondary center of the olfactory cortex LEC collects olfactory inputs directly from M/TCs and indirectly via PIR principle neurons (Sosulski et al., 2011). The axons of M/TCs and projection neurons in the PIR terminate on LEC layer I, and form synaptic connections with the dendrites of fan cells in layer II and the apical dendrites of pyramidal neurons (PYRs) in

layer II/III (Wouterlood & Nederlof, 1983; Canto et al., 2008), which in turn project to the hippocampal subregions dentate gyrus (DG) and CA1 respectively (Agster & Burwell, 2009; Bitzenhofer et al., 2022). Although both regions are essential for odor processing, PIR has more robust neural representations of odor identity (Bolding et al., 2020; Mena et al., 2023), while LEC is believed to be a top-down regulator especially for integrating olfactory and environmental information (Leitner et al., 2016; Y. Li et al., 2017).

The olfactory system is also strongly modulated by the feedback inputs from the cortical areas and the local OB network, depending on contextual factors like behavioral state and prior knowledge. Centrifugal projections to the OB mainly originate from the downstream cortical areas and target inhibitory neurons in the granule cell layer (GCL) and glomerular layer (GL) to control odor-evoked responses (Boyd et al., 2012; Padmanabhan et al., 2019). Within the OB, the extremely abundant and diverse interneurons (INs) are critical for regulating neurotransmitter release from OSNs and controlling lateral inhibition in glomeruli (Miyamichi et al., 2013; Borisovska et al., 2013; G. Liu et al., 2019; D. Wang et al., 2022), such as granule cells (GCs) and periglomerular cells (PGCs), which are differentiated from the neuroblasts migrating to OB (Livneh et al., 2014), and another subtype short axon cells exhibiting both dopaminergic (DA) and GABAergic features (Batista-Brito et al., 2008; Kiyokage et al., 2010; Vaaga et al., 2017). In addition, the OB receives diverse neuromodulatory innervation, such as serotonergic, cholinergic and noradrenergic inputs (McLean & Shipley, 1987; Le Jeune & Jourdan, 1991; McLean & Shipley, 1991; Geng et al., 2025).

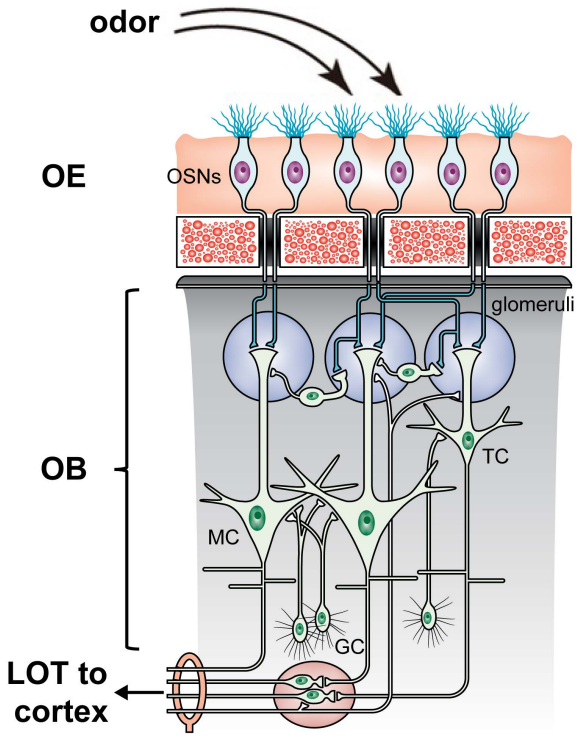

Figure 1.1 Schematic diagram for the olfactory system.

1.1.2 Network activity of the olfactory system

Sensory processing requires relevant neurons to coordinate the electrical activity with great temporal and spatial precision, which is ensured by brain oscillations with the neuronal firing set to a specific phase of the oscillatory cycle (Fries, 2005; M. A. Wilson et al., 2015). Such rhythmic activity has been commonly reported in a huge amount of brain regions and circuits, including the olfactory system.

Low-frequency oscillations in the olfactory system are shown to be driven by sensory and environmental inputs. For example, one of the earliest electrophysiological research discovered the olfactory system is largely entrained by nasal breathing even in the absence of odors (Adrian, 1942). In the past few years, respiration-related rhythm (RR) typically ranging between 2-4 Hz (Verhagen et al., 2007), has been confirmed to coordinate the communications between the OB and other distal brain regions (Moberly et al., 2018; Karalis & Sirota, 2022). This respiration-coupled activity is also found in both PIR and LEC (Fontanini et al., 2003; Tort et al., 2018), indicating respiration has a driving impact on the entire olfactory system. On the other hand, 4-12 Hz theta oscillations in the OB and olfactory cortex are sometimes overwhelmed within RR, owing to the increasing frequency of breathing during sniffing which causes an overlapping with theta frequency range. However, some findings implicated that the level of OB theta activity positively results from the amounts of OSNs (Gretenkord et al., 2019; M. Chen et al., 2020).

High-frequency oscillations are considered to be generated from local network processing in a shorter temporal scale (Buzsáki & Wang, 2012; Fernandez-Ruiz et al., 2023). In the OB, both beta (12-30 Hz) and gamma (30-100 Hz) oscillations arise through the dendro-dendritic reciprocal synapses between M/TCs and GCs (Neville & Haberly, 2003; Fourcaud-Trocmé et al., 2014; David et al., 2015). In particular, the emergence of beta oscillation also requires feedback projections from the olfactory cortex, while gamma oscillation can be locally generated (Neville & Haberly, 2003). On the inter-regional level, the synchrony of beta oscillations in olfactory- and cognitive-related brain regions facilitates the performance in working memory tasks and decision-making processes (Gourévitch et al., 2010; Mori et al., 2013; Rangel et al., 2016; Symanski et al., 2022). On the other hand, gamma oscillations spontaneously emerge out of the balanced excitation-inhibition in awake conditions, with relatively more prominent magnitude compared to that in anesthetized status (Lepousez & Lledo, 2013; A. Li et al., 2012). Moreover, endogenous and odor-induced gamma activity in the OB as well as olfactory cortex are associated with odor perception and discrimination (Beshel et al., 2007; Chapuis et al., 2013; Lepousez & Lledo, 2013; Q. Yang et al., 2022).

1.1.3 Development of the olfactory system

In mammals, most sensory systems are still completely immature at birth, but the olfactory system already maturates early from the embryonic stage (Humphrey, 1940; Walz et al., 2006). Prenatal and early postnatal axonal innervation from the OE to the OB critically contributes to the formation of the topographic olfactory map in which multiple glomeruli get activated with different magnitudes in response to odors (Mori & Sakano, 2011; Nakashima et al., 2019), shaping odor-specific spatial trajectories of neuronal activation that remain stable and firm until adulthood (Tsai & Barnea, 2014). On the functional level, olfactory detection and associated behaviors such as odor discrimination and odor learning emerge as soon as the birth (Miller & Spear, 2008; Schaal et al., 2020). More importantly, since the pups of various species, such as rodents, felines, canines and ursidae, have closed eyelids and ear canals as well as very limited sensorimotor abilities until the later postnatal weeks, the sense of smell is mandatory for their mother-infant interactions and harm avoidance early in life (Logan et al., 2012).

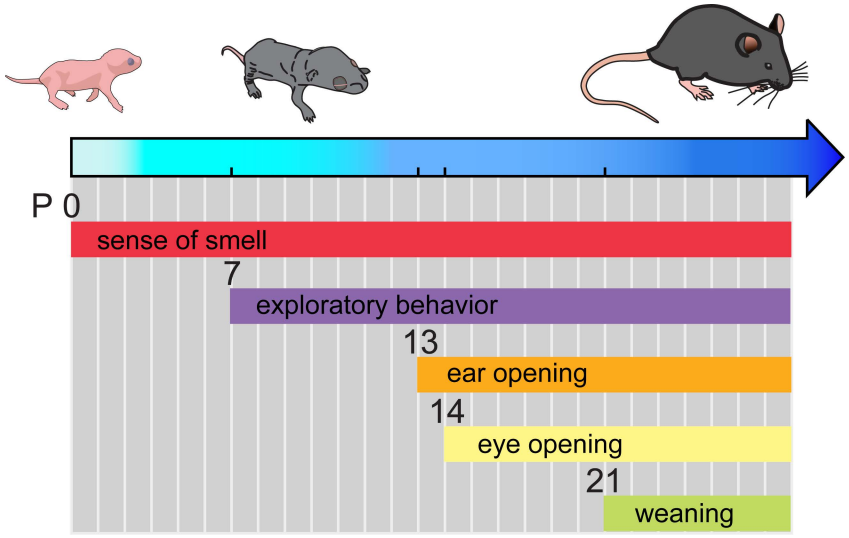

Figure 1.2 Developmental milestones of sensory systems in mice during the first three postnatal weeks.

Although the olfactory system is functional at birth and far more mature than other sensory modalities, it undergoes significant development during the postnatal stage. For instance, the refinement of the olfactory map and the segregation of glomeruli continue postnatally in an activity-dependent manner (H. Zhao & Reed, 2001; C. R. Yu et al., 2004; Albeanu et al., 2018). As a consequence, the neonatal OB requires higher concentrations of odors to get activated compared to the adult OB (Guthrie & Gall, 2003), with more time-locking to the inhalation cycle (Mair & Gesteland, 1982), indicating the response pattern of olfactory processing is also developing along the growth of the system. In addition, OSNs in the OE as well as GCs and PGCs in the OB, are continuously produced throughout life (Hahn et al., 2005; Batista-Brito et al., 2008; Lledo & Valley, 2016), supporting the

differentiation of diverse olfactory functions in the whole lifespan.

The olfactory cortex is a sort of evolutionarily conserved paleocortex with similar developmental chronology across different species (Neville & Haberly, 2004). While the structural formation of the olfactory cortex is well-documented, the postnatal development remains largely unclear. Previous studies have demonstrated different critical periods for the impacts of olfactory deprivation on long-term plasticity and structural modification of synapses in PIR during early days of life (Best & Wilson, 2003; Franks & Isaacson, 2005; Poo & Isaacson, 2007). A recent study recording electrophysiological activity in PIR of awake rat pups reported that the odor-evoked RR (<5Hz) and faster (10-15Hz) oscillations changed rapidly after the first two postnatal weeks (Z. Zhang et al., 2021). Moreover, it has been revealed that the patterns of olfactory-activated neurons in the PIR are different in stability along development for its anterior and posterior parts respectively (Illig, 2007). In terms of LEC, its centrifugal inputs to the OB increase strikingly from the 2nd postnatal week (Kostka & Bitzenhofer, 2022). Additionally, chemical-induced olfactory loss early in life can lead to disruption in oscillatory activity in LEC and less coherent activity between the OB and LEC (Gretenkord et al., 2019).

1.2 The cortical-hippocampal network: architecture, function and development

In mammals, the cortical-hippocampal network refers to an anatomical and functional system formed by many inter-connected brain regions, primarily containing associated neocortices and the hippocampal formation. It is an emerging neuronal framework with ground evidence for its support for cognitive functions, notably learning and memory.

1.2.1 Connection and function of cortical-hippocampal network

The hippocampus (HP) is a seahorse-shaped brain region located in the medial temporal lobe as an extension of the paleo- and archicortex along the biological evolution. It includes three main subregions: DG, the subiculum, and the cornu ammonis (CA) which is further divided into four different portions namely CA1-CA4 (Amaral & Witter, 1989). It is organized along a longitudinal septo-temporal axis which extends from an anterior to a posterior pole. The entorhinal cortex (EC) is not strictly part of the HP, but is included in the broader definition of hippocampal formation. CA1 serves as the main research focus of the HP, receiving inputs from PYRs located in LEC layer II/III and from CA3 through Schaffer collaterals (Witter et al., 2000). Aside from LEC, there are two other main external input sources of the HP: excitatory projections from the medial entorhinal cortex (MEC)

upper layers to CA3 and DG (Buzsáki & Moser, 2013; Donato et al., 2017), and long-range GABAergic projections from PFC to both CA1 and DG (Rajasethupathy et al., 2015; Malik et al., 2022). A yet-to-solve question is whether the functional division of HP simply fits the dichotomy that differentiates the HP along the dorsal-ventral axis. The dorsal part of HP is widely considered the "compass" in the brain responsible for spatial navigation characterized by the place cells (O'Keefe, 1978; Jeffery, 2007), and context memory encoding and consolidation (Moser et al., 1995; Maren & Holt, 2000), while the intermediated/ventral parts of HP are proposed to account for context representation, motivational and emotional regulation, and threat avoidance (Bannerman et al., 2014; Strange et al., 2014; Barr et al., 2018; Peng et al., 2024). In general, hippocampal formation, especially the coupling between HP and EC, is necessary for diverse forms of learning and memory (Suh et al., 2011; Y. Li et al., 2017; Kitamura et al., 2017; Fernández-Ruiz et al., 2021).

The PFC covers the front parts of the frontal lobe of neocortex in the mammalian brain, including the anterior cingulate, prelimbic and infralimbic subregions (Chini & Hanganu-Opatz, 2021). The organization of PFC laminar organization follows the same inside-out migration pattern as the other neocortical areas, in which early-born neurons form deep layers V/VI, while late-born neurons are located in upper layers II/III (Nadarajah & Parnavelas, 2002). Deep layer prefrontal PYRs are found to be the main receivers of the hippocampal projections, with intermediate/ventral CA1 providing the glutamatergic neuronal innervation (Jay et al., 1989; Brockmann et al., 2011; Bitzenhofer et al., 2015; Ahlbeck et al., 2018). In turn, PFC specifically projects to the dorsal portion of HP as mentioned above. Besides, PFC is modulated by diverse sensory systems including sensory thalamus and sensory cortices. Paticularly for the olfactory system, long-range monosynaptic axonal projections of LEC target the deep layer prefrontal neurons mainly in the prelimbic subregion (Hartung et al., 2016a; Xu et al., 2021), while PIR, AON and olfactory thalamus connect with more ventral parts of the PFC through unidirectional or bidirectional interactions (J. L. Price, 1985; Ray & Price, 1992; Vertes, 2004; Illig, 2005; Courtiol & Wilson, 2015). As a cortical area involved in top-order cognitive functions, PFC is believed to be the central processor in the brain to regulate a wide range of complex behaviors, such as reinforce learning (J. X. Wang et al., 2018; Muller et al., 2024), emotional and social controls (Volman et al., 2011; Franklin et al., 2017), and decision making (Barraclough et al., 2004; Aoi et al., 2020).

In the last decade, the interactions between the areas within the neocortical-hippocampal network have been shown to coordinate a broad spectrum of cognitive abilities, which are highly dynamic processes requiring precise timing of network activity. Impressively, different patterns of long-range coupling between electrical activity in PFC

and HP manifest during sensory and memory processing, including identical-frequency synchrony (Jones & Wilson, 2005; Sigurdsson et al., 2010; Nardin et al., 2023), cross-frequency coupling (Tamura et al., 2017; Wirt & Hyman, 2019; W. Yu et al., 2021), and intricate interaction of cortical ultra-slow oscillations (e.g., up-down states), hippocampal ripples with spiking activity (Staresina et al., 2023). Also, EC and HP mainly communicate via theta and gamma oscillations, which contributes to several forms of learning and memory, such as the encoding and retrieval of spatial information as well as association memory (Colgin et al., 2009; Buzsáki & Moser, 2013; Igarashi et al., 2014). Recently, cortical up-down states have been found to regulate hippocampal ripples during sleep memory consolidation (Zutshi & Buzsáki, 2023; Shin & Jadhav, 2024). The fundamental role of neocortical-hippocampal network architecture especially the inter-regional connectivity in adult brains is lately coming more and more into the research focus (Luo et al., 2022; Malik et al., 2022; Kim et al., 2023; Elston & Wallis, 2025).

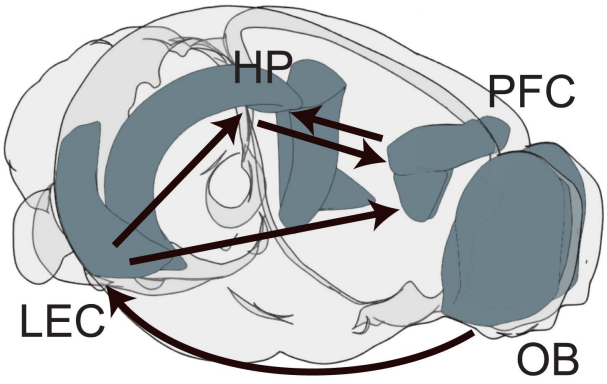

Figure 1.3 Schematic of main neuronal projections of the olfactory-hippocampal-prefrontal network.

1.2.2 Functional development of cortical-hippocampal network

The cortical differentiation starts from the late embryonic period and gets fine-tuned along development (Katz & Shatz, 1996; Hanganu-Opatz et al., 2021). Numerous experimental and theoretical findings have suggested that the development of sensory cortices, that are not responsive to sensory cues (e.g., visual and auditory stimuli) during the neonatal stage, critically depends on the endogenously-generated electrical activity of the corresponding sensory systems. For example, spontaneous retinal activity is relayed via the thalamus to the primary visual cortex (V1), where it drives coordinated burst-like oscillatory discharges and neuronal firing (Ackman et al., 2012; Hanganu et al., 2006). Visual deprivation from early postnatal days on decelerates synaptic formation and disrupts the maturational process in V1 (D. J. Price et al., 1994; Zheng et al., 2014) as well as its connectivity with the visual thalamus (Hofer et al., 2009). Similarly, acoustic inputs are necessary for the topography and activity in the auditory cortex along development (E. F. Chang & Merzenich, 2003; Nakahara et al., 2004; Xue et al., 2022), and whisker trimming impairs

both the morphological and functional development of the somatosensory cortex (L.-J. Lee et al., 2009; Sieben et al., 2015). The functional properties of the developing higher-order cortical regions, such as the PFC, were less well-investigated than the primary sensory cortices. This is largely due to their maturation starts only after the sensory cortices are functional (Gogtay et al., 2004) and continues into adulthood (Fuster, 2002). Except for the influence of sensory peripheries on cortical formation, recent studies showed that the functional maturation of PFC relies on coordinated patterns of neuronal activity during development, in which manual activation of PFC principle neurons during early postnatal development leads to long-lasting excitation/inhibition imbalance of PFC local circuit, and declined associated cognitive abilities (Bitzenhofer et al., 2021; Medendorp et al., 2021). It is also shown that PFC refinement during late development, together with the acceleration of gamma oscillations and maturation of INs, is essential for higher-order cognitive functions (Piekarski et al., 2017; Bitzenhofer et al., 2020; Schalbetter et al., 2022; Z. Wang et al., 2022; Pöpplau et al., 2024).

HP is one of the brain regions that have the most active electrical activity (Garaschuk et al., 2000; Leinekugel et al., 2002), with several network activity features manifesting in the early postnatal days, including transient bursts of low-frequency oscillatory activity (Brockmann et al., 2011; Ahlbeck et al., 2018) and early sharp waves (eSPWs) (Leinekugel et al., 2002; Karlsson et al., 2006). Both types of activity patterns are largely coordinated by the direct anatomical upstream regions, which are developmentally more mature, such as EC, medial septum (MS) and thalamus (Janiesch et al., 2011; Valeeva et al., 2019; Leprince et al., 2023; Shipkov et al., 2024). Interestingly, although the HP does not directly connect to the sensory peripheries, its functional development is also sensitive to diverse sensory modalities. For instance, manual eyelid parting earlier than normal eye-opening accelerates the development of excitatory synaptic transmission within HP and alters spatial working memory later in life (Dumas, 2004), and exposure to structured noise during development impairs later hippocampal-related learning (Y. Zhang et al., 2021). On the other hand, long-term postnatal whisker deprivation leads to impaired morphology of PYRs in HP (Yarmohammadi-Samani et al., 2022), and twitches during early postnatal days promote spontaneous HP activity (Leprince et al., 2023), indicating that sensorimotor activity also contributes to the development of HP.

Similar to what was found in the adult brain, the strength of hippocampal-prefrontal connections increases along the septo-temporal axis, which is established as a unidirectional monosynaptic pathway already within the first postnatal week (Brockmann et al., 2011; Ahlbeck et al., 2018). In line with this, the PFC activity, as well as long-range HP-PFC coupling, are driven by the direct neuronal innervations and the activity patterns in intermediate/ventral HP during early development (Brockmann et al., 2011; Ahlbeck et

al., 2018; L. Song et al., 2022; Pochinok et al., 2024). Furthermore, it has been shown that neonatal PFC activity is highly dependent on the direct/indirect inputs relayed by HP. For example, deactivation of LEC leads to reduced oscillatory power in PFC (Hartung et al., 2016a; Xu et al., 2021; Kostka & Hanganu-Opatz, 2023), which is comparable to the consequence after removing cholinergic inputs from MS (Janiesch et al., 2011). All of these suggest that the functional development of cortical–hippocampal network is not an island isolated from the broader brain circuits along development.

1.3 The link between olfaction and cognition in health and disease

The nature of the relationship between olfaction and cognition has not been well elucidated. However, based on the anatomic proximity of brain regions critical for learning and memory with the olfactory system (within 2-3 synapses), as well as their strong attachment to neurological conditions, it becomes a fundamental question to understand how they interact with each other.

1.3.1 The involvement of the olfactory network in cognitive processing

The existence of olfactory memory is prominent during developmental period. The preference for maternal odors is believed to be the initial olfactory memory of infants, which is already formed prenatally (Marlier et al., 1998). Gestational exposure to odors significantly influences the preferences for the same odorants, which can last several months or even years (Mennella et al., 2001; Wagner et al., 2019). For the contribution of postnatal odor experience on behavior, the research focus was mainly restricted to fear conditioning (Sullivan et al., 2000; Sevelinges et al., 2008), and emotional and social controls (Inoue et al., 2021; Mochizuki-Kawai et al., 2022). In contrast, the correlation between olfactory memory and the olfactory system has been well identified. For example, specific ensembles of PIR neurons are confirmed as critical contributors to fear memory recall induced by olfactory cues (Meissner-Bernard et al., 2019); activation of α-amino-3-hydroxy-5-methyl-4-isoxazolepropionic acid (AMPA) receptors in PIR impairs olfactory learning (Shimshek et al., 2005). LEC is required for odor-associative memory in both odor cue–reward association (J. Y. Lee et al., 2021), odor-negative valence association (P. Liu et al., 2023) and odor-environmental context association (Persson et al., 2022). As the first relay station of olfactory information, the OB is mainly top-down driven by the feedback inputs from higher-order brain regions during cognitive processing especially odor learning

to enhance odor discrimination in a "gain-control" manner (Boyd et al., 2012; Adams et al., 2019; Trejo et al., 2023). On the other hand, olfactory learning is shown to correlate with the neurogenesis within the OB local circuit (Sultan et al., 2011; Sakamoto et al., 2014), which is functionally comparable with that in hippocampal DG (Akers et al., 2014).

In the context of non-odor related behaviors, earlier studies have documented that lesions of the OB in adult animals caused various forms of behavioral dysfunctions, including lower levels of social facilitation, depressive-like behavior, and memory deficits (Guthman et al., 1979; Q. Li et al., 2023; Yuan et al., 2021). Suppression of OB neurons promotes anxiety in rats (Salimi et al., 2019; Q. Li et al., 2023), largely due to the involvement of the OB-driving HP-PFC pathway in anxiety-related behaviors (Padilla-Coreano et al., 2016). A recent study reported the important role of OB in spatial working memory by coordinating the oscillatory activity in the EC (Salimi et al., 2021, 2022). In humans, the RR which is prominent in the OB and other distal brain regions has been identified to coordinate memory retrieval and consolidation (Zelano et al., 2016; Arshamian et al., 2018; Nakamura et al., 2018; Sheriff et al., 2024), suggesting the influence of olfactory inputs on learning and memory. The olfactory cortical areas also show their involvement in non-odor memory. For example, the hyperexcitation of PIR is induced by chronic social stress, which further contributes to the impairments in learning and memory (H. Wang et al., 2022). In addition, LEC is regularly reported to encode context information during memory tasks, which is not restricted to odors but also objects and environments (Tsao et al., 2013; D. I. G. Wilson et al., 2013; Vandrey et al., 2020; Tozzi et al., 2024). Interestingly, despite HP being proposed to form the memorized information (Lisman & Morris, 2001; Teyler & Rudy, 2007), recent research showed that the long-range neocortical oscillatory synchrony mediated by LEC can restore the hippocampal-dependent memories in HP-lesioned mice (Luo et al., 2022), which indicates the olfactory system is tightly coupled to the neocortical-hippocampal networks on the functional level. As for the neurodevelopment aspect, it has been previously revealed that activity in OB boosts the oscillatory patterns in LEC and drives the synchronization of the neocortical-hippocampal network during early postnatal days (Gretenkord et al., 2019; Kostka & Hanganu-Opatz, 2022). However, it remains completely unknown whether neonatal olfactory inputs exert a pivotal influence on cognitive processing which is highly dependent on cortical-hippocampal networks.

1.3.2 Anosmia and cognitive disorders in neurological diseases: coexistence and progression

Neurodevelopmental diseases refer to a group of psychiatric disorders characterized by atypical brain development. A prominent feature of neurodevelopmental disorders is the impairments in sensory processing, which is correlated with altered patterns of coordinated network activity and connectivity (Schechter et al., 2003; Y.-S. Chang et al., 2014; Chini & Hanganu-Opatz, 2021; Siper et al., 2022). Accumulating evidence has indicated an association of olfactory impairment with neuropsychiatric disorders. For example, patients diagnosed with schizophrenia (SCZ) exhibit cognitive deficits along with olfactory dysfunction and reduced volumes of OB, PIR and EC measured by magnetic resonance imaging (MRI) (Turetsky et al., 2000; Corcoran et al., 2005; Nguyen et al., 2011; Kamath et al., 2019; K. Yang et al., 2021). A recent study shows a mouse model that mimics inflammatory processes in the OE of first-episode psychosis patients, has reduced glomerular size, decreased numbers of OSNs and M/TCs, and OB volume reduction (K. Yang et al., 2024). Similarly, children with autism spectrum disorder (ASD) are observed to have impaired odor identification and reduced odor-evoked activity (Bennetto et al., 2007; Koehler et al., 2018). Moreover, several susceptibility genes of ASD are highly relevant to the olfactory network dysfunction: Shank3 deficiency impairs synaptic transmission between the OB and PIR (Mihalj et al., 2024), while Tbr mutation results in reduced INs and morphological alteration of MCs in the OB (T.-N. Huang et al., 2019), both of which further contribute to impaired olfactory detection and discrimination (Drapeau et al., 2018; T.-N. Huang et al., 2019; Ryndych et al., 2023). Thus, in neurodevelopmental diseases, olfactory dysfunctions together with neurobiological alterations in the olfactory neuronal network are detected simultaneously.

Coincidentally, although neurodegeneration is primarily affected by aging and usually occurs in the later stage of life, the progression of neurodegenerative diseases is always accompanied by early onset olfactory deficits, including abnormal behavioral phenotypes and impaired neuronal networks. The pathology of Alzheimer's disease (AD) is featured by amyloid plaques formed by amyloid beta (Aβ) deposition and neurofibrillary tangles composed of hyperphosphorylated tau proteins which accumulate in age-related manners (Ballard et al., 2011; Goedert & Spillantini, 2006; Braak & Del Tredici, 2015). Both pathological markers have been shown to significantly impact the olfactory system, such as neuronal loss or damage (J. Zhang et al., 2018; S. Li et al., 2019; M. Chen et al., 2020; Ziegler-Waldkirch et al., 2022), regional volume reductions (Thomann et al., 2009a; Thomann et al., 2009b; Steinbart et al., 2023), and aberrant network patterns in olfactory circuits (Wesson et al., 2011; M. Chen et al., 2020; W. Li et al., 2019; S. Li et al., 2019). Interestingly, these structural and functional alternations often precede the onset of cognitive decline associated with the functions of HP and PFC, and the impaired inter-regional communications of neocortical-hippocampal networks (Attems et al., 2014;

Murphy, 2019; M. Chen et al., 2020; Salimi et al., 2022). Likewise, anosmia is an early and prevalent non-motor symptom in Parkinson's disease (PD) (Ross et al., 2008; Doty, 2012, 2017; Haehner et al., 2009), with impaired dendro-dendritic synaptic interplay in OB and long-range connectivity in olfactory circuits (F. Chen et al., 2021; Martin-Lopez et al., 2023; S.-S. Wang et al., 2024). In view of these findings, a basic question is whether olfactory dysfunction is a cause or consequence of these diseases.

One of the most notable shared clinical manifestations in both neurodevelopmental and neurodegenerative diseases is the cognitive decline strongly attributed to HP dysfunction (Roy et al., 2016; Hartung et al., 2016b; Dintica et al., 2019; S.-S. Wang et al., 2024; Rexrode et al., 2024). Lately, some long-term investigations revealed that the pandemic Coronavirus disease 2019 (COVID-19), with which nasal inflammation and anosmia as the predominant symptoms, result in long-lasting memory impairment and early-stage dementia in a large population of recovered patients (LaRovere et al., 2021; Méndez et al., 2022; S. Zhao et al., 2022; Hampshire et al., 2024). Also, the HP of COVID-19 patients is hugely affected by COVID-19 propagation, with neuronal atrophy and reduced neurogenesis (Nouraeinejad, 2023). Though the timelines for the occurrence of cognitive symptoms and olfactory dysfunction are different in the mentioned categories of diseases, the tight anatomical connections between the olfactory system and neocortical-hippocampal system provide some hints for speculating that the pathological changes of neurological disorders originate from the olfactory system.

1.4 Thesis overview and summary of results

The overarching priority of this thesis is to investigate whether olfactory processing during a specific period during neonatal age is crucially involved in the functional development of the cortical-hippocampal networks, and the long-term influence of olfactory inputs on higher-order cognitive abilities along development. To answer these questions, I mainly combined cutting-edge *in vivo* electrophysiology, odor/optogenetic stimulations, with morphological and behavioral assessments, and applied the data analysis of continuous time-series and behavioral assays using advanced computational methods, with the aim of evaluating the possible contributions of early olfactory inputs to cognitive formation on structural, functional and behavioral levels. Based on the inspiring findings, the correlation between olfaction and cognition in neurological conditions was examined by reviewing the literature and experimentally exploring the olfactory functions in a neuropsychiatric mouse model.

Chapter 2.2.1 identifies the potentially critical role of neonatal olfactory inputs in the functional development of entorhinal-hippocampal circuits by selectively silencing the

synaptic outputs of M/TCs, the main projection neurons in the OB, during postnatal days (P) 8–10 of mice using chemogenetics. Importantly, via monitoring the long-term consequences of this early manipulation on the network activity and communications as well as on cognitive abilities, it unveils that OB activity during a specific sensitive period of neonatal development shapes cognition later in life and its underlying circuitry structurally and functionally, with results showing a long-lasting decrease of inter-regional coupling and weaker responsiveness to stimuli within developing LEC-HP network, accompanied by the impairments in associated behavioral performance and entorhinal dendritic complexity after the transient M/TC silencing. Taking advantage of the uniquely tight connectivity between the olfactory system and hippocampal formation accounting for cognitive abilities throughout life, it fills the longstanding knowledge gap regarding the interplay between neonatal sensory and higher cognitive functions in the field.

Chapter 2.2.2 presents an efficient approach to dissecting functional brain formation during early development using optogenetics. By introducing the comprehensive workflow to combine time-precise activation of M/TCs mediated by viral tool transduction with *in vivo* acute electrophysiology, it provides a detailed possibility of how to implement *in vivo* optogenetics methods with millisecond-scale temporal precision on developing olfactory network, which helps to identify the function of the local and long-range neuronal connectivity, and adaptable for other brain circuits or cell types. A range of specific parameters of light stimulation are tested here with verifications on the network effect level through electrophysiological recordings, which offers a reference for the successful application of the method by monitoring light-evoked neuronal and network activity.

Chapter 2.2.3 is a review that tries to clarify the intricate relationship between olfactory deficits and neurodevelopmental/neurodegenerative diseases. Olfactory dysfunction has been found to manifest as a hallmark feature shared among diverse neurological conditions preceding the typical symptoms, including both neurodevelopmental and neurodegenerative disorders which are usually associated with impaired cognitive performance. Nonetheless, there is insufficient attention on the link between these diseases with common pathophysiological changes especially in the olfactory system. It details the olfactory deficiency accompanied by neurodegenerative and neurodegenerative disorders on the functional level, brain structural level and neural network level. With the existing sound evidence across species, it examines potential shared mechanisms underlying olfactory dysfunctions in both categories of neurological disorders, such as neuronal loss, reduced neurogenesis, impaired synaptic transmission, and altered neurotransmitter signaling, and concludes by highlighting that olfactory deficits are an important reflection of the disease propagation which can serve as a pre-clinical diagnostic indicator to identify individuals at clinically high risk, instead of simple

epiphenomenon.

Chapter 2.2.4 corroborates the assumption of the previous chapters by measuring the possible alternations in the olfactory network and behavior in a mouse model with the combination of genetic mutation and environmental stressors for mental disorders. Besides, it highlights the driving impact of endogenous OB activity on developing hippocampal-prefrontal networks in this mouse model with diminished inter-regional coupling and reduced directionality from the OB to HP and PFC respectively, which deepens the earlier findings for the impaired hippocampal-prefrontal circuitry at the same neonatal age. In a call with the last chapter, it points to the potential of olfactory network dysfunction as an early marker for neurodevelopmental diseases associated with cognitive deficits.

Chapter 2.2.5 probes into the statistical distribution of neuronal spiking properties by utilizing a large-scale *in vivo* extracellular recording dataset. Impressively during early development, different brain regions maturate at different speeds: basic sensory areas become mature relatively early, while areas involved in higher-order cognitive functions continue to develop into adolescence and early adulthood. Through the analysis of the neuronal firing parameters specifically recorded from OB—the early developed region, and PFC—the constantly developing region of mice in an age range of P4-60, it shows that firing rates and pairwise correlations of the single-unit spiking have a largely stable distribution shape along development, which is similar to what was found in the adult brain. The neural network modeling further supports that the extremely distributed synaptic parameters are necessary to recapitulate the experimental data, suggesting that functional and structural parameters in the developing brain already have an extreme distribution. It concludes with a preconfigured framework of the brain and that experience-dependent processes do not fundamentally alter this aspect of the organization of the brain.

2 | Methods and Results

2.1 Materials and methods

2.1.1 Animals

All experiments were performed in compliance with German laws and guidelines of the European Community for using animals in research and were approved by the local ethical committee (Behörde für Gesundheit und Verbraucherschutz Hamburg, G17/015, N18/015, N19/121). Timed-pregnant mice from the University Medical Center Hamburg-Eppendorf animal facility were housed individually at a 12 h light/12 h dark cycle and were given access to water and food *ad libitum*. The day of vaginal plug detection was considered as embryonic day (E) 0.5, and the day of birth was considered as P0. Experiments were carried out on wild-type (WT) C57BL/6J (JAX#000664) mice, Tbet-cre (B6; CBATg (Tbx21-cre) 1Dlc/J, JAX#024507) mice or DISC1 (B6.129S6-Disc1^{tm1Kara}) mice of both sexes. Genotypes of Tbet-cre positive (Tbet-cre^{+}) and Tbet-cre negative (Tbet-cre^{-}) mice were determined from polymerase chain reaction (PCR) and using genomic deoxyribonucleic acid (DNA) and the following primer sequences (Metabion, Planegg/Steinkirchen): forward primer 5'-ATCCGAAAAGAAAACGTTGA-3' and reverse primer 5'-ATCCAGGTTACGGATATAGT-3' and visualized with gel electrophoresis. For experiments in Chapters 2.2.1 and 2.2.2, Tbet-Cre^{+} and Tbet-Cre^{-} littermates were used for experimental or control groups, respectively. Genotypes of DISC1 mice were determined from PCR using genomic DNA and the following primer sequences: forward primer 5'-TAGCCACTCTCATTGTCAGC-3' and reverse primer 5'-CCTCATCCCTTCCACTCAGC-3' and visualized with gel electrophoresis. For experiments in Chapter 2.2.4, pregnant DISC1 mice received intraperitoneal (i.p.) injection of viral mimetic polyinosinic:polycytidylic acid (poly(I: C)) to induce maternal immune activation (MIA), with heterozygous offspring defined as dual-hit genetic-environmental (GE) mice. The offsprings of non-treated WT mice were used as controls.

2.1.2 *In vivo* microinjection and intraperitoneal injection

a) Virus injection for transfection of M/TCs with hm4Di and ChR2

On P1, Cre^+ and Cre^- mice were anesthetized with isoflurane (3 %) and fixed into a stereotaxic apparatus (Stoelting) and AAV9-EF1a-DIO-hM4Di-mCherry (Plasmid #50461, Addgene) at titer $\geq 1\times10^{13}$ vg/mL was injected bilaterally into both OBs (200 nL for each side) at a rate of 100 nL/min using a syringe infusion microinjector (MICRO4, WPI). Following the injections, the syringe was left in the injection place for an additional 2 min to avoid reflux of the fluid then slowly withdrawn. For the subset of animals used for optogenetics in Chapter 2.2.1, injection of AAV9-EF1a-DIO-hM4Di-mCherry was mixed with the simultaneous injection of AAV9-Ef1a-DIO-hChR2(E123T/T159C)-EYFP ($\geq1\times10^{13}$ vg/mL, Plasmid #35509, Addgene) at a ratio of 1:1. For the animals used for optogenetics in Chapter 2.2.2, injection of AAV9-Ef1a-DIO-hChR2(E123T/T159C)-EYFP was performed in the right OBs (200 nL) at a rate of 100 nL/min. After each injection, the tip of the syringe was left *in situ* for an additional 2 min to avoid leak or reflux of the fluid then slowly withdrawn. Next, the pup was maintained on a heating blanket until full recovery and returned to the dam. The illustration of the virus injection procedure is included in Chapter 2.2.2. Expression of hM4Di-mCherry and ChR2-EYFP were detected using a dual fluorescent protein flashlight (Electron Microscopy Sciences) before surgery and confirmed post-mortem. Only mice with sufficient expression of fluorescence were included in the experiments and analysis for the experimental group.

b) Virus injection for retrograde tracing in HP

For the retrograde labeling of CA1-projecting neurons, P3 or P9 hM4Di transfected (injected into bilateral OBs on P1) mice were anesthetized with isoflurane (3 %) and head fixed in a stereotactic apparatus. Retrograde virus AAVrg-CamKIIa-EYFP (50 ml at titer $\geq 1\times10^{12}$ vg/mL, #50469-AAVrg, Addgene) was injected into the dorsal CA1 of HP (1.0 mm posterior to bregma, 1.2 mm lateral from the midline, 0.8-0.9 mm deep from the skull for P3 and 1.1-1.2 mm deep from the skull for P9) at a rate of 50 nL/min. Following the injection, the syringe was left in the injection place for an additional 5 min then slowly withdrawn.

c) Intraperitoneal injection

For chemogenetical inhibition of vesicle release on M/TC axons in Chapter 2.2.1, Compound 21 (C21, Hello Bio, 0.3 mg/mL dissolved in 0.9% NaCl) was i.p. injected at P8, P9 and P10 (or at P13, P14 and P15) once a day into both Cre^+ and Cre^- mice at a dose of 3 mg/kg. Saline-injected Cre^+ pups (same dosage as for C21) were used as controls for the light-stimulation experiments. For generating GE mice in Chapter 2.2.4, timed-pregnant

DISC1 mice received i.p. injection of poly(I:C) at E9.5 at a dose of 25 mg/kg.

2.1.3 *In vivo* electrophysiology and stimulations

a) Surgery

In vivo extracellular recordings were performed on P4-P23 mice. Under isoflurane anesthesia (5 % for induction and 2.5 % for maintenance; Braxter), the skin above the skull was removed and the neck muscles were administered local anesthetic (0.25% bupivacaine/1%lidocaine) for pain relief. Then the neck muscles were cut off to reduce muscle artifacts. Two plastic bars for head fixation in the recording setup were mounted on the nasal and occipital bones with dental cement (Omin Dent) for tight head fixation during the recordings. The bone above the right OB (0.5-0.8 mm anterior to frontonasal suture, 0.5 mm lateral to inter-nasal suture), LEC (0 mm posterior to lambda, 6-7.5 mm lateral from the midline), HP (1.0 mm posterior to bregma, 1.2 mm lateral from the midline) and PFC (0.5 mm anterior to bregma, 0.1–0.5 mm lateral from the midline) was carefully removed by drilling a hole of <0.5 mm inside diameter. Another hole in the skull over the cerebellum was drilled to insert a reference wire. After a recovery period of 20 min, pups were transferred to the setup for electrophysiological recording where they were head-fixed into a stereotaxic apparatus (Stoelting). The temperature was maintained at 37℃ with a heating pad throughout the entire surgery and recording. The illustration of the surgery procedure is included in Chapter 2.2.2.

b) Acute multi-site electrophysiological recordings

One-shank electrodes (NeuroNexus) with 16 recording sites (50 µm inter-site spacing for recordings in OB and PFC, 100 µm inter-site spacing for recordings in LEC and HP), which were mounted on the headstages of a multichannel extracellular amplifier (Neuralynx), were stereotactically inserted into OB (1.6-2 mm, angle 0°), LEC (depth: 2-2.4mm, P11, angle: 90°; P16-23, angle: 15°), HP (1.2-1.7 mm, angle 0°) and PFC (1.8-2.1 mm, angle 0°) using micromanipulators. Before the insertion, the electrode tips were rinsed with DiI (1,1'-Dioctadecyl-3,3,3',3'-tetramethylindocarbocyanine perchlorate, Molecular Probes) to visualize the electrode position in post-mortem histological confirmation. For light stimulation, one-shank opto-electrodes (NeuroNexus) with the same configuration as the electrodes were attached with the optic patch cable and inserted into the OB. A silver wire was inserted into the hole over the cerebellum at an approximate depth of 1 mm as ground and reference. Pups were allowed to recover for 15 min before data acquisition to maximize the stability of the recordings and the quality of spiking activity. Extracellular signals were band-pass filtered (0.1-9,000 Hz) and digitized (32000 Hz) with the extracellular amplifier

and acquisition software (Neuralynx). The illustration of multi-site electrophysiological recordings procedure is included in Chapter 2.2.2. Spontaneous activity was recorded for at least 20 min before odor or light stimulation.

c) Olfactory stimulation

A custom-made olfactometer with a stream of clean air (900 ml/min) pointed at the mouse snout was used in Chapters 2.2.1 and 2.2.4. Odors were applied for 2 s triggered by the respiration cycle of the mice to ensure constant odor concentration at the 1st odor inhalation, and the odor delivery was controlled by a pre-programmed controller (Arduino). Two different odors (vanillin:, 1:100 m/v diluted in distilled water; isoamyl acetate: 1:100 v/v diluted in mineral oil) were delivered in a randomized order for 40-60 repetitions. The transistor-to-transistor logic (TTL) signals for odor On/Off were recorded together with the extracellular recording data.

d) Light stimulation

To activate M/TCs expressing ChR2 in Chapters 2.2.1 and 2.2.2, blue light (473 nm) stimulation was applied using a diode laser (Omicron) which was controlled by a pre-programmed controller (Arduino) to deliver 3 ms square pulses of blue light at a rate of 2/4/8/16/32 Hz (30 repetitions for each frequency), with alternating epochs of 3 s On/3 s Off. Laser power (ranging between 0.05–0.4 mW) at the tip of the optical fibers was adjusted for every recording to reliably induce neuronal spiking activity as the successful activation of M/TCs. The TTL pulse signals for light delivery were recorded together with the extracellular recording data.

2.1.4 Behavioral tests

a) Developmental milestones

Somatic and reflex development was examined every day in P2-11 mice (for P2-6 the tests were performed every 2nd day). Weight, body length and tail length were measured at the same time on each testing day. Forelimb grasp was assessed as time hanging on a toothpick grasped with the forepaws until falling. Cliff aversion was measured as the time until withdrawing after being positioned with forepaws and snout over an elevated edge. Surface righting was measured as time to flip over onto its abdomen after being positioned on the back. Ear twitch was measured as the pup responded to brushing the ear with the cotton tip (the test is terminated if the mouse does not respond within 30 s). Rooting was measured as the pup moved its head toward the cotton tip (the test is terminated if the mouse does not respond within 30 s). For spontaneous locomotion, the mouse is placed in the center of a circular arena (13 cm inside diameter) and allowed to freely explore the arena for 3 min.

The movements of mice were video tracked using a fixed camera (BOSCH).

b) Neonatal odor preference

Odor preference of neonatal mice was tested for 3 min using a testing apparatus that consisted of a rectangular acrylic chamber (17.5×6.5×6.5 cm) with metal grid flooring, divided into two 6.5 cm approach zones located on either end of the chamber, and a 4.5 cm neutral zone in the center. Left and right fields were odorized by placing 6.5 cm×6.5 cm acrylic trays beneath the grid flooring, each containing 10 g of bedding taken from either the homecage of the test pups or fresh bedding soaked with 1% vanillin (w/v, in distilled water). For each test, the pup was placed in the center of the arena. All tests were performed at room temperature. Between each test, the chamber was cleaned with distilled water thoroughly to neutralize all odors, and the positions of the odor field trays were randomized. Mice were video-tracked using a fixed camera (BOSCH).

c) Neonatal odor learning

Odor learning of neonatal mice was tested at P10 or P11. For one-trial associative odor learning, the dam was removed from the home cage for 2 h before the test odor was applied to the teats of the dam with a saturated cotton swab. Then the dam was placed back to the home cage for 1 h. 1% isoamyl acetate and ethyl butyrate (v/v, in mineral oil) were used randomly as test and control odors per litter. The dam was removed again for 2 h before the P10 pups were tested in the odor-place preference test with the same testing apparatus as above. Left and right fields were odorized by placing acrylic trays beneath the grid flooring with 500 µl of either the test odor or a control odor on filter paper. Test and control odors were randomized between the two odor zones. For each test, the pup was placed in the center of the arena and video-tracked for 3 min using the fixed camera. Between each test, the chamber was cleaned with 70% ethanol to eliminate the odors and allowed to dry. Odor-place preference tests were performed with pure odors (1% in mineral oil) or odor mixtures (90/10, 80/20 test/control odor). To assess long-term neonatal odor memory, the dam was removed for 2 h on the following day (P11) and the odor-place preference test was repeated with pure test versus control odor (1% in mineral oil).

d) Open field test

Mice at P15 were positioned in the center of a circular arena (34 cm inside diameter) and allowed to freely explore the arena for 10 min after 30 s adaptation. The test room was dimly illuminated. Additionally, the floor area of the arena was digitally subdivided into 8 zones (4 center zones and 4 border zones) using the zone monitor mode of the VideoMot 2 software (TSE Systems GmbH). Between each open field test (OFT), the arena was cleaned with 0.1% acetic acid. The spontaneous exploration was video-tracked with the fixed

camera.

e) Object recognition tests

All tests for assessing object recognition memory in pre-juvenile mice consisted of familiarization and testing trials. Novel object recognition (NOR, on P16) and object location preference (OLP, on P19) tests were performed in the same arena as the OFT. Objects used for object recognition tests were six differently shaped, textured and colored items with magnets for fixing them to the ground of the arena. Object sizes (height: 3 cm, diameter: 1.5-3 cm) were smaller than the size of a mouse and did not resemble living stimuli (no eyespots or predator shapes). For the NOR test, each mouse was allowed to explore two identical objects for 10 min during the familiarization trial. After a delay period of 5 min, the mouse was placed back in the arena for the test trial, where one of the objects was replaced by a novel object. In the OLP task, each mouse was allowed to explore two different objects for 10 min during the familiarization trial. After the 5 min delay period, the mouse was placed back to investigate one old object which was previously presented and a copy of the old object for 5 min. After each trail, both the arena and objects were cleaned with 0.1% acetic acid to eliminate the odors. Behavior was video-tracked with the fixed camera.

f) Spontaneous alternation

An elevated Y-maze which consisted of three identical arms with a 120° angle was used to test the spontaneous alternation of mice aged P23-24. Each mouse was placed in the start arm of the Y-maze and allowed to freely explore the maze for 10 min. To prevent mice from jumping out of the maze, the maze was covered by a plexiglass plate during the test. After each test, the maze was cleaned with 0.1% acetic acid. The behavior was video-tracked with the fixed camera.

2.1.5 Histology

a) Perfusion

Mice were deeply anesthetized with overdose i.p. injection of an anesthetic cocktail consisting of 10% ketamine and 2%xylazine diluted in 0.9% sodium chloride (NaCl) solution. After assessment of lack of pain reflexes with toe and tail pinch, mice were transcardially perfused with 0.9% NaCl to clean out the blood, followed by Histofix (Carl Roth) containing 4% paraformaldehyde (PFA) to preserve the tissue structure and morphology. Brains were carefully extracted from the skulls and post-fixed in 4% PFA at 4°C for 12–24 h before further cutting.

b) Immunohistochemistry

Brains were sliced using a vibratome (Leica). For brains injected with AAVrg-CamKIIa-EGFP in CA1, free-floating 50 mm-thick slices containing HP and LEC were permeabilized and blocked with phosphate-buffered saline (PBS) containing 0.2% Triton X-100 (Sigma-Aldrich), 5% normal bovine serum (BSA, Jackson Immuno Research) and 0.02% sodium azide (Sigma-Aldrich). Slices were incubated with primary antibody rabbit-anti-GFP (1:500, #ab6556, Abcam) diluted in 0.2% Triton X-100 and 3% BSA for 48 h at 4°C, followed by 2 h incubation with secondary antibody goat-anti-rabbit Alexa Fluor 488 (1:1000, #A11008, Thermo Fisher) at room temperature. Sections were washed 3 times in PBS (10 min per time) and covered with Vectorshield containing DAPI (Vector Laboratories) on glass slides.

c) Imaging

To verify the location of DiI-labeled extracellular electrode and sufficient expression of viral vectors, 100 mm-thick slices were mounted with Fluoromount (Thermo Fisher Scientific) mixed with Hoechst (Thermo Fisher Scientific) or DAPI (Sigma-Aldrich), then the positions of insertion/virus expression were imaged and reconstructed under a wide-field fluorescence microscope (Olympus) and cellSens software (Olympus) with magnification in the range of 2x to 8x. Sections containing LEC from AAVrg-CamKIIa-EGFP injected brains were imaged using a confocal microscope (Zeiss) and Zen Blue software (Zeiss). Image stacks of labeled PYRs were acquired using both 20x (2048×2048 pixels) and 40x (4096×4096 pixels) objectives.

2.1.6 Data analysis

a) Dendritic complexity and spine quantification

Images of LEC neurons were binarized (auto threshold) using the auto threshold function, and the dendrites were traced using the semi-automatic simple neurite tracer (SNT) plugin in ImageJ software (NIH). The geometric center was identified, and dendritic complexity was analyzed with Sholl analysis function of SNT plugin. For spine quantification, spines on apical dendrites were manually counted using the point picker tool along a randomly selected portion of PYR apical dendrites and measured with “line” tool for length in ImageJ. All the analysis was performed blind to the group identity.

b) Animal behavior analysis

Tracking videos of animal behaviors were analyzed using DeepLabCut (DLC Team) with at least 500000 repetitions of machine learning iteration in Python environment. The parameter of interest was quantified using custom-written scripts with MATLAB

programming language (MathWorks). The percentage of time spent over the odor fields was normalized to the total frames of the tracking video for each animal. For object recognition tests, the interaction with an object was defined as the snout being within 1 cm distance from the object, and the animals were excluded from the analysis if the total object interaction time was less than 20 s during the familiarization trial. Exploration for objects was quantified as the discrimination index of time spent interacting with the new and familiar object:

$$Discrimination\ index = \frac{time_{object2} - time_{object1}}{time_{object1} + time_{object2}}.$$

For Y-maze test, the visited arms during free exploration were quantified, and the percentage of spontaneous alternations was calculated as:

$$\frac{number\ of\ alterations}{total\ entries - 2}.$$

c) Time series analysis

In vivo electrophysiological data were analyzed offline using custom-written scripts in MATLAB environment. Data were first band-passed filtered (1-100 Hz for LFP or 500-9000 Hz for spike analysis) using a 3rd-order Butterworth filter before down-sampling to 1600 Hz in a manner preserving phase information for LFP analysis.

i. Power

Power spectral density (PSD) was computed using Welch's method (build-in pwelch.m function) with non-overlapping 3-s-long windows and 2^{12} fast Fourier transformation (FFT) size.

For odor stimulation experiments power was calculated on 2-s-long periods during odor presentation (Stim) and normalized by the power of the 2-s-long period preceding the odor stimulation (Pre) using the same FFT size:

$$\frac{PSD_{Stim} - PSD_{Pre}}{PSD_{Pre}}.$$

ii. Imaginary coherence

The imaginary part of complex coherence is insensitive to volume-conduction-based effects and is used to measure the functional interaction between two simultaneous time series (Nolte et al., 2004). The calculation is by taking the absolute value of the imaginary component of the normalized cross-spectral density (using build-in functions: cpds.m and pwelch.m) according to the formula:

$$C_{XY}(f) = \left| Im\left(\frac{P_{XY}(f)}{\sqrt{P_{XX}(f)P_{YY}(f)}}\right)\right|,$$

where C_{XY} is for the imaginary coherence of signals X and Y over frequency (f), P_{XX} and P_{YY} are the respective PSD of signals X and Y, and P_{XY} is the cross-spectral density. Shuffling

of the coherence calculation was performed 1000 repetitions.

iii. Partial directed coherence

To investigate the directionality of functional connectivity between brain regions, generalized partial directed coherence (gPDC) which is based on a linear Granger causality measure in the frequency domain was applied. The method attempts to describe the causal relationship between multivariate time-series based on the decomposition of multivariate partial coherence computed from multivariate autoregressive models. Before the calculation, each LFP signal was divided into 3-s long segments and de-noised using build-in wavelet toolbox. Then gPDC was computed as previously described (Baccalá & Sameshima, 2001).

iv. Light-induced field potential

For accessing the activity in response to light stimulations, raw extracellular recording signals were downsampled to 1600 Hz and data recorded during periods around the 3-ms light pulse (50 ms before to 100 ms after) were used for analysis. The peaks for the absolute value of the signals after the pulses were detected and averaged for each mouse.

v. Single unit analysis

Single-unit activity (SUA) was detected and clustered using klusta (kwikteam) and Kilosort (MouseLand) based on waveform features, and manually curated using phy (Cortex-lab) in Python environment. SUA data were then imported and analyzed using custom-written tools in MATLAB. The firing rate was calculated by dividing the total number of SUA by the length of the analyzed time window. To assess the firing probability after light stimulations with blue light pulses, histograms of spike count using 1 ms bins were calculated for periods around the 3-ms light pulse (50 ms before to 100 ms after) and normalized to the number of light pulses.

vi. Spiking correlation

Spike time tiling coefficient (STTC), a metric that tracks correlations between spike trains and is robust to changes in firing rate (Cutts & Eglen, 2014), was calculated on the manually curated SUA data according to the formula:

$$STTC = \frac{1}{2}\left(\frac{P_A - T_B}{1 - P_A T_B} + \frac{P_B - T_A}{1 - P_B T_A}\right),$$

where P_A is the proportion of spikes in spike train A that fall within $\pm\Delta t$ of a spike from spike train B. T_A is the proportion of time that occurs within $\pm\Delta t$ from the spikes of spike train A. The same applies to P_B and T_B. $\pm\Delta t$ stands for the timescale at which STTC is computed, varying from 5 ms to 1000 ms.

2.1.7 Statistics

Statistical analysis was carried out in MATLAB and R environment (R statistical software,

RStudio). Normally distributed data were tested for significance using paired and unpaired t-tests. Non-normally distributed data were tested for significance using Wilcoxon rank-sum test. Outlier removal was applied to datasets if values were more than 1.5 interquartile ranges above the upper quartile (75%) or below the lower quartile (25%). Longitudinal data were analyzed with linear mixed-effects models (LMEM; lmer and glmer functions of the "lme4" R package). Depending on the experimental designs, different random factors were used (e.g. "mouse", "neuron"). Post-hoc analysis was performed using the "emmeans" R package based on the estimated marginal means theory. A significance level of $p<0.05$ was considered statistically significant (*, **, *** represent $p<0.05$, $p<0.01$, $p<0.001$ respectively). Values of corresponding statistics can be found in the results and figure legends. All data were expressed as median and interquartile range unless otherwise stated.

2.2 Results

2.2.1 Olfactory Bulb Activity Shapes the Development of Entorhinal-Hippocampal Coupling and Associated Cognitive Abilities

Yu-Nan Chen, Johanna K. Kostka, Sebastian H. Bitzenhofer and Ileana L. Hanganu-Opatz

Current Biology 2023; DOI: 10.1016/j.cub.2023.08.072

Personal contribution

I designed the research.

I performed all the experiments. In specific, these included:

- *in vivo* microinjections and intraperitoneal injections;
- *in vivo* multi-site electrophysiological recordings;
- *in vivo* odor/optogenetic stimulations;
- immunohistochemistry and imaging;
- behavioral tests.

I carried out formal analysis, visualization and data curation.

I designed and generated the figures.

I wrote the original draft of the manuscript.

I reviewed and edited the manuscript.

I revised and finalized the manuscript.

Article

Current Biology

Olfactory bulb activity shapes the development of entorhinal-hippocampal coupling and associated cognitive abilities

Graphical abstract

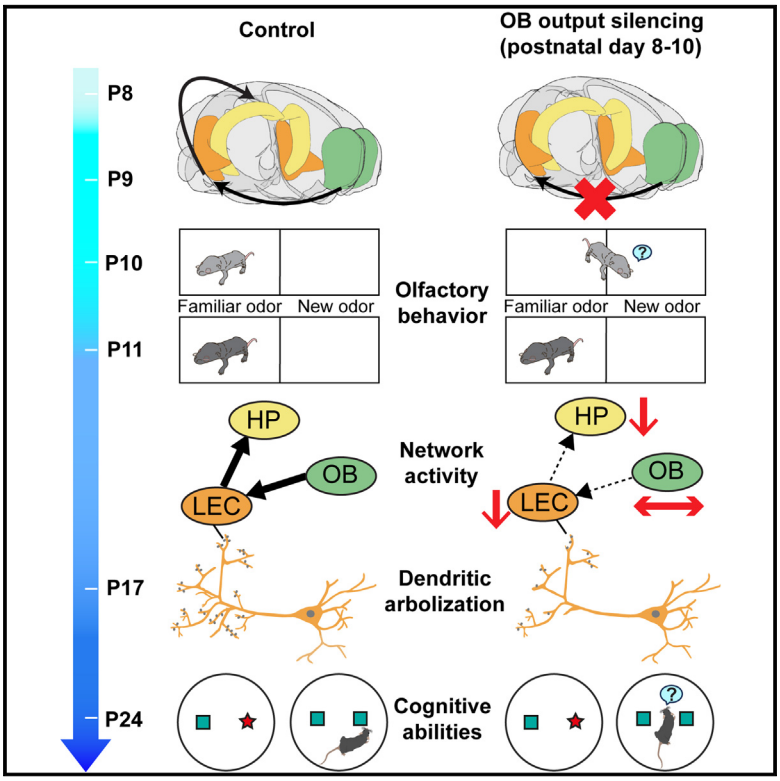

Highlights

- Transient OB output silencing early in life decreases later LEC-HP communication
- Neonatal OB output silencing persistently decreases LEC-HP responsiveness to stimuli
- Neonatal OB output silencing compromises the entorhinal dendritic complexity
- Cognitive abilities are long-lastingly impaired after neonatal OB output silencing

Authors

Yu-Nan Chen (陈裕楠), Johanna K. Kostka, Sebastian H. Bitzenhofer, Ileana L. Hanganu-Opatz

Correspondence

hangop@zmnh.uni-hamburg.de

In brief

Chen et al. show that transient silencing of olfactory bulb output during early development long-lastingly impairs the function and connectivity of downstream entorhinal-hippocampal networks, revealing that olfaction early in life is necessary for cognitive development.

Chen et al., 2023, Current Biology *33*, 4353–4366
October 23, 2023
https://doi.org/10.1016/j.cub.2023.08.072

CellPress

Current Biology

CellPress
OPEN ACCESS

Article

Olfactory bulb activity shapes the development of entorhinal-hippocampal coupling and associated cognitive abilities

Yu-Nan Chen (陈裕楠),[1] Johanna K. Kostka,[1] Sebastian H. Bitzenhofer,[1] and Ileana L. Hanganu-Opatz[1,2,3,*]
[1]Institute of Developmental Neurophysiology, Center of Molecular Neurobiology, Hamburg Center of Neuroscience, University Medical Center Hamburg-Eppendorf, 20251 Hamburg, Germany
[2]X (formerly Twitter): @HanganuOpatzLab
[3]Lead contact
*Correspondence: hangop@zmnh.uni-hamburg.de
https://doi.org/10.1016/j.cub.2023.08.072

SUMMARY

The interplay between olfaction and higher cognitive processing has been documented in the adult brain; however, its development is poorly understood. In mice, shortly after birth, endogenous and stimulus-evoked activity in the olfactory bulb (OB) boosts the oscillatory entrainment of downstream lateral entorhinal cortex (LEC) and hippocampus (HP). However, it is unclear whether early OB activity has a long-lasting impact on entorhinal-hippocampal function and cognitive processing. Here, we chemogenetically silenced the synaptic outputs of mitral/tufted cells, the main projection neurons in the OB, during postnatal days 8–10. The transient manipulation leads to a long-lasting reduction of oscillatory coupling and weaker responsiveness to stimuli within developing entorhinal-hippocampal circuits accompanied by dendritic sparsification of LEC pyramidal neurons. Moreover, the transient silencing reduces the performance in behavioral tests involving entorhinal-hippocampal circuits later in life. Thus, neonatal OB activity is critical for the functional LEC-HP development and maturation of cognitive abilities.

INTRODUCTION

An impressive spectrum of cognitive abilities relies on information processing within large-scale neuronal circuits involving the entorhinal cortex (EC) and hippocampus (HP). The communication between these cortical areas during cognitive tasks is a highly dynamic process that relates to precise timing within neuronal networks. This is ensured by brain oscillations[1–3] with the neuronal firing set to a specific phase of the oscillatory cycle.[4,5] Changes in oscillatory activity have been associated with entorhinal-hippocampal network functions involved in various cognitive tasks.[6,7] The EC has been proposed to act as the gatekeeper of the cortical memory network.[8] Its upper layers project to HP and PFC,[9,10] whereas the deep layers collect prefrontal-hippocampal output.[11] This connectivity represents the substrate for the oscillatory entrainment that synchronizes these dispersed circuits during the encoding and retrieval of declarative memory.[12]

In addition to interfacing HP and neocortex, the EC appears to act as a relay station for sensory control of limbic networks. In particular, the lateral entorhinal cortex (LEC), which together with the piriform cortex (PIR) belongs to the ''olfactory cortex,''[13] receives direct input from the olfactory bulb (OB).[14,15] For this, long-range axonal projections of OB mitral and tufted cells (M/TCs) through the lateral olfactory tract (LOT) target directly as well as indirectly via PIR the LEC.[16] Afferent fibers from olfactory areas are the dominant input to LEC in rodents.[17,18] In adult rodents, mitral cell axons terminate in layer I on apical dendrites of layer II/III pyramidal and fan cells.[19] In turn, LEC pyramidal cells project to the hippocampal CA1 area, whereas fan cells target the dentate gyrus.[20–23] Moreover, LEC, in tight interplay with HP, has been hypothesized to play a critical role in olfactory memory, a cognitive ability of particular relevance throughout life.[12,24,25]

Olfactory processing and odor learning emerge during early postnatal development.[26] Since rodent pups are blind and deaf and have limited sensorimotor abilities until the end of the second postnatal week, olfaction is mandatory for mother-infant interactions and harm avoidance early in life.[27] In light of the sense of smell's central role in newborn and juvenile animals, surprisingly few studies, mostly anatomical, have addressed functional aspects of early network maturation and consolidation in the postnatal OB and downstream cortical areas, such as PIR and LEC.[28–32] Recently, we showed that OB projections are functional from birth on, since coordinated M/TCs' activity, such as that evoked by odors, drives the generation of typical discontinuous patterns of oscillatory activity in the neonatal LEC and HP.[33,34] However, a fundamental, yet unresolved question is whether olfactory processing during neonatal development is necessary for the maturation of cognitive processing. Early life events, such as maternal deprivation or handling, have been reported to profoundly affect the limbic system.[35,36] The contribution of early odor exposure/learning to adult behavior is still poorly explored and mainly restricted to fear conditioning.[37,38]

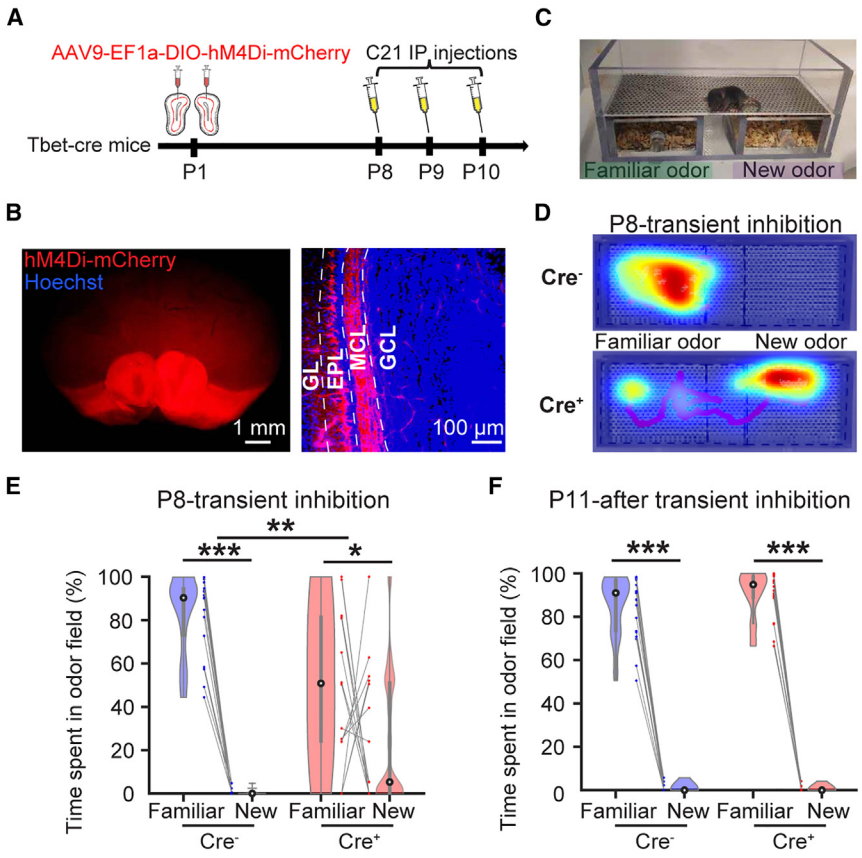

Figure 1. Effects of transient M/TC output silencing on odor discrimination/detection of neonatal mice

(A) Experimental timeline of the transient chemogenetic silencing of M/TC outputs. Expression of inhibitory hM4Di receptors in M/TCs was performed by AAV injections into OB of both hemispheres at P1 in Tbet-cre mice. C21 was intraperitoneally (i.p.) injected at P8, P9, and P10 once per day.

(B) Digital photomontages of nuclear Hoechst-staining and expression of hM4Di-mCherry in both OBs of a P11 Cre^+ mouse (front view of an intact brain, left) and in a coronal slice of the OB from the same mouse (right; GL, glomerular layer; EPL, external plexiform layer; MCL, mitral cell layer; GCL, granule cell layer).

(C) Photograph of the setup for non-contact odor preference test for neonatal mice. One field contains homecage beddings as familiar odor, whereas the other field contains fresh beddings soaked with 1% vanillin as new odor.

(D) Representative tracking paths merged with locomotion heatmaps of a Cre^- (top) and a Cre^+ mouse (bottom) in the odor preference test arena after the first C21 injection at P8.

(E) Violin plots displaying the relative time spent by P8 Cre^- (blue) and Cre^+ (red) mice over each odor field after the first C21 injection (Cre^-, n = 18; Cre^+, n = 16; $p < 0.0001$ for interaction of genotype and odor, $p < 0.0001$ for Cre^--familiar versus Cre^--new, p = 0.026 for Cre^+-familiar versus Cre^+-new, p = 0.0078 for Cre^--new versus Cre^+-new, nonparametric multiple comparisons with Bonferroni's post hoc test).

(F) Violin plots displaying the relative time spent by P11 Cre^- and Cre^+ mice over each odor field after 3-day C21 injections from P8 to P10 (Cre^-, n = 22; Cre^+, n = 17; p = 0.216 for interaction of genotype and odor, $p < 0.0001$ for Cre^--familiar versus Cre^--new, $p < 0.0001$ for Cre^+-familiar versus Cre^+-new, p = 0.908 for Cre^--new versus Cre^+-new, nonparametric multiple comparisons with Bonferroni's post hoc test). Data are presented as individual data points, median, and interquartile range. *$p < 0.05$, **$p < 0.01$, ***$p < 0.001$.

See also Figure S1 and Table S1.

Even more striking, it is fully unknown, how the coordinated M/TC activity that is present already at birth[33] influences the development and later function of the downstream networks. Here, we tested the hypothesis that early activity in the OB is necessary for the development of entorhinal-hippocampal function and cognitive processing. For this, we chemogenetically silenced the synaptic outputs of M/TCs transiently from postnatal day (P)8 to P10 in mice. Using multi-site *in vivo* electrophysiology and optogenetics as well as neuronal tracing, morphological assessment, and behavioral testing, we monitored the long-term consequences of this early manipulation on the activity and communication within OB-LEC-HP networks as well as on cognitive abilities.

RESULTS

Silencing of M/TC outputs in neonatal mice transiently impairs olfactory behavior

To investigate the contribution of early activity in the OB to the development of entorhinal-hippocampal networks, we set out to establish a protocol for the transient suppression of M/TC synaptic outputs at neonatal age. Inhibitory designer receptors exclusively activated by designer drugs (DREADDs) hM4Di have been successfully used to block the vesicle release from M/TC axons in neonatal mice, which acutely reduced network activity within LEC-HP networks.[34] To transiently silence the synaptic outputs of M/TCs in the OB during neonatal development, we injected the adeno-associated viruses (AAVs) encoding for cre-dependent expression of the inhibitory DREADDs hM4Di bilaterally into the OB of Tbet-cre mice at P1 (Figure 1A). Cre recombinase from Tbet promoter was expressed in M/TCs specifically in the brains of Cre^+ mice.[39] The fluorescent protein mCherry in the AAV construct was co-expressed with hM4Di to confirm that transfection is restricted to M/TCs and stable expression is achieved at P8 (Figure 1B). To silence the synaptic outputs via inhibition of synaptic vesicle release of M/TC axons, we intraperitoneally (i.p.) injected compound 21 (C21), a synthetic activator of DREADDs,[40] from P8 to P10 (once per day), the time window during which the OB activation boosts the oscillatory entrainment of entorhinal circuits.[33,34] Neither somatic development, reflexes, nor spontaneous locomotion behavior were affected by this manipulation (Figures S1A and S1B).

First, we assessed the efficacy of the hM4Di-mediated M/TC output silencing by monitoring the odor discrimination/detection of P8 mice, shortly (30 min) after the first injection of C21. For this, we used a non-contact odor preference test (Figure 1C). Mice

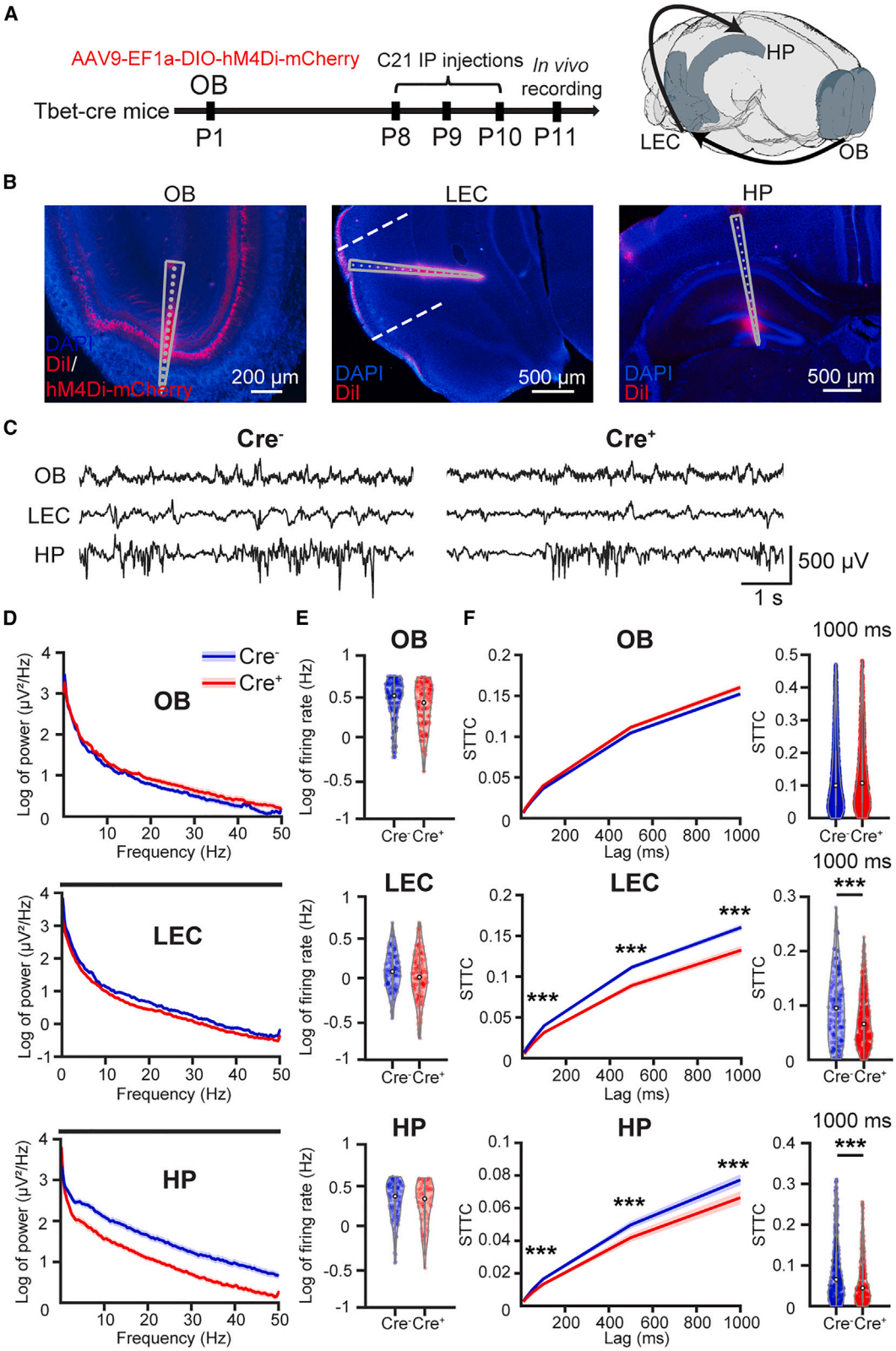

(legend on next page)

were presented with a familiar odor (homecage bedding) and an unfamiliar odor (fresh homecage bedding with 1% vanillin). In line with the natural preference of neonatal mice for their homecage bedding, both Cre^+ (i.e., manipulated) and Cre^- (i.e., controls) mice spend significantly more time in the compartment over the familiar odor when not injected with C21 (Figure S1C). In contrast, the preference for the familiar odor was significantly reduced in hM4Di-expressing Cre^+ mice treated with C21 at P8 (Figures 1D and 1E). This acute effect confirms that hM4Di-mediated silencing of M/TC outputs is sufficient to diminish odor discrimination/detection already at P8. The fact that the olfactory abilities are not completely abolished in Cre^+ mice most likely reflects an incomplete targeting of M/TCs with AAV or C21 injections. When the same test was performed on the same pups at P11, a day after the last C21 injection, both groups of mice showed a similar preference for the familiar odor (Figure 1F), indicating that the transient inhibition of M/TC outputs on odor discrimination/detection is reversible.

Thus, silencing of M/TC outputs from P8 to P10 only transiently impaired the olfactory processing in neonatal mice.

Transient silencing of M/TC outputs persistently impairs the activity and communication within LEC-HP networks

Next, we assessed the effects of transient chemogenetic silencing of M/TC outputs on neuronal activity. To this end, we performed multi-site extracellular recordings of the local field potential (LFP) and single-unit activity (SUA) simultaneously from the OB, LEC, and the CA1 area of the dorsal HP in awake, head-fixed Cre^-, and Cre^+ mice at P11 after transient silencing of M/TC outputs (Figures 2A–2C). Neither the broadband oscillatory power nor the neuronal firing rate in the OB was affected by transient M/TC output silencing (Figures 2D and 2E). These data are in line with the intact olfactory preference for familiar odors that both groups Cre^- and Cre^+ mice have at P11. In contrast, at the same age, the activity of downstream areas, LEC, and HP was impaired after the transient M/TC output silencing. The broadband power decrease detected in Cre^+ mice (Figure 2D) might result from an overall reduction of SUA or from reduced neuronal synchronization within local circuits. Although we did not observe significant changes in the firing rates of single units recorded from LEC and HP of Cre^+ mice (Figure 2E), the spike time tiling coefficients (STTCs), a measure of the correlation between neuronal spike trains and thus a proxy of synchrony within local circuits,[41] was significantly reduced for LEC and HP, but not OB (Figure 2F). This indicates that the transient silencing of M/TC outputs, although leaving the OB activity intact, disrupted the local interactions within LEC and, subsequently, hippocampal CA1 area.

The transient chemogenetic manipulation did not only affect activity in individual areas but also the communication between areas of P11 mice. When assessing the interregional communication within OB-LEC-HP networks using STTC, we detected significantly reduced correlations between the spiking activity of OB and LEC (Figure 3A), as well as LEC and HP (Figure 3D). Moreover, we assessed oscillatory synchrony between areas by calculating the imaginary part of coherence of simultaneous recorded LFPs, which is considered not to be corrupted by volume conductance. We found that OB-LEC (Figure 3B), LEC-HP (Figure 3B), and OB-HP coherence values (Figure S2A) were significantly lower in P11 Cre^+ mice when compared with Cre^- mice. This indicates a decrease in long-range synchrony within OB-LEC-HP networks. In particular, the 1–10 Hz coherence between OB and LEC was strongly reduced in Cre^+ mice, suggesting that the LEC is less responsive to the OB input that covers the slow respiration-related rhythm (1–4 Hz) and the theta rhythm (4–12 Hz), which were previously shown to reflect the entrainment of the limbic areas.[33,42] Moreover, the coupling between LEC and HP was affected not only in the theta frequency range but also at faster frequencies (12–40 Hz) that have a critical role in odor processing.[12,34]

To assess the directionality of the interactions within OB-LEC-HP networks after chemogenetic manipulation, we calculated the generalized partial directed coherence (gPDC).[43] The previously identified oscillatory drive from OB to LEC and subsequently from LEC to HP[33,34] was significantly decreased in Cre^+ mice after transient M/TC output silencing (Figures 3C and 3F). Although the OB does not directly project to the CA1 subdivision of the HP, Cre^+ mice had decreased gPDC values for OB→HP (Figure S2B), most likely as a result of the weaker drive from the OB along the downstream pathway OB → LEC and LEC → HP.

These data show that reduced M/TC outputs during a specific time window of early development, even if not compromising olfactory processing, persistently impair the communication and directed interactions along the downstream pathways to HP.

Figure 2. Effects of transient M/TC output silencing on the neuronal and network activity in OB, LEC, and HP of P11 mice

(A) Left: experimental timeline of the chemogenetic silencing of M/TC outputs during P8–P10 followed by *in vivo* multi-site extracellular recordings of OB, LEC, and HP at P11. Right: three-dimensional (3D) schematic of the recording sites in OB, LEC, and HP. Black arrows correspond to the axonal projections linking the OB, LEC, and HP.

(B) Digital photomontage reconstructing the location of the DiI-labeled extracellular recording electrodes in OB, LEC, and HP of a P11 hM4Di-mCherry expressing Cre^+ mouse.

(C) Representative extracellular recordings of the LFPs in the OB, LEC, and HP of P11 Cre^- (left) and Cre^+ (right) mice.

(D) Averaged power spectra of oscillatory activity recorded from P11 Cre^- (blue) and Cre^+ (red) mice in OB (Cre^-, n = 16; Cre^+, n = 15; p = 0.810 for genotype, linear mixed-effects model [LMEM]), LEC (Cre^-, n = 12; Cre^+, n = 12; p = 0.00104 for genotype, LMEM), and HP (Cre^-, n = 12; Cre^+, n = 11; p = 0.0411 for genotype, LMEM).

(E) Violin plot displaying the SUA firing rates in OB, LEC, and HP for P11 Cre^- and Cre^+ mice.

(F) Left: averaged correlation between spike trains quantified by STTC for P11 Cre^- and Cre^+ mice. The significance levels for comparisons at 100, 500, and 1,000 ms time lag are displayed. Right: violin plot displaying the corresponding STTC values for 1,000 ms time lag between spike trains in OB (p = 0.36, Wilcoxon rank-sum test), LEC (p < 0.0001, Wilcoxon rank-sum test), and HP (p < 0.0001, Wilcoxon rank-sum test). For line plots, data are presented as median ± standard error of the median. Horizontal black lines indicate p < 0.05. For violin plots, data are presented as individual data points, median, and interquartile range. ***p < 0.001.

See also Table S1.

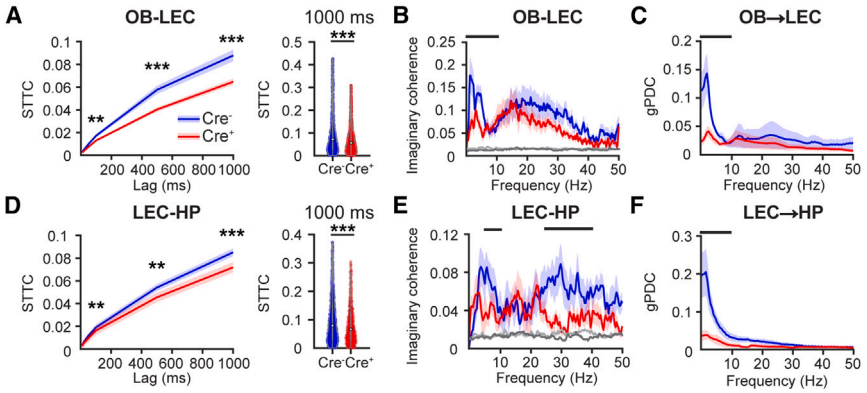

Figure 3. Effects of transient M/TC output silencing on long-range communication between OB, LEC, and HP for P11 mice

(A) Left: STTC between spike trains simultaneously recorded in OB and LEC from P11 Cre$^-$ (blue) and Cre$^+$ (red) mice. The significance levels for comparisons at 100, 500, and 1,000 ms time lag are displayed. Right: violin plot displaying the corresponding STTC values for 1,000 ms time lag ($p < 0.0001$, Wilcoxon rank-sum test).

(B) Averaged imaginary coherence for oscillatory activity simultaneously recorded in OB and LEC for P11 Cre$^-$ and Cre$^+$ mice (Cre$^-$, n = 12; Cre$^+$, n = 12; $p = 0.00212$ for interaction of genotype and frequency, LMEM). The gray lines at the bottom correspond to the imaginary coherence calculated for shuffled LFPs of both groups, respectively (light gray for Cre$^-$; dark gray for Cre$^+$).

(C) Information flow from OB to LEC within OB-LEC-HP network quantified by gPDC for simultaneous oscillatory activity of P11 Cre$^-$ and Cre$^+$ mice (Cre$^-$, n = 12; Cre$^+$, n = 12; $p = 0.0126$ for interaction of genotype and frequency, LMEM).

(D) Same as (A) for LEC-HP ($p < 0.0001$, Wilcoxon rank-sum test).

(E) Same as (B) for LEC-HP (Cre$^-$, n = 9; Cre$^+$, n = 9; $p = 0.0043$ for interaction of genotype and frequency, LMEM).

(F) Same as (C) for information flow from LEC to HP (Cre$^-$, n = 9; Cre$^+$, n = 9; $p = 0.0129$ for interaction of genotype and frequency, LMEM). For line plots, data are presented as median ± standard error of the median. Horizontal black lines indicate $p < 0.05$. For violin plots, data are presented as individual data points, median, and interquartile range. *$p < 0.05$, **$p < 0.01$.

See also Figure S2 and Table S1.

Transient silencing of M/TC outputs persistently decreases the responsiveness to stimuli within the OB-LEC-HP network

The reduced communication within OB-LEC-HP networks following the transient M/TC output silencing might cause weaker responsiveness to incoming stimuli later in life. To test this hypothesis, we tested the effects of the following two types of stimulations: odors and direct activation of channelrhodopsin (ChR2)-transfected M/TCs with light. We previously showed that odors lead to strong activation of the neonatal OB → LEC → HP pathway.[33,34] To test whether transient M/TC output silencing alters this downstream activation, P11 Cre$^-$ and Cre$^+$ mice were exposed to neutral odors while simultaneously recording the activity in OB, LEC, and HP (Figure 4A). In Cre$^-$ mice, all three investigated areas responded to odor exposure with a strong increase in 4–30 Hz oscillatory activity, as revealed by the normalized power values. In contrast, the odor-evoked response was smaller in Cre$^+$ mice (Figures 4B–4D and S3A–S3C). The effect was odor-independent and extended over a broad frequency range in OB and LEC but was confined to 10–20 Hz in the HP. The decreased odor-evoked activity in OB might result from altered local connections between M/TCs and inhibitory neurons or from altered feedback from downstream cortical areas affected by the transient M/TCs output silencing.

These results suggest that transient M/TC output silencing has long-lasting effects on the ability of LEC and HP to process inputs from the OB. To confirm these findings, we transfected light-sensitive ChR2 together with hM4Di by bilateral virus injections into the OB of Tbet-cre mice (Figure 4E). For specific expression of ChR2 in M/TCs, only Cre$^+$ mice were used. Transient M/TC output silencing was performed as described above by daily injection of C21 during P8–P10, whereas control mice were injected with saline. At P11, we simultaneously recorded the LFP and spiking activity from OB, LEC, and hippocampal CA1 area and activated ChR2-expressing M/TCs using blue light pulses (473 nm, 3 ms). In all investigated mice, direct M/TC activation by light-evoked field potentials with large amplitude peaked at ~8 ms after stimulus onset in OB. Similar potentials, yet of smaller amplitude, were detected in LEC after ~25 ms and HP after ~58 ms from stimulus onset (Figures 4F, 4H, and 4J). Amplitudes of the evoked peaks were quantified and were found to be significantly decreased in all three areas of C21-injected Cre$^+$ mice compared with saline-injected controls (Figures 4F, 4H, and 4J), indicating that information transmission from the OB to the LEC-HP network was impaired after transient silencing of M/TC outputs. We next analyzed the neuronal firing induced by optogenetic M/TC stimulation and found a reduced firing probability in OB, LEC, and HP with similar delays as the event-related potentials (Figures 4G, 4I, and 4K). These results are consistent with weaker odor-evoked responses described above.

Together, these findings confirm a weaker responsiveness to stimuli of downstream areas LEC and HP that persists after the transient M/TC output silencing.

Transient M/TC output silencing compromises the dendritic structure of LEC pyramidal neurons

Direct axonal projections from M/TCs converge in the LOT and directly synapse onto the apical dendrites of principal neurons in the superficial layer of LEC.[11,44] During the first two postnatal weeks, a substantial activity-dependent reorganization of dendritic arborization takes place in cortical areas and actively contributes to the emergence of adult patterns of activity.[45,46] The abnormal activity and communication within OB-LEC-HP networks after the transient M/TC output silencing might result from persistent structural deficits induced by the chemogenetic manipulation. To test this hypothesis, we monitored the structural development of CA1-projecting pyramidal neurons in LEC at P11 and P17 by injecting a retrograde virus encoding for green fluorescent protein (GFP) into hippocampal CA1 area (Figures 5A

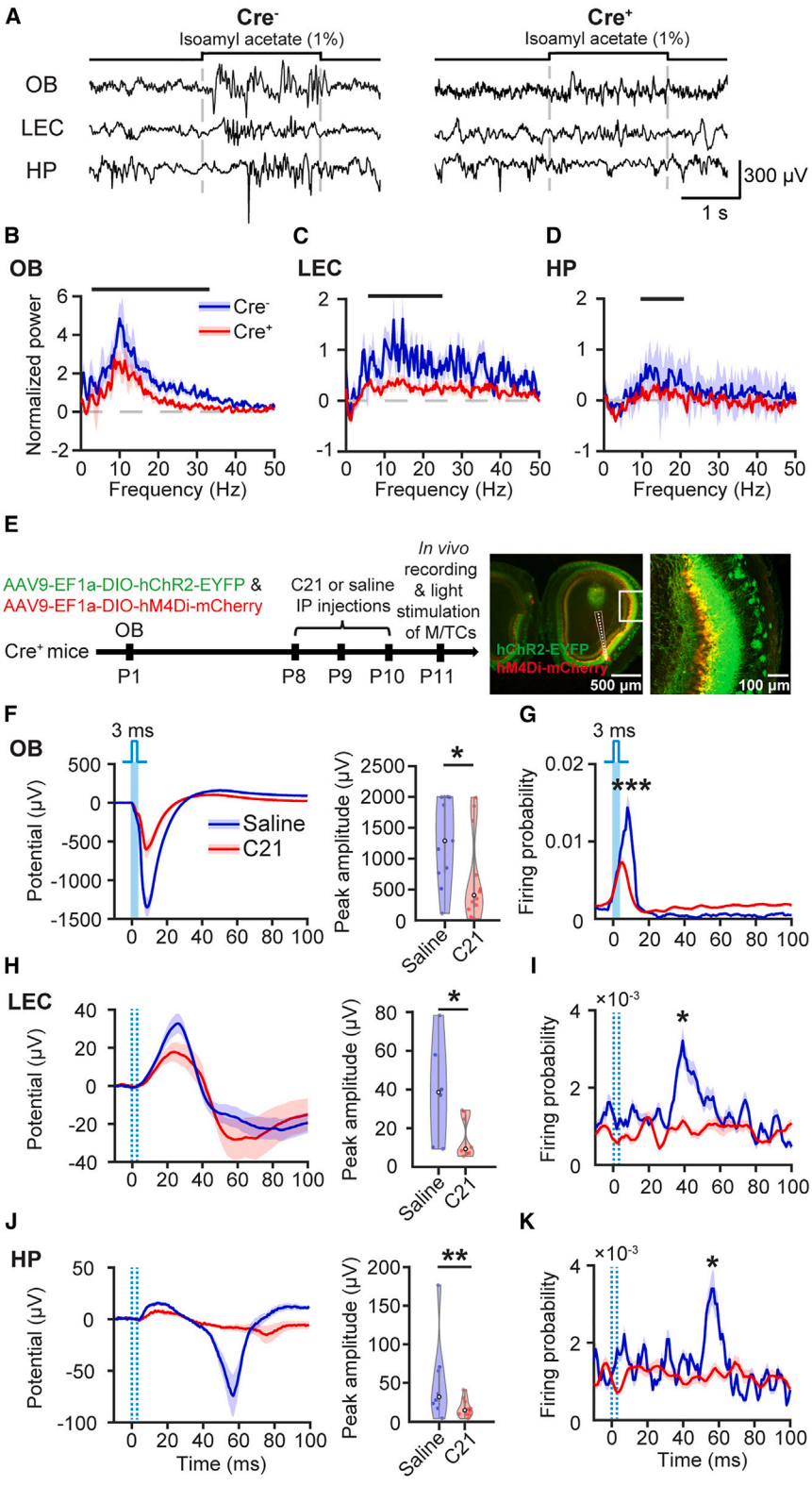

Figure 4. Effects of transient M/TC output silencing on odor- and M/TC optogenetically evoked activity in OB, LEC, and HP of P11 mice

(A) Representative extracellular recordings of the LFP in OB, LEC, and HP of P11 Cre$^-$ (left) and Cre$^+$ (right) mice during odor stimulation with 1% isoamyl acetate.

(B) Averaged power during odor stimulation with 1% isoamyl acetate normalized to the power before stimulation in OB of P11 Cre$^-$ (blue) and Cre$^+$ (red) mice (Cre$^-$, n = 12; Cre$^+$, n = 8; p = 0.0219 for interaction of genotype and frequency, LMEM).

(C) Same as (B) for LEC (Cre$^-$, n = 7; Cre$^+$, n = 7; p = 0.0308 for interaction of genotype and frequency, LMEM).

(D) Same as (B) for HP (Cre$^-$, n = 10; Cre$^+$, n = 8; p = 0.0163 for interaction of genotype and frequency, LMEM). Data are presented as median ± standard error of the median. Horizontal black lines indicate $p < 0.05$.

(E) Left: experimental timeline of acute optogenetic M/TC activation after transient M/TC output silencing of Tbet-cre mice. Expression of both inhibitory hM4Di and light-sensitive hChR2 receptors in M/TCs was performed by AAV injections into OBs of both hemispheres at P1 in Tbet-cre$^+$ mice, and C21 or saline was i.p. injected at P8, P9 and P10 once per day. Light stimulations were performed on M/TCs along with *in vivo* multi-site extracellular recordings of OB, LEC, and HP at P11. Right: digital photomontages of hChR2-EYFP- and hM4Di-mCherry-transfected OB from a P11 Cre$^+$ mouse, and transfection pattern over the OB layers from the same slice when displayed at larger magnification.

(F) Left: averaged light-induced field potentials recorded in the OB of P11 Cre$^+$ mice after daily saline (blue) or C21 (red) injections during P8–P10. Right: violin plots of the peak amplitude of light-induced field potentials (Cre$^+$-saline, n = 10; Cre$^+$-C21, n = 12; p = 0.0161, Wilcoxon rank-sum test).

(G) Averaged probability of SUA firing in OB induced by light stimulation of P11 Cre$^+$ mice after daily saline or C21 injections during P8–P10 (Cre$^+$-saline, n = 63; Cre$^+$-C21, n = 81; p = 0.000378, Wilcoxon rank-sum test). The 3-ms blue light square pulses (473 nm) delivered to M/TC layer are marked by light blue bars.

(H and I) Same as (F) and (G) for LEC (F, Cre$^+$-saline, n = 6; Cre$^+$-C21, n = 7; p = 0.0293, Wilcoxon rank-sum test; G, Cre$^+$-saline, n = 32; Cre$^+$-C21, n = 48; p = 0.0149, Wilcoxon rank-sum test).

(J and K) Same as (F) and (G) for HP (J, Cre$^+$-saline, n = 8; Cre$^+$-C21, n = 10; p = 0.00555, Wilcoxon rank-sum test; K, Cre$^+$-saline, n = 17; Cre$^+$-C21, n = 39; p = 0.0144, Wilcoxon rank-sum test). For line plots, data are presented as mean ± SEM. Horizontal black lines indicate $p < 0.05$. For violin plots, data are presented as individual data points, median, and interquartile range. *p < 0.05, **p < 0.01.

See also Figure S3 and Table S1.

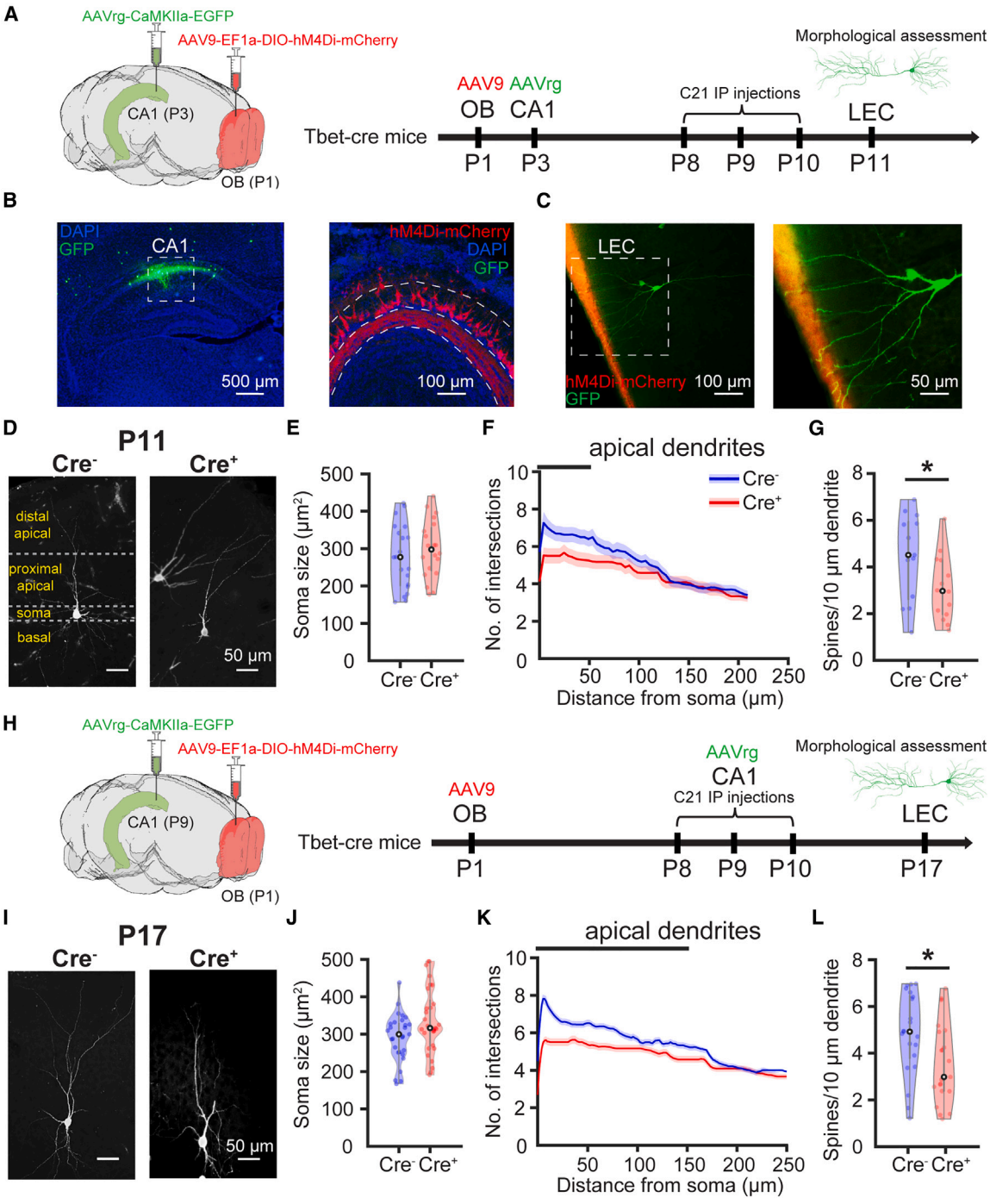

Figure 5. Long-lasting effects of transient M/TC output silencing on the morphology of LEC neurons

(A) Experimental design and timeline for retrograde tracing of CA1-projecting neurons in LEC of P11 mice.

(B) Digital photomontages displaying the injection site of viral construct AAVrg-CaMKIIa-EGFP in the hippocampal CA1, and AAV9-hM4Di-mCherry in OB of a Cre^+ mouse.

(C) GFP-labeled CA1-projecting neurons in LEC of the same Cre^+ mouse in (B). Note that the axonal terminals of M/TCs were also labeled by hM4Di-mCherry.

(D) Representative images of labeled pyramidal neurons in LEC of P11 Cre^- and Cre^+ mice.

(E) Violin plots displaying the soma area of labeled pyramidal neurons in LEC of P11 Cre^- (blue) and Cre^+ (red) mice.

(F) Dendritic intersections within a 250 µm radius from the soma center of LEC neurons from Cre^- (n = 3 mice, 13 neurons) and Cre^+ (n = 3 mice, 14 neurons) mice at P11.

(G) Violin plots of spine density on apical dendrites of labeled LEC pyramidal neurons from Cre^- and Cre^+ mice on P11 (Cre^-, n = 13; Cre^+, n = 14; p = 0.0404, Wilcoxon rank-sum test).

(legend continued on next page)

and 5H). To confirm the position of injection sites, the GFP expression was enhanced by immunostaining in postmortem brain slices (Figure 5B). Retrogradely labeled neurons were found in LEC superficial layers (Figure 5C), confirming that the direct projection from LEC to CA1 is present shortly after birth. Morphological characterization of the labeled LEC neurons that extend their apical dendrites to the LOT (Figure 5C) revealed no changes in soma size for Cre^+ mice when compared with Cre^- control mice (Figures 5D and 5E). However, the complexity of apical dendrites of these neurons was decreased at P11, shortly after the transient silencing of M/TC outputs, as shown by Sholl analysis (Figure 5F). The reduction of dendritic complexity was restricted to the apical dendrites, whereas the basal dendrites were not affected (Figure S4A). Furthermore, the decreased arborization was accompanied by a reduction of spine density on the apical dendrites of Cre^+ mice compared with Cre^- controls (Figure 5G).

The effects observed at P11, shortly after the chemogenetic manipulation, persisted also into later development. At P17, we found a similar decrease in the apical dendritic complexity for CA1-projecting LEC pyramidal neurons after transient M/TC output silencing (Figures 5H, 5I, and 5K). Neither the soma size of retrogradely labeled LEC neurons nor the basal dendrites of these neurons were affected (Figures 5J and S4B). The decreased spine density on the apical dendrites of Cre^+ mice when compared with Cre^- control mice also persisted until P17 (Figure 5L).

These results show that the temporary decrease of inputs as a result of transient M/TC output silencing causes long-lasting dendritic and spine sparsification of CA1-projecting pyramidal neurons in LEC.

Transient M/TC output silencing early in life causes cognitive impairment at pre-juvenile age

Since the chemogenetic manipulation confined to P8–P10 led to structural changes that persist until pre-juvenile age, it is likely that the function of the OB-LEC-HP network and the behavioral abilities this network accounts for are compromised too. To assess the long-lasting functional deficits of mice experiencing transient M/TC output silencing from P8 to P10, we performed multi-site extracellular recordings of LFP and spiking activity from OB, LEC, and HP of awake head-fixed P16–P19 mice (Figure 6A). Similar to P11 mice, Cre^+ mice at P16–P19 showed a significantly decreased LFP power of the oscillatory activity in LEC and HP, yet not in OB (Figure 6B). The decrease mainly affected the 25–60 Hz frequency range in both areas. Overall, SUA in LEC of Cre^+ mice significantly decreased (Cre^-, 0.610 Hz, n = 164 units; Cre^+, 0.427 Hz, n = 135 units; p = 0.0251, Wilcoxon rank-sum test), whereas the firing rates in OB and HP did not change (OB: Cre^-, 0.886 Hz, n = 188 units; Cre^+, 0.801 Hz, n = 170 units; p = 0.781; HP: Cre^-, 0.457 Hz, n = 90 units; Cre^+, 0.462 Hz, n = 121 units; p = 0.954; Wilcoxon rank-sum test). Moreover, local interactions between spike trains measured by STTC were significantly reduced for both LEC and HP, and less severely for OB (Figure 6C). Furthermore, we assessed interregional synchronization within the OB-LEC-HP network by calculating the imaginary coherence for OB-LEC, LEC-HP, and OB-HP. We found an overall decrease in synchrony within the network that mainly affected the 10–20 Hz frequency range (Figure 6D). As shown for P11 mice, the interregional communication between OB and LEC, as well as between LEC and HP quantified by STTC, was significantly reduced in P16–P19 Cre^+ mice (Figure 6E). These data confirm the persistent impairment of the downstream LEC-HP network as a result of transient M/TC output silencing.

These data indicate that the OB activity during early development is critical for later LEC-HP function, but the specificity of the chosen age window (P8–P10) for manipulation remains to be tested. To address this question, we performed similar chemogenetic silencing of M/TC outputs from P13 to P15, a later developmental time window that is characterized by important sensory maturation events (e.g., opening of the eyelids and ear channels) (Figure S5A). Neither the activity patterns nor the synchrony within OB-LEC-HP networks significantly differed between P20 and P23 Cre^+ and Cre^- mice after the manipulation (Figures S5B and S5C). These results indicate that the outcome of OB output silencing depends on the time window of manipulation, the period before the full maturation of other senses, such as vision or hearing, being of particular relevance.

Previous studies have shown that both LEC and HP account for object-place learning and memory tasks.[47–49] To investigate if the impaired LEC-HP network activity after transient M/TC output silencing ultimately leads to any impairment of memory functions at pre-juvenile age, we tested object recognition memory and associative recognition memory in mice with a novel object recognition (NOR) test at P16 (Figure 7A) and an object location preference (OLP) test at P19 (Figure 7B), respectively. Both tests are based on the innate curiosity of mice and need no prior training or deprivation. At this age, mice have well-developed sensory and motor abilities required for the tests.[50,51] In NOR test, Cre^+ mice and Cre^- control mice showed similar exploration of the two identical objects during the familiarization trial. In contrast, during the test trial, Cre^- control mice showed a preference for the novel object, whereas the Cre^+ mice did not, as an indicator that they do not distinguish the novel object from the familiar one (Figure 7A). The OLP test assesses whether mice associate an object with its location. Cre^- control mice preferred to interact with the object in the new location, whereas Cre^+ mice similarly interacted with both objects (Figure 7B). Poorer performance in object recognition tasks might result not only from dysfunction of LEC-HP network but also from abnormal motor abilities. To exclude this confounding effect, we analyzed the spontaneous locomotion of mice in the open field test (OFT). Cre^+ and Cre^- control mice at P15 behave similarly in OFT, and no significant differences were found for the distance traveled (Cre^-, 16.026 m, n = 30; Cre^+, 11.182 m, n = 25;

(H) Experimental design and timeline for retrograde tracing of CA1-projecting neurons in LEC of P17 mice.
(I–L) Same as (D)–(G) for P17 mice (K, Cre^-, n = 3 mice, 21 neurons; Cre^+, n = 3 mice, 21 neurons; $p < 0.0001$ for interaction of genotype and distance from the soma, LMEM; L, Cre^-, n = 21; Cre^+, n = 21; p = 0.0221, Wilcoxon rank-sum test). For line plots, data are presented as median ± standard error of the median. Horizontal black lines indicate $p < 0.05$. For violin plots, data are presented as individual data points, median, and interquartile range. *$p < 0.05$.
See also Figure S4 and Table S1.

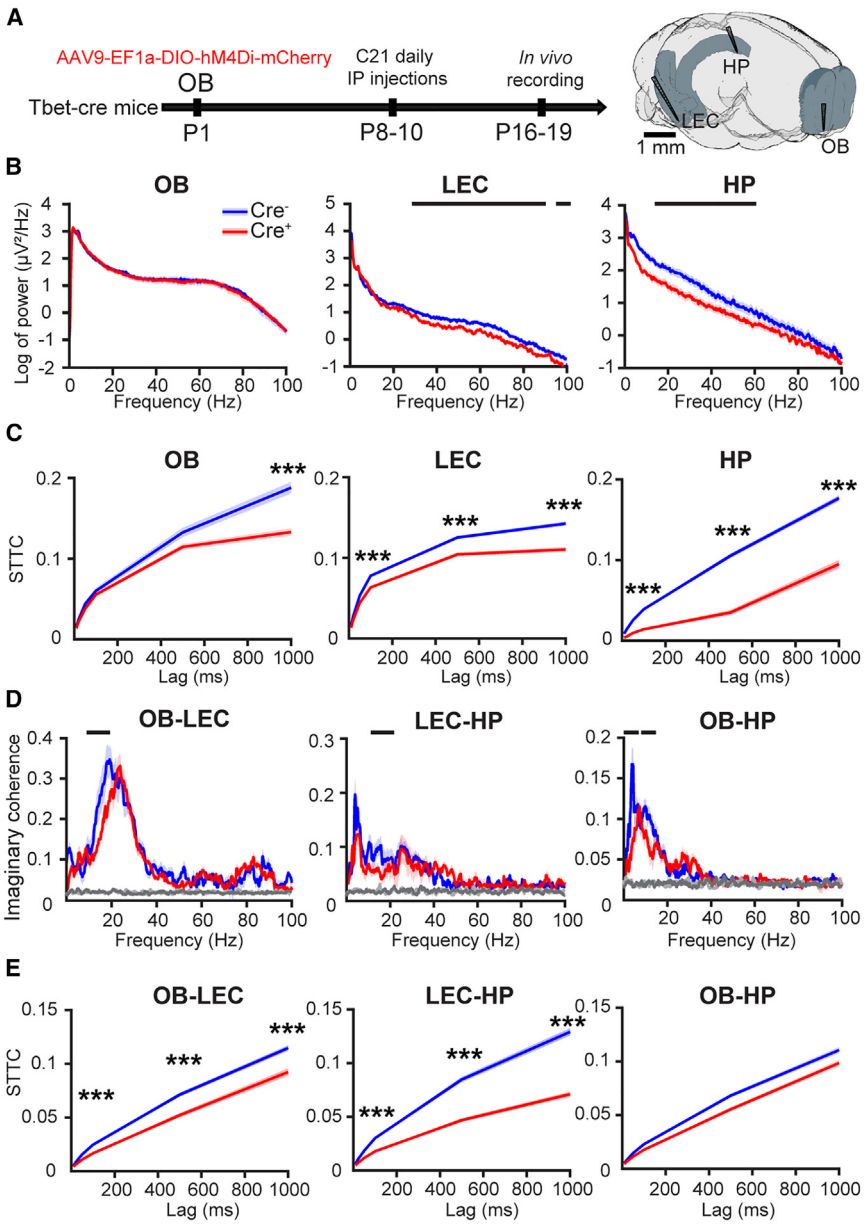

Figure 6. Effects of transient M/TC output silencing on neuronal and network activity in the OB-LEC-HP network of P16–P19 mice

(A) Left: experimental timeline of the chemogenetic silencing of M/TC outputs during P8–P10 followed by *in vivo* multi-site extracellular recordings of OB, LEC, and HP at P16–P19. Right: 3D schematic of the recording sites in OB, LEC, and HP of P16–P19 mice.

(B) Averaged power spectra of oscillatory activity recorded from Cre^- (blue) and Cre^+ (red) mice during P16–P19 in OB (Cre^-, n = 16; Cre^+, n = 15; p = 0.296 for genotype, LMEM), LEC (Cre^-, n = 10; Cre^+, n = 12; p = 0.00883 for genotype, LMEM), and HP (Cre^-, n = 11; Cre^+, n = 13; p = 0.0472 for genotype, LMEM).

(C) Averaged correlation between spike trains quantified by STTC in OB, LEC, and HP recorded from Cre^- and Cre^+ mice during P16–P19. The significance levels for comparisons at 100, 500, and 1,000 ms time lag are displayed, respectively.

(D) Averaged imaginary coherence for simultaneous oscillatory activity recorded in OB and LEC (Cre^-, n = 10; Cre^+, n = 12; p = 0.0248 for interaction of genotype and frequency, LMEM), LEC, and HP (Cre^-, n = 10; Cre^+, n = 12; p = 0.0493 for interaction of genotype and frequency, LMEM), as well as OB and HP (Cre^-, n = 11; Cre^+, n = 13; p = 0.00058 for interaction of genotype and frequency, LMEM) from Cre^- and Cre^+ mice during P16–P19. The gray lines at the bottom correspond to the imaginary coherence calculated for shuffled LFPs (light gray for Cre^-; dark gray for Cre^+).

(E) Pairwise correlation between spike trains simultaneously recorded in OB and LEC (left), LEC and HP (middle), as well as OB and HP (right) from P16 to P19 Cre^- and Cre^+ mice quantified by STTC. The significance levels for comparisons at 100, 500, and 1,000 ms time lag are displayed. Data are presented as median ± standard error of the median. Horizontal black lines indicate $p < 0.05$.

See also Figure S5 and Table S1.

p = 0.166, Wilcoxon rank-sum test). Thus, transient M/TC output silencing at P8–P10 impairs both object recognition and association recognition memory later in life.

Spatial memory, which is highly dependent on intact HP function,[52] is not observed in developing rodents until the 3rd postnatal week.[53,54] Recently, it has been reported that the OB activity that boosts the LEC-HP communication is relevant for spatial working memory evaluated by spontaneous alternations in the Y-maze test.[55] To determine whether the spatial working memory was altered as a consequence of the transient silencing of M/TC outputs during P8–P10, we tested spontaneous alternations of P23 and P24 mice that navigated freely in a Y-maze containing 3 identical and equally spaced arms with walls (Figure 7C). Although the overall exploratory activity in the Y-maze quantified by the total number of entries into the arms was similar in both groups, Cre^+ mice showed a significantly lower percentage of spontaneous alternations compared with Cre^- controls (Figure 7C). These data suggest that transient M/TC output silencing during P8–P10 impaired spatial memory later in life.

Thus, transient M/TC output silencing during P8–P10 leads to a long-lasting OB-LEC-HP network dysfunction, which is sufficient to impair the behavioral performance in object-related and spatial memory tasks.

DISCUSSION

The investigation of the environmental impact on brain development is a constant topic in neuroscience research. Abundant literature documented the role of sensory inputs early in life for the emergence of cortical topographies (e.g., barrels, ocular dominance columns, and tonotopic maps) and fine-tuned sensory discrimination.[56–58] Much less is known about the early sensory influence on brain areas that later account for cognitive processing, such as HP and LEC. Being one of the first senses to

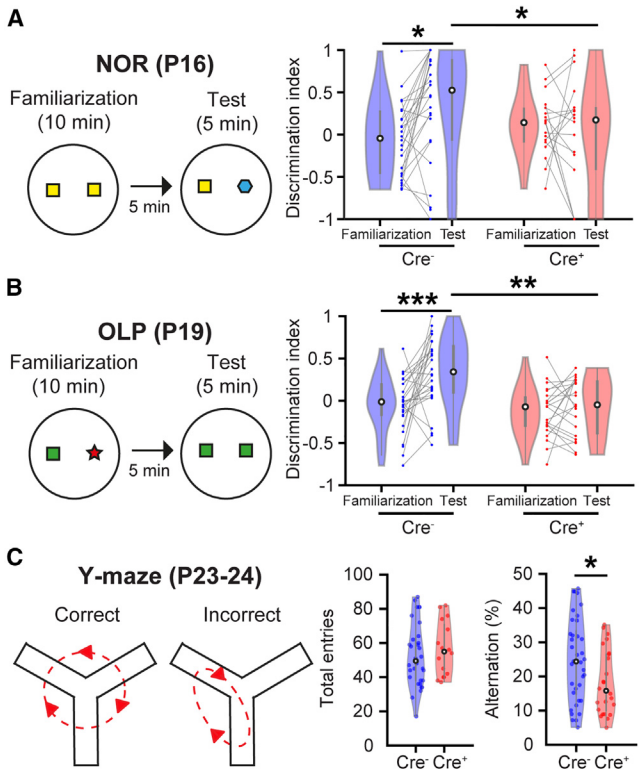

Figure 7. Effects of transient M/TC output silencing on the behavioral performance of pre-juvenile mice in recognition and spatial memory tasks

(A) Left: schematic of the protocol for the NOR test. Right: violin plots displaying the discrimination indices in both familiarization and test trials for Cre^- (blue) and Cre^+ (red) mice (Cre^-, n = 26; Cre^+, n = 18; p = 0.0141 for interaction of genotype and trial, p = 0.0119 for Cre^--familiarization versus Cre^--test, p = 0.828 for Cre^+-familiarization versus Cre^+-new, p = 0.0301 for Cre^--new versus Cre^+-new, nonparametric multiple comparisons with Bonferroni's post hoc test).

(B) Left: schematic of the protocol for OLP test of mice. Right: violin plots displaying the discrimination indices in both familiarization and test trials for Cre^- and Cre^+ mice (Cre^-, n = 27; Cre^+, n = 23; p = 0.0122 for interaction of genotype and trial, p < 0.0001 for Cre^--familiarization versus Cre^--test, p = 0.444 for Cre^+-familiarization versus Cre^+-test, p = 0.00539 for Cre^--test versus Cre^+-test, nonparametric multiple comparisons with Bonferroni's post hoc test).

(C) Left: schematic illustrating a correct and an incorrect alternation in the Y-maze test for mice. Middle: violin plot displaying the total number of arm entries in the Y-maze for Cre^- and Cre^+ mice (Cre^-, n = 37; Cre^+, n = 25; p = 0.511, Wilcoxon rank-sum test). Right: violin plot displaying the percentage of spontaneous alternations in the Y-maze test for Cre^- and Cre^+ mice (p = 0.0355, Wilcoxon rank-sum test). Data are presented as individual data points, median, and interquartile range. *p < 0.05, **p < 0.01, ***p < 0.001.
See also Table S1.

maturate and by-passing the thalamic relay,[14,15] olfaction might act as a booster of the development of these areas. However, experimental evidence for this hypothesis was still lacking. In this study, we investigate the role of early coordinated activity in the OB, which is either endogenously generated or odor evoked,[33,34] for the activation of downstream LEC-HP networks and cognitive processing along development. Combining *in vivo* electrophysiology, odor, and optogenetic stimulations with morphological and behavioral assessment, we show that transient chemogenetic silencing of M/TC outputs from P8 to P10 (1) reduces the odor processing only during the time window of manipulation and has no effects on the endogenous OB activity at P11; (2) persistently alters the network and spiking activity in the downstream areas LEC and HP, as well as the interregional OB-LEC-HP communication; (3) reduces the responsiveness of LEC and HP to odors and light stimulation of ChR2-transfected M/TCs; (4) persistently sparsifies the dendritic arborization and spine densities of HP-projecting LEC neurons; and (5) impairs LEC-HP-dependent cognitive performance later in life.

Although the broadband oscillatory power and spiking of OB did not change after chemogenetic M/TC output silencing, the OB responsiveness to acute stimuli (both odor and light pulses) was persistently affected. These changes within OB circuits most likely emerged as a result of disrupted interactions between M/TCs and local inhibitory neurons that have been reported to modulate the gain of OB output.[59–61] In addition, the reduced OB responsiveness could result from abnormal feedback from downstream areas that target the OB via centrifugal projections and emerge during postnatal development.[62,63]

The most prominent effect of the transient chemogenetic silencing of M/TC outputs was the diminished activation and communication within OB-LEC-HP networks. Correspondingly, a long-lasting decrease in the dendritic arborization and complexity of CA1-projecting pyramidal neurons in LEC was detected at both P11 and P17 after transient M/TC output silencing. The decreased dendritic complexity was confined to the apical dendrites that receive synaptic inputs from OB and PIR inputs. It is likely that these morphological alterations are not restricted to pyramidal neurons but also affect DG-projecting fan cells in LEC, which are known to receive the strongest inputs from OB and PIR.[23]

The lower level of OB-LEC-HP communication as a result of fewer synaptic inputs throughout development ultimately led to poorer performance in cognitive tasks that involve LEC and HP. The strong LEC input to HP provides non-spatial (contextual) information and facilitates the binding of information related to objects, places, and contexts. The used behavioral tests, which capitalized on the preference of mice to explore a novel object and recognize when an object has been relocated, rely on the LEC and HP function.[49,64] The persistent circuit perturbation caused by a diminished level of neuronal activity and network connectivity, which follows the transient chemogenetic manipulation on M/TC outputs, was sufficient to impair the behavioral performance in tasks involving LEC-HP networks.

The present results highlight the critical role of olfactory activity during a defined developmental period (P8–P10) for the functional maturation of LEC and HP. They complement previous findings showing that, in P8–P10 mice, OB activity boosts the oscillatory entrainment of LEC via mono- and poly-synaptic projections[33] and synchronizes the neonatal hippocampal-prefrontal networks in the beta frequency range.[34] Moreover, the findings document the long-lasting function of early electrical activity in the OB. Numerous experimental and theoretical studies have shown that the development of sensory systems, which are not responsive to stimuli during the neonatal stage (e.g., visual and auditory), critically depends on the endogenously generated electrical activity of the corresponding sensory

periphery. For example, spontaneous retinal activity is relayed via the thalamus to the primary visual cortex (V1), where it drives coordinated burst-like oscillatory discharges and neuronal firing.[65,66] Visual deprivation from early Ps decelerates synapse formation and disrupts the maturational processes in V1[58,67] as well as its connectivity with the visual thalamus.[68] Likewise, disruption of acoustic inputs alters the topography and activity in the auditory cortex along development,[69–71] and whisker trimming impairs both the morphological and functional development of the somatosensory cortex.[72,73] Considering the unique features of the olfactory system that by-passes the thalamus[14,15] and has a functional periphery generating odor-induced, respiration-induced, and endogenous patterns of activity already during early stages of development,[33] the sparsity of knowledge on the olfactory control of downstream limbic system refinement is very surprising. The present findings fill this gap and highlight the long-lasting impact of early OB activity on the downstream areas, LEC and HP. They complement previously reported data on early critical periods for long-term plasticity and structural modification of sensory synapses in olfactory cortex.[74,75]

It is worth noting that HP development is sensitive not only to olfactory inputs but also to other sensory modalities. For instance, manual eyelid parting earlier than normal eye-opening accelerates the development of excitatory synaptic transmission within HP and alters spatial working memory later in life.[76] On the other hand, exposure to structured noise during development impairs later HP-related learning.[77] Recent research revealed that twitches during early Ps promote spontaneous HP activity,[78] indicating that sensorimotor activity also contributes to the development of HP. Presumably, the strong impact of M/TC silencing on the LEC-HP communication and cognitive processing depends on the time window of chemogenetic manipulation. At P8–P10 mice have limited motor abilities, closed eyelids and ears, and do not whisker. Indeed, transiently silencing M/TC outputs at a later age (P13–P15), when the ears and eyes are opened, did not affect OB-LEC-HP network activity later in life, confirming the significance of OB activity during early postnatal development. Given that cross-modal plasticity might compensate for the missing sensory inputs,[79,80] silencing OB activity at a time window when visual and auditory systems are both functional (i.e., eyes and ears opened) has a much less detrimental effect on the development of the hippocampal formation and cognitive abilities.

The decreased activity and functional communication within developing LEC-HP networks following transient M/TC output silencing resemble the deficits previously identified in a mouse model of neuropsychiatric disorders at the same age.[64] The link between respiratory entrainment and limbic function in cognitive processing in humans as well as the olfactory dysfunction and disorders is coming more and more into the research focus. Nasal breathing coordinates neuronal oscillations to support stimulus processing and memory retrieval.[42] Moreover, it has been shown that the OB of schizophrenia patients has structural and functional abnormalities, which precede the onset of abnormal cognitive performance.[81,82] Impaired odor perception was also found in patients with autism spectrum disorder.[83,84] Both diseases share developmental abnormalities of the hippocampal formation and cortical areas.[85–87] The present findings let us hypothesize that early olfactory dysfunction that causes long-lasting impairment of electrical activity and sparse connectivity within LEC-HP circuits, contributes to the poor cognitive abilities reported among patients with neuropsychiatric disorders. Further studies addressing this hypothesis might provide new mechanistic insights and targets amenable to therapeutic interventions.

STAR★METHODS

Detailed methods are provided in the online version of this paper and include the following:

- KEY RESOURCES TABLE
- RESOURCE AVAILABILITY
  - Lead contact
  - Materials availability
  - Data and code availability
- EXPERIMENTAL MODEL AND SUBJECT DETAILS
  - Animals
- METHOD DETAILS
  - Microinjection and intraperitoneal injection
  - *In vivo* electrophysiology
  - Histology
  - Behavior
- QUANTIFICATION AND STATISTICAL ANALYSIS
  - Power
  - Imaginary coherence
  - Partial directed coherence
  - Single unit analysis
  - Light-induced field potential
  - Spiking correlation
  - Statistics

SUPPLEMENTAL INFORMATION

Supplemental information can be found online at https://doi.org/10.1016/j.cub.2023.08.072.

ACKNOWLEDGMENTS

We thank P. Putthoff, A. Dahlmann, A. Marquardt, A.M. Thies, and C. Waas for excellent technical assistance; Dr. I. Braren from the Vector Facility of the UKE for the virus production; and Dr. M. Chini and Dr. L. Song for helpful discussions. This work was funded by grants from the German Research Foundation (Ha4466/11-1, Ha4466/20-1, Ha4466/22-1, and SFB 936 178316478 to I.L.H.-O.), European Research Council (ERC-2015-CoG 681577 to I.L.H.-O.), Horizon 2020 DEEPER (101016787 to I.L.H.-O.), MSCA-ITN (860563 to I.L.H.-O.), and Landesforschungsförderung Hamburg (LFF73 and LFF76 to I.L.H.-O.).

AUTHOR CONTRIBUTIONS

Y.-N.C., J.K.K., S.H.B., and I.L.H.-O. designed the experiments and interpreted the data. Y.-N.C. carried out experiments. Y.-N.C. and J.K.K. performed data analysis. I.L.H.-O., Y.-N.C., J.K.K., and S.H.B wrote the paper. All authors approved the submitted version.

DECLARATION OF INTERESTS

The authors declare no competing interests.

INCLUSION AND DIVERSITY

We support inclusive, diverse, and equitable conduct of research.

Received: July 21, 2023
Revised: August 15, 2023
Accepted: August 23, 2023
Published: September 19, 2023

REFERENCES

1. Fries, P. (2005). A mechanism for cognitive dynamics: neuronal communication through neuronal coherence. Trends Cogn. Sci. *9*, 474–480. https://doi.org/10.1016/j.tics.2005.08.011.
2. Buzsáki, G. (2010). Neural syntax: cell assemblies, synapsembles, and readers. Neuron *68*, 362–385. https://doi.org/10.1016/j.neuron.2010.09.023.
3. Voytek, B., and Knight, R.T. (2015). Dynamic network communication as a unifying neural basis for cognition, development, aging, and disease. Biol. Psychiatry *77*, 1089–1097. https://doi.org/10.1016/j.biopsych.2015.04.016.
4. Wilson, M.A., Varela, C., and Remondes, M. (2015). Phase organization of network computations. Curr. Opin. Neurobiol. *31*, 250–253. https://doi.org/10.1016/j.conb.2014.12.011.
5. Quirk, C.R., Zutshi, I., Srikanth, S., Fu, M.L., Devico Marciano, N., Wright, M.K., Parsey, D.F., Liu, S., Siretskiy, R.E., Huynh, T.L., et al. (2021). Precisely timed theta oscillations are selectively required during the encoding phase of memory. Nat. Neurosci. *24*, 1614–1627. https://doi.org/10.1038/s41593-021-00919-0.
6. Fernández-Ruiz, A., Oliva, A., Soula, M., Rocha-Almeida, F., Nagy, G.A., Martin-Vazquez, G., and Buzsáki, G. (2021). Gamma rhythm communication between entorhinal cortex and dentate gyrus neuronal assemblies. Science *372*, https://doi.org/10.1126/science.abf3119.
7. Luo, W., Yun, D., Hu, Y., Tian, M., Yang, J., Xu, Y., Tang, Y., Zhan, Y., Xie, H., and Guan, J.S. (2022). Acquiring new memories in neocortex of hippocampal-lesioned mice. Nat. Commun. *13*, 1601. https://doi.org/10.1038/s41467-022-29208-5.
8. Takehara-Nishiuchi, K., Maal-Bared, G., and Morrissey, M.D. (2011). Increased entorhinal–prefrontal theta synchronization parallels decreased entorhinal–hippocampal theta synchronization during learning and consolidation of associative memory. Front. Behav. Neurosci. *5*, 90. https://doi.org/10.3389/fnbeh.2011.00090.
9. Burwell, R.D., and Amaral, D.G. (1998). Cortical afferents of the perirhinal, postrhinal, and entorhinal cortices of the rat. J. Comp. Neurol. *398*, 179–205. https://doi.org/10.1002/(SICI)1096-9861(19980824)398:2<179::AID-CNE3>3.0.CO;2-Y.
10. Witter, M.P., Wouterlood, F.G., Naber, P.A., and Van Haeften, T. (2000). Anatomical organization of the parahippocampal-hippocampal network. Ann. N. Y. Acad. Sci. *911*, 1–24. https://doi.org/10.1111/j.1749-6632.2000.tb06716.x.
11. Canto, C.B., Wouterlood, F.G., and Witter, M.P. (2008). What does the anatomical organization of the entorhinal cortex tell us? Neural Plast. *2008*, 381243. https://doi.org/10.1155/2008/381243.
12. Igarashi, K.M., Lu, L., Colgin, L.L., Moser, M.B., and Moser, E.I. (2014). Coordination of entorhinal–hippocampal ensemble activity during associative learning. Nature *510*, 143–147. https://doi.org/10.1038/nature13162.
13. Cleland, T.A., and Linster, C. (2019). Central olfactory structures. In Handbook of Olfaction and Gustation (CRC Press), pp. 79–96.
14. Luskin, M.B., and Price, J.L. (1983). The topographic organization of associational fibers of the olfactory system in the rat, including centrifugal fibers to the olfactory bulb. J. Comp. Neurol. *216*, 264–291. https://doi.org/10.1002/cne.902160305.
15. Neville, K.R., and Haberly, L.B. (2004). Olfactory cortex. In The Synaptic Organization of the Brain, G.M. Shepherd, ed. (Oxford University Press), pp. 415–454. https://doi.org/10.1093/acprof:oso/9780195159561.003.0010.
16. Sosulski, D.L., Bloom, M.L., Cutforth, T., Axel, R., and Datta, S.R. (2011). Distinct representations of olfactory information in different cortical centres. Nature *472*, 213–216. https://doi.org/10.1038/nature09868.
17. Kerr, K.M., Agster, K.L., Furtak, S.C., and Burwell, R.D. (2007). Functional neuroanatomy of the parahippocampal region: the lateral and medial entorhinal areas. Hippocampus *17*, 697–708. https://doi.org/10.1002/hipo.20315.
18. Chen, Y., Chen, X., Baserdem, B., Zhan, H., Li, Y., Davis, M.B., Kebschull, J.M., Zador, A.M., Koulakov, A.A., and Albeanu, D.F. (2022). High-throughput sequencing of single neuron projections reveals spatial organization in the olfactory cortex. Cell *185*, 4117–4134.e28. https://doi.org/10.1016/j.cell.2022.09.038.
19. Luskin, M.B., and Price, J.L. (1983). The laminar distribution of intracortical fibers originating in the olfactory cortex of the rat. J. Comp. Neurol. *216*, 292–302. https://doi.org/10.1002/cne.902160306.
20. Witter, M.P. (2007). The perforant path: projections from the entorhinal cortex to the dentate gyrus. In Progress in Brain Research the Dentate Gyrus: A Comprehensive Guide to Structure, Function, and Clinical Implications, H.E. Scharfman, ed. (Elsevier), pp. 43–61. https://doi.org/10.1016/S0079-6123(07)63003-9.
21. Agster, K.L., and Burwell, R.D. (2009). Cortical efferents of the perirhinal, postrhinal, and entorhinal cortices of the rat. Hippocampus *19*, 1159–1186. https://doi.org/10.1002/hipo.20578.
22. Leitner, F.C., Melzer, S., Lütcke, H., Pinna, R., Seeburg, P.H., Helmchen, F., and Monyer, H. (2016). Spatially segregated feedforward and feedback neurons support differential odor processing in the lateral entorhinal cortex. Nat. Neurosci. *19*, 935–944. https://doi.org/10.1038/nn.4303.
23. Bitzenhofer, S.H., Westeinde, E.A., Zhang, H.-X.B., and Isaacson, J.S. (2022). Rapid odor processing by layer 2 subcircuits in lateral entorhinal cortex. eLife *11*, e75065. https://doi.org/10.7554/eLife.75065.
24. Li, Y., Xu, J., Liu, Y., Zhu, J., Liu, N., Zeng, W., Huang, N., Rasch, M.J., Jiang, H., Gu, X., et al. (2017). A distinct entorhinal cortex to hippocampal CA1 direct circuit for olfactory associative learning. Nat. Neurosci. *20*, 559–570.
25. Persson, B.M., Ambrozova, V., Duncan, S., Wood, E.R., O'Connor, A.R., and Ainge, J.A. (2022). Lateral entorhinal cortex lesions impair odor-context associative memory in male rats. J. Neurosci. Res. *100*, 1030–1046. https://doi.org/10.1002/jnr.25027.
26. Mouly, A.-M., and Sullivan, R. (2009). Memory and plasticity in the olfactory system: from infancy to adulthood. In The Neurobiology of Olfaction Frontiers in Neuroscience, A. Menini, ed. (CRC Press/Taylor & Francis), pp. 367–394.
27. Logan, D.W., Brunet, L.J., Webb, W.R., Cutforth, T., Ngai, J., and Stowers, L. (2012). Learned recognition of maternal signature odors mediates the first suckling episode in mice. Curr. Biol. *22*, 1998–2007. https://doi.org/10.1016/j.cub.2012.08.041.
28. Pomeroy, S.L., LaMantia, A.S., and Purves, D. (1990). Postnatal construction of neural circuitry in the mouse olfactory bulb. J. Neurosci. *10*, 1952–1966. https://doi.org/10.1523/JNEUROSCI.10-06-01952.1990.
29. Potter, S.M., Zheng, C., Koos, D.S., Feinstein, P., Fraser, S.E., and Mombaerts, P. (2001). Structure and emergence of specific olfactory glomeruli in the mouse. J. Neurosci. *21*, 9713–9723. https://doi.org/10.1523/JNEUROSCI.21-24-09713.2001.
30. Bailey, M.S., Puche, A.C., and Shipley, M.T. (1999). Development of the olfactory bulb: evidence for glia-neuron interactions in glomerular formation. J. Comp. Neurol. *415*, 423–448. https://doi.org/10.1002/(SICI)1096-9861(19991227)415:4<423::AID-CNE2>3.0.CO;2-G.
31. Schwob, J.E., and Price, J.L. (1984). The development of lamination of afferent fibers to the olfactory cortex in rats, with additional observations in the adult. J. Comp. Neurol. *223*, 203–222. https://doi.org/10.1002/cne.902230205.

32. Treloar, H.B., Miller, A.M., Ray, A., and Greer, C.A. (2009). Development of the olfactory system. In The Neurobiology of Olfaction Frontiers in Neuroscience, A. Menini, ed. (CRC Press/Taylor & Francis), pp. 131–155.

33. Gretenkord, S., Kostka, J.K., Hartung, H., Watznauer, K., Fleck, D., Minier-Toribio, A., Spehr, M., and Hanganu-Opatz, I.L. (2019). Coordinated electrical activity in the olfactory bulb gates the oscillatory entrainment of entorhinal networks in neonatal mice. PLoS Biol. *17*, e2006994. https://doi.org/10.1371/journal.pbio.2006994.

34. Kostka, J.K., and Hanganu-Opatz, I.L. (2023). Olfactory-driven beta band entrainment of limbic circuitry during neonatal development. J. Physiol. *601*, 3605–3630. https://doi.org/10.1113/JP284401.

35. Meaney, M.J., Aitken, D.H., van Berkel, C., Bhatnagar, S., and Sapolsky, R.M. (1988). Effect of neonatal handling on age-related impairments associated with the hippocampus. Science *239*, 766–768. https://doi.org/10.1126/science.3340858.

36. Rüedi-Bettschen, D., Pedersen, E.M., Feldon, J., and Pryce, C.R. (2005). Early deprivation under specific conditions leads to reduced interest in reward in adulthood in Wistar rats. Behav. Brain Res. *156*, 297–310. https://doi.org/10.1016/j.bbr.2004.06.001.

37. Sullivan, R.M., Landers, M., Yeaman, B., and Wilson, D.A. (2000). Good memories of bad events in infancy. Nature *407*, 38–39. https://doi.org/10.1038/35024156.

38. Sevelinges, Y., Sullivan, R.M., Messaoudi, B., and Mouly, A.M. (2008). Neonatal odor-shock conditioning alters the neural network involved in odor fear learning at adulthood. Learn. Mem. *15*, 649–656. https://doi.org/10.1101/lm.998508.

39. Mitsui, S., Igarashi, K.M., Mori, K., and Yoshihara, Y. (2011). Genetic visualization of the secondary olfactory pathway in Tbx21 transgenic mice. Neural Syst. Circuits *1*, 5. https://doi.org/10.1186/2042-1001-1-5.

40. Thompson, K.J., Khajehali, E., Bradley, S.J., Navarrete, J.S., Huang, X.P., Slocum, S., Jin, J., Liu, J., Xiong, Y., Olsen, R.H.J., et al. (2018). DREADD Agonist 21 is an effective agonist for muscarinic-based DREADDs in vitro and in vivo. ACS Pharmacol. Transl. Sci. *1*, 61–72. https://doi.org/10.1021/acsptsci.8b00012.

41. Cutts, C.S., and Eglen, S.J. (2014). Detecting pairwise correlations in spike trains: an objective comparison of methods and application to the study of retinal waves. J. Neurosci. *34*, 14288–14303. https://doi.org/10.1523/JNEUROSCI.2767-14.2014.

42. Zelano, C., Jiang, H., Zhou, G., Arora, N., Schuele, S., Rosenow, J., and Gottfried, J.A. (2016). Nasal respiration entrains human limbic oscillations and modulates cognitive function. J. Neurosci. *36*, 12448–12467. https://doi.org/10.1523/JNEUROSCI.2586-16.2016.

43. Baccalá, L.A., and Sameshima, K. (2001). Partial directed coherence: a new concept in neural structure determination. Biol. Cybern. *84*, 463–474. https://doi.org/10.1007/PL00007990.

44. Walz, A., Omura, M., and Mombaerts, P. (2006). Development and topography of the lateral olfactory tract in the mouse: imaging by genetically encoded and injected fluorescent markers. J. Neurobiol. *66*, 835–846. https://doi.org/10.1002/neu.20266.

45. Wayman, G.A., Impey, S., Marks, D., Saneyoshi, T., Grant, W.F., Derkach, V., and Soderling, T.R. (2006). Activity-dependent dendritic arborization mediated by CaM-kinase I activation and enhanced CREB-dependent transcription of Wnt-2. Neuron *50*, 897–909. https://doi.org/10.1016/j.neuron.2006.05.008.

46. Bitzenhofer, S.H., Pöpplau, J.A., Chini, M., Marquardt, A., and Hanganu-Opatz, I.L. (2021). A transient developmental increase in prefrontal activity alters network maturation and causes cognitive dysfunction in adult mice. Neuron *109*, 1350–1364.e6. https://doi.org/10.1016/j.neuron.2021.02.011.

47. Connor, C.E., and Knierim, J.J. (2017). Integration of objects and space in perception and memory. Nat. Neurosci. *20*, 1493–1503. https://doi.org/10.1038/nn.4657.

48. Wang, C., Chen, X., Lee, H., Deshmukh, S.S., Yoganarasimha, D., Savelli, F., and Knierim, J.J. (2018). Egocentric coding of external items in the lateral entorhinal cortex. Science *362*, 945–949. https://doi.org/10.1126/science.aau4940.

49. Sun, Y., Jin, S., Lin, X., Chen, L., Qiao, X., Jiang, L., Zhou, P., Johnston, K.G., Golshani, P., Nie, Q., et al. (2019). CA1-projecting subiculum neurons facilitate object–place learning. Nat. Neurosci. *22*, 1857–1870. https://doi.org/10.1038/s41593-019-0496-y.

50. Hartung, H., Cichon, N., De Feo, V., Riemann, S., Schildt, S., Lindemann, C., Mulert, C., Gogos, J.A., and Hanganu-Opatz, I.L. (2016). From shortage to surge: a developmental switch in hippocampal–prefrontal coupling in a gene–environment model of neuropsychiatric disorders. Cereb. Cortex *26*, 4265–4281. https://doi.org/10.1093/cercor/bhw274.

51. Schepanski, S., Chini, M., Sternemann, V., Urbschat, C., Thiele, K., Sun, T., Zhao, Y., Poburski, M., Woestemeier, A., Thieme, M.T., et al. (2022). Pregnancy-induced maternal microchimerism shapes neurodevelopment and behavior in mice. Nat. Commun. *13*, 4571. https://doi.org/10.1038/s41467-022-32230-2.

52. Blair, M.G., Nguyen, N.N.-Q., Albani, S.H., L'Etoile, M.M., Andrawis, M.M., Owen, L.M., Oliveira, R.F., Johnson, M.W., Purvis, D.L., Sanders, E.M., et al. (2013). Developmental changes in structural and functional properties of hippocampal AMPARs parallels the emergence of deliberative spatial navigation in juvenile rats. J. Neurosci. *33*, 12218–12228. https://doi.org/10.1523/JNEUROSCI.4827-12.2013.

53. Rudy, J.W., Stadler-Morris, S., and Albert, P. (1987). Ontogeny of spatial navigation behaviors in the rat: dissociation of "proximal"- and "distal"--cue-based behaviors. Behav. Neurosci. *101*, 62–73. https://doi.org/10.1037//0735-7044.101.1.62.

54. Albani, S.H., McHail, D.G., and Dumas, T.C. (2014). Developmental studies of the hippocampus and hippocampal-dependent behaviors: insights from interdisciplinary studies and tips for new investigators. Neurosci. Biobehav. Rev. *43*, 183–190. https://doi.org/10.1016/j.neubiorev.2014.04.009.

55. Salimi, M., Tabasi, F., Nazari, M., Ghazvineh, S., Salimi, A., Jamaati, H., and Raoufy, M.R. (2021). The olfactory bulb modulates entorhinal cortex oscillations during spatial working memory. J. Physiol. Sci. *71*, 21. https://doi.org/10.1186/s12576-021-00805-1.

56. Fox, K. (2002). Anatomical pathways and molecular mechanisms for plasticity in the barrel cortex. Neuroscience *111*, 799–814. https://doi.org/10.1016/S0306-4522(02)00027-1.

57. Fox, K., and Wong, R.O.L. (2005). A comparison of experience-dependent plasticity in the visual and somatosensory systems. Neuron *48*, 465–477. https://doi.org/10.1016/j.neuron.2005.10.013.

58. Zheng, J.J., Li, S.J., Zhang, X.D., Miao, W.Y., Zhang, D., Yao, H., and Yu, X. (2014). Oxytocin mediates early experience–dependent cross-modal plasticity in the sensory cortices. Nat. Neurosci. *17*, 391–399. https://doi.org/10.1038/nn.3634.

59. Kato, H.K., Gillet, S.N., Peters, A.J., Isaacson, J.S., and Komiyama, T. (2013). Parvalbumin-expressing interneurons linearly control olfactory bulb output. Neuron *80*, 1218–1231. https://doi.org/10.1016/j.neuron.2013.08.036.

60. Linster, C., and Cleland, T.A. (2009). Glomerular microcircuits in the olfactory bulb. Neural Netw. *22*, 1169–1173. https://doi.org/10.1016/j.neunet.2009.07.013.

61. Fukunaga, I., Herb, J.T., Kollo, M., Boyden, E.S., and Schaefer, A.T. (2014). Independent control of gamma and theta activity by distinct interneuron networks in the olfactory bulb. Nat. Neurosci. *17*, 1208–1216. https://doi.org/10.1038/nn.3760.

62. Kostka, J.K., and Bitzenhofer, S.H. (2022). Postnatal development of centrifugal inputs to the olfactory bulb. Front. Neurosci. *16*, 815282. https://doi.org/10.3389/fnins.2022.815282.

63. Padmanabhan, K., Osakada, F., Tarabrina, A., Kizer, E., Callaway, E.M., Gage, F.H., and Sejnowski, T.J. (2018). Centrifugal inputs to the main olfactory bulb revealed through whole brain circuit-mapping. Front. Neuroanat. *12*, 115. https://doi.org/10.3389/fnana.2018.00115.

64. Xu, X., Song, L., Kringel, R., and Hanganu-Opatz, I.L. (2021). Developmental decrease of entorhinal-hippocampal communication in immune-challenged DISC1 knockdown mice. Nat. Commun. *12*, 6810. https://doi.org/10.1038/s41467-021-27114-w.

65. Hanganu, I.L., Ben-Ari, Y., and Khazipov, R. (2006). Retinal waves trigger spindle bursts in the neonatal rat visual cortex. J. Neurosci. *26*, 6728–6736. https://doi.org/10.1523/JNEUROSCI.0752-06.2006.

66. Ackman, J.B., Burbridge, T.J., and Crair, M.C. (2012). Retinal waves coordinate patterned activity throughout the developing visual system. Nature *490*, 219–225. https://doi.org/10.1038/nature11529.

67. Price, D.J., Ferrer, J.M., Blakemore, C., and Kato, N. (1994). Postnatal development and plasticity of corticocortical projections from area 17 to area 18 in the cat's visual cortex. J. Neurosci. *14*, 2747–2762. https://doi.org/10.1523/JNEUROSCI.14-05-02747.1994.

68. Hofer, S.B., Mrsic-Flogel, T.D., Bonhoeffer, T., and Hübener, M. (2009). Experience leaves a lasting structural trace in cortical circuits. Nature *457*, 313–317. https://doi.org/10.1038/nature07487.

69. Chang, E.F., and Merzenich, M.M. (2003). Environmental noise retards auditory cortical development. Science *300*, 498–502. https://doi.org/10.1126/science.1082163.

70. Nakahara, H., Zhang, L.I., and Merzenich, M.M. (2004). Specialization of primary auditory cortex processing by sound exposure in the "critical period". Proc. Natl. Acad. Sci. USA *101*, 7170–7174. https://doi.org/10.1073/pnas.0401196101.

71. Xue, B., Meng, X., Xu, Y., Kao, J.P.Y., and Kanold, P.O. (2022). Transient coupling between infragranular and subplate layers to layer 1 neurons before ear opening and throughout the critical period depends on peripheral activity. J. Neurosci. *42*, 1702–1718. https://doi.org/10.1523/JNEUROSCI.2505-20.2021.

72. Lee, L.J., Chen, W.J., Chuang, Y.W., and Wang, Y.C. (2009). Neonatal whisker trimming causes long-lasting changes in structure and function of the somatosensory system. Exp. Neurol. *219*, 524–532. https://doi.org/10.1016/j.expneurol.2009.07.012.

73. Sieben, K., Bieler, M., Röder, B., and Hanganu-Opatz, I.L. (2015). Neonatal restriction of tactile inputs leads to long-lasting impairments of cross-modal processing. PLoS Biol. *13*, e1002304. https://doi.org/10.1371/journal.pbio.1002304.

74. Best, A.R., and Wilson, D.A. (2003). A postnatal sensitive period for plasticity of cortical afferents but not cortical association fibers in rat piriform cortex. Brain Res. *961*, 81–87. https://doi.org/10.1016/S0006-8993(02)03847-7.

75. Poo, C., and Isaacson, J.S. (2007). An early critical period for long-term plasticity and structural modification of sensory synapses in olfactory cortex. J. Neurosci. *27*, 7553–7558. https://doi.org/10.1523/JNEUROSCI.1786-07.2007.

76. Dumas, T.C. (2004). Early eyelid opening enhances spontaneous alternation and accelerates the development of perforant path synaptic strength in the hippocampus of juvenile rats. Dev. Psychobiol. *45*, 1–9. https://doi.org/10.1002/dev.20011.

77. Zhang, Y., Zhu, M., Sun, Y., Tang, B., Zhang, G., An, P., Cheng, Y., Shan, Y., Merzenich, M.M., and Zhou, X. (2021). Environmental noise degrades hippocampus-related learning and memory. Proc. Natl. Acad. Sci. USA *118*. e2017841117. https://doi.org/10.1073/pnas.2017841117.

78. Leprince, E., Dard, R.F., Mortet, S., Filippi, C., Giorgi-Kurz, M., Bourboulou, R., Lenck-Santini, P.P., Picardo, M.A., Bocchio, M., Baude, A., et al. (2023). Extrinsic control of the early postnatal CA1 hippocampal circuits. Neuron *111*, 888–902.e8. https://doi.org/10.1016/j.neuron.2022.12.013.

79. Xu, X., Hanganu-Opatz, I.L., and Bieler, M. (2020). Cross-talk of low-level sensory and high-level cognitive processing: development, mechanisms, and relevance for cross-modal abilities of the brain. Front. Neurorobot. *14*, 7. https://doi.org/10.3389/fnbot.2020.00007.

80. Ewall, G., Parkins, S., Lin, A., Jaoui, Y., and Lee, H.K. (2021). Cortical and subcortical circuits for cross-modal plasticity induced by loss of vision. Front. Neural Circuits *15*, 665009. https://doi.org/10.3389/fncir.2021.665009.

81. Turetsky, B.I., Moberg, P.J., Yousem, D.M., Doty, R.L., Arnold, S.E., and Gur, R.E. (2000). Reduced olfactory bulb volume in patients with schizophrenia. Am. J. Psychiatry *157*, 828–830. https://doi.org/10.1176/appi.ajp.157.5.828.

82. Corcoran, C., Whitaker, A., Coleman, E., Fried, J., Feldman, J., Goudsmit, N., and Malaspina, D. (2005). Olfactory deficits, cognition and negative symptoms in early onset psychosis. Schizophr. Res. *80*, 283–293. https://doi.org/10.1016/j.schres.2005.07.028.

83. Bennetto, L., Kuschner, E.S., and Hyman, S.L. (2007). Olfaction and taste processing in autism. Biol. Psychiatry *62*, 1015–1021. https://doi.org/10.1016/j.biopsych.2007.04.019.

84. Koehler, L., Fournel, A., Albertowski, K., Roessner, V., Gerber, J., Hummel, C., Hummel, T., and Bensafi, M. (2018). Impaired odor perception in autism spectrum disorder is associated with decreased activity in olfactory cortex. Chem. Senses *43*, 627–634. https://doi.org/10.1093/chemse/bjy051.

85. Arnold, S.E. (2000). Cellular and molecular neuropathology of the parahippocampal region in schizophrenia. Ann. N. Y. Acad. Sci. *911*, 275–292. https://doi.org/10.1111/j.1749-6632.2000.tb06732.x.

86. Hazlett, H.C., Gu, H., Munsell, B.C., Kim, S.H., Styner, M., Wolff, J.J., Elison, J.T., Swanson, M.R., Zhu, H., Botteron, K.N., et al. (2017). Early brain development in infants at high risk for autism spectrum disorder. Nature *542*, 348–351. https://doi.org/10.1038/nature21369.

87. Chini, M., and Hanganu-Opatz, I.L. (2021). Prefrontal cortex development in health and disease: lessons from rodents and humans. Trends Neurosci. *44*, 227–240. https://doi.org/10.1016/j.tins.2020.10.017.

88. Hill, J.M., Lim, M.A., and Stone, M.M. (2008). Developmental milestones in the newborn mouse. In Neuropeptide Techniques Neuromethods, I. Gozes, ed. (Humana Press), pp. 131–149. https://doi.org/10.1007/978-1-60327-099-1_10.

89. Meyer, P.M., and Alberts, J.R. (2016). Non-nutritive, thermotactile cues induce odor preference in infant mice (Mus musculus). J. Comp. Psychol. *130*, 369–379. https://doi.org/10.1037/com0000044.

90. Leger, M., Quiedeville, A., Bouet, V., Haelewyn, B., Boulouard, M., Schumann-Bard, P., and Freret, T. (2013). Object recognition test in mice. Nat. Protoc. *8*, 2531–2537. https://doi.org/10.1038/nprot.2013.155.

91. Nolte, G., Bai, O., Wheaton, L., Mari, Z., Vorbach, S., and Hallett, M. (2004). Identifying true brain interaction from EEG data using the imaginary part of coherency. Clin. Neurophysiol. *115*, 2292–2307. https://doi.org/10.1016/j.clinph.2004.04.029.

92. Rossant, C., Kadir, S.N., Goodman, D.F.M., Schulman, J., Hunter, M.L.D., Saleem, A.B., Grosmark, A., Belluscio, M., Denfield, G.H., Ecker, A.S., et al. (2016). Spike sorting for large, dense electrode arrays. Nat. Neurosci. *19*, 634–641. https://doi.org/10.1038/nn.4268.

93. Bates, D., Mächler, M., Bolker, B., and Walker, S. (2015). Fitting linear mixed-effects models using lme4. J. Stat. Softw. *67*, 1–48. https://doi.org/10.18637/jss.v067.i01.

94. Searle, S.R., Speed, F.M., and Milliken, G.A. (1980). Population marginal means in the linear model: an alternative to least squares means. Am. Stat. *34*, 216–221. https://doi.org/10.1080/00031305.1980.10483031.

STAR★METHODS

KEY RESOURCES TABLE

REAGENT or RESOURCE	SOURCE	IDENTIFIER
Antibodies		
Rabbit-anti-GFP	Abcam	Cat# Ab6556, RRID: AB_305564
Alexa Fluor-488 goat anti-rabbit IgG secondary Antibody	Thermo Fisher Scientific	Cat# A11008, RRID: AB_143165
Bacterial and virus strains		
AAV9-EF1a-DIO-hM4Di-mCherry	Addgene	Cat# 50461, RRID: Addgene_50461
AAV9-Ef1a-DIO-hChR2(E123T/T159C)-EYFP	Addgene	Cat# 35509, RRID: Addgene_35509
AAVrg-CamKIIa-EGFP	Addgene	Cat# 50469, RRID: Addgene_50469
Chemicals, peptides, and recombinant proteins		
Isoflurane	Baxter	Cat# HDG9623
Ketamine	Richter Pharma AG	Ketamidor
Xylazine	Bayer	Rompun
Compound 21	Hello Bio	Cat# HB6124, CAS# 2250025-92-2
Isoamyl acetate	Sigma-Aldrich	Cat# W205532, CAS# 123-92-2
Vanillin	Sigma-Aldrich	Cat# W310700, CAS# 121-33-5
Omnifill C	Omin Dent	Cat# 85182
DiI (1,1'-Dioctadecyl-3,3,3',3'-tetramethylindocarbocyanine perchlorate)	Molecular Probes	Cat# D282, CAS# 41085-99-8
ROTI Histofix	Carl Roth	Cat# P087.1
Triton X-100	Sigma-Aldrich	Cat# T8787, CAS# 9036-19-5
Sodium azide	Sigma-Aldrich	Cat# 71289, CAS# 26628-22-8
Fluoromount	Thermo Fisher Scientific	Cat# 00-4958-02
Hoechst	Thermo Fisher Scientific	Cat# 33342, CAS# 23491-52-3
DAPI	Sigma-Aldrich	Cat# D9542, CAS# 28718-90-3
VECTASHIELD Antifade Mounting Medium with DAPI	Vector Laboratories	H-1200-10
Deposited data		
Extracellular recording data and sorted single unit data	This paper	N/A
Experimental models: Organisms/strains		
Mouse: Tbet-cre (B6; CBA-Tg(Tbx21-cre) 1Dlc/J)	Jackson Laboratory	RRID: IMSR_JAX: 024507
Software and algorithms		
Cheetah 6	Neuralynx	http://neuralynx.com/
Video Mot2	TSE Systems	https://www.tsesystems.com/productdetails/videomot
Zen Blue 3.4	Zeiss	RRID: SCR_021725
MATLAB R2018b	MathWorks	RRID: SCR_001622
Anaconda 1.9.12	Conda	RRID: SCR_018317
Python 3.8	Python	RRID: SCR_008394
R Statistical Software 4.2.2	RStudio	RRID: SCR_001905
ImageJ	NIH	RRID: SCR_002285
Klusta	kwikteam	https://github.com/kwikteam/klusta
Phy	Cortex-lab	https://github.com/cortex-lab/phy
DeepLabCut	DLC Team	RRID: SCR_021391
Custom-written MATLAB code	This paper	https://github.com/OpatzLab/HanganuOpatzToolbox
Other		
Multichannel extracellular amplifier	Neuralynx	Digital Lynx SX
Arduino Uno SMD	Arduino	A000073

(*Continued on next page*)

Continued

REAGENT or RESOURCE	SOURCE	IDENTIFIER
Diode laser (473 nm)	Omicron	LuxX 473-100
Recording electrode (1 shank, 16 channels, 50 μm inter-site spacing)	Neuronexus	A1x16-5mm-50-703-A16
Recording electrode (1 shank, 16 channels, 100 μm inter-site spacing)	Neuronexus	A1x16-5mm-100-703-A16
Recording optrode (1 shank, 16 channels, 50 μm inter-site spacing)	Neuronexus	A1x16-5mm-50-703-OA16LP
Vibratome	Leica	VT1000S
Confocal microscope	Zeiss	LSM 700, RRID: SCR_017377

RESOURCE AVAILABILITY

Lead contact

Further information and requests for resources and reagents should be directed to and will be fulfilled by the Lead Contact, Ileana L. Hanganu-Opatz (hangop@zmnh.uni-hamburg.de).

Materials availability

The study did not generate new unique reagents.

Data and code availability

- All data needed to evaluate the conclusions are available in the main manuscript or the supplementary materials.
- The original analysis code to generate the results is described in the STAR Methods section or is available at the following open-access repository: https://github.com/OpatzLab/HanganuOpatzToolbox.
- Any additional information required to reanalyze the data reported in this paper is available from the lead contact upon request.

EXPERIMENTAL MODEL AND SUBJECT DETAILS

Animals

All experiments were performed in compliance with German laws and the guidelines of the European Community for the use of animals in research and were approved by the local ethical committee (G17/015). Experiments were carried out on Tbet-cre (B6; CBA-Tg (Tbx21-cre) 1Dlc/J, JAX#024507) mice of both sexes. Timed-pregnant Tbet-cre mice from the animal facility of the University Medical Center Hamburg-Eppendorf were housed individually in breeding cages at a 12-h light/dark cycle and fed *ad libitum*. The day of vaginal plug detection was considered E0.5 and the day of birth was considered P0. These transgenic mice express *Cre* recombinase from the mouse *T-box 21* (also called Tbet) promoter in mitral cells of the main and accessory olfactory bulbs.[39] Genotypes were determined using genomic DNA and the following primer sequences (Metabion, Planegg/Steinkirchen): PCR forward primer 5'-ATCCGAAAAGAAAACGTTGA-3' and reverse primer 5'-ATCCAGGTTACGGATATAGT-3'. Cre^+ and Cre^- littermates were used for experimental or control groups, respectively.

METHOD DETAILS

Microinjection and intraperitoneal injection

Virus injection for transfection of M/TCs with hm4Di and ChR2

P1 pups were anesthetized with isoflurane (3 %) and fixed into a stereotaxic apparatus and AAV9-EF1a-DIO-hM4Di-mCherry (Plasmid #50461, Addgene) at titer $\geq 1\times10^{13}$ vg/mL was injected bilaterally into both OBs (200 nL for each side) at a rate of 100 nL/min using a syringe infusion microinjector (MICRO4, WPI). Following the injections, the syringe was left in the injection place for an additional 2 min to avoid reflux of the fluid then slowly withdrawn. For the subset of animals used for optogenetics, injection of AAV9-EF1a-DIO-hM4Di-mCherry was mixed with the simultaneous injection of AAV9-Ef1a-DIO-hChR2(E123T/T159C)-EYFP ($\geq 1\times10^{13}$ vg/mL, Plasmid #35509, Addgene) at a ratio of 1:1. After injections, pups were maintained on a heating blanket until full recovery and returned to the dam. Expression of hM4Di-mCherry and ChR2-EYFP were detected using a dual fluorescent protein flashlight (Electron Microscopy Sciences) before surgery and confirmed post-mortem. Only mice with sufficient bilateral expression of fluorescence were included in the experiments and analysis for the experimental group.

Virus injection in HP for retrograde tracing

For the retrograde labeling of CA1-projecting neurons, P3 or P9 hM4Di transfected (injected into OBs on P1) mice were anesthetized with isoflurane (3 %) and head fixed in a stereotactic apparatus. Retrograde virus AAVrg-CamKIIa-EYFP (50 μl at titer $\geq 1\times10^{12}$ vg/mL, #50469-AAVrg, Addgene) was injected into the dorsal CA1 of HP (1.0 mm posterior to bregma, 1.2 mm lateral from the midline, 0.8-0.9 mm deep from the skull for P3 and 1.1-1.2 mm deep from the skull for P9) at a rate of 50 nL/min. Following the injections, the syringe was left in the injection place for an additional 5 min to avoid reflux of the fluid then slowly withdrawn.

Compound 21 injection

For chemogenetic inhibition of vesicle release on M/TC axons, Compound 21 (C21, Hello Bio, 0.3 $mg \cdot mL^{-1}$ dissolved in 0.9% NaCl) was injected intraperitoneally (IP) at P8, P9 and P10 (or at P13, P14 and P15) once a day into both Cre^+ and Cre^- mice.

In vivo electrophysiology

Acute multi-site electrophysiological recordings

In vivo acute extracellular recordings were conducted as described previously.[34,64] Multi-site extracellular recordings were performed in the OB, LEC and dorsal HP of P11 or P16-23 mice. Under isoflurane anesthesia (5 % for induction and 2.5 % for maintenance; Braxter), the skin above the skull was removed and 0.25 % bupivacaine/1 % lidocaine was locally applied to the neck muscles for pain relief. Two plastic bars for head fixation in the recording setup were mounted on the nasal and occipital bones with dental cement (Omnifill C, Omin Dent). The bone above the right OB (0.5-0.8 mm anterior to frontonasal suture, 0.5 mm lateral to inter-nasal suture), LEC (0 mm posterior to lambda, 6-7.5 mm lateral from the midline) and HP (1.0 mm posterior to bregma, 1.2 mm lateral from the midline) was carefully removed by drilling a hole of <0.5 mm inside diameter. After a recovery period of 20 min, pups were transferred to the setup for electrophysiological recording where they were head-fixed into a stereotaxic apparatus. One-shank electrodes (NeuroNexus) with 16 recording sites (50 μm inter-site spacing for recordings in OB, 100 μm inter-site spacing for recordings in LEC and HP) were stereotactically inserted into OB (1.8-2 mm, angle 0°), LEC (depth: 2-2.4mm, P11: angle: 90°; P16-23, angle: 15°), HP (1.2-1.7 mm, angle 0°) using micromanipulators. For light stimulation, one-shank optrodes (NeuroNexus) with the same configuration as the electrodes were inserted in the OB. A silver wire was inserted into the cerebellum as ground and reference. Pups were allowed to recover for 15 min before data acquisition. Extracellular signals were band-pass filtered (0.1-9,000 Hz) and digitized (32 kHz) with a multichannel extracellular amplifier (Digital Lynx SX; Neuralynx) and acquisition software (Cheetah, Neuralynx). Spontaneous activity was recorded for at least 20 min before odor or light stimulation. Electrode position was confirmed in brain slices post-mortem with DiI (Molecular Probes).

Olfactory stimulation

For olfactory stimulation, a custom-made olfactometer was used and odors were applied for 2 s triggered by the respiration of the mice and controlled by a pre-programmed controller (Arduino). Two different odors (Vanillin and isoamyl acetate, 1:100 diluted in distilled water and mineral oil respectively) were delivered in a randomized order for 40-60 repetitions. A stream of clean air was pointed at the snout of the mice at 900 ml/min controlled by mass flow controllers.

Light stimulation

To stimulate ChR2-expressing M/TCs, light stimulation was applied using a diode laser (Omicron) which was controlled by a pre-programmed controller (Arduino) to deliver 3 ms square pulses of blue light (473 nm, 90 repetitions). Laser power at the tip of the optical fibers was adjusted for every recording to reliably induce neuronal firing.

Histology

Immunohistochemistry

Mice were deeply anesthetized with 10 % ketamine (Ketamidor, Richter Pharma AG)/2 % xylazine (Rompun, Bayer) diluted in 0.9 % NaCl solution (10 μg/g body weight, intraperitoneal injection) and transcardially perfused with 4 % paraformaldehyde (PFA, Histofix, Carl Roth). Brains were extracted from the skulls and post-fixed in 4% PFA at 4 °C overnight, then sliced using a vibratome (VT1000S, Leica). Slices (100 μm-thick) were mounted with Fluoromount (Thermo Fisher Scientific) and Hoechst (Thermo Fisher Scientific) or DAPI (Sigma-Aldrich). The positions of the DiI-labeled extracellular electrodes were reconstructed to confirm the location of insertion.

For brains injected with AAVrg-CamKIIa-EGFP in CA1, free-floating 50 μm-thick slices containing HP and LEC were permeabilized and blocked with PBS containing 0.2% Triton X-100 (Sigma-Aldrich), 5% normal bovine serum (BSA, Jackson Immuno Research) and 0.02% sodium azide (Sigma-Aldrich). Slices were incubated with primary antibody rabbit-anti-GFP (1:500, #ab6556, Abcam) for 48 h, followed by 2 h incubation with secondary antibody goat-anti-rabbit Alexa Fluor 488 (1:1000, #A11008, Thermo Fisher). Sections were washed three times in PBS (10 min per time) and covered with Vectorshield containing DAPI (Vector Laboratories) on glass slides.

Dendritic complexity and spine quantification

Sections containing LEC were imaged using a confocal microscope (LSM700, Zeiss) and Zen Blue software (Zeiss). Image stacks of GFP-labeled neurons were acquired using both 20x (2048x2048 pixel) and 40x (4096x4096 pixel) objectives. Images were binarized (auto threshold) using the auto threshold function, and the dendrites were traced using the semi-automatic simple neurite tracer (SNT) plugin in ImageJ environment. The geometric center was identified, and dendritic complexity was analyzed with Sholl analysis function of SNT plugin. For spine quantification, spines on apical dendrites were manually counted using the *point picker* tool and measured with *line* tool for length in ImageJ.

Behavior

Developmental milestones

Somatic and reflex development was examined every day in P2-11 mice (for P2-6 the tests were performed every second day) as previously described.[46,88] Weight, body length and tail length were measured at the same time on each testing day. Forelimb grasp was assessed as time hanging on a toothpick grasped with the forepaws until falling. Cliff aversion was measured as the time until withdrawing after being positioned with forepaws and snout over an elevated edge. Surface righting was measured as time to flip over onto its abdomen after being positioned on the back. Ear twitch was measured as the pup responds to brushing the ear with the cotton tip (the test is terminated if the mouse does not respond within 30 s). Rooting was measured as the pup moves its head toward the cotton tip (the test is terminated if the mouse does not respond within 30 s). For spontaneous locomotion, the mouse is placed in the center of a circular arena (13 cm inside diameter) and allowed to freely explore the arena for 3 min. Mice were video tracked using a fixed camera (BOSCH) with the zone monitor mode of the VideoMot 2 software (TSE Systems GmbH). The moving distance was quantified in MATLAB environment.

Odor preference test

Odor preference of neonatal mice was tested for 3 min using a testing apparatus similar as described.[89] The testing apparatus consists of a rectangular acrylic chamber (17.5 × 6.5 × 6.5 cm) with metal grid flooring, divided into two 6.5 cm approach zones, located on either end of the chamber and a 4.5 cm neutral zone in the center. Left and right fields were odorized by placing 6.5 cm × 6.5 cm acrylic trays beneath the grid flooring, each containing 10 g of bedding taken from either the homecage of the test pups or fresh bedding soaked with 1% vanillin (w/v, in distilled water). For each test, the pup was placed in the center of the arena (i.e., neutral zone). All tests were performed at room temperature. Between each test, the chamber was cleaned with distilled water thoroughly and the positions of the odor field trays were reorganized. Mice were video-tracked using a fixed camera (BOSCH) with the zone monitor mode of the VideoMot 2 software. The percentage of time spent over the different odor fields was quantified in MATLAB environment. Analysis was performed blind to the group identity of mice.

Open Field Test (OFT)

Mice at P15 were positioned in the center of a circular arena (34 cm inside diameter) and allowed to freely explore the arena for 10 min after 30 s adaptation. The test room was dimly illuminated. Additionally, the floor area of the arena was digitally subdivided into 8 zones (4 center zones and 4 border zones) using the zone monitor mode of the VideoMot 2 software (TSE Systems GmbH). The spontaneous exploration was video-tracked, and the moving distance was quantified.

Object recognition tests

All protocols for assessing object recognition memory in pre-juvenile mice consisted of familiarization and testing trials. Novel object recognition (NOR, on P16) and object location preference (OLP, on P19) tests were performed in the same arena as the OFT.[50,64,90] For the NOR test, each mouse was allowed to explore two identical objects for 10 min during the familiarization trial. After a delay period of 5 min, the mouse was placed back in the arena for the test trial, where one of the objects was replaced by a novel object. In the OLP task, each mouse was allowed to explore two different objects for 10 min during the familiarization trial. After the 5 min delay period, the mouse was placed back to investigate one old object which was previously presented and a copy of the old object for 5 min. After each trail, both the arena and objects were cleaned with 0.1% acetic acid to eliminate the odors. Behavior was video-tracked and analyzed using DeepLabCut in Python environment. Object interaction was defined as the snout being within < 1 cm distance from an object and the animals were excluded from the analysis if the total object exploration time was less than 20 s during the familiarization trial. Exploration for objects was quantified as the discrimination index of time spent interacting with the new and familiar object:

$$Discrimination\ index = \frac{time_{object2} - time_{object1}}{time_{object1} + time_{object1}}.$$

Spontaneous alternation

An elevated Y-maze was used to test the spontaneous alternation of mice at P23-24. Each mouse was positioned in the start arm of the Y-maze and allowed to freely explore the maze for 10 min.[46] Visited arms during free exploration were quantified using MATLAB environment. The percentage of alternations was calculated as (number of alterations/(entries - 2)).

QUANTIFICATION AND STATISTICAL ANALYSIS

Data were analyzed offline using custom-written scripts in MATLAB environment (MathWorks). Data were first band-passed filtered (1-100 Hz for LFP or 500-9000 Hz for spike analysis) using a third-order Butterworth filter before down-sampling to 1.6 kHz in a manner preserving phase information for LFP.

Power

Power spectral density (PSD) was computed using Welch's method (MATLAB build-in pwelch.m function) with non-overlapping 3-s-long windows.

For odor stimulation experiments power was calculated on 2-s-long periods during odor presentation (Stim) and normalized by the power of the 2-s-long period preceding the odor stimulation (Pre):

$$\frac{PSD_{Stim} - PSD_{Pre}}{PSD_{Pre}}.$$

Imaginary coherence

The imaginary part of complex coherence, which is insensitive to volume-conduction-based effects,[91] was calculated by taking the absolute value of the imaginary component of the normalized cross-spectral density (using MATLAB build-in functions: cpds.m and pwelch.m) according to the formula:

$$C_{XY}(f) = \left| Im\left(\frac{P_{XY}(f)}{\sqrt{P_{XX}(f)P_{YY}(f)}} \right) \right|,$$

where C_{XY} is for the imaginary coherence of signals X and Y over frequency (f), P_{XX} and P_{YY} are their PSD respectively, and P_{XY} is the cross-spectral density. Shuffling of the coherence calculation was performed 1000 times.

Partial directed coherence

To investigate the directionality of functional connectivity between brain regions, generalized partial directed coherence (gPDC) which is based on a linear Granger causality measure in the frequency domain was calculated using a previously described algorithm.[43] The method attempts to describe the causal relationship between multivariate time series based on the decomposition of multivariate partial coherence computed from multivariate autoregressive models. The LFP signal was divided into 3-s long segments and de-noising was applied using MATLAB build-in wavelet toolbox (ddencmp.m and wdencmp.m) before the calculation.

Single unit analysis

Single unit activity (SUA) was detected and clustered using klusta (https://github.com/kwikteam/klusta) based on waveform features and manually curated using phy (https://github.com/cortex-lab/phy)[92] in Python environment. SUA data were then imported and analyzed using custom-written tools in MATLAB. The firing rate was calculated by dividing the total number of spikes by the duration of the analyzed time window. To assess the spike probability after blue light pulses, histograms of spike count using 1 ms bins were calculated for periods around the 3-ms light pulse (50 ms before to 100 ms after) and normalized to the number of light pulses.

Light-induced field potential

For accessing the light-induced response, unfiltered extracellular recording signals were downsampled to 1600 Hz and data recorded during periods around the 3-ms light pulse (50 ms before to 100 ms after) were used for analysis. The peaks for the absolute value of the signals after the pulses were detected and averaged for each mouse.

Spiking correlation

Spike time tiling coefficient (STTC), a metric that tracks correlations between spike trains and is robust to changes in firing rate,[41] was calculated as previously described according to the formula:

$$STTC = \frac{1}{2}\left(\frac{P_A - T_B}{1 - P_A T_B} + \frac{P_B - T_A}{1 - P_B T_A} \right),$$

where P_A is the proportion of spikes in spike train A that falls within $\pm\Delta t$ of a spike from spike train B. T_A is the proportion of time that occurs within $\pm\Delta t$ from the spikes of spike train A. The same applies for P_B and T_B. $\pm\Delta t$ stands for the timescale at which STTC is computed, variying from 5 ms to 1000 ms.

Statistics

Statistical analysis was performed in MATLAB and R statistical software. Non-normally distributed data were tested for significance using Wilcoxon rank-sum test. Outlier removal was applied to datasets if values are more than 1.5 interquartile ranges above the upper quartile (75%) or below the lower quartile (25%). Longitudinal data were analyzed with linear mixed-effects models (LMEM; lmer and glmer functions of the "lme4" R package)[93] with 'mouse' as a random effect. Post-hoc analysis was carried out using the "emmeans" R package based on the estimated marginal means theory.[94] C21-injected Cre$^-$ littermates were used as controls except for saline-injected Cre$^+$ pups (same injections as for C21) served as controls for the light-stimulation dataset. All data were expressed as median and interquartile range unless otherwise stated. A significance level of $p < 0.05$ was considered statistically significant. If not included in the text, values of corresponding statistics can be found in the supplementary information.

2.2.2 Protocol for Adeno-associated Virus-mediated Optogenetic Activation of Olfactory Output Neurons in Neonatal Mice

Yu-Nan Chen, Johanna K. Kostka, Sebastian H. Bitzenhofer and Ileana L. Hanganu-Opatz

STAR Protocols, 2024; DOI: 10.1016/j.xpro.2024.103164

Personal contribution

I designed the research.

I performed *in vivo* microinjections, electrophysiology and optogenetics.

I carried out formal analysis, visualization and data curation.

I designed and generated the figures.

I wrote the original draft of the manuscript.

I reviewed and edited the manuscript.

I revised and finalized the manuscript.

STAR Protocols

CellPress
OPEN ACCESS

Protocol

Protocol for adeno-associated virus-mediated optogenetic activation of olfactory output neurons in neonatal mice

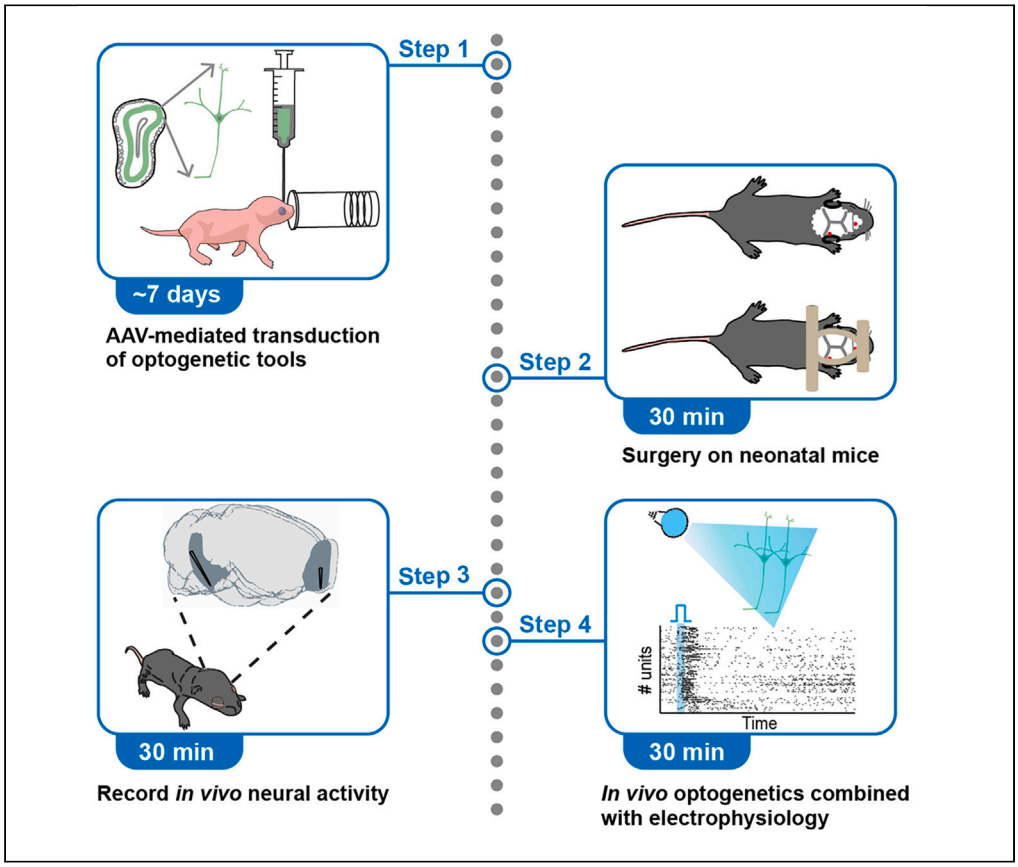

Optogenetic manipulation has proven a powerful tool for investigating the mechanisms underlying the function of neuronal networks, but implementing the technique on mammals during early development remains challenging. Here, we present a comprehensive workflow to specifically manipulate mitral/tufted cells (M/TCs), the output neurons in the olfactory circuit, mediated by adeno-associated virus (AAV) transduction and light stimulation in neonatal mice and monitor neuronal and network activity with *in vivo* electrophysiology. This method represents an efficient approach to elucidate functional brain development.

Publisher's note: Undertaking any experimental protocol requires adherence to local institutional guidelines for laboratory safety and ethics.

Yu-Nan Chen (陈裕楠), Johanna K. Kostka, Sebastian H. Bitzenhofer, Ileana L. Hanganu-Opatz

yunan.chen@zmnh.uni-hamburg.de (Y.-N.C.)
hangop@zmnh.uni-hamburg.de (I.L.H.-O.)

Highlights

Steps for combined *in vivo* optogenetics and electrophysiology in awake mice

Cell-type specific optogenetic manipulation mediated by AAV transduction in neonatal mice

Monitoring light-evoked neuronal and network activity of the olfactory circuits

Adaptable for other brain areas and cell types

Chen et al., STAR Protocols 5, 103164
September 20, 2024
https://doi.org/10.1016/j.xpro.2024.103164

STAR Protocols

CellPress
OPEN ACCESS

Protocol

Protocol for adeno-associated virus-mediated optogenetic activation of olfactory output neurons in neonatal mice

Yu-Nan Chen (陈裕楠),[1,2,*] Johanna K. Kostka,[1] Sebastian H. Bitzenhofer,[1] and Ileana L. Hanganu-Opatz[1,3,*]

[1]Institute of Developmental Neurophysiology, Center of Molecular Neurobiology, Hamburg Center of Neuroscience, University Medical Center Hamburg-Eppendorf, 20251 Hamburg, Germany

[2]Technical contact

[3]Lead contact

*Correspondence: yunan.chen@zmnh.uni-hamburg.de (Y.-N.C.), hangop@zmnh.uni-hamburg.de (I.L.H.-O.)
https://doi.org/10.1016/j.xpro.2024.103164

SUMMARY

Optogenetic manipulation has proven a powerful tool for investigating the mechanisms underlying the function of neuronal networks, but implementing the technique on mammals during early development remains challenging. Here, we present a comprehensive workflow to specifically manipulate mitral/tufted cells (M/TCs), the output neurons in the olfactory circuit, mediated by adeno-associated virus (AAV) transduction and light stimulation in neonatal mice and monitor neuronal and network activity with *in vivo* electrophysiology. This method represents an efficient approach to elucidate functional brain development.

For complete details on the use and execution of this protocol, please refer to Chen et al.[1–3]

BEFORE YOU BEGIN

How sensory perception interplays with cognitive functions is a fascinating topic in the field of neuroscience. In mammals, olfaction is one of the first senses that maturates.[4,5] While previous studies have identified the tight anatomical connections between olfactory system and higher-order cortical regions,[6,7] their role is still largely unknown. Until recently, the impact of olfactory outputs on cognitive processing along development represented an open question, mainly due to technical challenges. For example, the neonatal stage is characterized by rapid and dynamic changes in the structure and function of the brain, therefore dissecting the developmental trajectory of the circuits linking olfaction with cognition requires complex and longitudinal experimental designs. During the last decade, optogenetics has become the tool of choice for dissecting brain circuits and identifying their function, since it allows precise manipulation of distinct neuronal populations by light.[8,9] Recently, we adapted this method for developing olfactory circuit and revealed the critical role of neonatal olfactory bulb (OB) activity in the development of the entorhinal-hippocampal system accounting for cognitive abilities.[1–3] We provide here a detailed description of how to implement *in vivo* optogenetics to M/TCs of neonatal mice, which can be also applied to other brain regions or cell types with simple experimental modifications.

Institutional permissions

All experiments described in this protocol were carried out on transgenic mice of both sexes which express Cre recombinase controlled by the mouse T-box 21 (also called Tbet) promoter in M/TCs of the OB. These mice together with their mothers were housed in the animal facility of the University Medical Center Hamburg-Eppendorf at a 12-h light/12-h dark cycle and the mothers were fed ad

libitum. The viral vector (AAV9) used in our experiments is listed as a biosafety level 1 agent in Germany. All procedures were performed in accordance with German laws and the guidelines of the European Community for the use of animals in research and were approved by the local ethical committee (G17/015). Readers who want to adhere to this protocol for experimental practice will need to obtain similar permission and guidance from the animal care/biosafety committee at the relevant institution(s).

Mating and breeding of animals

Timing: 3 weeks

1. Set up a mating cage by putting two healthy adult female mice with a single adult male in a cage with fresh beddings and nesting materials at a 12-h light/dark cycle as well as ad libitum feeding and water.

   Note: We use male heterozygous Tbet-cre mice to cross with female wild-type C57BL/6J mice. According to Mendelian inheritance, 50% of the mouse descendants are Tbet-cre positive and the others are Tbet-cre negative.

2. Perform vaginal plug checking and document the day, to schedule the experiments (the day of plug detection was considered E0.5 and the day of birth was considered P0).
3. When the pregnancy is confirmed, house the pregnant female mouse individually and place a small shelter in the home cage.

Acquire viral vectors

Timing: depends on virus production and shipping

4. Choose AAV according to the opsin, desired expression pattern, serotype, promoter, fluorophore and titer.

   Note: We use AAV9 encoding cre-dependent channelrhodopsin (ChR2) and enhanced yellow fluorescent protein (EYFP) to specifically manipulate M/TCs in the OB. The expression of the virus is controlled by the Ef1a promotor and the transduction performance of AAV9 is relatively more efficient for neonatal mice compared to other AAV serotypes.[10] We recommend a virus at a high titer for adequate ChR2 expression in all M/TCs (e.g., $\geq 1\times10^{13}$ vg/mL from Addgene virus facility).

5. Aliquot the virus on ice and store it at −80°C.

   ⚠ CRITICAL: To prevent the degradation of virus quality, we recommend 3–4 μL aliquots for single use and avoid repeated freezing-thawing cycles of the virus.

KEY RESOURCES TABLE

REAGENT or RESOURCE	SOURCE	IDENTIFIER
Bacterial and virus strains		
AAV9-Ef1a-DIO-hChR2(E123T/T159C)-EYFP (stored at −80°C)	Addgene	Cat# 35509, RRID: Addgene_35509
Chemicals, peptides, and recombinant proteins		
Isoflurane (stored at 20°C–25°C)	Baxter	Cat# HDG9623
Omnifill C dental cement	Omnident	Cat# 85182

(*Continued on next page*)

Continued

REAGENT or RESOURCE	SOURCE	IDENTIFIER
Phosphate-buffered saline (PBS; stored at 20°C–25°C)	Gibco	Cat# 20012027
Isotonic sodium chloride (0.9%; stored at 20°C–25°C)	B. Braun	Cat# 3570310
Mixture of 0.25% bupivacaine & 1% lidocaine (stored at 20°C–25°C)	University Medical Center Hamburg-Eppendorf	N/A
Hydrogen peroxide (3%; stored at 20°C–25°C)	Carl Roth	Cat# 1A8Y.1
Ethanol (stored at 20°C–25°C)	Carl Roth	Cat# K928.3
Paraformaldehyde (PFA, 4%; stored at 20°C–25°C)	Carl Roth	Cat# P087.1
DiI (1,1′-Dioctadecyl-3,3,3′,3′-tetramethylindocarbocyanine perchlorate; stored at 4°C)	Molecular Probes	Cat# D282
Ketamine (stored at 20°C–25°C)	Richter Pharma AG	Ketamidor
Xylazine (stored at 20°C–25°C)	Bayer	Rompun
MetriZyme detergent (stored at 20°C–25°C)	Metrex	Cat# SKU 10-4000
Experimental models: Organisms/strains		
Mouse: Tbet-cre (B6; CBA-Tg(Tbx21-cre) 1Dlc/J; male/female, postnatal day (P) 8–11)	Jackson Laboratory	RRID: IMSR_JAX: 024507
Mouse: Tbet-cre (B6; CBA-Tg(Tbx21-cre) 1Dlc/J; male, ≥2 months)	Jackson Laboratory	RRID: IMSR_JAX: 024507
Mouse: C57BL/6J (female, ≥2 months)	Jackson Laboratory	RRID: IMSR_JAX: 000664
Software and algorithms		
Cheetah 6	NeuraLynx	http://neuralynx.com/
OMICRON Control Center	Omicron-Laserage	v3.6.10
Other		
Sterican single-use hypodermic needle (27G)	B. Braun	N/A
Microdissection scissors	Fine Science Tools	Cat# 14084-08
Dumont forceps	Fine Science Tools	Cat# 11270-20
Hot bead sterilizer	Fine Science Tools	Cat# 18000-50
Microliter syringe (model 701 RN, 33G)	Hamilton	Cat# 65460-05
Infusion microinjector and pump controller (not substitutable)	World Precision Instruments	MICRO4
Animal anesthesia system (not substitutable)	Harvard Apparatus	Cat# 75-0235
Temperature controller (not substitutable)	FHC	Cat# 40-90-8D
Heating pad (not substitutable)	FHC	Cat# 40-90-2
Stereomicroscope	Olympus	SZX10
Cotton bud	DM	Cat# 724841
Round plastic bar (outer diameter: 2 mm)	aero-naut Modellbau	Cat# 772831
Silver wire (diameter: 200 μm; not substitutable)	Science Products	AG-8W
Stereotaxic apparatus	Stoelting	Cat# 51603
Diode laser (473 nm; not substitutable)	Omicron-Laserage	LuxX 473-100
Optic patch cable (not substitutable)	Thorlabs	Cat# FG050UGA
Optical power meter	Thorlabs	Cat# PM121D
Recording optrode (1 shank, 16 channels, 50 μm inter-site spacing)	NeuroNexus	A1x16-5mm-50-703-OA16LP
Recording electrode (1 shank, 16 channels, 100 μm inter-site spacing)	NeuroNexus	A1x16-5mm-100-703-A16
Multichannel extracellular amplifier	NeuraLynx	Digital Lynx SX
Arduino Uno SMD	Arduino	A000073

STEP-BY-STEP METHOD DETAILS

Virus injection for ChR2 transduction

Timing: 5 min/animal

Here we describe the procedure for microinjection of an AAV construct into the OB of Tbet-Cre mice at P1 (Figure 1A) to enable the expression of ChR2 in M/TCs. For specifically targeting other types of neurons or other brain regions, small modifications regarding mouse line, virus type, and injection volume would be needed.

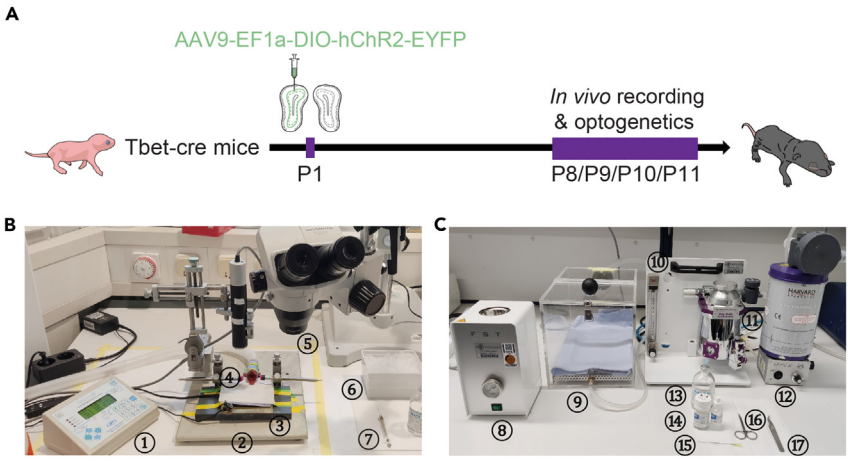

Figure 1. Experimental design and setups

(A) Experimental timeline. At P1, transduction of light-gated ChR2 channels in M/TCs was performed by AAV injections into the right OB of Tbet-cre mice. At P8, P9, P10 or P11, acute *in vivo* electrophysiological recordings were performed in the right OB combined with optogenetic activation of ChR2-expressing M/TCs.

(B) The setup for microinjections on neonatal mice (devices corresponding to the numbers: ①infusion pump; ②stereotaxic apparatus; ③heating pad; ④anesthesia mask; ⑤stereomicroscope; ⑥ice box with viral construct; ⑦microliter syringe).

(C) The setup for *in vivo* surgery (devices corresponding to the numbers: ⑧hot bead sterilizer; ⑨anesthesia induction box; ⑩anesthesia flow meter; ⑪isoflurane vaporizer; ⑫gas evacuation unit; ⑬isotonic sodium chloride solution; ⑭dental cement powder (left) and aqueous solution (right); ⑮needle; ⑯scissors; ⑰forceps).

1. Set up the injection system (Figure 1B).
   a. Attach the microliter syringe to the infusion pump fixed on the stereotaxic apparatus.
   b. Set the volume of withdrawal via the pump controller according to the number of pups and the amount of each injection.

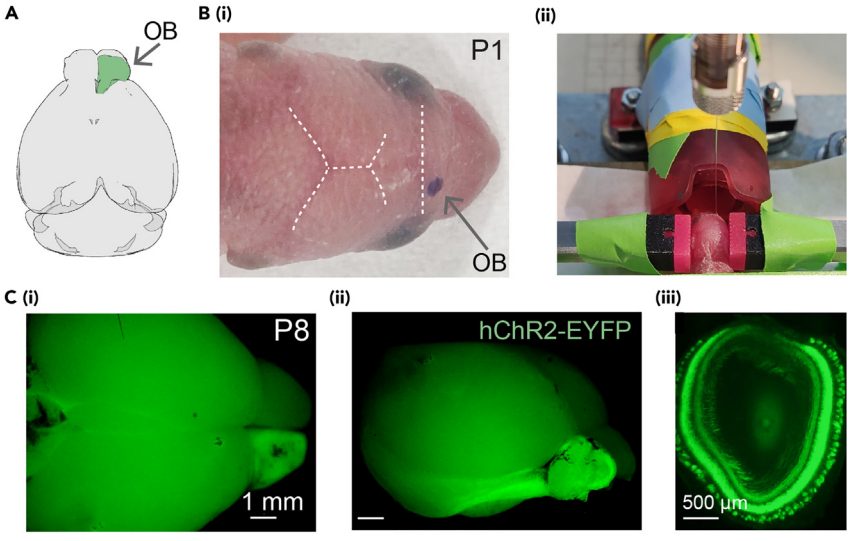

Figure 2. Procedure for ChR2 transduction in the OB by virus injection at P1

(A) (i) 3D schematic of the OB position in the brain with the injected area in green (top view).

(B) (i) An anesthetized P1 mouse with injection location for the right OB marked. (ii) A head-fixed P1 mouse in front of the anesthesia mask and the tip of the microliter syringe positioned into the right OB for viral injection.

(C) Pictures showing hChR2-EYFP expression in the right OB (i: top view; ii: lateral view of the brain) from a P8 Tbet-cre mouse, and expression pattern across the OB layers on a coronal brain slice (iii).

c. Withdraw the set amount of ice-cooled virus-containing solution into the syringe.

⚠ CRITICAL: Make sure the tip of the syringe is completely embedded in the solution during withdrawal and no air bubbles are present in the syringe.

Optional: Depending on the experimental design, dilute the virus aliquot in 0.01 M PBS to the final working concentration if necessary.

2. Take half the pups from the homecage litter and make a temporary shelter for them on the heating pad at 37°C.

⚠ CRITICAL: We recommend taking half of the total number of pups for each round of injection and keeping the remaining pups with their mother. Taking all pups at once increases the chance that the mother mouse will neglect them when they are returned.

3. Anesthetize the animal.
   a. Tenderly place one pup in the stereotaxic apparatus equipped with an anesthesia mask and a heating pad. Turn on the anesthesia system and adjust the vaporizer to change the isoflurane concentration (5% for initial induction for around 3 min then 3% for maintenance of anesthesia).
   b. Gently advance the non-traumatic bars of the stereotaxic apparatus to both sides of the head to fix the pup.
   c. Confirm the depth of anesthesia by assessing the response to a slight tail pinch with forceps.
4. Microinjection into the OB.
   a. Set the volume of infusion to 200 nL via the pump controller.
   b. Disinfect the skin of the pup with 70% ethanol (or other local disinfectant).
   c. Mark the location of the right OB which is in front of the blood vessel over the frontonasal suture and clearly visible through the skin (Figure 2B (i)).
   d. Puncture the skin and skull on the marked location with the tip of a sterilized fine needle.

Note: For mice aged at P0-1, no incision or sutures are needed to inject the OB.

   e. Slowly lower the attached microliter syringe to advance the tip into the OB at a 1–1.2 mm depth (Figure 2B (ii)).
   f. Start the microinjection under the infusion mode at a rate of 100 nL/min.

⚠ CRITICAL: Avoid excessive injection pressure which might cause damage to brain tissue.

   g. Following the microinjection, leave the tip of the syringe *in situ* for an additional 2 min to avoid leak or reflux of the fluid.
   h. Carefully retract the syringe out of the brain.
   i. Clean the fluid on the injection site and disinfect the skin of the pup again.

Optional: Obtain tail biopsies for genotyping to identify Tbet-Cre positive animals following the PCR protocol provided by the Jackson Laboratory.[11]

Optional: To differentiate the pups, mark them (e.g., by tattooing the paws).

   j. Remove the pup from the apparatus and place it into a recovery box on the heating pad with beddings from the homecage.

⚠ CRITICAL: Make sure the pup has regular vital signs after recovery from anesthesia. This takes 5–10 minutes.

5. Repeat the anesthesia and microinjection (major steps 3–4) on the other pups.
6. Return the injected pups to their homecage after full recovery.

Surgery for *in vivo* electrophysiological recordings

Timing: 30 min/animal

Here we describe the procedure for the *in vivo* surgery preceding electrophysiological recording simultaneously performed in both OB and lateral entorhinal cortex (LEC) of neonatal mice (P8-11) expressing ChR2 in M/TCs.

7. Anesthetize the animal.
   a. Take one pup out from the homecage.
   b. Anesthetize the pup.
      i. Weigh the pup and put it in the induction box (Figure 1C).
      ii. Turn on the animal anesthesia system and adjust the vaporizer to increase the isoflurane concentration to 5% for around 5 min.
      iii. Confirm deep anesthesia by tail or toe pinch.
   c. Transfer the anesthetized pup to the surgery table equipped with anesthesia mask and temperature controller set at 37°C.
   d. Adjust the isoflurane concentration to the required range and test the depth of anesthesia again.

   Note: We recommend 2.5%–3% for the maintenance of anesthesia in neonatal mice. It is necessary to adjust the concentration according to the breathing of the pup.

8. Surgery on the animal under anesthesia.
   a. Disinfect the skin above the skull with 70% ethanol (or other local disinfectant).
   b. Apply the mixture of bupivacaine (0.25%) and lidocaine (1%) by subcutaneous injection for local anesthesia and pain relief.

   Note: Follow your local animal care guidelines regarding pre- and postoperative analgesia.

   Pause point: Wait for 5 min for the analgesia to work before the next steps.

   c. Cut the fur and make an incision on the skin above the skull with sterilized scissors.
   d. Remove the skin above the skull and residual tissue gently (Figure 3A (i)).
   e. Clean the skull using 3% hydrogen peroxide-soaked cotton buds.
   f. Dry the skull and mark the locations of the target areas and reference site on cerebellum (Figure 3A (i)).

   Note: Stereotaxic coordinates of OB: 0.5–0.8 mm anterior to frontonasal suture, 0.5 mm lateral to midline; LEC: 0–0.3 mm anterior to lambda, 6.5 mm lateral to the midline. The mark over cerebellum location is for drilling a hole to insert a silver wire as ground and reference for the recording.

   g. Under a blue light (wavelength 440–514 nm) such as a fluorescent flashlight or microscope, the hChR2-EYFP expression in the OB can be easily visualized through the surface of the brain (Figure 3A (iii)).
   h. Use dental cement to strengthen the fragile skull of neonatal mice and to fix two round plastic bars for tight head fixation during the recording (Figure 3A (ii)).
      i. Prepare Omnifill C dental cement by appropriately mixing the powder and liquid.

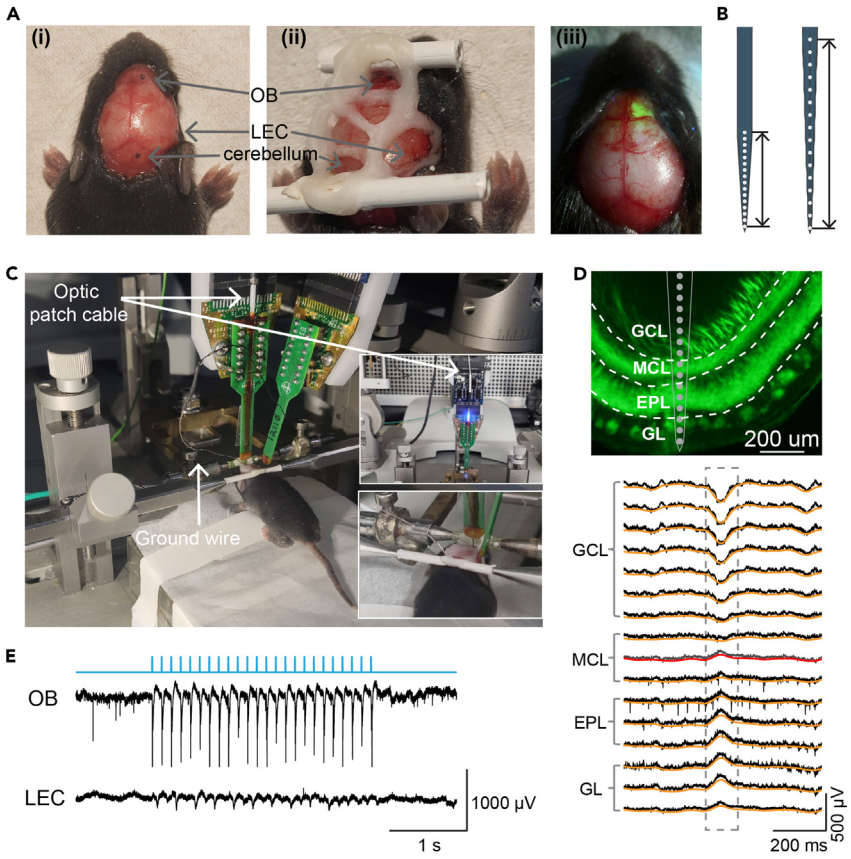

Figure 3. Procedure for *in vivo* electrophysiological recording combined with optogenetics

(A) Anesthetized neonatal mouse with recording locations marked (i) and exposed (ii) for multi-site extracellular recordings. The two plastic bars were mounted on the nasal and occipital bones respectively with the dental cement for tight head fixation during the recording. (iii) Overlaid photograph (from pictures taken under 440 nm blue light and neutral white light) showing the expression of hChR2-EYFP in the OB through the surface of the brain.

(B) Schematic reconstruction of extracellular recording electrode tips with 50 µm (left) and 100 µm (right) inter-site spacing. Scale bars correspond to 750 µm (left) and 1500 µm (right) respectively.

(C) Head-fixed neonatal mouse in the stereotaxic apparatus with optrode inserted in OB and electrode inserted in LEC. The optrode is attached to the laser delivery system (upper inner photo) for optogenetic stimulation. The silver wire is positioned into the cerebellum as ground and reference (lower inner photo).

(D) Digital post-mortem photomontage reconstructing the location of the 16 recording channels of optrode in ventral OB of a P11 hChR2-EYFP expressing mouse (top; GCL: granule cell layer; MCL: mitral cell layer; EPL: external plexiform layer; GL: glomerular layer), and the laminar spontaneous activity across the corresponding OB layers (down; raw recording traces in black, 1–12 Hz band-pass filtered LFP traces in orange). Note that the 1–12 Hz LFPs reverse at the channel below the first MCL recording channel (traces in gray and red).

(E) Representative traces of simultaneous extracellular recordings in OB and LEC with both LFPs and MUA during blue light (473 nm) pulse stimulation at 8 Hz. The TTL signals indicating 3-ms light square pulses are marked in light blue.

Note: The amount can be adjusted to change the viscosity upon preference.

ii. Mount the plastic bars on the nasal and occipital bones with the dental cement.
iii. Add more dental cement between the two bars for tighter connection.

Note: For recording in other regions, adjust the cement amount and position to ensure the accessibility of the targeted regions. Also, take care that the cement does not adhere to the nose or eyelids of the pup.

i. Perform craniotomies under the stereomicroscope (Figure 3A (ii)).
   i. Drill two small holes of 0.5 mm radii on the marked locations on the skull (i.e., OB and LEC) and carefully drip 0.9% sodium chloride to reduce bleeding and heat damage to brain tissue. Also, drill a hole in the skull over the cerebellum for inserting a reference wire.

⚠ CRITICAL: To ensure the quality of the recordings, avoid impertinent drilling to minimize the damage to brain tissues, neuronal death and neuroinflammation.

   ii. Gently remove the dura mater of the holes with the tip of a sterilized fine needle.

In vivo multi-site electrophysiological recordings and optogenetic stimulation

Timing: 1 h/animal

Here we describe the procedure for *in vivo* acute electrophysiological recordings performed simultaneously in both OB and LEC, as well as the simultaneous light stimulation in P8-11 mice with M/TCs expressing ChR2. Detailed descriptions for post-hoc brain dissection with intact OB for verification of ChR2 expression after the recordings and stimulations are also provided here. The protocol for light stimulation is also applicable to other brain regions with the presence of the opsin.

9. Multi-site extracellular recordings on the awake animal.
   a. Transfer the pup to the setup for electrophysiological recording and fix it with the plastic bars in the stereotaxic apparatus.
   b. Mount the optrode and electrode (with 16 recording sites, Figures 3B and 3C) on the headstages of the extracellular amplifier.

Note: To combine *in vivo* electrophysiology and light stimulation, the optrode needs to be attached with the optic patch cable. Also check the connection between the optrode, optic patch cable and diode laser before inserting the optrode into the OB.

Optional: To better visualize the electrode track in post-mortem histological confirmation, use a micropipette to drop 1 μL of fluorescent dye (e.g., 1 μg/μL DiI diluted in pure ethanol) to the tip of the electrode and wait for the dye to dry before mounting it to the headstage.

   c. Turn on the extracellular amplifier and data acquisition software.
   d. Insert a silver wire into the hole over the cerebellum as ground and reference for the recordings.
   e. By adjusting the manipulator arms of the stereotaxic apparatus, slowly insert then lower the mounted optrode and electrode into appropriate coordinates of OB and LEC respectively (optrode for ventral OB: 1.8–2 mm deep, 0° from the vertical plane; electrode for LEC: 2–2.4 mm deep, 15° from the vertical plane).
   f. Confirm the position of the optrode in mitral cell layer (MCL) according to the reversal of low-frequency (1–12 Hz) oscillations which is prominent and visible in the raw recording traces of the local field potentials (LFPs) between MCL and granule cell layer (GCL) of ventral OB (Figure 3D).

Pause point: For stable recording quality, pups should be allowed to recover for 20 min after the insertion of electrodes.

   g. Collect the digitized raw extracellular recording data of spontaneous activity with both LFPs and multi-unit activity (MUA).

Note: In our experiments, the signals were sampled at 32000 Hz and band-pass (0.1–9000 Hz) filtered by the acquisition software.

10. Prepare the light stimulation system.
    a. Turn the 473 nm laser on through the control software.
    b. Adjust the optical output to the desired power.

⚠ CRITICAL: Avoid tangling the optic patch cable for stable optical output.

    c. Give a short light pulse (3 ms duration, intensities ranging between 0.05–0.4 mW measured at the tip of the optrode) to test the light-induced activity and confirm the successful activation of M/TCs in the OB.
11. Apply light stimulation on the awake animal.
    a. Set the parameters to deliver the desired stimulation sequence using a pulse generator.

Note: We use 3 ms square pulses at a rate of 2/4/8/16/32 Hz, with alternating epochs of 3 s On/3 s Off and repeating 30 times generated by a custom-written controlling program in Arduino.

    b. Monitor and collect the digitized extracellular recording data as well as the transistor-to-transistor logic (TTL) pulse signals for light delivery (Figure 3E).
12. Sacrifice the pup after the recording procedure for post-mortem verification of ChR2 expression and electrode location.
    a. Carefully retract the optrode/electrode out of the brain.

Note: For cleaning the optrode/electrode, soak the probe in a detergent containing proteolytic enzyme for 15 min and rinse it with a few drops of distilled water afterward.

    b. Remove the pup from the stereotaxic apparatus.
    c. Euthanize the pup and perform transcardiac perfusion with 0.9% sodium chloride then 4% PFA at a constant speed of ~0.2 mL/s for 20 min.

Note: We use an overdose intraperitoneal injection of 10% ketamine/2% xylazine. Please follow your local animal care guidelines regarding animal euthanasia.

    d. Remove the brain for post-mortem verifications.
        i. Cut off the head from the neck.
        ii. Make an incision from the back of the head with the scissors.
        iii. Cut along the midline of the skull to the extremity of the nasal bone then cut laterally across the lambda and the frontal bone over the OB.
        iv. Peel back the segments of the skull to expose the underlying brain with the forceps.

⚠ CRITICAL: The frontal bone is tougher than the other parts of the skull. Avoid too strong pressure when cutting and moving the frontal bone to prevent OB damage.

        v. Gently resect all the connective tissue and nerves anchoring the brain to the lower skull cavity with the scissors.
        vi. Carefully lift the OBs from the connection with the remaining frontal bone.
        vii. Carefully separate the intact brain from the cranial vault.
        viii. Transfer the brain to the fixing solution (e.g., 4% PFA with a pH of 7.2) for 12–24 h to preserve the tissue structure and morphology before post-mortem histology.

EXPECTED OUTCOMES

Optogenetic techniques provide a spatially and temporally precise approach for studying the function of diverse brain circuits, including the sensory systems. Taking the advantages of a transgenic cre-recombinase mouse line and cre-dependent expression of an optogenetic tool, we injected an AAV9 encoding light-gated ChR2 into the right OB of P1 Tbet-cre mice to target the opsin expression specifically in M/TCs. At P8, the robust co-expression of the fluorophore EYFP with ChR2 was observed in the OB, labeling both the soma and axonal projections of M/TCs (Figure 2C). This indicates a stable expression of ChR2 and the feasibility of performing light stimulation at this developmental time point. Adequate ChR2 expression following virus injection targeting other brain regions was also found at either this time point or even earlier in our previous research.[12,13] Thus, the protocol enables the manipulation of specific neuronal populations during the neonatal period.

Based on the sufficient ChR2 expression at P8 and the fact that olfaction is already functional in mice at this age, we activated the ChR2-expressing M/TCs in the OB of head-fixed neonatal (P8-11) mice using blue light pulses (473 nm, 3 ms). The extracellular neural activity in OB and LEC were simultaneously recorded to investigate the influence of light-activated M/TCs on the neuronal activity within the olfactory network. In addition to adequate virus expression, the successful activation of the opsin-expressing neurons is also dependent on the appropriate stimulation parameters (Figure 4). First, we visualized the LFPs and spiking activity (extracted by spike sorting according to the waveform features beforehand) in the OB in response to the first 3-ms light pulse under different light intensities to evaluate the effects of *in vivo* M/TC activation. The magnitude of the light-induced averaged LFPs (Figure 4A) as well as the numbers of the responding single units (Figure 4B) grew with the increasing intensities from 0.05 mW to 0.2 mW (1%–10% of the maximal laser power), and the responses to 0.2 mW are comparable with that to 0.4 mW (20% of the maximal laser power), indicating sufficient optogenetic activation at light intensities in a range between 0.2-0.4 mW in this experimental setup.

We next measured the LFP responses in the MCL in response to rhythmic light pulse sequences delivered at different frequencies. Reliable light-evoked field potentials with large amplitude were found in MCL following each single light pulse (Figures 5A and 5B), which confirms the effective repetitive activation of M/TCs. Notably, the direct activation of M/TCs causes a reversal of transmembrane currents shown by current-source density (CSD) analysis with a sink at the reversal channel of MCL and time-aligned with the peak amplitude of LFPs (Figure 5A (ii)), which can be used for the further dissection of the neuronal population involved in generating LFP dynamics in the OB. Quantification of peak amplitudes of the light-evoked LFPs revealed lower peak amplitudes for the 2nd pulses at higher frequencies (16 and 32 Hz, i.e., with 62.5 and 31.25 ms inter-pulse interval) even though the 1st pulses could trigger LFPs with comparable peak amplitudes (Figure 5C (i)). This correspondingly leads to a lower paired-pulse ratio (given by responses to 2nd pulse/responses to 1st pulse) at higher frequencies (Figure 5C (ii)), which is in line with our previous findings from *in vitro* patch-clamp recordings showing that the M/TC firing follows progressively less in response to the stimulation at higher frequencies.[3] This indicates that the activation of the neuronal population in the OB triggered by the 2nd pulse is lower when compared with that triggered by the 1st pulse. Similarly, laminar CSD analysis for the light-evoked LFPs following the 2nd pulse *in vivo* showed progressively weaker magnitude of inversion, which could reflect the decay for excitatory synaptic activation of neuronal ensemble along the increasing stimulation frequencies. These results together not only rule out that the evoked activity is induced by a photovoltaic effect of light stimulation,[14] but also suggest that even though ChR2 (E123T/T159C mutant) used here rapidly responds to light stimulation at the millisecond level,[15] the repetitive light pulses at a high frequency might cause less efficient synaptic transmission or lower synaptic currents triggered by the light activation, which lead to a reduction of response amplitude upon the 2nd pulse. Thus, the frequency of the rhythmic light pulses is also an important parameter to consider for light stimulation design.

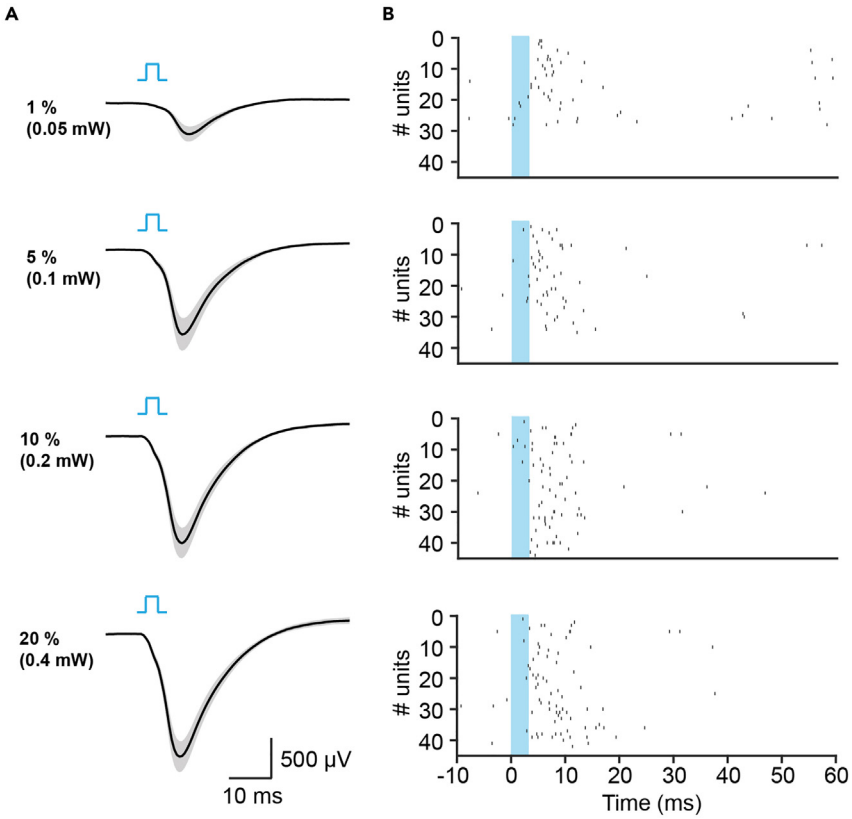

Figure 4. Effects of optogenetic stimulation on ChR2-expressing M/TCs with different light intensities

(A) Averaged MCL field potentials induced by the first blue light (473 nm) pulse delivered to the OB of P8-11 mice with the light intensity set as 1%, 5% 10% and 20% of the maximal intensity (1.75 mW) of laser power. The corresponding light intensities measured at the tip of the optrode are indicated following the percentage. The 3-ms light square pulses are denoted by light blue bars.

(B) Raster plots of OB neuronal firing in response to the first blue light pulse delivered in M/TCs of P8-11 mice at the corresponding intensity in (A).

Due to its spatiotemporal precision, optogenetics represents a useful method in dissecting the function of the large-scale neural network including the olfactory circuits. For example, we simultaneously recorded the activity in the LEC, one of the target areas of M/TC axonal projections, and investigated the light-evoked activity in OB and LEC, in particular the evoked spike timing. Light stimulation of M/TCs increased neuronal firing in both regions, with the peak of evoked firing activity in downstream LEC being substantially delayed when compared to the OB (Figure 6; OB peaked at ~8 ms after stimulus onset, LEC peaked at ~40 ms after stimulus onset). This indicates that the direct activation of M/TCs not only elicits the firing in OB, but also induces neuronal firing in LEC through long-range functional connections already at neonatal age.

LIMITATIONS

We introduce here a comprehensive protocol for combining *in vivo* acute electrophysiology with AAV-mediated optogenetic activation of M/TCs in mice at neonatal age. Special care for the animals is mandatory for the successful application of the methods. Thus, a certain amount of time in practice should be invested before executing the entire protocol described here. Neonatal pups require regular interactions and feeding by their mother and therefore, it is almost infeasible to perform extracellular recordings chronically, given the implantation of recording devices significantly interferes with normal maternal care and restricts both the somatic and brain development of the pups.

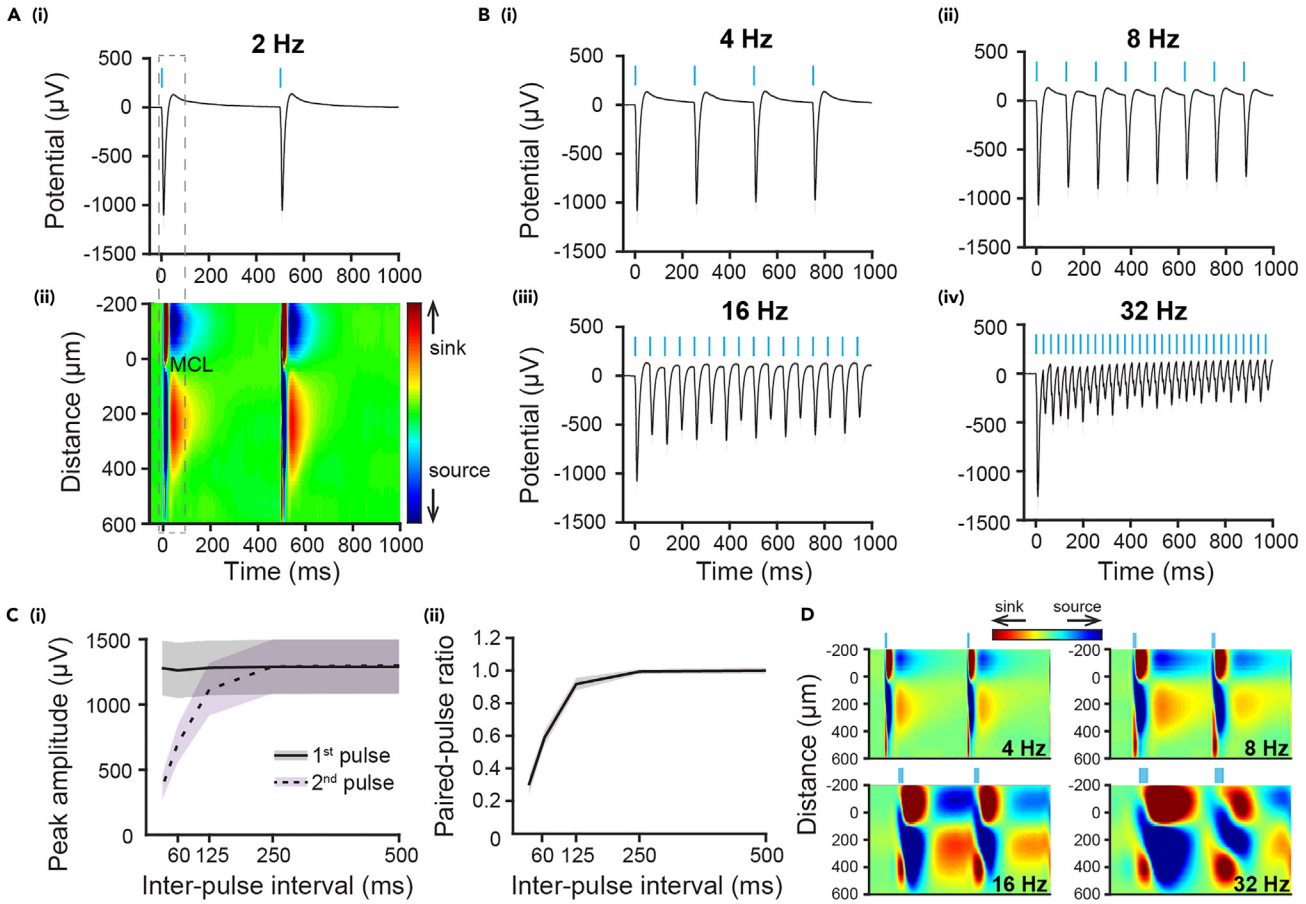

Figure 5. LFP responses to light stimulation of ChR2-expressing M/TCs

(A) (i) Averaged field potentials induced by 2 Hz blue light (473 nm) pulses in the MCL of OB from P8-11 mice. The 3-ms light square pulses are denoted by light blue bars. (ii) Color map of current source density (CSD) across 16 recording channels in the OB during the same periods as (i).

(B) Averaged field potentials induced by blue light pulses delivered at 4 Hz (i)/8 Hz (ii)/16 Hz (iii)/32 Hz (iv) in the MCL of OB from P8-11 mice. Data are presented as median ± standard error of the median.

(C) (i) Averaged peak amplitude of potentials induced by the first (black solid line) and second (black dashed line) light pulses at different inter-pulse intervals. (ii) Quantified paired-pulse ratio (2^{nd} peak amplitude/1^{st} peak amplitude). Data are presented as median ± standard error of the median.

(D) Color maps of CSD in the OB in response to the first and second blue light pulses at 4 Hz, 8 Hz, 16 Hz and 32 Hz. The 3-ms light square pulses are denoted by light blue bars.

Expression of optogenetic actuators can be achieved with different strategies, such as injecting the viral vector encoding the desired opsin into the brain region of interest,[14] crossing a transgenic mouse line carrying the desired opsin with another line with cre recombinase expressed in specific neuronal populations,[16] or prenatally transfecting the neuronal precursor cells by *in utero* electroporation (IUE).[17] The cre-dependent AAV-driven ChR2 expression described here to manipulate the principal projection neurons in OB is region and cell-type specific, but it also has relatively low flexibility for the experimental timing, since it requires several days after the injection to achieve adequate expression. On the other hand, while crossing transgenic mouse lines provides a possibility for cell type-specific opsin expression without additional experimental operation, it is costly and time-consuming to generate and maintain the required mouse lines. IUE proves to successfully target cortical and sub-cortical areas for optogenetic studies shortly after birth with sufficient opsin expression among the specific neuronal population,[17] but there is a potential for off-target opsin expression in other brain areas. In addition, not all cell populations can be targeted through the labeling with IUE. Furthermore, the *in utero* operation might be technically challenging particularly for those without expertise in embryonic manipulation techniques and can cause negative stress on the

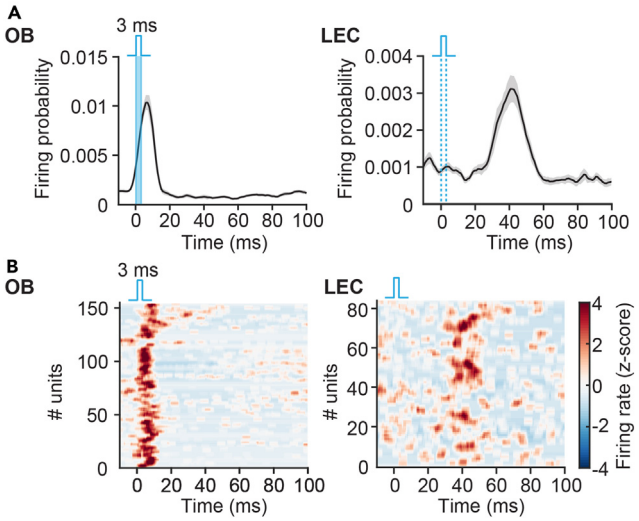

Figure 6. Neuronal firing responses to light stimulation of ChR2-expressing M/TCs

(A) Averaged probability of neuronal firing in the OB and LEC of P8-11 mice in response to 3-ms blue light (473 nm) pulses delivered to the OB. The 3-ms light square pulses are denoted by light blue bars. Data are presented as median ± standard error of the median.

(B) Z-scored firing rates of neurons in OB and LEC of P8-11 mice in response to 3-ms blue light pulses delivered to the OB.

mother mice. In general, the expression strategy should be designed according to the experimental aims. Thus, experimenters have to consider, which neuronal type(s), brain areas and layers as well as which developmental time window to be targeted and manipulated.

TROUBLESHOOTING

Problem 1

Mice do not recover after the anesthesia (refer to steps 3–4 and 7–8).

Potential solution

There are several possibilities.

- The temperature of the heating pad is too high or too low.
- The concentration of the isoflurane is set too high.
- Brain damage during microinjections or craniotomies.

We suggest checking the setup before every injection and making sure the breathing is regular under isoflurane anesthesia. Careful and attentive injection and drilling are also crucial.

Problem 2

The injected region does not express the virus or has inadequate virus expression (refer to step 4). This is the most common possibility accounting for failed stimulation.

Potential solution

- Optimize the injection site according to the post-mortem histology.
- Avoid using a virus after multiple freeze/thaw cycles.
- Make sure the needle is not clogged (e.g., confirming the outflow of virus from the needle before and after every injection through the stereoscope, or using a micro-pressure injection system coupled with a glass micropipette).
- After the injection, leave the needle inserted for a longer time and raise it as slowly as possible.

- Allow sufficient time for expression before the next step experiment(s).
- Check the appropriate virus-genotype pairing.

Problem 3

The mother of the injected pups does not take care of the pups (refer to step 6).

Potential solution

- Clean up and disinfect the possible bleeding on the injection sites.
- Return the pups only after they fully recover (i.e., breathing normally, adjusting body posture autonomously and showing healthy pink coloring and body temperature).
- Keep some beddings with the pups when returning them to the homecage to make them have sufficient homecage smell.
- Make sure the homecage has appropriate nesting materials for better maternal care.

Problem 4

The signal-to-noise ratio of the recording is low (refer to step 9).

Potential solution

- Shield the recording table and all noisy power sources (if not possible to remove them).
- Make sure the ground silver wire is fully embedded inside the reference site and securely pinned to the head stage.
- Confirm the tight head fixation of the pup.
- Clean the recording electrodes after every recording.
- If necessary, use a new electrode.

Problem 5

Low or inadequate effect of the optogenetic stimulation (refer to step 11).

Potential solution

- Make sure the stimulated region has sufficient opsin expression.
- Make sure the connection of the devices for stimulation is correct.
- Adjust the power and frequency of light for reliable firing activity.
- Test the light transition through the optic fiber and optrode to confirm the sufficient light intensity before every recording.
- Perform careful histological verification for both opsin expression and optrode insertion following the failed stimulation.

RESOURCE AVAILABILITY

Lead contact

Further information and requests for resources and reagents should be directed to and will be fulfilled by the lead contact, Ileana L. Hanganu-Opatz (hangop@zmnh.uni-hamburg.de).

Technical contact

Technical questions on executing this protocol should be directed to and will be answered by the technical contact, Yu-Nan Chen (yunan.chen@zmnh.uni-hamburg.de).

Materials availability

The study did not generate new unique reagents.

Data and code availability

- The original datasets and analysis code for the current study are available from the corresponding authors upon request.
- Any additional information required to reanalyze the data reported in this paper is available from the corresponding authors upon request.

ACKNOWLEDGMENTS

We thank Dr. Sabine Gretenkord for her contribution to the establishment of the methodology, as well as Peggy Putthoff, Achim Dahlmann, and Annette Marquardt for their excellent technical assistance. This work was funded by grants from the German Research Foundation (Ha4466/11-1, Ha4466/20-1, Ha4466/22-1, and SFB 936 178316478 to I.L.H.-O.), European Research Council (ERC-2015-CoG 681577 to I.L.H.-O.), Horizon 2020 DEEPER (101016787 to I.L.H.-O.), MSCA-ITN (860563 to I.L.H.-O.), and Landesforschungsförderung Hamburg (LFF73 and LFF76 to I.L.H.-O.).

AUTHOR CONTRIBUTIONS

Investigation, Y.-N.C. and J.K.K.; analysis and visualization, Y.-N.C.; writing – original draft, Y.-N.C.; writing – review and editing, Y.-N.C., J.K.K., S.H.B., and I.L.H.-O.; funding acquisition, I.L.H.-O.

DECLARATION OF INTERESTS

The authors declare no competing interests.

REFERENCES

1. Chen, Y.-N., Kostka, J.K., Bitzenhofer, S.H., and Hanganu-Opatz, I.L. (2023). Olfactory bulb activity shapes the development of entorhinal-hippocampal coupling and associated cognitive abilities. Curr. Biol. *33*, 4353–4366.e5. https://doi.org/10.1016/j.cub.2023.08.072.

2. Gretenkord, S., Kostka, J.K., Hartung, H., Watznauer, K., Fleck, D., Minier-Toribio, A., Spehr, M., and Hanganu-Opatz, I.L. (2019). Coordinated electrical activity in the olfactory bulb gates the oscillatory entrainment of entorhinal networks in neonatal mice. PLoS Biol. *17*, e2006994. https://doi.org/10.1371/journal.pbio.2006994.

3. Kostka, J.K., and Hanganu-Opatz, I.L. (2023). Olfactory-driven beta band entrainment of limbic circuitry during neonatal development. J. Physiol. *601*, 3605–3630. https://doi.org/10.1113/JP284401.

4. Schaal, B., Saxton, T.K., Loos, H., Soussignan, R., and Durand, K. (2020). Olfaction scaffolds the developing human from neonate to adolescent and beyond. Philos. Trans. R. Soc. Lond. B Biol. Sci. *375*, 20190261. https://doi.org/10.1098/rstb.2019.0261.

5. Miller, S.S., and Spear, N.E. (2008). Olfactory learning in the rat neonate soon after birth. Dev. Psychobiol. *50*, 554–565. https://doi.org/10.1002/dev.20318.

6. Burwell, R.D. (2000). The Parahippocampal Region: Corticocortical Connectivity. Ann. N. Y. Acad. Sci. *911*, 25–42. https://doi.org/10.1111/j.1749-6632.2000.tb06717.x.

7. Shepherd, G.M. (2007). Perspectives on olfactory processing, conscious perception, and orbitofrontal cortex. Ann. N. Y. Acad. Sci. *1121*, 87–101. https://doi.org/10.1196/annals.1401.032.

8. Deisseroth, K. (2015). Optogenetics: 10 years of microbial opsins in neuroscience. Nat. Neurosci. *18*, 1213–1225. https://doi.org/10.1038/nn.4091.

9. Deisseroth, K., and Hegemann, P. (2017). The form and function of channelrhodopsin. Science *357*, eaan5544. https://doi.org/10.1126/science.aan5544.

10. Gombash, S.E., Cowley, C.J., Fitzgerald, J.A., Hall, J.C.E., Mueller, C., Christofi, F.L., and Foust, K.D. (2014). Intravenous AAV9 efficiently transduces myenteric neurons in neonate and juvenile mice. Front. Mol. Neurosci. *7*, 81.

11. Protocol 27165 - Tg(Tbx21-cre)1Dlc. https://www.jax.org/Protocol?stockNumber=024507&protocolID=27165.

12. Xu, X., Song, L., Kringel, R., and Hanganu-Opatz, I.L. (2021). Developmental decrease of entorhinal-hippocampal communication in immune-challenged DISC1 knockdown mice. Nat. Commun. *12*, 6810–6817. https://doi.org/10.1038/s41467-021-27114-w.

13. Chini, M., Pfeffer, T., and Hanganu-Opatz, I. (2022). An increase of inhibition drives the developmental decorrelation of neural activity. Elife *11*, e78811. https://doi.org/10.7554/eLife.78811.

14. Cardin, J.A., Carlén, M., Meletis, K., Knoblich, U., Zhang, F., Deisseroth, K., Tsai, L.-H., and Moore, C.I. (2010). Targeted optogenetic stimulation and recording of neurons in vivo using cell-type-specific expression of Channelrhodopsin-2. Nat. Protoc. *5*, 247–254. https://doi.org/10.1038/nprot.2009.228.

15. Berndt, A., Schoenenberger, P., Mattis, J., Tye, K.M., Deisseroth, K., Hegemann, P., and Oertner, T.G. (2011). High-efficiency channelrhodopsins for fast neuronal stimulation at low light levels. Proc. Natl. Acad. Sci. USA *108*, 7595–7600. https://doi.org/10.1073/pnas.1017210108.

16. Haddad, R., Lanjuin, A., Madisen, L., Zeng, H., Murthy, V.N., and Uchida, N. (2013). Olfactory cortical neurons read out a relative time code in the olfactory bulb. Nat. Neurosci. *16*, 949–957. https://doi.org/10.1038/nn.3407.

17. Bitzenhofer, S.H., Ahlbeck, J., and Hanganu-Opatz, I.L. (2017). Methodological Approach for Optogenetic Manipulation of Neonatal Neuronal Networks. Front. Cell. Neurosci. *11*, 239. https://doi.org/10.3389/fncel.2017.00239.

2.2.3 Beyond Anosmia: Olfactory Dysfunction as a Common Denominator in Neurodegenerative and Neurodevelopmental Disorders

Yu-Nan Chen and Johanna K. Kostka

Frontiers in Neuroscience 2024; DOI: 10.3389/fnins.2024.1502779

Personal contribution

I conceptualized the review.

I carried out literature searching and validated the papers.

I designed and generated the figure.

I wrote the original draft of the manuscript.

I reviewed and edited the manuscript.

I revised and finalized the manuscript.

frontiers | Frontiers in Neuroscience

TYPE Mini Review
PUBLISHED 30 October 2024
DOI 10.3389/fnins.2024.1502779

OPEN ACCESS

EDITED BY
Thomas Heinbockel,
Howard University, United States

REVIEWED BY
Samir Ranjan Panda,
National Institute of Pharmaceutical Education and Research, India

*CORRESPONDENCE
Johanna Katharina Kostka
✉ johanna.kostka@zmnh.uni-hamburg.de
Yu-Nan Chen
✉ yunan.chen@zmnh.uni-hamburg.de

RECEIVED 27 September 2024
ACCEPTED 21 October 2024
PUBLISHED 30 October 2024

CITATION
Chen Y-N and Kostka JK (2024) Beyond anosmia: olfactory dysfunction as a common denominator in neurodegenerative and neurodevelopmental disorders.
Front. Neurosci. 18:1502779.
doi: 10.3389/fnins.2024.1502779

Beyond anosmia: olfactory dysfunction as a common denominator in neurodegenerative and neurodevelopmental disorders

Yu-Nan Chen* and Johanna Katharina Kostka*

Institute of Developmental Neuroscience, Center of Molecular Neurobiology, Hamburg Center of Neuroscience, University Medical Center Hamburg-Eppendorf, Hamburg, Germany

Olfactory dysfunction has emerged as a hallmark feature shared among several neurological conditions, including both neurodevelopmental and neurodegenerative disorders. While diseases of both categories have been extensively studied for decades, their association with olfaction has only recently gained attention. Olfactory deficits often manifest already during prodromal stages of these diseases, yet it remains unclear whether common pathophysiological changes along olfactory pathways cause such impairments. Here we probe into the intricate relationship between olfactory dysfunction and neurodegenerative and neurodevelopmental disorders, shedding light on their commonalities and underlying mechanisms. We begin by providing a brief overview of the olfactory circuit and its connections to higher-associated brain areas. Additionally, we discuss olfactory deficits in these disorders, focusing on potential common mechanisms that may contribute to olfactory dysfunction across both types of disorders. We further debate whether olfactory deficits contribute to the disease propagation or are simply an epiphenomenon. We conclude by emphasizing the significance of olfactory function as a potential pre-clinical diagnostic tool to identify individuals with neurological disorders that offers the opportunity for preventive intervention before other symptoms manifest.

KEYWORDS

olfaction, olfactory dysfunction, neurodegenerative disorders, neurodevelopmental disorders, Alzheimer's disease, Parkinson's disease, schizophrenia, autism spectrum disorder

Introduction

In humans, the sense of smell is often overlooked due to the dominance of vision and hearing in our daily lives. However, olfactory perception plays an important role in modulating cognition and emotions in healthy individuals (Richardson and Zucco, 1989; Sohrabi et al., 2012; Stevenson, 2013; Yahiaoui-Doktor et al., 2019). Olfactory performance decreases with age and correlates with cognitive abilities in the elderly (Attems et al., 2015; Murman, 2015; Uchida et al., 2020). Yet, olfactory impairments are also common symptoms of various neurodevelopmental and neurodegenerative disorders. Key olfactory functions—such as odor identification, odor discrimination, odor detection threshold, and odor memory processing—are frequently affected. Deficits in those olfactory functions can be readily assessed in humans using tests like Sniffin' Sticks or the University of Pennsylvania Smell Identification Test (Doty et al., 1984; Hummel et al., 1997). Similarly, tests such as the buried pellet test, olfactory habituation/dishabituation tests, and olfactory preference/

avoidance assays can be employed to evaluate olfactory impairments in mouse models of neurodevelopmental and neurodegenerative diseases, providing a valuable link between animal studies and human conditions (Yang and Crawley, 2009; Meyer and Alberts, 2016). The prevalence of olfactory deficits as a symptom of numerous neurodevelopmental and neurodegenerative diseases is striking. For instance, approximately 90% of patients with Alzheimer's Disease (AD) and Parkinson's disease (PD) exhibit olfactory impairments (Doty et al., 1988; Doty, 2017). Crucially, deficits in odor detection and discrimination alongside pathological changes in olfactory brain areas, often precede cognitive and/or motor symptoms by years (Ross et al., 2008; Devanand et al., 2010). Similarly, a significant proportion of individuals with schizophrenia (SCZ) or autism spectrum disorder (ASD) experience problems with their sense of smell, often without being aware of it (Moberg et al., 1999; Corcoran et al., 2005; Bennetto et al., 2007; Koehler et al., 2018). Given the early onset of olfactory deficits in a broad spectrum of distinct neurological disorders, early damage to the olfactory system could play a significant role in the progression of these diseases. Thus, a deeper understanding of the mechanisms underlying olfactory dysfunction could provide valuable insights into disease progression. Additionally, screening for olfactory deficits may offer a means of pre-clinical diagnostics and intervention before more severe cognitive symptoms emerge.

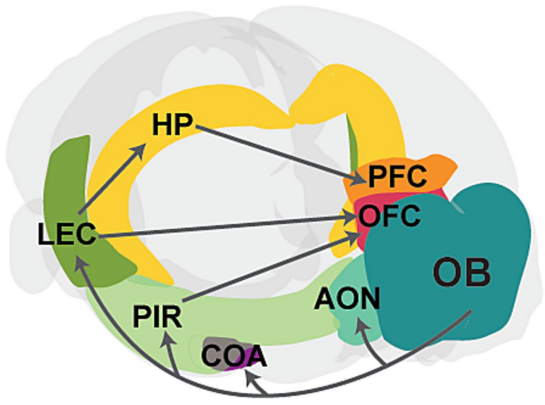

FIGURE 1
Schematic showing the main connectivity between the olfactory bulb and higher-order brain regions. The OB projects to primary cortical regions, including the anterior olfactory nucleus (AON), cortical amygdaloid nucleus (COA), piriform cortex (PIR), and lateral entorhinal cortex (LEC). Further, PIR and LEC send projections to higher-order cognitive regions, such as the hippocampus (HP), prefrontal cortex (PFC), and orbitofrontal cortex (OFC). The PFC also receives input from the HP. Gray arrows represent axonal projections, and individual areas are highlighted in different colors.

Tight anatomical and functional coupling between olfactory and cortical brain areas

Olfactory sensing begins when odor molecules bind to diverse olfactory receptors on olfactory sensory neurons (OSNs) located within the olfactory epithelium (OE) in the nasal cavity (Zhang and Firestein, 2002). Sensory afferents from OSNs transmit excitatory signals to the olfactory bulb (OB), the main olfactory processing center. Mitral and tufted cells (M/TCs) in the OB relay this preprocessed information to various cortical and subcortical regions, such as the anterior olfactory nucleus (AON), piriform cortex (PIR), amygdala, and lateral entorhinal cortex (LEC; Sosulski et al., 2011; Igarashi et al., 2012; Imai, 2014). Olfactory cortical areas such as PIR and LEC subsequently project to higher-order brain areas, including the prefrontal cortex (PFC), orbitofrontal cortex (OFC), and hippocampus (HP), which are critical for cognitive functions (Witter et al., 2017; Figure 1). Unlike other sensory modalities, olfactory information bypasses the thalamus and directly connects to these higher-order brain regions. These direct connections are crucial for the processing of odor information. For instance, direct projections from LEC to HP are important for odor discrimination and memory (Leitner et al., 2016; Li et al., 2017), while connections from PIR to OFC are important for learning odor values (Wang et al., 2020). Moreover, slow respiration-driven oscillations in the OB modulate local field potentials in PIR, LEC, HP, and PFC (Zelano et al., 2016; Biskamp et al., 2017; Tort et al., 2018; Heck et al., 2022), and beta oscillations synchronize across olfactory and cognitive brain areas during working memory and decision-making, influencing task performance (Gourévitch et al., 2010; Mori et al., 2013; Igarashi et al., 2014; Rangel et al., 2016; Symanski et al., 2022). Studies have also shown that odor-induced fast oscillations in OB and PIR correlate with odor perception and discrimination (Beshel et al., 2007; Lepousez and Lledo, 2013; Yang et al., 2022).

OB networks are also strongly influenced by neuromodulatory inputs such as noradrenergic, serotonergic, and cholinergic inputs, which are involved in odor discrimination and odor learning (Linster and Fontanini, 2014; Brunert and Rothermel, 2021). Sparse dopaminergic (DA) input from the substantia nigra also terminates in the OB (Höglinger et al., 2015). A subpopulation of OB interneurons is both DA and GABAergic (Borisovska et al., 2013; Pignatelli and Belluzzi, 2017; Liu et al., 2019) and undergoes adult neurogenesis (Altman, 1969; Lazarini et al., 2014). These neurons modulate neurotransmitter release from OSNs and lateral inhibition within glomeruli (Hsia et al., 1999; Liu et al., 2013a; McGann, 2013) and are important for odor discrimination (Tillerson et al., 2006). Moreover, granule (GC) and periglomerular (PGC) interneurons in the OB, along with OSNs in the OE, are continuously generated throughout life (Murrell et al., 1996; Hahn et al., 2005; Batista-Brito et al., 2008; Lledo and Valley, 2016).

The olfactory system is anatomically and functionally interconnected with brain regions essential for cognitive processing. Importantly, pathological changes associated with neurodegenerative and neurodevelopmental disorders have been observed throughout the olfactory circuitry - from the OE and OB to primary olfactory cortices and downstream targets like LEC, HP, and PFC.

Olfactory dysfunction in neurodegenerative disorders

Neurodegenerative disorders, like AD and PD, are characterized by progressive decline of cognitive and motor functions (Goedert and Spillantini, 2006; Wilson et al., 2023). Emerging evidence indicates

that olfactory deficits—such as impaired odor detection and discrimination—manifest early in these diseases, preceding cognitive and motor symptoms by several years (Ross et al., 2008; Doty, 2017).

In AD, olfactory dysfunction correlates closely with the progression of cognitive decline (Roberts et al., 2016; Dintica et al., 2019; Papadatos and Phillips, 2023). Pathological features of AD include amyloid plaques (deposition of amyloid beta (Aβ) protein) and neurofibrillary tangles (aggregates of hyperphosphorylated tau proteins; Goedert and Spillantini, 2006; Ballard et al., 2011; Braak and Del Tredici, 2015). These pathological aggregations affect the OE and brain areas involved in odor processing, such as OB, AON, PIR, and LEC, often before clinical symptoms occur (Attems and Jellinger, 2006; Arnold et al., 2010; Murphy, 2019). Animal studies suggest that overexpression of the Aβ precursor protein causes olfactory deficits by progressive Aβ deposition, starting from the OE and expanding to the OB, PIR, entorhinal cortex (EC), and HP (Wesson et al., 2010; Wu et al., 2013). Similarly, in humans, areas like EC are among the first to be affected by AD pathology (Braak and Braak, 1991). Further, higher levels of phosphorylated tau (P-tau) in the OBs of AD patients correlate with MC loss, impaired dendro-dendritic inhibition, and diminished olfactory detection abilities before cognitive impairments emerged (Li et al., 2019a). Mouse models of Aβ pathology also show early olfactory deficits, alongside a loss of OSNs and decreased odor-evoked potentials in the OE, altered dendro-dendritic inhibition, and increased gamma oscillations in the OB, PIR, and LEC (Wesson et al., 2011; Xu et al., 2015; Li et al., 2019b; Chen et al., 2021b). These symptoms occur before Aβ plaque formation, suggesting that soluble Aβ might be responsible. In line with this, overexpression of a mutated human Aβ precursor protein in OSNs disrupts the glomerular axon targeting of those neurons and causes olfactory deficits before Aβ deposition forms in the OB (Cao et al., 2012). Similarly, injecting soluble Aβ oligomers into the OB damages the olfactory detection abilities of rodents (Alvarado-Martínez et al., 2013).

Similarly, olfactory dysfunction is an early and prominent non-motor symptom of PD (Ross et al., 2008; Doty, 2012, 2017; Haehner et al., 2019). PD patients score lower on the Sniffin' Sticks Test compared to healthy controls (Haehner et al., 2007, 2009; Trentin et al., 2022), and brain areas such as the OB, AON, PIR and EC show early volume reductions (Wattendorf et al., 2009; Wang et al., 2011; Chen et al., 2014; Lee et al., 2014; Tanik et al., 2016). Characterized by α-synuclein aggregation forming Lewy bodies (Mezey et al., 1998), PD shows early pathological changes in the OB and AON (Braak et al., 2003). A transgenic mouse model of α-synuclein pathology confirms the prevalence of α-synuclein aggregation in the OB, AON, and PIR and shows reduced odor detection and diminished adult neurogenesis in the OB (Martin-Lopez et al., 2023). This aggregation is associated with increased odor-evoked gamma oscillations and altered neuronal firing in the OB (Chen et al., 2021a).

Thus, neurodegenerative disorders like AD and PD exhibit early olfactory deficits that coincide with the initial accumulation of pathological proteins in olfactory-related brain regions, before spreading to other parts of the brain.

Olfactory dysfunction in neurodevelopmental disorders

Neurodevelopmental disorders, including SCZ and ASD, are characterized by atypical brain development and impaired cognitive, social, or motivation-related behaviors (Owen et al., 2016; Thye et al., 2018; Chini and Hanganu-Opatz, 2021). A prominent feature is impaired sensory processing (Schechter et al., 2003; Chang et al., 2014; Siper et al., 2021). In particular, reduced odor detection early in life, accompanied by anatomical and functional alterations in olfactory and higher-order cortical networks, is typical (Crow et al., 2020).

For instance, SCZ patients exhibit olfactory deficits and reduced OB, PIR EC, HP, and amygdala volumes, which precede the onset of cognitive deficits (Turetsky et al., 2000; Corcoran et al., 2005; Rupp et al., 2005; Nguyen et al., 2010, 2011; Kamath et al., 2018; Yang et al., 2021). Additionally, reduced olfactory-evoked potentials are associated with impaired odor identification in SCZ patients (Turetsky et al., 2003). Both genetic and environmental factors play a significant role in shaping the development of the olfactory system and are implicated in neurodevelopmental disorders. One prominent susceptibility factor for SCZ is the mutation of the Disrupted-in-Schizophrenia 1 (DISC1) gene, which is involved in various neuropsychiatric disorders (Blackwood et al., 2001; Chubb et al., 2008; Brandon et al., 2009) and is highly expressed in M/TCs (Schurov et al., 2004). DISC1 knockdown, combined with a prenatal environmental stressor - maternal immune activation (MIA) - leads to impaired oscillatory activity in the OB and reduced functional connectivity within olfactory-limbic networks of neonatal mice (Parbst et al., 2024; Xu et al., 2021).

In ASD, children often exhibit early olfactory deficits, including impaired odor identification along with reduced odor-evoked activity (Bennetto et al., 2007; Koehler et al., 2018). Like SCZ, both genetic and environmental factors contribute to the etiology of ASD. Genetic mutations, such as those affecting Shank proteins, involved in postsynaptic scaffolding, are prevalent in patients with ASD and are associated with olfactory deficits. Shank3 deficiency impairs odor detection, reduces odor-evoked potentials, and alters synaptic transmission in the OB and PIR (Drapeau et al., 2018; Ryndych et al., 2023; Mihalj et al., 2024). Moreover, mutation of the autism-related gene Tbr leads to smaller OBs, reduced numbers of OB interneurons, and abnormal dendritic morphology of MCs (Huang et al., 2019). Environmental factors like MIA, which largely increases the risks for both ASD and SCZ (Hartung et al., 2016; Schepanski et al., 2022; Dutra et al., 2023; Godavarthi et al., 2024), can impair adult neurogenesis in the OB and contribute to decreased olfactory discrimination abilities (Liu et al., 2013b).

Thus, olfactory dysfunctions accompanied by pathophysiological changes in brain areas associated with olfaction, are frequently observed in neurodevelopmental disorders.

Shared structural and functional alterations and their underlying mechanisms in neurodegenerative and neurodevelopmental disorders

Olfactory deficits in neurodevelopmental and neurodegenerative disorders often coincide with structural alterations across brain regions involved in olfactory processing. For example, reduced OB volume has been documented in AD (Thomann et al., 2009b; Thomann et al., 2009a), PD (Wattendorf et al., 2009; Wang et al., 2011), and SCZ (Turetsky et al., 2000; Nguyen et al., 2011; Yang et al., 2021). This reduction in OB volume might be caused by multiple

mechanisms, including altered neuronal morphology and neuronal loss. For example, postmortem OB tissue of PD patients reveals substantial loss of ventral glomerular areas in the OB, correlated with phosphorylated α-synuclein load (Zapiec et al., 2017). This α-synuclein accumulation specifically induces apoptosis of DA neurons (Xu et al., 2002), likely contributing to the reduced size or number of glomeruli in the OB. In AD, the accumulation of P-tau and Aβ drives neuronal atrophy throughout the brain, including M/TCs in the OB (Struble and Clark, 1992; Yao et al., 2017; Li et al., 2019b). This aligns with studies showing that the MC layer is predominantly affected by tau pathology in an AD mouse model (Yang et al., 2016). While reduced OB volume is also common in SCZ, direct evidence for altered neuronal morphology in OB is limited for neurodevelopmental disorders. However, it was recently shown that a mouse model of OE inflammation which closely mimics inflammatory processes in the OE of first-episode psychosis patients shows reduced glomerular size and OB volume, alongside decreased numbers of OSNs and M/TCs (Yang et al., 2024). Further, animal models of SCZ, such as immune-challenged DISC1 knockdown mice and 22q11-deletion mice, show reduced soma size and dendritic arborization of pyramidal neurons in brain regions such as LEC, HP, and PFC (Chini et al., 2020; Kringel et al., 2023; Stark et al., 2008; Fénelon et al., 2013). However, so far it is unknown whether the same holds for M/TCs, which strongly express DISC (Schurov et al., 2004). Impaired neurogenesis might also contribute to OB volume reduction in both neurodegenerative and neurodevelopmental disorders. Neuroblasts generated in the subventricular zone (SVZ) continuously migrate to the OB, where they differentiate into GCs and PGCs (Belluzzi et al., 2003; Livneh et al., 2014). Impairments of adult SVZ neurogenesis are evident early in animal models of AD and PD (Winner et al., 2008, 2011; Rodríguez et al., 2009; Scopa et al., 2020; Esteve et al., 2022; Martin-Lopez et al., 2023). Similarly, disruptions in SVZ neurogenesis are seen in neurodevelopmental disorders. DISC1 knockdown leads to reduced progenitor cell proliferation in the SVZ during embryonic stages (Mao et al., 2009). Additionally, MIA leads to altered proliferation in the SVZ of neonatal mice and further contributes to reduced adult neurogenesis in the OB (Liu et al., 2013b; Loayza et al., 2023).

Aside from structural changes, alterations in the neuronal activity within olfactory circuits are common in these disorders. OSNs, the first neurons to receive odor information, are reduced in numbers and show smaller odor-evoked responses in AD, resulting in diminished excitatory input to the OB (Chen et al., 2021b). This, combined with reduced dendritic spine density in GCs and impaired dendro-dendritic inhibition onto MCs, leads to increased gamma-band OB network activity (Wesson et al., 2011; Chen et al., 2021b; Li et al., 2019a, 2019b). Similarly, overexpression of α-synuclein in the OB, one of the key features of PD, leads to reduced GC activity and impaired dendro-dendritic inhibition onto MCs, along with elevated odor-evoked gamma oscillations (Chen et al., 2021a). In neuropsychiatric disorders, a broadband reduction of oscillatory power in the OBs of a SCZ mouse model was accompanied by reduced firing of M/TCs (Parbst et al., 2024). Furthermore, compromised functional connectivity between brain regions accounting for olfactory and cognitive processing is evident in both neurodegenerative and neurodevelopmental disorders. For instance, patients with SCZ show reduced functional connectivity between PIR, PFC, and nucleus accumbens (Kiparizoska and Ikuta, 2017) as well as between the HP and PFC (Adams et al., 2020). In AD, disruption of functional connectivity between olfactory networks (including PIR and OFC) and HP is linked to cognitive decline (Lu et al., 2019a, 2019b). Already during neonatal development, desynchronization between LEC, HP, and PFC manifests in an animal model of neuropsychiatric disorders such as SCZ (Hartung et al., 2016; Xu et al., 2021). A recent study showed that functional connectivity between OB and HP, as well as, OB and PFC was significantly reduced in the same animal model (Parbst et al., 2024). Similarly, in animal models of ASD, reduced OB activity and altered connectivity between HP and PFC have been reported (Cheaha et al., 2015; Richter et al., 2019). During early development, olfactory inputs are critical in synchronizing brain regions involved in olfactory and cognitive processing (Gretenkord et al., 2019; Kostka and Hanganu-Opatz, 2023). Notably, silencing M/TC activity in the OB during early development impairs the maturation of olfactory-hippocampal networks and cognitive abilities later in life (Chen et al., 2023). These findings suggest that altered olfactory activity can disrupt the development of functional coupling within neuronal networks, potentially contributing to cognitive impairments, seen in many neurodegenerative and neurodevelopmental disorders (Bennetto et al., 1996; Jahn, 2013; Davis and Racette, 2016; Guo et al., 2019).

Alterations in neurotransmitter systems, particularly the DA system, also significantly contribute to olfactory deficits in neurodegenerative and neurodevelopmental disorders. DA neurons in the OB inhibit olfactory transmission in the olfactory glomeruli (Wilson and Sullivan, 1995; Hsia et al., 1999) and are important for the encoding of innate odor values (Kato et al., 2023). In PD and AD, loss of DA neurons in the substantia nigra and ventral tegmental area leads to impaired DA outflow to several brain areas, including the OB (German et al., 1989; Nobili et al., 2017). Interestingly, increased numbers of DA neurons have been observed in the OBs of PD and AD patients (Huisman et al., 2004; Mundiñano et al., 2011). Neurodevelopmental disorders, such as ASD, also exhibit altered DA signaling and DA receptor abnormalities (Pavăl, 2017; Kosillo and Bateup, 2021; Pavăl and Micluția, 2021). Beyond DA, cholinergic transmission plays an important role in olfactory processing and is frequently altered in these disorders (Doty, 2017). For example, acetylcholine dysfunction exacerbates Aβ pathology in AD and cholinergic receptor abnormalities are present in ASD (Gil-Bea et al., 2012; Ovsepian et al., 2019; Vallés and Barrantes, 2021).

Overall, several intertwined mechanisms, such as neuronal loss, reduced neurogenesis, impaired synaptic transmission, and altered neurotransmitter signaling can lead to structural and functional alterations in olfactory circuits, contributing to the olfactory deficits characteristic of both neurodevelopmental and neurodegenerative diseases.

Conclusion

Olfactory deficits emerge early, often preceding the clinical diagnosis of neurodegenerative and neurodevelopmental disorders. Whether this relationship is causal or merely an epiphenomenon remains an open question. However, the presence of olfactory dysfunction and alterations in olfactory-related brain areas well before cognitive and motor symptoms suggest a potential causal relationship. Notably, individuals at high risk for psychiatric disorders, such as

relatives of SCZ patients, often exhibit olfactory impairments, indicating that these deficits are unlikely due to secondary effects of treatment (Turetsky et al., 2018).

The OE as well as primary olfactory areas such as OB and AON often show pathological changes in prodromal disease stages before the involvement of other brain areas. In line with the α-synuclein transmission hypothesis (McCann et al., 2016) injection of human α-synuclein fibrils into the OBs of young mice leads to a spread of α-synuclein aggregates across several brain regions, correlating with increasing olfactory deficits (Rey et al., 2016). Similarly, the injection of soluble Aβ in an AD mouse model shows similar spreading patterns (He et al., 2018). This suggests that in neurodegenerative diseases, pathological aggregation of proteins originates in olfactory areas and spreads in a prion-like manner to higher-order cortical regions, contributing to disease progression. Moreover, in both neurodegenerative and neurodevelopmental disorders, olfactory dysfunction is linked to reduced functional connectivity with downstream brain regions, potentially accelerating cognitive decline. For example, layer 2 neurons in LEC, which receive direct OB input and project to HP, are especially vulnerable, showing functional and morphological alterations in AD (Stranahan and Mattson, 2010). Thus disrupted inputs from the OB may, cause structural and functional changes along olfactory pathways. Supporting this, studies have shown that recently acquired sensory loss can alter both morphology and functional connectivity between the PIR and higher-order cortical brain regions (Bitter et al., 2010; Iravani et al., 2021). Thus, olfactory circuits may play a dual role: they could serve as a route for the spread of pathogenic proteins to downstream brain areas, and disruptions in olfactory processing in the OE and OB could have lasting consequences on higher-order cortical regions, potentially contributing to cognitive deficits.

On the other hand, olfactory impairments might coincide with disease progression or result from secondary effects. For example, disruptions in forebrain development and altered neurotransmitter signaling can lead to olfactory dysfunctions (Doty, 2017). Furthermore, the propagation of tau, from the temporal lobe to olfactory circuits was shown to drive the degradation of odor perception as individuals get older (Diez et al., 2024). Moreover, while many patients with neurodevelopmental and neurodegenerative disorders experience impaired olfaction, this is not universal, suggesting that olfactory system involvement is not a necessary feature of disease progression in all cases.

Regardless of whether olfactory dysfunction is a cause or consequence of these diseases, it consistently occurs early, often before a clinical diagnosis is made. Testing olfactory abilities for example with simple Sniffn' Sticks tests or the University of Pennsylvania Smell Identification Test is an effective and inexpensive way to identify individuals with olfactory deficits. Since reliable biomarkers for early diagnostics are lacking, monitoring olfactory deficits in individuals at risk or incorporating olfactory testing into routine health checks has great potential (Dan et al., 2021). In addition, olfactory testing may serve as a tool for monitoring disease progression or evaluating therapeutic effects (Berendse et al., 2011). Further research is necessary to understand the mechanisms underlying olfactory dysfunctions, as this could offer valuable insights into the etiology and progression of these diseases.

Author contributions

Y-NC: Conceptualization, Validation, Writing – original draft, Writing – review & editing. JK: Conceptualization, Methodology, Project administration, Supervision, Validation, Writing – original draft, Writing – review & editing.

Funding

The author(s) declare that financial support was received for the research, authorship, and/or publication of this article. This work was funded by grants from the German Research Foundation (526195732 and FOR5159 TP1: 437610067) and grants from the European Union (Horizon 2020 DEEPER: 101016787 and MSCA-ITN: 860563) to Ileana L. Hanganu-Opatz.

Acknowledgments

We thank Ileana L. Hanganu-Opatz for comments on the manuscript and financial support. A large language model (ChatGPT 4; open AI) was used to improve grammatical accuracy, and to correct syntactical errors. It was not used to create or curate the scientific content in any way.

Conflict of interest

The authors declare that the research was conducted in the absence of any commercial or financial relationships that could be construed as a potential conflict of interest.

Publisher's note

References

Adams, R. A., Bush, D., Zheng, F., Meyer, S. S., Kaplan, R., Orfanos, S., et al. (2020). Impaired theta phase coupling underlies frontotemporal dysconnectivity in schizophrenia. *Brain* 143, 1261–1277. doi: 10.1093/brain/awaa035

Altman, J. (1969). Autoradiographic and histological studies of postnatal neurogenesis. IV. Cell proliferation and migration in the anterior forebrain, with special reference to persisting neurogenesis in the olfactory bulb. *J. Comp. Neurol.* 137, 433–457. doi: 10.1002/cne.901370404

Alvarado-Martínez, R., Salgado-Puga, K., and Peña-Ortega, F. (2013). Amyloid Beta inhibits olfactory bulb activity and the ability to smell. *PLoS One* 8:e75745. doi: 10.1371/journal.pone.0075745

Arnold, S. E., Lee, E. B., Moberg, P. J., Stutzbach, L., Kazi, H., Han, L., et al. (2010). Olfactory epithelium amyloid-β and paired helical filament-tau pathology in Alzheimer disease. *Ann. Neurol.* 67, 462–469. doi: 10.1002/ana.21910

Attems, J., and Jellinger, K. A. (2006). Olfactory tau pathology in Alzheimer disease and mild cognitive impairment. *Clin. Neuropathol.* 25, 265–271

Attems, J., Walker, L., and Jellinger, K. A. (2015). Olfaction and aging: a Mini-review. *Gerontology* 61, 485–490. doi: 10.1159/000381619

Ballard, C., Gauthier, S., Corbett, A., Brayne, C., Aarsland, D., and Jones, E. (2011). Alzheimer's disease. *Lancet* 377, 1019–1031. doi: 10.1016/S0140-6736(10)61349-9

Batista-Brito, R., Close, J., Machold, R., and Fishell, G. (2008). The distinct temporal origins of olfactory bulb interneuron subtypes. *J. Neurosci.* 28, 3966–3975. doi: 10.1523/JNEUROSCI.5625-07.2008

Belluzzi, O., Benedusi, M., Ackman, J., and LoTurco, J. J. (2003). Electrophysiological differentiation of new neurons in the olfactory bulb. *J. Neurosci.* 23, 10411–10418. doi: 10.1523/JNEUROSCI.23-32-10411.2003

Bennetto, L., Kuschner, E. S., and Hyman, S. L. (2007). Olfaction and taste processing in autism. *Biol. Psychiatry* 62, 1015–1021. doi: 10.1016/j.biopsych.2007.04.019

Bennetto, L., Pennington, B. F., and Rogers, S. J. (1996). Intact and impaired memory functions in autism. *Child Dev.* 67, 1816–1835. doi: 10.2307/1131734

Berendse, H. W., Roos, D. S., Raijmakers, P., and Doty, R. L. (2011). Motor and non-motor correlates of olfactory dysfunction in Parkinson's disease. *J. Neurol. Sci.* 310, 21–24. doi: 10.1016/j.jns.2011.06.020

Beshel, J., Kopell, N., and Kay, L. M. (2007). Olfactory bulb gamma oscillations are enhanced with task demands. *J. Neurosci.* 27, 8358–8365. doi: 10.1523/JNEUROSCI.1199-07.2007

Biskamp, J., Bartos, M., and Sauer, J.-F. (2017). Organization of prefrontal network activity by respiration-related oscillations. *Sci. Rep.* 7:45508. doi: 10.1038/srep45508

Bitter, T., Brüderle, J., Gudziol, H., Burmeister, H. P., Gaser, C., and Guntinas-Lichius, O. (2010). Gray and white matter reduction in hyposmic subjects — a voxel-based morphometry study. *Brain Res.* 1347, 42–47. doi: 10.1016/j.brainres.2010.06.003

Blackwood, D. H. R., Fordyce, A., Walker, M. T., Porteous, D. J., and Muir, W. J. (2001). Schizophrenia and affective disorders—Cosegregation with a translocation at chromosome 1q42 that directly disrupts brain-expressed genes: clinical and P300 findings in a family. *Am. J. Hum. Genet.* 69, 428–433. doi: 10.1086/321969

Borisovska, M., Bensen, A. L., Chong, G., and Westbrook, G. L. (2013). Distinct modes of dopamine and GABA release in a dual transmitter neuron. *J. Neurosci.* 33, 1790–1796. doi: 10.1523/JNEUROSCI.4342-12.2013

Braak, H., and Braak, E. (1991). Neuropathological stageing of Alzheimer-related changes. *Acta Neuropathol. (Berl.)* 82, 239–259. doi: 10.1007/BF00308809

Braak, H., and Del Tredici, K. (2015). The preclinical phase of the pathological process underlying sporadic Alzheimer's disease. *Brain* 138, 2814–2833. doi: 10.1093/brain/awv236

Braak, H., Del Tredici, K., Rüb, U., de Vos, R. A. I., Jansen Steur, E. N. H., and Braak, E. (2003). Staging of brain pathology related to sporadic Parkinson's disease. *Neurobiol. Aging* 24, 197–211. doi: 10.1016/s0197-4580(02)00065-9

Brandon, N. J., Millar, J. K., Korth, C., Sive, H., Singh, K. K., and Sawa, A. (2009). Understanding the role of DISC1 in psychiatric disease and during Normal development. *J. Neurosci.* 29, 12768–12775. doi: 10.1523/JNEUROSCI.3355-09.2009

Brunert, D., and Rothermel, M. (2021). Extrinsic neuromodulation in the rodent olfactory bulb. *Cell Tissue Res.* 383, 507–524. doi: 10.1007/s00441-020-03365-9

Cao, L., Schrank, B. R., Rodriguez, S., Benz, E. G., Moulia, T. W., Rickenbacher, G. T., et al. (2012). Aβ alters the connectivity of olfactory neurons in the absence of amyloid plaques in vivo. *Nat. Commun.* 3:1009. doi: 10.1038/ncomms2013

Chang, Y.-S., Owen, J. P., Desai, S. S., Hill, S. S., Arnett, A. B., Harris, J., et al. (2014). Autism and sensory processing disorders: shared White matter disruption in sensory pathways but divergent connectivity in social-emotional pathways. *PLoS One* 9:e103038. doi: 10.1371/journal.pone.0103038

Cheaha, D., Bumrungsri, S., Chatpun, S., and Kumarnsit, E. (2015). Characterization of in utero valproic acid mouse model of autism by local field potential in the hippocampus and the olfactory bulb. *Neurosci. Res.* 98, 28–34. doi: 10.1016/j.neures.2015.04.006

Chen, M., Chen, Y., Huo, Q., Wang, L., Tan, S., Misrani, A., et al. (2021b). Enhancing GABAergic signaling ameliorates aberrant gamma oscillations of olfactory bulb in AD mouse models. *Mol. Neurodegener.* 16:14. doi: 10.1186/s13024-021-00434-7

Chen, Y.-N., Kostka, J. K., Bitzenhofer, S. H., and Hanganu-Opatz, I. L. (2023). Olfactory bulb activity shapes the development of entorhinal-hippocampal coupling and associated cognitive abilities. *Curr. Biol.* 33, 4353–4366.e5. doi: 10.1016/j.cub.2023.08.072

Chen, F., Liu, W., Liu, P., Wang, Z., Zhou, Y., Liu, X., et al. (2021a). α-Synuclein aggregation in the olfactory bulb induces olfactory deficits by perturbing granule cells and granular–mitral synaptic transmission. *Npj Park. Dis.* 7, 114–115. doi: 10.1038/s41531-021-00259-7

Chen, S., Tan, H., Wu, Z., Sun, C., He, J., Li, X., et al. (2014). Imaging of olfactory bulb and gray matter volumes in brain areas associated with olfactory function in patients with Parkinson's disease and multiple system atrophy. *Eur. J. Radiol.* 83, 564–570. doi: 10.1016/j.ejrad.2013.11.024

Chini, M., and Hanganu-Opatz, I. L. (2021). Prefrontal cortex development in health and disease: lessons from rodents and humans. *Trends Neurosci.* 44, 227–240. doi: 10.1016/j.tins.2020.10.017

Chini, M., Pöpplau, J. A., Lindemann, C., Carol-Perdiguer, L., Hnida, M., Oberländer, V., et al. (2020). Resolving and rescuing developmental Miswiring in a mouse model of cognitive impairment. *Neuron* 105, 60–74.e7. doi: 10.1016/j.neuron.2019.09.042

Chubb, J. E., Bradshaw, N. J., Soares, D. C., Porteous, D. J., and Millar, J. K. (2008). The DISC locus in psychiatric illness. *Mol. Psychiatry* 13, 36–64. doi: 10.1038/sj.mp.4002106

Corcoran, C., Whitaker, A., Coleman, E., Fried, J., Feldman, J., Goudsmit, N., et al. (2005). Olfactory deficits, cognition and negative symptoms in early onset psychosis. *Schizophr. Res.* 80, 283–293. doi: 10.1016/j.schres.2005.07.028

Crow, A. J. D., Janssen, J. M., Vickers, K. L., Parish-Morris, J., Moberg, P. J., and Roalf, D. R. (2020). Olfactory dysfunction in neurodevelopmental disorders: a Meta-analytic review of autism Spectrum disorders, attention deficit/hyperactivity disorder and obsessive-compulsive disorder. *J. Autism Dev. Disord.* 50, 2685–2697. doi: 10.1007/s10803-020-04376-9

Dan, X., Wechter, N., Gray, S., Mohanty, J. G., Croteau, D. L., and Bohr, V. A. (2021). Olfactory dysfunction in aging and neurodegenerative diseases. *Ageing Res. Rev.* 70:101416. doi: 10.1016/j.arr.2021.101416

Davis, A. A., and Racette, B. (2016). Parkinson disease and cognitive impairment. *Neurol. Clin. Pract.* 6, 452–458. doi: 10.1212/CPJ.0000000000000285

Devanand, D. P., Tabert, M. H., Cuasay, K., Manly, J. J., Schupf, N., Brickman, A. M., et al. (2010). Olfactory identification deficits and MCI in a multi-ethnic elderly community sample. *Neurobiol. Aging* 31, 1593–1600. doi: 10.1016/j.neurobiolaging.2008.09.008

Diez, I., Ortiz-Terán, L., Ng, T. S. C., Albers, M. W., Marshall, G., Orwig, W., et al. (2024). Tau propagation in the brain olfactory circuits is associated with smell perception changes in aging. *Nat. Commun.* 15:4809. doi: 10.1038/s41467-024-48462-3

Dintica, C. S., Marseglia, A., Rizzuto, D., Wang, R., Seubert, J., Arfanakis, K., et al. (2019). Impaired olfaction is associated with cognitive decline and neurodegeneration in the brain. *Neurology* 92, e700–e709. doi: 10.1212/WNL.0000000000006919

Doty, R. L. (2012). Olfaction in Parkinson's disease and related disorders. *Neurobiol. Dis.* 46, 527–552. doi: 10.1016/j.nbd.2011.10.026

Doty, R. L. (2017). Olfactory dysfunction in neurodegenerative diseases: is there a common pathological substrate? *Lancet Neurol.* 16, 478–488. doi: 10.1016/S1474-4422(17)30123-0

Doty, R. L., Deems, D. A., and Stellar, S. (1988). Olfactory dysfunction in parkinsonism: a general deficit unrelated to neurologic signs, disease stage, or disease duration. *Neurology* 38, 1237–1244. doi: 10.1212/wnl.38.8.1237

Doty, R. L., Shaman, P., Kimmelman, C. P., and Dann, M. S. (1984). University of Pennsylvania Smell Identification Test: a rapid quantitative olfactory function test for the clinic. *Laryngoscope* 94, 176–178. doi: 10.1288/00005537-198402000-00004

Drapeau, E., Riad, M., Kajiwara, Y., and Buxbaum, J. D. (2018). Behavioral phenotyping of an improved mouse model of Phelan–McDermid syndrome with a complete deletion of the *Shank3* gene. *eneuro* 5:ENEURO.0046-18.2018. doi: 10.1523/ENEURO.0046-18.2018

Dutra, M. L., Dias, P., Freiberger, V., Ventura, L., Comim, C. M., Martins, D. F., et al. (2023). Maternal immune activation induces autism-like behavior and reduces brain-derived neurotrophic factor levels in the hippocampus and offspring cortex of C57BL/6 mice. *Neurosci. Lett.* 793:136974. doi: 10.1016/j.neulet.2022.136974

Esteve, D., Molina-Navarro, M. M., Giraldo, E., Martínez-Varea, N., Blanco-Gandia, M.-C., Rodríguez-Arias, M., et al. (2022). Adult neural stem cell migration is impaired in a mouse model of Alzheimer's disease. *Mol. Neurobiol.* 59, 1168–1182. doi: 10.1007/s12035-021-02620-6

Fénelon, K., Xu, B., Lai, C. S., Mukai, J., Markx, S., Stark, K. L., et al. (2013). The pattern of cortical dysfunction in a mouse model of a schizophrenia-related microdeletion. *J. Neurosci.* 33, 14825–14839. doi: 10.1523/JNEUROSCI.1611-13.2013

German, D. C., Manaye, K., Smith, W. K., Woodward, D. J., and Saper, C. B. (1989). Midbrain dopaminergic cell loss in parkinson's disease: computer visualization. *Ann. Neurol.* 26, 507–514. doi: 10.1002/ana.410260403

Gil-Bea, F. J., Gerenu, G., Aisa, B., Kirazov, L. P., Schliebs, R., and Ramírez, M. J. (2012). Cholinergic denervation exacerbates amyloid pathology and induces hippocampal atrophy in Tg2576 mice. *Neurobiol. Dis.* 48, 439–446. doi: 10.1016/j.nbd.2012.06.020

Godavarthi, S. K., Li, H., Pratelli, M., and Spitzer, N. C. (2024). Embryonic exposure to environmental factors drives transmitter switching in the neonatal mouse cortex causing autistic-like adult behavior. *Proc. Natl. Acad. Sci.* 121:e2406928121. doi: 10.1073/pnas.2406928121

Goedert, M., and Spillantini, M. G. (2006). A century of Alzheimer's disease. *Science* 314, 777–781. doi: 10.1126/science.1132814

Gourévitch, B., Kay, L. M., and Martin, C. (2010). Directional coupling from the olfactory bulb to the Hippocampus during a go/no-go odor discrimination task. *J. Neurophysiol.* 103, 2633–2641. doi: 10.1152/jn.01075.2009

Gretenkord, S., Kostka, J. K., Hartung, H., Watznauer, K., Fleck, D., Minier-Toribio, A., et al. (2019). Coordinated electrical activity in the olfactory bulb gates the oscillatory entrainment of entorhinal networks in neonatal mice. *PLoS Biol.* 17:e2006994. doi: 10.1371/journal.pbio.2006994

Guo, J. Y., Ragland, J. D., and Carter, C. S. (2019). Memory and cognition in schizophrenia. *Mol. Psychiatry* 24, 633–642. doi: 10.1038/s41380-018-0231-1

Haehner, A., Boesveldt, S., Berendse, H. W., Mackay-Sim, A., Fleischmann, J., Silburn, P. A., et al. (2009). Prevalence of smell loss in Parkinson's disease – a multicenter study. *Parkinsonism Relat. Disord.* 15, 490–494. doi: 10.1016/j.parkreldis.2008.12.005

Haehner, A., Hummel, T., Hummel, C., Sommer, U., Junghanns, S., and Reichmann, H. (2007). Olfactory loss may be a first sign of idiopathic Parkinson's disease. *Mov. Disord.* 22, 839–842. doi: 10.1002/mds.21413

Haehner, A., Masala, C., Walter, S., Reichmann, H., and Hummel, T. (2019). Incidence of Parkinson's disease in a large patient cohort with idiopathic smell and taste loss. *J. Neurol.* 266, 339–345. doi: 10.1007/s00415-018-9135-x

Hahn, C.-G., Han, L.-Y., Rawson, N. E., Mirza, N., Borgmann-Winter, K., Lenox, R. H., et al. (2005). In vivo and in vitro neurogenesis in human olfactory epithelium. *J. Comp. Neurol.* 483, 154–163. doi: 10.1002/cne.20424

Hartung, H., Cichon, N., De Feo, V., Riemann, S., Schildt, S., Lindemann, C., et al. (2016). From shortage to surge: a developmental switch in hippocampal-prefrontal coupling in a gene-environment model of neuropsychiatric disorders. *Cereb. Cortex N. Y. N* 26, 4265–4281. doi: 10.1093/cercor/bhw274

He, Z., Guo, J. L., McBride, J. D., Narasimhan, S., Kim, H., Changolkar, L., et al. (2018). Amyloid-β plaques enhance Alzheimer's brain tau-seeded pathologies by facilitating neuritic plaque tau aggregation. *Nat. Med.* 24, 29–38. doi: 10.1038/nm.4443

Heck, D. H., Correia, B. L., Fox, M. B., Liu, Y., Allen, M., and Varga, S. (2022). Recent insights into respiratory modulation of brain activity offer new perspectives on cognition and emotion. *Biol. Psychol.* 170:108316. doi: 10.1016/j.biopsycho.2022.108316

Höglinger, G. U., Alvarez-Fischer, D., Arias-Carrión, O., Djufri, M., Windolph, A., Keber, U., et al. (2015). A new dopaminergic nigro-olfactory projection. *Acta Neuropathol. (Berl.)* 130, 333–348. doi: 10.1007/s00401-015-1451-y

Hsia, A. Y., Vincent, J. D., and Lledo, P. M. (1999). Dopamine depresses synaptic inputs into the olfactory bulb. *J. Neurophysiol.* 82, 1082–1085. doi: 10.1152/jn.1999.82.2.1082

Huang, T.-N., Yen, T.-L., Qiu, L. R., Chuang, H.-C., Lerch, J. P., and Hsueh, Y.-P. (2019). Haploinsufficiency of autism causative gene Tbr1 impairs olfactory discrimination and neuronal activation of the olfactory system in mice. *Mol. Autism.* 10:5. doi: 10.1186/s13229-019-0257-5

Huisman, E., Uylings, H. B. M., and Hoogland, P. V. (2004). A 100% increase of dopaminergic cells in the olfactory bulb may explain hyposmia in Parkinson's disease. *Mov. Disord. Off. J. Mov. Disord. Soc.* 19, 687–692. doi: 10.1002/mds.10713

Hummel, T., Sekinger, B., Wolf, S. R., Pauli, E., and Kobal, G. (1997). "Sniffin" sticks': olfactory performance assessed by the combined testing of odor identification, odor discrimination and olfactory threshold. *Chem. Senses* 22, 39–52. doi: 10.1093/chemse/22.1.39

Igarashi, K. M., Ieki, N., An, M., Yamaguchi, Y., Nagayama, S., Kobayakawa, K., et al. (2012). Parallel mitral and tufted cell pathways route distinct odor information to different targets in the olfactory cortex. *J. Neurosci.* 32, 7970–7985. doi: 10.1523/JNEUROSCI.0154-12.2012

Igarashi, K. M., Lu, L., Colgin, L. L., Moser, M.-B., and Moser, E. I. (2014). Coordination of entorhinal–hippocampal ensemble activity during associative learning. *Nature* 510, 143–147. doi: 10.1038/nature13162

Imai, T. (2014). Construction of functional neuronal circuitry in the olfactory bulb. *Semin. Cell Dev. Biol.* 35, 180–188. doi: 10.1016/j.semcdb.2014.07.012

Iravani, B., Peter, M. G., Arshamian, A., Olsson, M. J., Hummel, T., Kitzler, H. H., et al. (2021). Acquired olfactory loss alters functional connectivity and morphology. *Sci. Rep.* 11:16422. doi: 10.1038/s41598-021-95968-7

Jahn, H. (2013). Memory loss in Alzheimer's disease. *Dialogues Clin. Neurosci.* 15, 445–454. doi: 10.31887/DCNS.2013.15.4/hjahn

Kamath, V., Lasutschinkow, P., Ishizuka, K., and Sawa, A. (2018). Olfactory functioning in first-episode psychosis. *Schizophr. Bull.* 44, 672–680. doi: 10.1093/schbul/sbx107

Kato, A., Ohta, K., Okanoya, K., and Kazama, H. (2023). Dopaminergic neurons dynamically update sensory values during olfactory maneuver. *Cell Rep.* 42:113122. doi: 10.1016/j.celrep.2023.113122

Kiparizoska, S., and Ikuta, T. (2017). Disrupted olfactory integration in schizophrenia: functional connectivity study. *Int. J. Neuropsychopharmacol.* 20, 740–746. doi: 10.1093/ijnp/pyx045

Koehler, L., Fournel, A., Albertowski, K., Roessner, V., Gerber, J., Hummel, C., et al. (2018). Impaired odor perception in autism Spectrum disorder is associated with decreased activity in olfactory cortex. *Chem. Senses* 43, 627–634. doi: 10.1093/chemse/bjy051

Kosillo, P., and Bateup, H. S. (2021). Dopaminergic dysregulation in syndromic autism Spectrum disorders: insights from genetic mouse models. *Front. Neural Circuits* 15:700968. doi: 10.3389/fncir.2021.700968

Kostka, J. K., and Hanganu-Opatz, I. L. (2023). Olfactory-driven beta band entrainment of limbic circuitry during neonatal development. *J. Physiol.* 601, 3605–3630. doi: 10.1113/JP284401

Kringel, R., Song, L., Xu, X., Bitzenhofer, S. H., and Hanganu-Opatz, I. L. (2023). Layer-specific impairment in the developing lateral entorhinal cortex of immune-challenged Disc1+/− mice. *J. Physiol.* 601, 847–857. doi: 10.1113/JP283896

Lazarini, F., Gabellec, M.-M., Moigneu, C., De Chaumont, F., Olivo-Marin, J.-C., and Lledo, P.-M. (2014). Adult neurogenesis restores dopaminergic neuronal loss in the olfactory bulb. *J. Neurosci.* 34, 14430–14442. doi: 10.1523/JNEUROSCI.5366-13.2014

Lee, E.-Y., Eslinger, P. J., Du, G., Kong, L., Lewis, M. M., and Huang, X. (2014). Olfactory-related cortical atrophy is associated with olfactory dysfunction in Parkinson's disease. *Mov. Disord. Off. J. Mov. Disord. Soc.* 29, 1205–1208. doi: 10.1002/mds.25829

Leitner, F. C., Melzer, S., Lütcke, H., Pinna, R., Seeburg, P. H., Helmchen, F., et al. (2016). Spatially segregated feedforward and feedback neurons support differential odor processing in the lateral entorhinal cortex. *Nat. Neurosci.* 19, 935–944. doi: 10.1038/nn.4303

Lepousez, G., and Lledo, P.-M. (2013). Odor discrimination requires proper olfactory fast oscillations in awake mice. *Neuron* 80, 1010–1024. doi: 10.1016/j.neuron.2013.07.025

Li, W., Li, S., Shen, L., Wang, J., Wu, X., Li, J., et al. (2019b). Impairment of Dendrodendritic inhibition in the olfactory bulb of APP/PS1 mice. *Front. Aging Neurosci.* 11:2. doi: 10.3389/fnagi.2019.00002

Li, S., Li, W., Wu, X., Li, J., Yang, J., Tu, C., et al. (2019a). Olfactory deficit is associated with mitral cell dysfunction in the olfactory bulb of P301S tau transgenic mice. *Brain Res. Bull.* 148, 34–45. doi: 10.1016/j.brainresbull.2019.03.006

Li, Y., Xu, J., Liu, Y., Zhu, J., Liu, N., Zeng, W., et al. (2017). A distinct entorhinal cortex to hippocampal CA1 direct circuit for olfactory associative learning. *Nat. Neurosci.* 20, 559–570. doi: 10.1038/nn.4517

Linster, C., and Fontanini, A. (2014). Functional neuromodulation of chemosensation in vertebrates. *Curr. Opin. Neurobiol.* 29, 82–87. doi: 10.1016/j.conb.2014.05.010

Liu, G., Froudarakis, E., Patel, J. M., Kochukov, M. Y., Pekarek, B., Hunt, P. J., et al. (2019). Target specific functions of EPL interneurons in olfactory circuits. *Nat. Commun.* 10:3369. doi: 10.1038/s41467-019-11354-y

Liu, Y.-H., Lai, W.-S., Tsay, H.-J., Wang, T.-W., and Yu, J.-Y. (2013b). Effects of maternal immune activation on adult neurogenesis in the subventricular zone-olfactory bulb pathway and olfactory discrimination. *Schizophr. Res.* 151, 1–11. doi: 10.1016/j.schres.2013.09.007

Liu, S., Plachez, C., Shao, Z., Puche, A., and Shipley, M. T. (2013a). Olfactory bulb short axon cell release of GABA and dopamine produces a temporally biphasic inhibition-excitation response in external tufted cells. *J. Neurosci.* 33, 2916–2926. doi: 10.1523/JNEUROSCI.3607-12.2013

Livneh, Y., Adam, Y., and Mizrahi, A. (2014). Odor processing by adult-born neurons. *Neuron* 81, 1097–1110. doi: 10.1016/j.neuron.2014.01.007

Lledo, P.-M., and Valley, M. (2016). Adult olfactory bulb neurogenesis. *Cold Spring Harb. Perspect. Biol.* 8:a018945. doi: 10.1101/cshperspect.a018945

Loayza, M., Lin, S., Carter, K., Ojeda, N., Fan, L.-W., Ramarao, S., et al. (2023). Maternal immune activation alters fetal and neonatal microglia phenotype and disrupts neurogenesis in mice. *Pediatr. Res.* 93, 1216–1225. doi: 10.1038/s41390-022-02239-w

Lu, J., Testa, N., Jordan, R., Elyan, R., Kanekar, S., Wang, J., et al. (2019a). Functional connectivity between the resting-state olfactory network and the Hippocampus in Alzheimer's disease. *Brain Sci.* 9:338. doi: 10.3390/brainsci9120338

Lu, J., Yang, Q. X., Zhang, H., Eslinger, P. J., Zhang, X., Wu, S., et al. (2019b). Disruptions of the olfactory and default mode networks in Alzheimer's disease. *Brain Behav.* 9:e01296. doi: 10.1002/brb3.1296

Mao, Y., Ge, X., Frank, C. L., Madison, J. M., Koehler, A. N., Doud, M. K., et al. (2009). Disrupted in schizophrenia 1 regulates neuronal progenitor proliferation via modulation of GSK3β/β-catenin signaling. *Cell* 136, 1017–1031. doi: 10.1016/j.cell.2008.12.044

Martin-Lopez, E., Vidyadhara, D. J., Liberia, T., Meller, S. J., Harmon, L. E., Hsu, R. M., et al. (2023). α-Synuclein pathology and reduced neurogenesis in the olfactory system affect olfaction in a mouse model of Parkinson's disease. *J. Neurosci.* 43, 1051–1071. doi: 10.1523/JNEUROSCI.1526-22.2022

McCann, H., Cartwright, H., and Halliday, G. M. (2016). Neuropathology of α-synuclein propagation and braak hypothesis. *Mov. Disord.* 31, 152–160. doi: 10.1002/mds.26421

McGann, J. P. (2013). Presynaptic inhibition of olfactory sensory neurons: new mechanisms and potential functions. *Chem. Senses* 38, 459–474. doi: 10.1093/chemse/bjt018

Meyer, P. M., and Alberts, J. R. (2016). Non-nutritive, thermotactile cues induce odor preference in infant mice (*Mus musculus*). *J. Comp. Psychol. Wash. DC* 130, 369–379. doi: 10.1037/com0000044

Mezey, E., Dehejia, A. M., Harta, G., Suchy, S. F., Nussbaum, R. L., Brownstein, M. J., et al. (1998). Alpha synuclein is present in Lewy bodies in sporadic Parkinson's disease. *Mol. Psychiatry* 3, 493–499. doi: 10.1038/sj.mp.4000446

Mihalj, D., Borbelyova, V., Pirnik, Z., Bacova, Z., Ostatnikova, D., and Bakos, J. (2024). Shank3 deficiency results in a reduction in GABAergic postsynaptic puncta in the olfactory brain areas. *Neurochem. Res.* 49, 1008–1016. doi: 10.1007/s11064-023-04097-2

Moberg, P. J., Agrin, R., Gur, R. E., Gur, R. C., Turetsky, B. I., and Doty, R. L. (1999). Olfactory dysfunction in schizophrenia: a qualitative and quantitative review. *Am. College Neuropsychopharmacol.* 21, 325–340. doi: 10.1016/S0893-133X(99)00019-6

Mori, K., Manabe, H., Narikiyo, K., and Onisawa, N. (2013). Olfactory consciousness and gamma oscillation couplings across the olfactory bulb, olfactory cortex, and orbitofrontal cortex. *Front. Psychol.* 4:743. doi: 10.3389/fpsyg.2013.00743

Mundiñano, I.-C., Caballero, M.-C., Ordóñez, C., Hernandez, M., DiCaudo, C., Marcilla, I., et al. (2011). Increased dopaminergic cells and protein aggregates in the olfactory bulb of patients with neurodegenerative disorders. *Acta Neuropathol. (Berl.)* 122, 61–74. doi: 10.1007/s00401-011-0830-2

Murman, D. L. (2015). The impact of age on cognition. *Semin. Hear.* 36, 111–121. doi: 10.1055/s-0035-1555115

Murphy, C. (2019). Olfactory and other sensory impairments in Alzheimer disease. *Nat. Rev. Neurol.* 15, 11–24. doi: 10.1038/s41582-018-0097-5

Murrell, W., Bushell, G. R., Livesey, J., McGrath, J., MacDonald, K. P. A., Bates, P. R., et al. (1996). Neurogenesis in adult human. *Neuroreport* 7, 1189–1194. doi: 10.1097/00001756-199604260-00019

Nguyen, A. D., Pelavin, P. E., Shenton, M. E., Chilakamarri, P., McCarley, R. W., Nestor, P. G., et al. (2011). Olfactory sulcal depth and olfactory bulb volume in patients with schizophrenia: an MRI study. *Brain Imaging Behav.* 5, 252–261. doi: 10.1007/s11682-011-9129-0

Nguyen, A. D., Shenton, M. E., and Levitt, J. J. (2010). Olfactory dysfunction in schizophrenia: a review of neuroanatomy and psychophysiological measurements. *Harv. Rev. Psychiatry* 18, 279–292. doi: 10.3109/10673229.2010.511060

Nobili, A., Latagliata, E. C., Viscomi, M. T., Cavallucci, V., Cutuli, D., Giacovazzo, G., et al. (2017). Dopamine neuronal loss contributes to memory and reward dysfunction in a model of Alzheimer's disease. *Nat. Commun.* 8:14727. doi: 10.1038/ncomms14727

Ovsepian, S. V., O'Leary, V. B., Zaborszky, L., Ntziachristos, V., and Dolly, J. O. (2019). Amyloid plaques of Alzheimer's disease as hotspots of glutamatergic activity. *Neurosci. Rev. J. Bringing Neurobiol. Neurol. Psychiatry* 25, 288–297. doi: 10.1177/1073858418791128

Owen, M. J., Sawa, A., and Mortensen, P. B. (2016). Schizophrenia. *Lancet* 388, 86–97. doi: 10.1016/S0140-6736(15)01121-6

Papadatos, Z., and Phillips, N. A. (2023). Olfactory function reflects episodic memory performance and atrophy in the medial temporal lobe in individuals at risk for Alzheimer's disease. *Neurobiol. Aging* 128, 33–42. doi: 10.1016/j.neurobiolaging.2023.04.001

Parbst, F., Kostka, J. K., Günther, A., Chen, Y.-N., Hanganu-Opatz, I. L., and Bitzenhofer, S. H. (2024). Developmental olfactory dysfunction and abnormal odor memory in immune-challenged Disc1+/− mice. *bioRxiv* 2024-05:663. doi: 10.1101/2024.05.17.594663

Pavăl, D. (2017). A dopamine hypothesis of autism Spectrum disorder. *Dev. Neurosci.* 39, 355–360. doi: 10.1159/000478725

Pavăl, D., and Micluția, I. V. (2021). The dopamine hypothesis of autism Spectrum disorder revisited: current status and future prospects. *Dev. Neurosci.* 43, 73–83. doi: 10.1159/000515751

Pignatelli, A., and Belluzzi, O. (2017). Dopaminergic Neurones in the Main olfactory bulb: An overview from an electrophysiological perspective. *Front. Neuroanat.* 11:7. doi: 10.3389/fnana.2017.00007

Rangel, L. M., Rueckemann, J. W., Riviere, P. D., Keefe, K. R., Porter, B. S., Heimbuch, I. S., et al. (2016). Rhythmic coordination of hippocampal neurons during associative memory processing. *eLife* 5:e09849. doi: 10.7554/eLife.09849

Rey, N. L., Steiner, J. A., Maroof, N., Luk, K. C., Madaj, Z., Trojanowski, J. Q., et al. (2016). Widespread transneuronal propagation of α-synucleinopathy triggered in olfactory bulb mimics prodromal Parkinson's disease. *J. Exp. Med.* 213, 1759–1778. doi: 10.1084/jem.20160368

Richardson, J. T. E., and Zucco, G. M. (1989). Cognition and olfaction: a review. *Psychol. Bull.* 105, 352–360. doi: 10.1037/0033-2909.105.3.352

Richter, M., Murtaza, N., Scharrenberg, R., White, S. H., Johanns, O., Walker, S., et al. (2019). Altered TAOK2 activity causes autism-related neurodevelopmental and cognitive abnormalities through RhoA signaling. *Mol. Psychiatry* 24, 1329–1350. doi: 10.1038/s41380-018-0025-5

Roberts, R. O., Christianson, T. J. H., Kremers, W. K., Mielke, M. M., Machulda, M. M., Vassilaki, M., et al. (2016). Association between olfactory dysfunction and amnestic mild cognitive impairment and Alzheimer disease dementia. *JAMA Neurol.* 73, 93–101. doi: 10.1001/jamaneurol.2015.2952

Rodríguez, J. J., Jones, V. C., and Verkhratsky, A. (2009). Impaired cell proliferation in the subventricular zone in an Alzheimer's disease model. *Neuroreport* 20, 907–912. doi: 10.1097/WNR.0b013e32832be77d

Ross, G. W., Petrovitch, H., Abbott, R. D., Tanner, C. M., Popper, J., Masaki, K., et al. (2008). Association of olfactory dysfunction with risk for future Parkinson's disease. *Ann. Neurol.* 63, 167–173. doi: 10.1002/ana.21291

Rupp, C. I., Fleischhacker, W. W., Kemmler, G., Kremser, C., Bilder, R. M., Mechtcheriakov, S., et al. (2005). Olfactory functions and volumetric measures of orbitofrontal and limbic regions in schizophrenia. *Schizophr. Res.* 74, 149–161. doi: 10.1016/j.schres.2004.07.010

Ryndych, D., Sebold, A., Strassburg, A., Li, Y., Ramos, R. L., and Otazu, G. H. (2023). Haploinsufficiency of Shank3 in mice selectively impairs target odor recognition in novel background odors. *J. Neurosci.* 43, 7799–7811. doi: 10.1523/JNEUROSCI.0255-23.2023

Schechter, I., Butler, P. D., Silipo, G., Zemon, V., and Javitt, D. C. (2003). Magnocellular and parvocellular contributions to backward masking dysfunction in schizophrenia. *Schizophr. Res.* 64, 91–101. doi: 10.1016/S0920-9964(03)00008-2

Schepanski, S., Chini, M., Sternemann, V., Urbschat, C., Thiele, K., Sun, T., et al. (2022). Pregnancy-induced maternal microchimerism shapes neurodevelopment and behavior in mice. *Nat. Commun.* 13:4571. doi: 10.1038/s41467-022-32230-2

Schurov, I. L., Handford, E. J., Brandon, N. J., and Whiting, P. J. (2004). Expression of disrupted in schizophrenia 1 (DISC1) protein in the adult and developing mouse brain indicates its role in neurodevelopment. *Mol. Psychiatry* 9, 1100–1110. doi: 10.1038/sj.mp.4001574

Scopa, C., Marrocco, F., Latina, V., Ruggeri, F., Corvaglia, V., La Regina, F., et al. (2020). Impaired adult neurogenesis is an early event in Alzheimer's disease neurodegeneration, mediated by intracellular Aβ oligomers. *Cell Death Differ.* 27, 934–948. doi: 10.1038/s41418-019-0409-3

Siper, P. M., Layton, C., Levy, T., Lurie, S., Benrey, N., Zweifach, J., et al. (2021). Sensory reactivity symptoms are a Core feature of ADNP syndrome irrespective of autism diagnosis. *Gen. Dent.* 12:351. doi: 10.3390/genes12030351

Sohrabi, H. R., Bates, K. A., Weinborn, M. G., Johnston, A. N. B., Bahramian, A., Taddei, K., et al. (2012). Olfactory discrimination predicts cognitive decline among community-dwelling older adults. *Transl. Psychiatry* 2:e118. doi: 10.1038/tp.2012.43

Sosulski, D. L., Bloom, M. L., Cutforth, T., Axel, R., and Datta, S. R. (2011). Distinct representations of olfactory information in different cortical centres. *Nature* 472, 213–216. doi: 10.1038/nature09868

Stark, K. L., Xu, B., Bagchi, A., Lai, W.-S., Liu, H., Hsu, R., et al. (2008). Altered brain microRNA biogenesis contributes to phenotypic deficits in a 22q11-deletion mouse model. *Nat. Genet.* 40, 751–760. doi: 10.1038/ng.138

Stevenson, R. J. (2013). Olfactory perception, cognition, and dysfunction in humans. *WIREs Cogn. Sci.* 4, 273–284. doi: 10.1002/wcs.1224

Stranahan, A. M., and Mattson, M. P. (2010). Selective vulnerability of neurons in layer II of the entorhinal cortex during aging and Alzheimer's disease. *Neural Plast.* 2010, 1–8. doi: 10.1155/2010/108190

Struble, R. G., and Clark, H. B. (1992). Olfactory bulb lesions in Alzheimer's disease. *Neurobiol. Aging* 13, 469–473. doi: 10.1016/0197-4580(92)90074-8

Symanski, C. A., Bladon, J. H., Kullberg, E. T., Miller, P., and Jadhav, S. P. (2022). Rhythmic coordination of hippocampal-prefrontal ensembles for odor-place associative memory and decision making. *bioRxiv* 2020-06:140939. doi: 10.1101/2020.06.08.140939

Tanik, N., Serin, H. I., Celikbilek, A., Inan, L. E., and Gundogdu, F. (2016). Associations of olfactory bulb and depth of olfactory sulcus with basal ganglia and hippocampus in patients with Parkinson's disease. *Neurosci. Lett.* 620, 111–114. doi: 10.1016/j.neulet.2016.03.050

Thomann, P. A., Dos Santos, V., Seidl, U., Toro, P., Essig, M., and Schröder, J. (2009a). MRI-derived atrophy of the olfactory bulb and tract in mild cognitive impairment and Alzheimer's disease. *J. Alzheimers Dis.* 17, 213–221. doi: 10.3233/JAD-2009-1036

Thomann, P. A., Dos Santos, V., Toro, P., Schönknecht, P., Essig, M., and Schröder, J. (2009b). Reduced olfactory bulb and tract volume in early Alzheimer's disease—a MRI study. *Neurobiol. Aging* 30, 838–841. doi: 10.1016/j.neurobiolaging.2007.08.001

Thye, M. D., Bednarz, H. M., Herringshaw, A. J., Sartin, E. B., and Kana, R. K. (2018). The impact of atypical sensory processing on social impairments in autism spectrum disorder. *Dev. Cogn. Neurosci.* 29, 151–167. doi: 10.1016/j.dcn.2017.04.010

Tillerson, J. L., Caudle, W. M., Parent, J. M., Gong, C., Schallert, T., and Miller, G. W. (2006). Olfactory discrimination deficits in mice lacking the dopamine transporter or the D2 dopamine receptor. *Behav. Brain Res.* 172, 97–105. doi: 10.1016/j.bbr.2006.04.025

Tort, A. B. L., Brankačk, J., and Draguhn, A. (2018). Respiration-entrained brain rhythms are global but often overlooked. *Trends Neurosci.* 41, 186–197. doi: 10.1016/j.tins.2018.01.007

Trentin, S., Fraiman de Oliveira, B. S., Ferreira Felloni Borges, Y., and de Mello Rieder, C. R. (2022). Systematic review and meta-analysis of Sniffin sticks test performance in Parkinson's disease patients in different countries. *Eur. Arch. Otorrinolaringol.* 279, 1123–1145. doi: 10.1007/s00405-021-06970-8

Turetsky, B. I., Moberg, P. J., Owzar, K., Johnson, S. C., Doty, R. L., and Gur, R. E. (2003). Physiologic impairment of olfactory stimulus processing in schizophrenia. *Biol. Psychiatry* 53, 403–411. doi: 10.1016/s0006-3223(02)01865-6

Turetsky, B. I., Moberg, P. J., Quarmley, M., Dress, E., Calkins, M. E., Ruparel, K., et al. (2018). Structural anomalies of the peripheral olfactory system in psychosis high-risk subjects. *Schizophr. Res.* 195, 197–205. doi: 10.1016/j.schres.2017.09.015

Turetsky, B. I., Moberg, P. J., Yousem, D. M., Doty, R. L., Arnold, S. E., and Gur, R. E. (2000). Reduced olfactory bulb volume in patients with schizophrenia. *Am. J. Psychiatry* 157, 828–830. doi: 10.1176/appi.ajp.157.5.828

Uchida, S., Shimada, C., Sakuma, N., Kagitani, F., Kan, A., and Awata, S. (2020). The relationship between olfaction and cognitive function in the elderly. *J. Physiol. Sci.* 70:48. doi: 10.1186/s12576-020-00777-8

Vallés, A. S., and Barrantes, F. J. (2021). Dysregulation of neuronal nicotinic acetylcholine receptor-cholesterol crosstalk in autism Spectrum disorder. *Front. Mol. Neurosci.* 14:744597. doi: 10.3389/fnmol.2021.744597

Wang, P. Y., Boboila, C., Chin, M., Higashi-Howard, A., Shamash, P., Wu, Z., et al. (2020). Transient and persistent representations of odor value in prefrontal cortex. *Neuron* 108, 209–224.e6. doi: 10.1016/j.neuron.2020.07.033

Wang, J., You, H., Liu, J.-F., Ni, D.-F., Zhang, Z.-X., and Guan, J. (2011). Association of olfactory bulb volume and olfactory sulcus depth with olfactory function in patients with Parkinson disease. *AJNR Am. J. Neuroradiol.* 32, 677–681. doi: 10.3174/ajnr.A2350

Wattendorf, E., Welge-Lüssen, A., Fiedler, K., Bilecen, D., Wolfensberger, M., Fuhr, P., et al. (2009). Olfactory impairment predicts brain atrophy in Parkinson's disease. *J. Neurosci.* 29, 15410–15413. doi: 10.1523/JNEUROSCI.1909-09.2009

Wesson, D. W., Borkowski, A. H., Landreth, G. E., Nixon, R. A., Levy, E., and Wilson, D. A. (2011). Sensory network dysfunction, behavioral impairments, and their reversibility in an Alzheimer's β-amyloidosis mouse model. *J. Neurosci.* 31, 15962–15971. doi: 10.1523/JNEUROSCI.2085-11.2011

Wesson, D. W., Levy, E., Nixon, R. A., and Wilson, D. A. (2010). Olfactory dysfunction correlates with amyloid-β burden in an Alzheimer's disease mouse model. *J. Neurosci.* 30, 505–514. doi: 10.1523/JNEUROSCI.4622-09.2010

Wilson, D. M., Cookson, M. R., Van Den Bosch, L., Zetterberg, H., Holtzman, D. M., and Dewachter, I. (2023). Hallmarks of neurodegenerative diseases. *Cell* 186, 693–714. doi: 10.1016/j.cell.2022.12.032

Wilson, D. A., and Sullivan, R. M. (1995). The D2 antagonist spiperone mimics the effects of olfactory deprivation on mitral/tufted cell odor response patterns. *J. Neurosci.* 15, 5574–5581. doi: 10.1523/JNEUROSCI.15-08-05574.1995

Winner, B., Melrose, H. L., Zhao, C., Hinkle, K. M., Yue, M., Kent, C., et al. (2011). Adult neurogenesis and neurite outgrowth are impaired in LRRK2 G2019S mice. *Neurobiol. Dis.* 41, 706–716. doi: 10.1016/j.nbd.2010.12.008

Winner, B., Rockenstein, E., Lie, D. C., Aigner, R., Mante, M., Bogdahn, U., et al. (2008). Mutant α-synuclein exacerbates age-related decrease of neurogenesis. *Neurobiol. Aging* 29, 913–925. doi: 10.1016/j.neurobiolaging.2006.12.016

Witter, M. P., Doan, T. P., Jacobsen, B., Nilssen, E. S., and Ohara, S. (2017). Architecture of the entorhinal cortex a review of entorhinal anatomy in rodents with some comparative notes. *Front. Syst. Neurosci.* 11:46. doi: 10.3389/fnsys.2017.00046

Wu, N., Rao, X., Gao, Y., Wang, J., and Xu, F. (2013). Amyloid-β deposition and olfactory dysfunction in an Alzheimer's disease model. *J. Alzheimers Dis.* 37, 699–712. doi: 10.3233/JAD-122443

Xu, W., Fitzgerald, S., Nixon, R. A., Levy, E., and Wilson, D. A. (2015). Early hyperactivity in lateral entorhinal cortex is associated with elevated levels of AβPP metabolites in the Tg2576 mouse model of Alzheimer's disease. *Exp. Neurol.* 264, 82–91. doi: 10.1016/j.expneurol.2014.12.008

Xu, J., Kao, S.-Y., Lee, F. J. S., Song, W., Jin, L.-W., and Yankner, B. A. (2002). Dopamine-dependent neurotoxicity of α-synuclein: a mechanism for selective neurodegeneration in Parkinson disease. *Nat. Med.* 8, 600–606. doi: 10.1038/nm0602-600

Xu, X., Song, L., Kringel, R., and Hanganu-Opatz, I. L. (2021). Developmental decrease of entorhinal-hippocampal communication in immune-challenged DISC1 knockdown mice. *Nat. Commun.* 12:6810. doi: 10.1038/s41467-021-27114-w

Yahiaoui-Doktor, M., Luck, T., Riedel-Heller, S. G., Loeffler, M., Wirkner, K., and Engel, C. (2019). Olfactory function is associated with cognitive performance: results from the population-based LIFE-adult-study. *Alzheimers Res. Ther.* 11:43. doi: 10.1186/s13195-019-0494-z

Yang, M., and Crawley, J. N. (2009). Simple behavioral assessment of mouse olfaction. *Curr. Protoc. Neurosci.* 8:48. doi: 10.1002/0471142301.ns0824s48

Yang, K., Hasegawa, Y., Bhattarai, J. P., Hua, J., Dower, M., Etyemez, S., et al. (2024). Inflammation-related pathology in the olfactory epithelium: its impact on the olfactory system in psychotic disorders. *Mol. Psychiatry* 29, 1453–1464. doi: 10.1038/s41380-024-02425-8

Yang, K., Hua, J., Etyemez, S., Paez, A., Prasad, N., Ishizuka, K., et al. (2021). Volumetric alteration of olfactory bulb and immune-related molecular changes in olfactory epithelium in first episode psychosis patients. *Schizophr. Res.* 235, 9–11. doi: 10.1016/j.schres.2021.07.016

Yang, S., Kuan, W.-L., and Spillantini, M. G. (2016). Progressive tauopathy in P301S tau transgenic mice is associated with a functional deficit of the olfactory system. *Eur. J. Neurosci.* 44, 2396–2403. doi: 10.1111/ejn.13333

Yang, Q., Zhou, G., Noto, T., Templer, J. W., Schuele, S. U., Rosenow, J. M., et al. (2022). Smell-induced gamma oscillations in human olfactory cortex are required for accurate perception of odor identity. *PLoS Biol.* 20:e3001509. doi: 10.1371/journal.pbio.3001509

Yao, Z.-G., Hua, F., Zhang, H.-Z., Li, Y.-Y., and Qin, Y.-J. (2017). Olfactory dysfunction in the APP/PS1 transgenic mouse model of Alzheimer's disease: morphological evaluations from the nose to the brain. *Neuropathology* 37, 485–494. doi: 10.1111/neup.12391

Zapiec, B., Dieriks, B. V., Tan, S., Faull, R. L. M., Mombaerts, P., and Curtis, M. A. (2017). A ventral glomerular deficit in Parkinson's disease revealed by whole olfactory bulb reconstruction. *Brain J. Neurol.* 140, 2722–2736. doi: 10.1093/brain/awx208

Zelano, C., Jiang, H., Zhou, G., Arora, N., Schuele, S., Rosenow, J., et al. (2016). Nasal respiration entrains human limbic oscillations and modulates cognitive function. *J. Neurosci.* 36, 12448–12467. doi: 10.1523/JNEUROSCI.2586-16.2016

Zhang, X., and Firestein, S. (2002). The olfactory receptor gene superfamily of the mouse. *Nat. Neurosci.* 5, 124–133. doi: 10.1038/nn800

2.2.4 Developmental Olfactory Dysfunction and Abnormal Odor Memory in Immune-Challenged Disc1$^{+/-}$ Mice

Fiona Parbst, Johanna K. Kostka, Anne Günther, **Yu-Nan Chen**, Ileana L. Hanganu-Opatz and Sebastian H. Bitzenhofer

Preprint on *bioRxiv* 2024, accepted by *Journal of Neuroscience*; DOI: 10.1101/2024.05.17.594663

Personal contribution

I performed part of *in vivo* electrophysiological recordings for neonatal OB.

I reviewed and commented on the manuscript.

Developmental olfactory dysfunction and abnormal odor memory in immune-challenged *Disc1*$^{+/-}$ mice

Fiona Parbst[1], Johanna K. Kostka[1], Anne Günther[1], Yu-Nan Chen[1], Ileana L. Hanganu-Opatz[1,*], Sebastian H. Bitzenhofer[2,*]

[1] *Institute of Developmental Neurophysiology, Center for Molecular Neurobiology Hamburg, Hamburg Center of Neuroscience, University Medical Center Hamburg-Eppendorf, 20251, Hamburg, Germany*
[2] *Neural Circuit Physiology, Center for Molecular Neurobiology Hamburg, University Medical Center Hamburg-Eppendorf, 20251, Hamburg, Germany*

* Corresponding authors:
Ileana L. Hanganu-Opatz
hangop@zmnh.uni-hamburg.de

Sebastian H. Bitzenhofer
sebastian.bitzenhofer@zmnh.uni-hamburg.de

Short title
Developmental OB dysfunction relates to memory deficits in GE mice

Author contributions
S.H.B., J.K.K. and I.L.H.-O. designed the experiments. F.P., A.G., Y.-N.C. and S.H.B. carried out the experiments. J.K.K., and S.H.B. wrote the analysis code. F.P., J.K.K., and S.H.B. analyzed the data. S.H.B., I.L.H.-O., J.K.K., A.G., and F.P. interpreted the data. S.H.B. and F.P. wrote the manuscript. All authors discussed and commented on the manuscript.

Conflict of interest
The authors declare no competing financial interests.

Funding
This work was funded by grants from the German Research Foundation (Ha4466/20-1, Ha4466/22-1, and SFB 936 178316478 to I.L.H.-O.), Horizon 2020 DEEPER (101016787 to I.L.H.-O.), and the European Research Council (ERC-2023-StG 101114633 to S.H.B.).

Abstract

Neuronal activity in the olfactory bulb (OB) drives coordinated activity in the hippocampal-prefrontal network during early development. Inhibiting OB output in neonatal mice disrupts functional development of the hippocampal formation as well as cognitive abilities. These impairments manifest early in life and resemble dysfunctions of the hippocampus and the prefrontal cortex that have been linked to neuropsychiatric disorders. Thus, we investigated a disease mouse model and asked whether activity in the OB might be altered, thereby contributing to the dysfunctional development of the hippocampal-prefrontal network. We addressed this question by combining in vivo electrophysiology with behavioral assessment of immune-challenged *Disc1*$^{+/-}$ mice that mimic the dual genetic-environmental etiology of neuropsychiatric disorders. In wildtype mice, we found high DISC1 expression levels in OB projection neurons during development. Furthermore, neuronal and network activity in the OB, as well as the drive from the bulb to the hippocampal-prefrontal network were reduced in immune-challenged *Disc1*$^{+/-}$ mice during early development. This early deficit did not affect odor-evoked activity and odor perception but resulted in impaired long-term odor memory. We propose that reduced endogenous activity in the developing OB contributes to altered maturation of the hippocampal-prefrontal network, leading to memory impairment in immune-challenged *Disc1*$^{+/-}$ mice.

Introduction

Functional maturation of the central nervous system is shaped by neuronal activity during development [1–4]. This activity can be intrinsically generated within local networks or driven by input from the sensory periphery. For example, studies in rodents revealed that activity in the visual cortex during early development is critical for the refinement of the network and can be generated locally or driven by retinal waves that occur before eye opening [5,6]. Similarly, spontaneous activity from the cochlea is required for the maturation of the auditory cortex [7,8]. As for sensory areas, the maturation of higher association areas, such as the prefrontal cortex (PFC), is influenced by coordinated patterns of neuronal activity during development. Their perturbation during early postnatal development causes long-lasting circuit dysfunction, as result of an excitation-inhibition imbalance, and impairment of associated cognitive abilities [9,10].

However, what is driving early activity in the PFC is less clear. During development, inputs from the mediodorsal thalamus increase the activity level in the PFC and their inhibition impairs prefrontal maturation [11]. Monosynaptic projections from the intermediate and ventral hippocampus provide another excitatory drive for prefrontal activity during development [12,13]. A prominent candidate for the drive of developmental neuronal activity in these areas in turn is the olfactory system. From birth on, mouse pups rely on olfactory inputs to find the teats of the dam for feeding [14]. In line with this vital function, mitral and tufted cells, the projection neurons of the olfactory bulb (OB), as well as their axonal projections develop prenatally and their downstream connectivity is largely established at birth [15,16]. Consequently, coordinated neuronal activity in the OB emerges early in life and is more prominent in comparison to other brain areas during early postnatal development [17,18]. Even without a direct connection from the OB to the hippocampus or the PFC, strong projections from OB to the piriform cortex and lateral entorhinal cortex provide a short pathway by which the olfactory system can influence the hippocampal-prefrontal network [19–21]. In line with this, we previously showed that rhythmic activity in the OB entrains activity in the

entorhinal cortex, hippocampus, and PFC already during early postnatal development [18,22]. Thus, activity in the olfactory system might play a similar role for the development of the hippocampal-prefrontal network as neuronal activity in the retina and the cochlea has for the maturation of the visual and the auditory system, respectively.

Indeed, we recently demonstrated that transient inhibition of OB outputs at the start of the second postnatal week in mice reduces coordinated activity in the hippocampal formation and impairs cognitive abilities later in life [23]. These findings resemble the developmental deficits observed in mouse models of neuropsychiatric disorders [24,25]. Accumulating evidence suggests an association of olfactory impairment with neuropsychiatric disorders. For example, inflammation of the olfactory epithelium, reduced OB volume, and deficits in odor perception have been reported for schizophrenia, psychosis, and depression [26–30]. However, it is unknown how alterations in the olfactory system might contribute to the pathogenesis of neuropsychiatric disorders that involve prefrontal-hippocampal dysfunction [24,31].

Here, we investigated the interactions of the olfactory system with the hippocampal-prefrontal network during neonatal development in a mouse model of neuropsychiatric disorders. Immune-challenged *Disc1*$^{+/-}$ mice are a dual-hit mouse model that combines two well-established models for neuropsychiatric disorders: a heterozygous mutation in the gene disrupted-in-schizophrenia 1 (*Disc1*$^{+/-}$) resulting in a truncated DISC1 protein [32,33] and maternal immune activation by the viral RNA mimetic poly(I:C) [34]. This dual-hit gene-environment (GE) mouse model mimics the etiology of neuropsychiatric disorders and shows an impairment of coordinated activity in the hippocampal-prefrontal network during early development, as well as reduced performance in associated cognitive tasks [35–37].

Results

High developmental DISC1 expression in OB projection neurons

The DISC1 protein is involved in the regulation of several developmental processes, such as progenitor proliferation, neuronal migration, and synapse formation [38–40]. The regulation of the formation and maintenance of synaptic connections by DISC1 is considered particularly important in the context of its association with neuropsychiatric disorders [33,41]. In adult mice, DISC1 is expressed in several brain areas including the OB, the hippocampus, and the cerebral cortex [42–44].

As a first test for a potential role of the olfactory system in the pathophysiology of GE mice, we investigated DISC1 expression during postnatal development. Using immunohistochemistry, we found high expression levels of DISC1 in the OB of wildtype (WT) mice at the beginning of the second postnatal week (Fig 1A,B). DISC1 expression was significantly higher in the OB compared to the hippocampal subdivision CA1 ($p=4.39x10^{-4}$) and the PFC ($p=5.52x10^{-4}$) in WT mice. In GE mice, DISC1 expression was significantly reduced compared to WT controls in all areas (OB $p=3.50x10^{-4}$, CA1 $p=9.37x10^{-5}$, PFC $p=1.7x10^{-3}$). More detailed examination of the OB revealed increased DISC1 expression in the neuronal processes but also in the cell bodies of neurons in the mitral cell layer (MCL) and the external plexiform layer (EPL) (Fig 1C).This is indicative for a strong DISC1 expression in mitral/tufted cells, the projections neurons of the OB. Immunostaining of OB slices of postnatal day (P) 10 WT mice, injected with the retrograde tracer CTB555 into the piriform cortex at P5, confirmed the expression of DISC1 in OB projection neurons (Fig 1D).

Together, these results support the idea of a potential developmental dysfunction of the OB in GE mice.

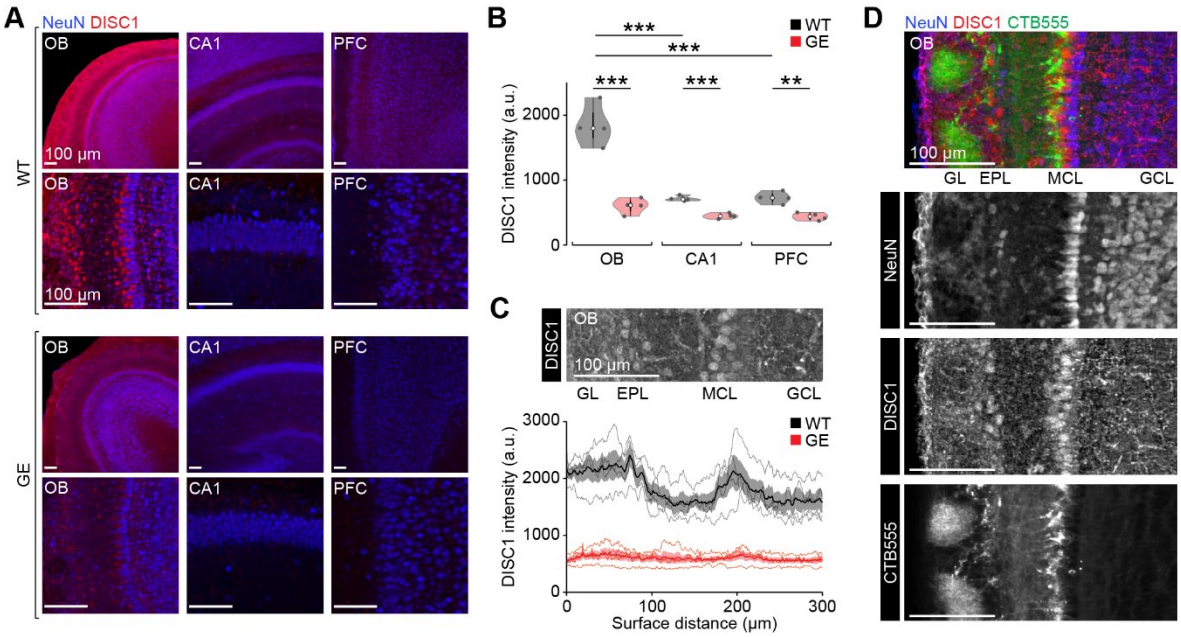

Fig 1. Strong expression of DISC1 in OB projection neurons at P10.
A Coronal sections of OB, CA1, and PFC from P10 WT (top) and GE (bottom) mice immunostained for NeuN (blue) and DISC1 (red) at low and high magnification. Slices from different areas were stained in parallel and images were acquired with identical settings.
B Fluorescence intensity of DISC1 immunolabeling in OB, CA1, and PFC in P9-10 WT (n=4) and GE (n=4) mice.
C Top, coronal section of OB from a P10 WT mouse immunostained for DISC1. Bottom, spatially resolved DISC1 intensity in P9-10 WT (n=4) and GE (n=4) mice.
D Coronal section of OB from a P10 WT mouse immunostained for DISC1 with OB projection neurons labeled by injection of the retrograde tracer CTB555 into the piriform cortex.
Shaded areas in C correspond to standard error of the mean (SEM). Significant differences are indicated as *, **, *** for p<0.05, 0.01, 0.001, respectively. GL glomerular layer; GCL granule cell layer.

Reduced OB activity in immune-challenged Disc1$^{+/-}$ mice during development

To investigate developmental OB activity in GE mice, we performed *in vivo* electrophysiological recordings using multi-site silicon probes. We monitored endogenous and odor-evoked activity in the ventral OB of WT and GE mice at P8-10 (Fig 2A,B). The extracellular recordings were combined with respiration measurements using a pressure sensor. Both, WT and GE mice showed continuous activity in the local field potential (LFP) recorded in the OB with the typical dominant respiration rhythm (RR, 2-4 Hz) that reverses polarity at the MCL (Fig 2C). However, the power in RR and theta (4-12 Hz) frequency bands were significantly reduced in GE mice (RR $p=5.1x10^{-4}$, theta p=0.004), whereas the power in beta (12-30 Hz) was not significantly different (p=0.09) (Fig 2D). Further, the firing rate of single units in the OB was reduced in GE mice, particularly for neurons in the MCL (MCL p=0.023; GCL p=0.51), indicating a reduction in the activity of OB projection neurons in the absence of odor stimulation (Fig 2E).

Next, we used the respiration measurement for closed-loop respiration-triggered odor stimulation to investigate odor-evoked activity in the OB of WT and GE mice. Odor stimulation

with the pure odorants isoamyl acetate or ethyl butyrate (1% v/v in mineral oil) was triggered by exhalations to guarantee for stable odor presentation at the subsequent inhalation. Odor presentation induced strong activation of the OB in WT and GE mice (Fig 2F). In contrast to endogenous activity, odor-evoked activity was similar for WT and GE mice across all frequency bands (Isoamyl acetate: RR p=0.088, theta p=0.36, beta p=0.32; Ethyl butyrate: RR p=0.12, theta p=0.29, beta p=0.39) (Fig 2G).

Notably, mice that only carry the genetic mutation (G) had a similar reduction to GE mice in the power of endogenous OB activity (G to WT: RR p=0.015, theta p=0.085, beta p=0.58; G to GE: RR p=0.75, theta p=0.82, beta p=0.69), whereas OB activity in mice that only received the environmental hit (E) of maternal immune activation was comparable to WT controls (E to WT: RR p=0.64, theta p=0.48, beta p=0.060; E to GE: RR p=0.056, theta p=0.82, beta p=0.26) (Fig 3).

Thus, odor stimulation evokes activity in the OB of GE mice that is similar to WT controls whereas endogenous activity in the absence of odor stimulation is significantly reduced in GE mice.

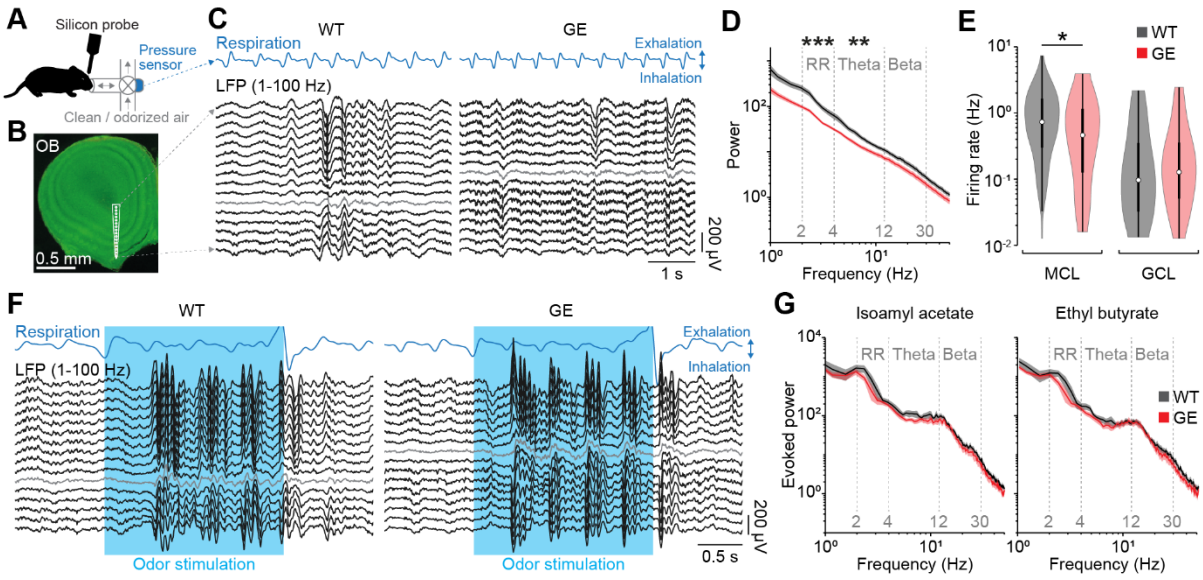

Fig 2. Reduced endogenous, but normal odor-evoked activity in the OB of immune-challenged *Disc1*$^{+/-}$ mice at P8-10.

A Experimental setup for recordings of endogenous and respiration-triggered odor-evoked activity in the OB of P8-10 mice.

B Example coronal section with a reconstruction of the DiI-labeled silicon probe tip in the ventral OB.

C Example extracellular recording of endogenous activity from the ventral OB of a P10 WT and GE mouse using a silicon probe with 16 recording sites spanning across the MCL (gray). Down- and upward deflections on the respiration trace from the pressure sensor indicate inhalation and exhalation, respectively.

D Power spectra of endogenous OB activity in P8-10 WT (n=17) and GE (n=14) mice.

E Firing rate of endogenous OB activity in P8-10 WT and GE mice for units recorded in MCL (WT n=172, GE n=49 units) and GCL (WT n=55, GE n=38 units).

F Same as C for odor-evoked activity.

G Power spectra of odor-evoked OB activity in P8-10 WT (n=11) and GE (n=11) mice.

Shaded areas in D,G correspond to SEM. Significant differences are indicated as *, **, *** for p<0.05, 0.01, 0.001, respectively.

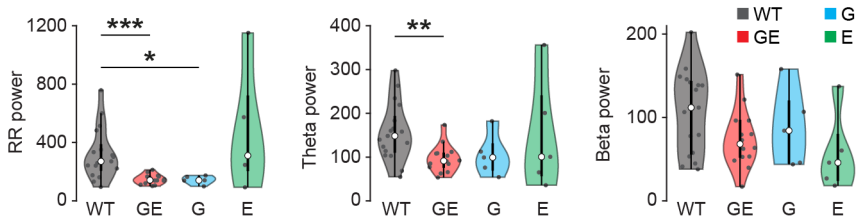

Fig 3. Reduced endogenous OB activity in *Disc1*$^{+/-}$, but not in immune-challenged mice at P8-10.

Power of endogenous OB activity quantified in different frequency bands (left, RR; middle, theta; right, beta) in P8-10 WT (n=17), GE (n=14), G (n=5), and E (n=5) mice.

Significant differences are indicated as *, **, *** for p<0.05, 0.01, 0.001, respectively.

Reduced OB activity results in weaker drive of the hippocampal-prefrontal network

Does altered activity in the OB of GE mice affect activity in downstream areas? To address this question, we performed simultaneous recordings from OB, CA1 of the intermediate hippocampus, and the medial PFC of P8-10 WT and GE mice (Fig 4A,B). While OB activity was already continuous at this age, CA1 and PFC showed discontinuous patterns of electrical activity (Fig 4C) characteristic for this age [12]. As reported in our previous publications [35,36], prefrontal LFP power in theta and beta frequency range was reduced (theta $p=8.6x10^{-4}$, beta p=0.0094) in GE mice when compared to WT controls, whereas no differences were detected for CA1 (theta p=0.19 , beta p=0.49) (Fig 4D). Of note, the power in RR frequency band was reduced in both areas (CA1 p= 0.015, PFC p=0.0016) for GE mice in line with reduced RR power in the OB. Firing rates of single units in CA1 (p=0.41) and PFC (p=0.65) were similar for WT and GE (Fig 4E). In this study, mostly deep layers of the PFC were recorded, which explains the lack of altered firing rates that are characteristic for prefrontal layer 2/3 in neonatal GE mice [36].

Next, we tested whether there is a difference in the propagation of odor-evoked activity to the hippocampal-prefrontal network in GE mice. Odor stimulation evoked pronounced activation in CA1 and PFC of WT and GE mice (Fig 4F). As for OB, we found no significant differences for odor-evoked activity in CA1 (RR p=0.92, theta p=0.86, beta p= 0.75) and PFC (RR p=0.062, theta p=0.28, beta p= 0.55) of P8-10 WT and GE mice (Fig 4G).

Thus, similar to the OB, endogenous activity in CA1 and PFC of P8-10 GE mice is decreased, yet odor-induced activity is similar to age-matched WT controls.

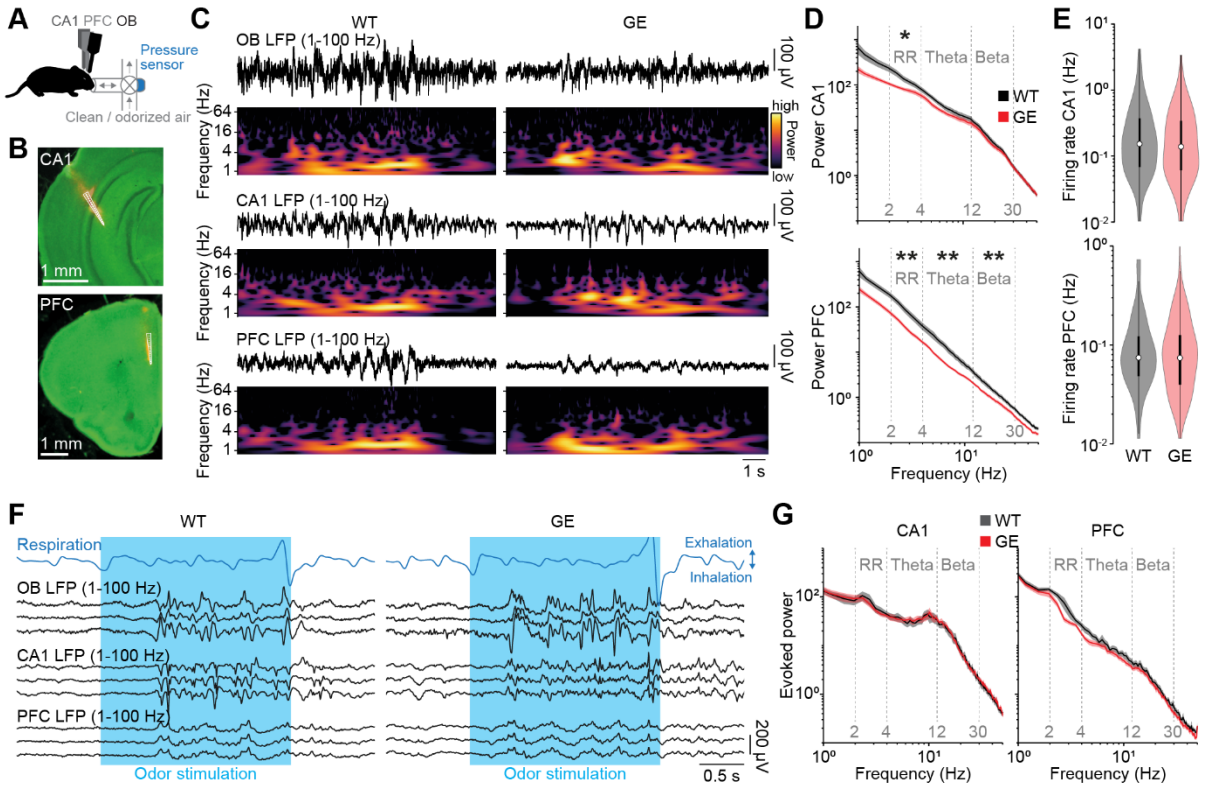

Fig 4. Reduced activity in the hippocampal-prefrontal network in immune-challenged *Disc1*$^{+/-}$ mice at P8-10.

A Experimental setup for triple recordings of endogenous and respiration-triggered odor-evoked activity in OB, CA1, and PFC of P8-10 mice.

B Example coronal sections with a reconstruction of the DiI-labelled silicon probe tips in CA1 of the intermediate hippocampus (top) and the medial part of the PFC (bottom).

C Examples of endogenous LFP activity recorded simultaneously from OB, CA1, and PFC of a P10 WT and GE mouse and the corresponding wavelet spectra.

D Power spectra of endogenous CA1 and PFC activity in P8-10 WT (CA1 n=15, PFC n=14) and GE (CA1 n=14, PFC n=14) mice.

E Firing rate of endogenous CA1 and PFC single unit activity in P8-10 WT (CA1 n=270, PFC n=167 units) and GE (CA1 n=182, PFC n=153 units) mice.

F Examples of odor-evoked LFP activity recorded simultaneously from OB, CA1, and PFC of a P10 WT and GE mouse.

G Power spectra of odor-evoked CA1 and PFC activity in P8-10 WT (n=11) and GE (n=11) mice.

Shaded areas in D,G correspond to SEM. Significant differences are indicated as *, **, *** for p<0.05, 0.01, 0.001, respectively.

Reduced RR power in OB, CA1, and PFC of GE mice during development suggests a possible reduction in the drive from the OB to the hippocampal-prefrontal network. To test this hypothesis, we used pairwise analyses of the simultaneously recorded areas to test their functional interactions in P8-10 WT and GE mice. First, we calculated the amplitude correlation of the LFP between areas as a measure for non-directed interactions that is based on the similarity of the amplitude fluctuations at a given frequency. We found a significant reduction in the interaction between OB and CA1 (RR p=0.018, theta p=0.012, beta p=0.49), OB and PFC (RR p=0.045, theta p=0.023, beta p=0.063), as well as CA1 and PFC (RR p=0.011, theta p=0.039, beta p=0.37) in RR and theta frequency but not in beta frequency for GE mice (Fig 5A). Next, we tested more directed measures of functional interactions.

Generalized partial directed coherence (gPDC), which assesses the directionality of pairwise interactions, revealed a strong reduction in the drive from OB to CA1 (RR p=0.011, theta p=0.0044 beta p=0.0037) and OB to PFC (RR p=0.011, theta p=0.0051 beta p=0.0016) in all frequency bands for GE mice (Fig 5B). The directed interaction from CA1 to PFC was reduced in RR (p=0.024) and theta (p=0.018) but not beta (p=0.76) frequency for GE mice, as previously reported [37]. Finally, we quantified phase-amplitude coupling (PAC) to evaluate the cross-frequency modulation of oscillatory power at fast frequencies (12-50 Hz) in CA1 and PFC by the slow RR generated in the OB. The strength of PAC from OB to CA1 and PFC was reduced in GE mice, as was the percentage of recordings with significant cross-frequency coupling (OB to CA1: WT 11 of 16, GE 5 of 14 mice; OB to PFC: WT 12 of 14, GE 10 of 14 mice) (Fig 5C,D).

Together, these findings show that the drive from OB to CA1 and PFC is reduced in GE mice.

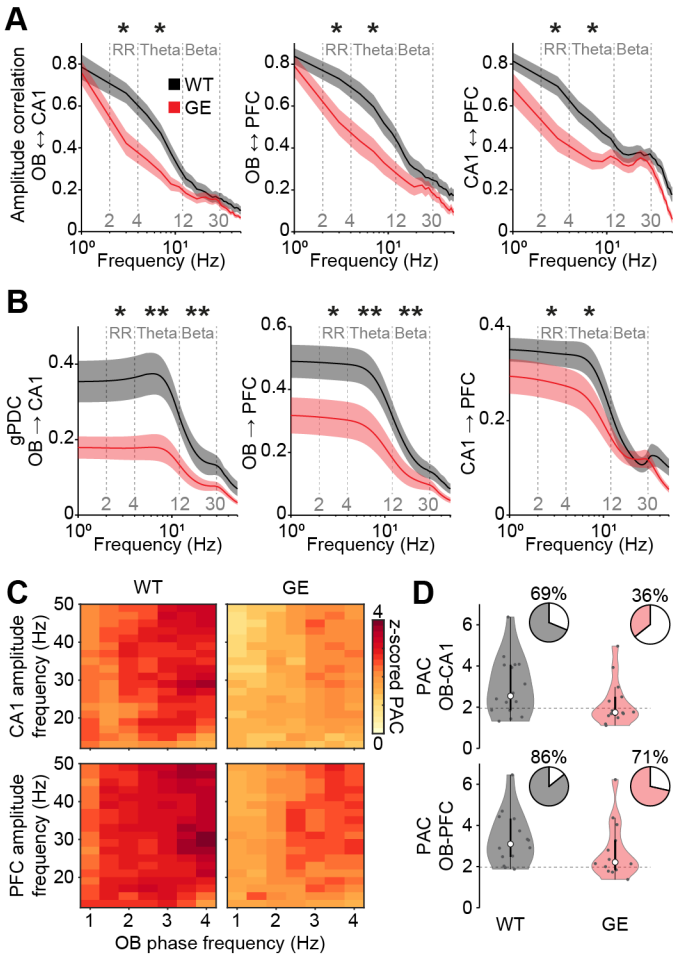

Fig 5. Reduced drive of the hippocampal-prefrontal network in immune-challenged *Disc1*$^{+/-}$ mice at P8-10.

A Frequency-resolved amplitude correlation between OB-CA1 (WT n=16, GE n=14), OB-PFC (WT n=14, GE n=14), and CA1-PFC (WT n=13, GE n=14) for P8-10 WT and GE mice.

B Frequency-resolved gPDC from OB to CA1 (WT n=16, GE n=14), from OB to PFC (WT n=14, GE n=14), and from CA1 to PFC (WT n=13, GE n=14) for P8-10 WT and GE mice.

C Color-coded average PAC of CA1 (WT n=16, GE n=14) and PFC (WT n=14, GE n=14) LFP amplitude at fast frequencies (12-50 Hz) to slow frequency oscillations (1-4 Hz) in OB for P8-10 WT and GE mice.

D Z-scored PAC of CA1 and PFC LFP amplitude at fast frequencies to slow frequencies in the OB for P8-10 WT and GE mice. Pie charts show the percentage of recordings with significant coupling. Dotted lines correspond to a z-score of 1.96 indicating the significance level.

Shaded areas in A,B correspond to SEM. Significant differences are indicated as *, **, *** for p<0.05, 0.01, 0.001, respectively.

Normal odor detection, but impaired odor memory in immune-challenged Disc1$^{+/-}$ mice

Normal propagation of odor-evoked activity from OB to the hippocampal-prefrontal network suggests that GE mice might have normal odor processing during development. To address this hypothesis, we recorded ultrasonic vocalizations (USV) of P9 WT and GE mice when

exposed to the odorant citral. Citral triggers an innate aversive response and reduces USV calls in neonatal mice, similar to the odor of adult males [45]. Pups were placed in a small chamber with a continuous flow of clean air for a baseline period after which citral was added to the airstream (Fig 6A-C). This procedure was repeated with increasing concentrations of citral. While concentrations of 0.0001% (WT p=0.50, GE p=0.17) and 0.01% (WT p=0.37, GE p=0.40) of citral (v/v in mineral oil) did not reduce call rates, both, WT and GE mice similarly reduced their call rate in response to citral at 1% (WT $p=1.1x10^{-4}$, GE $p=3.4x10^{-6}$, WT vs. GE p=0.32) (Fig 6D).

Thus, simple odor detection is not impaired in developing GE mice, consistent with normal odor-evoked activity.

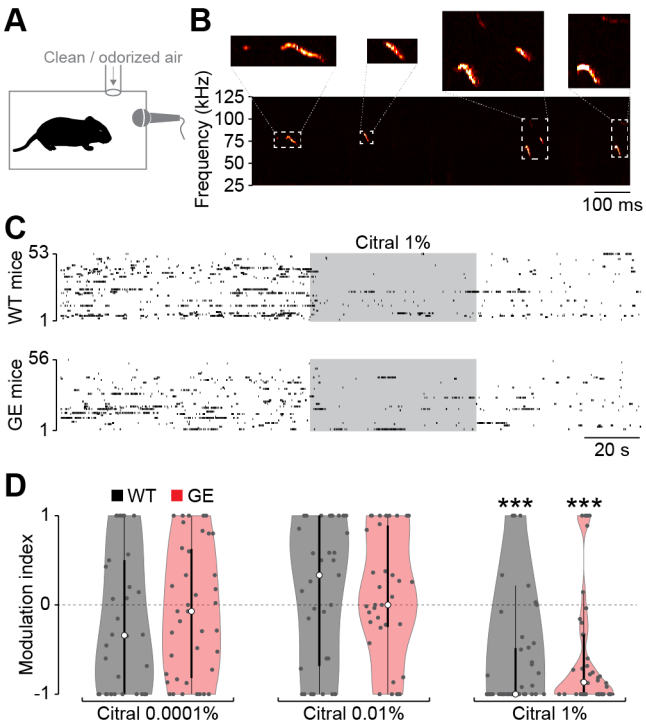

Fig 6. Odor detection is intact in immune-challenged *Disc1*$^{+/-}$ mice at P9.
A Experimental setup for USV recordings during odor exposure.
B Example spectrogram of USVs of a P9 mouse.
C Raster plot of USV suppression in response to the odorant citral for P9 WT (n=53) and GE (n=56) mice. Each line represents one mouse.
D Modulation index of USV numbers in response to the odorant citral at different concentrations.
Significant differences are indicated as *, **, *** for p<0.05, 0.01, 0.001, respectively.

We recently reported that transient inhibition of OB outputs from P8 to P10 in WT mice perturbs the functional maturation of the hippocampal formation and results in long-lasting cognitive deficits [23]. Thus, we hypothesized that the reduced endogenous OB activity and drive to the hippocampal-prefrontal network in developing GE mice might cause similar impairments. We used neonatal odor learning, a one-trial associative odor learning task for mouse pups [46], to test the learning and memory abilities in P10-11 WT and GE mice (Fig 7A). For this test, the dam was separated from the pups for 2 hours. Subsequently, a novel odor was applied to the teats before the dam was returned to the pups. The separation period guarantees feeding of the pups soon after odor application such that an association between food consumption and the odor can be formed. After a second separation period, pups were tested in an odor-place preference test with the learned test odor and a novel control odor (Fig 7B). Isoamyl acetate and ethyl butyrate (1% in mineral oil) were randomly assigned as test and control odor for each litter and the position of the test odor was randomized for each pup.

Both, WT and GE mice spend more time on the side of the test odor when pure odors were presented in the odor-place preference test (WT p=0.0075, GE p=0.021) and no difference was found between the groups (p=0.73) (Fig 7C). To increase the difficulty of the test, mice were presented with a mixture of test and control odors during the odor-place

preference test. Interestingly, only WT controls were able to distinguish the learned test odor at a mixture of 90/10% (WT p=0.015, GE p=0.31) but there was no significant group difference for WT and GE mice (p=0.39). Neither WT nor GE mice showed a place preference when odors were presented at a mixture of 80/20% (WT p=0.48, GE p=0.22). These results indicate that odor-learning is not impaired in GE mice at P10. However, when the odor-place preference test was done with a 24h delay period after neonatal odor learning, WT pups strongly preferred the learned test odor (p=0.012), whereas GE mice did not distinguish between test and control odor (p=0.18) and their performance was significantly reduced compared to WT mice (p=0.0026) (Fig 7D).

Together, these data revealed that odor detection and learning are largely normal in developing GE mice, whereas their long-term memory is impaired.

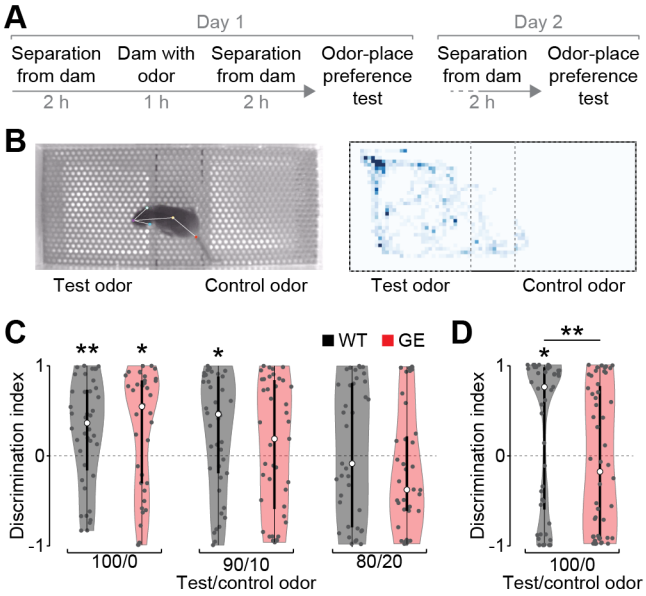

Fig 7. Impaired long-term odor-memory in immune-challenged *Disc1*$^{+/-}$ mice at P10/11.
A Timeline of neonatal odor learning and odor-place preference test for P10-11 mice.
B Left, example image of a P10 mouse in the odor-place preference test chamber. Right, example color-coded position of a mouse's nose traced by DeepLabCut during the odor-place preference test.
C Discrimination index of test and control odor in the odor-place preference test on the same day of neonatal odor learning for P10 WT and GE mice. Test and control odors were presented pure (100/0, WT n=40, GE n=38 mice) or mixed (90/10, WT n=42, GE n=41 mice; 80/20, WT n=37, GE n=36 mice).
D Discrimination index of test and control odor in the odor-place preference test the day after neonatal odor learning for P11 WT (n=57) and GE (n=52) mice.
Significant differences are indicated as *, **, *** for p<0.05, 0.01, 0.001, respectively.

Discussion

In this study, we examined early OB activity and its influence on developing hippocampal-prefrontal networks in GE mice. We found strong DISC1 expression in OB projection neurons during development, which was significantly reduced in GE mice. GE pups displayed reduced endogenous activity in the OB, whereas odor-evoked activity was comparable to WT controls. Correspondingly, the drive from the OB to the hippocampal-prefrontal network was reduced for endogenous activity, but the propagation of odor-evoked activity to HP and PFC was not altered. Consistent with these findings, odor detection and learning were not affected in GE

mouse pups, but their long-term odor memory was impaired. We conclude that reduced endogenous activity in the OB contributes to the altered maturation of the hippocampal-prefrontal network as well as memory deficits in GE mice.

During development, endogenous and sensory-evoked activity is required for the refinement of immature neuronal networks. Neuronal activity influences a range of developmental processes such as neuronal survival and dendritic growth, as well as synapse formation and pruning [1–3,10]. The endogenous and odor-induced OB activity is a major drive for developing hippocampal-prefrontal networks [18,22,47]. Transient inhibition of OB outputs at the beginning of the second postnatal week disrupts the functional maturation in the hippocampal formation, which causes long-lasting deficits in cognitive abilities [23]. Here, we show that the reduction of endogenous activity in the OB of GE mice appears to have similar consequences for the maturation of the hippocampal-prefrontal network. We found a significant reduction in the activity of OB projection neurons and a concurrent decrease in the coordinated activity in slow oscillatory rhythms in GE mice. Particularly, the power in RR, oscillatory activity within 2-4 Hz, was significantly reduced in OB, as well as in CA1 and PFC. This rhythm is driven by repetitive input to the OB generated by the inhalation-exhalation cycle and coordinates activity in downstream areas in neonatal and adult mice [18,22,48–50]. Reduced coordination of activity in CA1 and PFC as a result of a reduced coordination of OB activity by respiration in GE mice might underlie the detrimental effect on the maturation of the hippocampal-prefrontal network. Interestingly, the single-hit mouse model carrying the genetic disruption of *Disc1*$^{+/-}$ without the environmental hit showed a similar reduction of RR power in OB, indicating that the genetic deficit alone is sufficient for RR impairment. In contrast, oscillatory activity in CA1 and PFC is only affected when the *Disc1*$^{+/-}$ mutation is combined with maternal immune activation [51]. This distinction might be linked to the strong expression of DISC1 in the developing OB of WT mice.

DISC1 is also expressed in CA1 and PFC during development and previous studies found that specific knockdown of DISC1 in these areas in combination with maternal immune activation suffices to impair hippocampal-prefrontal activity [52,53]. However, strong DISC1 expression in OB projection neurons and high levels of OB activity during development in WT mice indicate a particular role of reduced OB activity in disturbed maturation of the hippocampal-prefrontal network in GE mice. The clear directionality in the drive of activity from OB to CA1 and PFC is consistent with anatomical data showing that feedback projections to the OB develop late and are still sparse at the beginning of the second postnatal week (Kostka & Bitzenhofer, 2022).

The axons of OB projection neurons are bundled in the lateral olfactory tract that distributes olfactory information to a range of brain areas [19]. While the OB has no direct projections to CA1 and PFC in mice, strong projections through the piriform cortex and the lateral entorhinal cortex provide a short pathway from the OB to the hippocampal-prefrontal network. This pathway is functional early during development [18,22,47] and, notably, impaired activity in the lateral entorhinal cortex has been found in GE mice [37]. In adult mice, inhibition of the lateral entorhinal cortex impairs performance in odor discrimination tasks [54] and odor-context learning [55]. This is not to say that odor detection or discrimination happens in the lateral entorhinal cortex but it shows that this pathway from OB to the hippocampal-prefrontal network is critical for the execution of odor-related tasks. Parallel pathways, such as direct projections from the anterior olfactory nucleus and the lateral entorhinal cortex to the PFC [37,56], might provide alternative routes for olfactory information to higher associative areas. However, the pathway through the lateral entorhinal cortex might be particularly vulnerable to reduced OB activity during early postnatal development as indicated by lasting

morphological and functional alterations of entorhinal neurons after transient inhibition of OB projection neurons [23], as well as in GE mice [57].

For now, we can only speculate how these findings relate to deficits of the olfactory system reported for neuropsychiatric disorders. Olfactory impairment has been suggested as an early indicator for several neuropsychiatric disorders, such as schizophrenia and psychosis [26–28]. Patients with first episode psychosis were shown to display deficits in odor identification tasks, and a reduced OB volume and inflammation of the olfactory epithelium have been associated with schizophrenia [28,30]. We found largely normal odor detection and odor learning in GE mice consistent with normal odor-evoked activity during development, but long-term odor memory was impaired. More rigorous behavioral testing might reveal subtle olfactory dysfunctions early on but the options for behavioral tests in neonatal mice are limited. Alternatively, altered functional maturation of the OB and the feedback projections from higher association areas might accumulate throughout development and only result in olfactory deficits later in life. Future investigations deepening the present approaches could provide valuable insights on how olfactory deficits might act as valuable early diagnostic markers in neuropsychiatric disorders.

Materials and methods

Ethical approval

All experiments were performed in compliance with German laws and guidelines of the European Union for the use of animals in research (EU Directive 2010/63/EU) and were approved by the local ethical committee (Behörde für Gesundheit und Verbraucherschutz Hamburg, G17/015, N18/015).

Animals

Timed-pregnant mice from the University Medical Center Hamburg-Eppendorf animal facility were housed individually in a 12/12 h light/dark cycle and had access to water and food ad libitum. The day of vaginal plug detection was defined as gestational day 0.5, and the day of birth was defined as postnatal day (P)0. Experiments were performed on pups of both sexes during neonatal development (i.e. P8–P11).

Pregnant *Disc1* mice (B6.129S6-Disc1^{tm1Kara}) carrying a mutation resulting in a truncated transcript on a C57BL6/J background [32] received viral RNA mimetic poly(I:C) (25 mg/kg) injected intraperitoneally (i.p.) at gestational day 9.5 to induce maternal immune activation. Immune-challenged *Disc1*$^{+/-}$ mice (referred to as GE) combine genetic and environmental risk factors in the pathogenesis of neuropsychiatric disorders. Offspring of C57BL/6J mice were used as wild-type control animals (referred to as WT).

Histology

P9-10 mice were anesthetized with 10% ketamine (aniMedica, Germany) / 2% xylazine (WDT, Germany) in 0.9% NaCl (10 µg/g body weight, intraperitoneal) and transcardially perfused with 4% paraformaldehyde (Histofix, Carl Roth, Germany). Brains were removed and postfixed in 4% paraformaldehyde for 24 h. Brains were sectioned coronally with a vibratome at 100 µm for immunostaining.

Immunostaining. Free-floating slices were permeabilized and unspecific binding sites were blocked in PBS containing 0.8% Triton X-100 (Sigma-Aldrich, MO, USA), 5% normal goat serum, and 5% normal donkey serum (Jackson Immuno Research, PA, USA) for 1 h. Slices

were incubated with primary antibodies in 0.8% Triton X-100, 1% normal goat serum, and 1% normal donkey serum for 3d at 4°C. Subsequently, slices were washed in PBS and incubated with secondary antibodies for 3 h at room temperature. Slices were washed and transferred to glass slides, before being covered with Vectashield(Vectorlabs, CA, USA). Images of immunostainings were acquired with a confocal microscope (FV1000, Olympus, Japan). Images were processed and analyzed with ImageJ.
Retrograde tracing. P5 mice were injected with the retrograde tracer CTB555 (200 nl at 100 nl/min, cholera toxin subunit B, Alexa Fluor 455 conjugate) into the piriform cortex under isoflurane anesthesia (induction: 5%, maintenance: 2%). Pups were transcardially perfused and brains were removed for immunostaining at P10.

Surgical procedure for electrophysiology

For *in vivo* electrophysiological recordings, P8-10 mice underwent surgery under isoflurane anesthesia (induction: 5%, maintenance: 2%). The skin above the skull was removed and local anesthetic (0.5% bupivacaine/1% lidocaine) was applied on the neck muscles. Two plastic bars were fixed on the nasal and occipital bones with dental cement. Craniotomies of about 0.5 mm diameter were performed above the right OB (0.5-0.8 mm anterior to the frontonasal suture, 0.5 mm lateral to the internasal suture), the CA1 subdivision of the intermediate hippocampus (2.5 mm anterior to lambda, 3.5 mm lateral to the midline), and the medial part of the PFC (0.5 mm anterior to bregma, 0.1-0.5 mm lateral to the midline). Throughout surgery, recovery, and recording mice were kept on a heating blanket at 37°C.

Electrophysiological recordings

Extracellular recordings were performed simultaneously from the ventral OB, hippocampal CA1, and PFC in non-anesthetized P8-10 mice. For this, one-shank silicon probes (NeuroNexus, MI, USA) with 16 recording sites (50 µm inter-site spacing) were inserted into OB (0.5-1.8 mm deep, angle 0°), CA1 (1.3-1.9 mm deep, angle 20°), and PFC (1.8-2.1 mm deep, angle 0°). Before insertion, the electrodes were covered with DiI (1,1'-Dioctadecyl-3,3,3',3'-tetramethylindocarbocyanine perchlorate, Molecular Probes, Eugene, OR) for confirmation of electrode position post mortem. A silver wire was inserted into the cerebellum and served as ground and reference electrode. A recovery period of 20 min after the insertion of electrodes was provided before data acquisition. Extracellular signals were band-pass filtered (0.1–9000 Hz) and digitized (32 kHz) with a multichannel extracellular amplifier (Digital Lynx SX; Neuralynx, Bozeman, MO, USA) and the Cheetah acquisition software (Neuralynx). After recordings, mice were deeply anesthetized with 10% ketamine/2% xylazine in 0.9% NaCl solution (10 µg/g body weight, i.p.) and transcardially perfused with Histofix (Carl Roth, Karlsruhe, Germany) containing 4% paraformaldehyde for subsequent identification of electrode positions in coronal slices.

Olfactory stimulation

A custom-made, Arduino-controlled olfactometer with a constant stream of clean air (0.9 L/min) to the nose was used to present odors to the animals. Odors were presented for 2 s triggered by the respiration cycle of mice to ensure constant odor concentration at the first odor inhalation. Two different odors (ethyl butyrate and isoamyl acetate, 1% in mineral oil) were delivered in a randomized order for 40 repetitions each.

Analysis of electrophysiological data

Electrophysiological data were analyzed with custom-written algorithms in Matlab R2021a environment. For LFP analysis data were band-passfiltered (1-100 Hz) using a phase preserving third-order Butterworth filter. For LFP data recorded in the OB, the recording site centered in the EPL was used, whereas, for the analysis of spiking activity, recording sites in the MCL or GCL were considered. For the analysis of hippocampal LFP, a recording site located in CA1 below the pyramidal layer was selected, while for the analysis of spiking activity, all recording sites located in CA1 were used. For LFP analysis in the PFC, a recording site centered in the prelimbic region was considered and spiking activity from all recording sites was included.

Power spectral density. Power spectral density was calculated using Welch's method with non-overlapping windows of 2 s for endogenous activity or for a 2 s window for odor stimulation. Time-frequency power plots were calculated with a continuous wavelet transform (Morlet wavelet). Frequency bands for statistical comparisons were defined as RR (2-4 Hz), theta (4-12 Hz) and beta (12-30 Hz).

Frequency resolved amplitude correlation. LFP from OB, CA1 and PFC was band-pass filtered in frequency bins of 2 Hz from 1 to 30 Hz and Hilbert transformed to extract the absolute amplitude. Subsequently, pairwise Pearson correlation coefficients of frequency resolved envelopes were calculated for OB, CA1, and PFC.

Generalized partial directed coherence. gPDC was calculated in the frequency domain to investigate the directional interaction between areas. This linear Granger causality measure is based on the decomposition of multivariate partial coherence computed from multivariate autoregressive models. LFP signals of 1 s length were denoised using the MATLAB wavelet toolbox (ddencmp.m and wdencmp.m) before gPDC was calculated with a previously described algorithm [58].

Phase–amplitude coupling. Cross-frequency coupling was calculated between the phase of the slow frequency in OB and the amplitude at fast frequencies (12-80 Hz) in CA1 and PFC according to a previously described algorithm [59]. Band-pass filtered LFP was Hilbert transformed to extract the phase and amplitude. The amplitude of the 12 to 50 Hz filtered LFP in CA1 and PFC was determined at each phase of the filtered OB signal. PAC matrices were z-scored and the average was calculated for RR (2–4 Hz) phase to higher frequencies (13-50 Hz) coupling.

Spiking analysis. Single units were automatically detected and clustered using the python-based software klusta [60] and manually curated using phy (https://github.com/cortex-lab/phy). For OB recordings, units detected around the channel (+/1 1 channels) where the RR reverses in polarity were considered for MCL spiking activity, whereas units in channels >3 channels central from the MCL were considered for GCL spiking activity.

Behavior

Neonatal odor detection. The suppression of ultrasonic vocalizations (USVs) of neonatal mice when exposed to the odor citral was used to test for neonatal odor detection. For each test, a P9 mouse was removed from the home cage, placed in a soundproof test box, and allowed to accommodate for 120 s. Pressurized air was pumped through the box at a rate of 2 L/min. USVs were recorded with an ultrasonic microphone (Avisoft UltraSoundGate, Avisoft Bioacoustics) at a sampling rate of 250 kHz for 90 s with clean air, 60 s with citral, and 60 s of clean air, followed by a 60 s break. Each test consisted of three consecutive trials with

increasing concentration of citral at 10^{-4}, 10^{-2}, and 1% diluted in mineral oil. USVs from 25 to 125 kHz were detected using DeepSqueak [61].

Neonatal Odor Learning. Neonatal odor learning of P10 mice was assessed with a modified version of a previously established protocol [46]. For one-trial associative odor learning, the dam was removed from the home cage for 2 h before the test odor was applied to the teats of the dam with a saturated cotton swab and she was placed back to the home cage for 1 h. Isoamyl acetate and ethyl butyrate (1% mineral oil) were used randomly as test and control odors per litter. The dam was removed again for 2 h before the pups were tested in an odor place preference test. The test arena consisted of a rectangular acrylic chamber (17.5 × 6.5 × 6.5 cm) with metal grid flooring, divided into two 6.5 cm odor zones at the ends and a 4.5 cm neutral zone in the center. Odor zones were odorized by placing acrylic trays beneath the grid flooring with 500 µl of either the test odor or a control odor on a filter paper. Test and control odors were randomized between the two odor zones. For the test, a pup was placed in the center of the arena (i.e., neutral zone) and video-taped from above for 3 min using a camera (UI 2250-SE-M, IDS GMBH). Between each test, the chamber was cleaned with ethanol and allowed to dry. Odor place preference tests were performed with pure odors (1% in mineral oil) or odor mixtures (90/10, 80/20 test/control odor). Mice were tracked using DeepLabCut [62]. The time spent over the different zones was quantified and analyzed in Matlab.

To assess long-term neonatal odor memory, the dam was removed for 2 h on the following day (P11) and the odor place preference test was repeated with pure test versus control odor (1% in mineral oil).

Statistics

Statistical analysis was performed in Matlab R2021a environment. Data were tested for normal distribution. Paired and unpaired t-tests were used for normally distributed data, whereas non-parametric Wilcoxon rank sum and sign rank tests were used for non-normally distributed data to test for significant differences. Data are presented as violin plots or as mean ± SEM. Significance levels of $P < 0.05$ (*), $P < 0.01$ (**) or $P < 0.001$ (***) were considered.

Acknowledgements

We thank Dr. Joseph Gogos for providing the Disc1 mice. We thank A. Marquardt, A. Dahlmann, and P. Putthoff for excellent technical assistance.

References

1. Katz LC, Shatz CJ. Synaptic Activity and the Construction of Cortical Circuits. Science. 1996;274: 1133–1138. doi:10.1126/science.274.5290.1133
2. Kirkby LA, Sack GS, Firl A, Feller MB. A Role for Correlated Spontaneous Activity in the Assembly of Neural Circuits. Neuron. 2013;80: 1129–1144. doi:10.1016/j.neuron.2013.10.030
3. Kirischuk S, Sinning A, Blanquie O, Yang J-W, Luhmann HJ, Kilb W. Modulation of Neocortical Development by Early Neuronal Activity: Physiology and Pathophysiology. Frontiers in Cellular Neuroscience. 2017;11. Available: https://www.frontiersin.org/articles/10.3389/fncel.2017.00379
4. Hanganu-Opatz IL, Butt SJB, Hippenmeyer S, García NVDM, Cardin JA, Voytek B, et al. The Logic of Developing Neocortical Circuits in Health and Disease. J Neurosci. 2021;41: 813–822. doi:10.1523/JNEUROSCI.1655-20.2020
5. Hanganu IL, Ben-Ari Y, Khazipov R. Retinal Waves Trigger Spindle Bursts in the Neonatal Rat Visual Cortex. J Neurosci. 2006;26: 6728–6736. doi:10.1523/JNEUROSCI.0752-06.2006
6. Ackman JB, Burbridge TJ, Crair MC. Retinal waves coordinate patterned activity throughout the developing visual system. Nature. 2012;490: 219–225. doi:10.1038/nature11529
7. Clause A, Kim G, Sonntag M, Weisz CJC, Vetter DE, Rűbsamen R, et al. The Precise Temporal Pattern of Prehearing Spontaneous Activity Is Necessary for Tonotopic Map Refinement. Neuron. 2014;82: 822–835. doi:10.1016/j.neuron.2014.04.001
8. Kersbergen CJ, Babola TA, Rock J, Bergles DE. Developmental spontaneous activity promotes formation of sensory domains, frequency tuning and proper gain in central auditory circuits. Cell Reports. 2022;41: 111649. doi:10.1016/j.celrep.2022.111649
9. Medendorp WE, Bjorefeldt A, Crespo EL, Prakash M, Pal A, Waddell ML, et al. Selective postnatal excitation of neocortical pyramidal neurons results in distinctive behavioral and circuit deficits in adulthood. iScience. 2021;24: 102157. doi:10.1016/j.isci.2021.102157
10. Bitzenhofer SH, Pöpplau JA, Chini M, Marquardt A, Hanganu-Opatz IL. A transient developmental increase in prefrontal activity alters network maturation and causes cognitive dysfunction in adult mice. Neuron. 2021;109: 1350-1364.e6. doi:10.1016/j.neuron.2021.02.011
11. Benoit LJ, Holt ES, Posani L, Fusi S, Harris AZ, Canetta S, et al. Adolescent thalamic inhibition leads to long-lasting impairments in prefrontal cortex function. Nat Neurosci. 2022;25: 714–725. doi:10.1038/s41593-022-01072-y
12. Brockmann MD, Pöschel B, Cichon N, Hanganu-Opatz IL. Coupled oscillations mediate directed interactions between prefrontal cortex and hippocampus of the neonatal rat. Neuron. 2011;71: 332–347. doi:10.1016/j.neuron.2011.05.041
13. Ahlbeck J, Song L, Chini M, Bitzenhofer SH, Hanganu-Opatz IL. Glutamatergic drive along the septo-temporal axis of hippocampus boosts prelimbic oscillations in the neonatal mouse. Elife. 2018;7: e33158. doi:10.7554/eLife.33158
14. Logan DW, Brunet LJ, Webb WR, Cutforth T, Ngai J, Stowers L. Learned recognition of maternal signature odors mediates the first suckling episode in mice. Curr Biol. 2012;22: 1998–2007. doi:10.1016/j.cub.2012.08.041
15. Walz A, Omura M, Mombaerts P. Development and topography of the lateral olfactory tract in the mouse: Imaging by genetically encoded and injected fluorescent markers. Journal of Neurobiology. 2006;66: 835–846. doi:10.1002/neu.20266
16. Hirata T, Shioi G, Abe T, Kiyonari H, Kato S, Kobayashi K, et al. A Novel Birthdate-Labeling Method Reveals Segregated Parallel Projections of Mitral and External Tufted

Cells in the Main Olfactory System. eNeuro. 2019;6: ENEURO.0234-19.2019. doi:10.1523/ENEURO.0234-19.2019

17. Fletcher ML, Smith AM, Best AR, Wilson DA. High-Frequency Oscillations Are Not Necessary for Simple Olfactory Discriminations in Young Rats. J Neurosci. 2005;25: 792–798. doi:10.1523/JNEUROSCI.4673-04.2005
18. Gretenkord S, Kostka JK, Hartung H, Watznauer K, Fleck D, Minier-Toribio A, et al. Coordinated electrical activity in the olfactory bulb gates the oscillatory entrainment of entorhinal networks in neonatal mice. PLoS Biol. 2019;17: e2006994. doi:10.1371/journal.pbio.2006994
19. Igarashi KM, Ieki N, An M, Yamaguchi Y, Nagayama S, Kobayakawa K, et al. Parallel Mitral and Tufted Cell Pathways Route Distinct Odor Information to Different Targets in the Olfactory Cortex. J Neurosci. 2012;32: 7970–7985. doi:10.1523/JNEUROSCI.0154-12.2012
20. Witter MP, Doan TP, Jacobsen B, Nilssen ES, Ohara S. Architecture of the Entorhinal Cortex A Review of Entorhinal Anatomy in Rodents with Some Comparative Notes. Front Syst Neurosci. 2017;11: 46. doi:10.3389/fnsys.2017.00046
21. Kostka JK, Bitzenhofer SH. How the sense of smell influences cognition throughout life. Neuroforum. 2022;28: 177–185. doi:10.1515/nf-2022-0007
22. Kostka JK, Hanganu-Opatz IL. Olfactory-driven beta band entrainment of limbic circuitry during neonatal development. The Journal of Physiology. 2023;601: 3605–3630. doi:10.1113/JP284401
23. Chen Y-N, Kostka JK, Bitzenhofer SH, Hanganu-Opatz IL. Olfactory bulb activity shapes the development of entorhinal-hippocampal coupling and associated cognitive abilities. Current Biology. 2023;0. doi:10.1016/j.cub.2023.08.072
24. Chini M, Hanganu-Opatz IL. Prefrontal Cortex Development in Health and Disease: Lessons from Rodents and Humans. Trends Neurosci. 2021;44: 227–240. doi:10.1016/j.tins.2020.10.017
25. Günther A, Hanganu-Opatz IL. Neuronal oscillations: early biomarkers of psychiatric disease? Frontiers in Behavioral Neuroscience. 2022;16. Available: https://www.frontiersin.org/articles/10.3389/fnbeh.2022.1038981
26. Turetsky BI, Moberg PJ, Owzar K, Johnson SC, Doty RL, Gur RE. Physiologic impairment of olfactory stimulus processing in schizophrenia. Biological Psychiatry. 2003;53: 403–411. doi:10.1016/S0006-3223(02)01865-6
27. Nguyen AD, Shenton ME, Levitt JJ. Olfactory dysfunction in schizophrenia: a review of neuroanatomy and psychophysiological measurements. Harv Rev Psychiatry. 2010;18: 279–292. doi:10.3109/10673229.2010.511060
28. Hasegawa Y, Ma M, Sawa A, Lane AP, Kamiya A. Olfactory impairment in psychiatric disorders: Does nasal inflammation impact disease psychophysiology? Transl Psychiatry. 2022;12: 1–11. doi:10.1038/s41398-022-02081-y
29. Herrmann T, Koeppel C, Linn J, Croy I, Hummel T. Olfactory brain activations in patients with Major Depressive Disorder. Sci Rep. 2023;13: 10072. doi:10.1038/s41598-023-36783-0
30. Yang K, Hasegawa Y, Bhattarai JP, Hua J, Dower M, Etyemez S, et al. Inflammation-related pathology in the olfactory epithelium: its impact on the olfactory system in psychotic disorders. Mol Psychiatry. 2024; 1–12. doi:10.1038/s41380-024-02425-8
31. Uhlhaas PJ, Singer W. Abnormal neural oscillations and synchrony in schizophrenia. Nat Rev Neurosci. 2010;11: 100–113. doi:10.1038/nrn2774
32. Kvajo M, McKellar H, Arguello PA, Drew LJ, Moore H, MacDermott AB, et al. A mutation in mouse Disc1 that models a schizophrenia risk allele leads to specific alterations in neuronal architecture and cognition. Proceedings of the National Academy of Sciences. 2008;105: 7076–7081. doi:10.1073/pnas.0802615105

33. Brandon NJ, Sawa A. Linking neurodevelopmental and synaptic theories of mental illness through DISC1. Nat Rev Neurosci. 2011;12: 707–722. doi:10.1038/nrn3120
34. Meyer U, Feldon J. To poly(I:C) or not to poly(I:C): Advancing preclinical schizophrenia research through the use of prenatal immune activation models. Neuropharmacology. 2012;62: 1308–1321. doi:10.1016/j.neuropharm.2011.01.009
35. Hartung H, Cichon N, De Feo V, Riemann S, Schildt S, Lindemann C, et al. From Shortage to Surge: A Developmental Switch in Hippocampal-Prefrontal Coupling in a Gene-Environment Model of Neuropsychiatric Disorders. Cereb Cortex. 2016;26: 4265–4281. doi:10.1093/cercor/bhw274
36. Chini M, Pöpplau JA, Lindemann C, Carol-Perdiguer L, Hnida M, Oberländer V, et al. Resolving and Rescuing Developmental Miswiring in a Mouse Model of Cognitive Impairment. Neuron. 2020;105: 60-74.e7. doi:10.1016/j.neuron.2019.09.042
37. Xu X, Song L, Kringel R, Hanganu-Opatz IL. Developmental decrease of entorhinal-hippocampal communication in immune-challenged DISC1 knockdown mice. Nat Commun. 2021;12: 6810. doi:10.1038/s41467-021-27114-w
38. Kamiya A, Kubo K, Tomoda T, Takaki M, Youn R, Ozeki Y, et al. A schizophrenia-associated mutation of DISC1 perturbs cerebral cortex development. Nat Cell Biol. 2005;7: 1167–1178. doi:10.1038/ncb1328
39. Mao Y, Ge X, Frank CL, Madison JM, Koehler AN, Doud MK, et al. Disrupted in Schizophrenia 1 Regulates Neuronal Progenitor Proliferation via Modulation of GSK3β/β-Catenin Signaling. Cell. 2009;136: 1017–1031. doi:10.1016/j.cell.2008.12.044
40. Ishizuka K, Kamiya A, Oh EC, Kanki H, Seshadri S, Robinson JF, et al. DISC1-dependent switch from progenitor proliferation to migration in the developing cortex. Nature. 2011;473: 92–96. doi:10.1038/nature09859
41. Hayashi-Takagi A, Takaki M, Graziane N, Seshadri S, Murdoch H, Dunlop AJ, et al. Disrupted-in-Schizophrenia 1 (DISC1) regulates spines of the glutamate synapse via Rac1. Nat Neurosci. 2010;13: 327–332. doi:10.1038/nn.2487
42. Ma L, Liu Y, Ky B, Shughrue PJ, Austin CP, Morris JA. Cloning and Characterization of Disc1, the Mouse Ortholog of DISC1 (Disrupted-in-Schizophrenia 1). Genomics. 2002;80: 662–672. doi:10.1006/geno.2002.7012
43. Schurov IL, Handford EJ, Brandon NJ, Whiting PJ. Expression of disrupted in schizophrenia 1 (DISC1) protein in the adult and developing mouse brain indicates its role in neurodevelopment. Mol Psychiatry. 2004;9: 1100–1110. doi:10.1038/sj.mp.4001574
44. Meyer KD, Morris JA. Immunohistochemical analysis of Disc1 expression in the developing and adult hippocampus. Gene Expression Patterns. 2008;8: 494–501. doi:10.1016/j.gep.2008.06.005
45. Lemasson M, Delbé C, Gheusi G, Vincent J-D, Lledo P-M. Use of ultrasonic vocalizations to assess olfactory detection in mouse pups treated with 3-methylindole. Behavioural Processes. 2005;68: 13–23. doi:10.1016/j.beproc.2004.09.001
46. Armstrong CM, DeVito LM, Cleland TA. One-Trial Associative Odor Learning in Neonatal Mice. Chem Senses. 2006;31: 343–349. doi:10.1093/chemse/bjj038
47. Kostka JK, Gretenkord S, Spehr M, Hanganu-Opatz IL. Bursting mitral cells time the oscillatory coupling between olfactory bulb and entorhinal networks in neonatal mice. J Physiol. 2020;598: 5753–5769. doi:10.1113/JP280131
48. Biskamp J, Bartos M, Sauer J-F. Organization of prefrontal network activity by respiration-related oscillations. Sci Rep. 2017;7: 45508. doi:10.1038/srep45508
49. Karalis N, Sirota A. Breathing coordinates cortico-hippocampal dynamics in mice during offline states. Nat Commun. 2022;13: 467. doi:10.1038/s41467-022-28090-5

50. Basha D, Chauvette S, Sheroziya M, Timofeev I. Respiration organizes gamma synchrony in the prefronto-thalamic network. Sci Rep. 2023;13: 8529. doi:10.1038/s41598-023-35516-7
51. Oberlander VC, Xu X, Chini M, Hanganu-Opatz IL. Developmental dysfunction of prefrontal-hippocampal networks in mouse models of mental illness. Eur J Neurosci. 2019;50: 3072–3084. doi:10.1111/ejn.14436
52. Xu X, Chini M, Bitzenhofer SH, Hanganu-Opatz IL. Transient Knock-Down of Prefrontal DISC1 in Immune-Challenged Mice Causes Abnormal Long-Range Coupling and Cognitive Dysfunction throughout Development. J Neurosci. 2019;39: 1222–1235. doi:10.1523/JNEUROSCI.2170-18.2018
53. Xu X, Song L, Hanganu-Opatz IL. Knock-Down of Hippocampal DISC1 in Immune-Challenged Mice Impairs the Prefrontal-Hippocampal Coupling and the Cognitive Performance Throughout Development. Cereb Cortex. 2021;31: 1240–1258. doi:10.1093/cercor/bhaa291
54. Bitzenhofer SH, Westeinde EA, Zhang H-XB, Isaacson JS. Rapid odor processing by layer 2 subcircuits in lateral entorhinal cortex. Uchida N, editor. eLife. 2022;11: e75065. doi:10.7554/eLife.75065
55. Persson BM, Ambrozova V, Duncan S, Wood ER, O'Connor AR, Ainge JA. Lateral entorhinal cortex lesions impair odor-context associative memory in male rats. Journal of Neuroscience Research. 2022;100: 1030–1046. doi:10.1002/jnr.25027
56. Moberly AH, Schreck M, Bhattarai JP, Zweifel LS, Luo W, Ma M. Olfactory inputs modulate respiration-related rhythmic activity in the prefrontal cortex and freezing behavior. Nat Commun. 2018;9: 1528. doi:10.1038/s41467-018-03988-1
57. Kringel R, Song L, Xu X, Bitzenhofer SH, Hanganu-Opatz IL. Layer-specific impairment in the developing lateral entorhinal cortex of immune-challenged Disc1+/- mice. J Physiol. 2023. doi:10.1113/JP283896
58. Baccalá LA, Sameshima K. Partial directed coherence: a new concept in neural structure determination. Biol Cybern. 2001;84: 463–474. doi:10.1007/PL00007990
59. Tort ABL, Komorowski R, Eichenbaum H, Kopell N. Measuring Phase-Amplitude Coupling Between Neuronal Oscillations of Different Frequencies. J Neurophysiol. 2010;104: 1195–1210. doi:10.1152/jn.00106.2010
60. Rossant C, Kadir SN, Goodman DFM, Schulman J, Hunter MLD, Saleem AB, et al. Spike sorting for large, dense electrode arrays. Nat Neurosci. 2016;19: 634–641. doi:10.1038/nn.4268
61. Coffey KR, Marx RG, Neumaier JF. DeepSqueak: a deep learning-based system for detection and analysis of ultrasonic vocalizations. Neuropsychopharmacol. 2019;44: 859–868. doi:10.1038/s41386-018-0303-6
62. Mathis A, Mamidanna P, Cury KM, Abe T, Murthy VN, Mathis MW, et al. DeepLabCut: markerless pose estimation of user-defined body parts with deep learning. Nat Neurosci. 2018;21: 1281–1289. doi:10.1038/s41593-018-0209-y

2.2.5 Preconfigured Architecture of the Developing Mouse Brain

Mattia Chini, Marilena Hnida, Johanna K. Kostka, **Yu-Nan Chen** and Ileana L. Hanganu-Opatz

Cell Reports 2024; DOI: 10.1016/j.celrep.2024.114267

Personal contribution

I performed part of *in vivo* electrophysiology experiments for neonatal OB.

I performed part of spike sorting for neonatal OB recordings.

I reviewed and commented on the manuscript.

Cell Reports

Article

Preconfigured architecture of the developing mouse brain

Graphical abstract

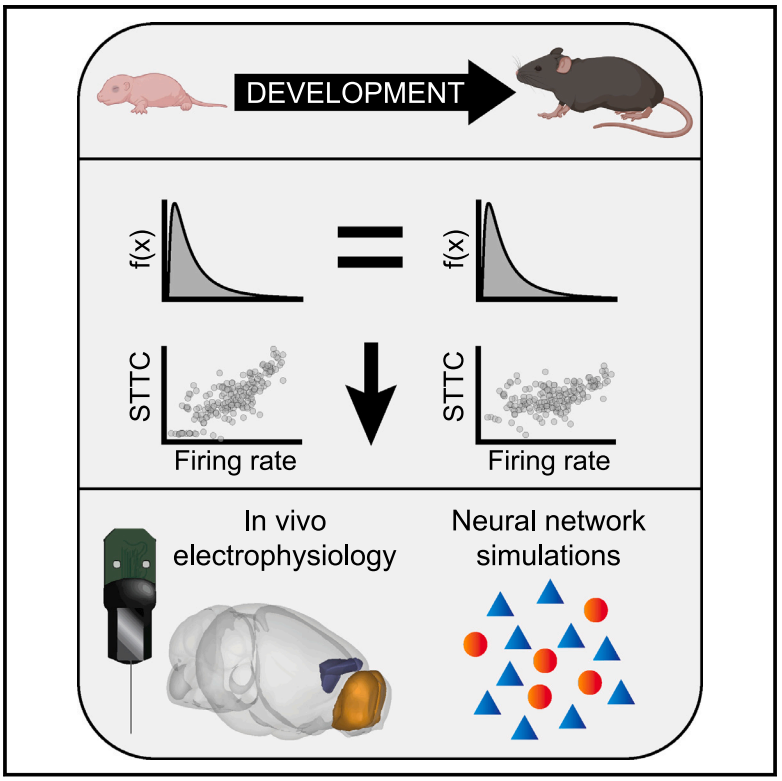

Highlights

- Single-unit parameters have a right-skewed and heavy-tailed distribution across development
- Synaptic parameters with this type of distribution are needed to stably model the data
- In early development, neurons display an oligarchical organization that decreases with age
- Inhibitory synaptic plasticity recapitulates the decrease in the oligarchical organization

Authors

Mattia Chini, Marilena Hnida, Johanna K. Kostka, Yu-Nan Chen, Ileana L. Hanganu-Opatz

Correspondence

mattia.chini@zmnh.uni-hamburg.de

In brief

Chini et al. show that the distribution shape of single-unit-related parameters is largely stable across the early development of cortical circuits. Using computational modeling, they predict that synaptic parameters have similar dynamics. Thus, they conclude that this aspect of cortical organization is preconfigured and experience independent.

Chini et al., 2024, Cell Reports *43*, 114267
June 25, 2024
https://doi.org/10.1016/j.celrep.2024.114267

CellPress

Cell Reports

CellPress
OPEN ACCESS

Article

Preconfigured architecture of the developing mouse brain

Mattia Chini,[1,2,*] Marilena Hnida,[1] Johanna K. Kostka,[1] Yu-Nan Chen,[1] and Ileana L. Hanganu-Opatz[1]
[1]Institute of Developmental Neurophysiology, Center for Molecular Neurobiology, University Medical Center Hamburg-Eppendorf, Hamburg, Germany
[2]Lead contact
*Correspondence: mattia.chini@zmnh.uni-hamburg.de
https://doi.org/10.1016/j.celrep.2024.114267

SUMMARY

In the adult brain, structural and functional parameters, such as synaptic sizes and neuronal firing rates, follow right-skewed and heavy-tailed distributions. While this organization is thought to have significant implications, its development is still largely unknown. Here, we address this knowledge gap by investigating a large-scale dataset recorded from the prefrontal cortex and the olfactory bulb of mice aged 4–60 postnatal days. We show that firing rates and spike train interactions have a largely stable distribution shape throughout the first 60 postnatal days and that the prefrontal cortex displays a functional small-world architecture. Moreover, early brain activity exhibits an oligarchical organization, where high-firing neurons have hub-like properties. In a neural network model, we show that analogously right-skewed and heavy-tailed synaptic parameters are instrumental to consistently recapitulate the experimental data. Thus, functional and structural parameters in the developing brain are already extremely distributed, suggesting that this organization is preconfigured and not experience dependent.

INTRODUCTION

In the adult brain, many structural and functional parameters follow right-skewed distributions with heavy right tails, such as the log-normal,[1,2] gamma,[3] or power law[4,5] distribution. A non-exhaustive list of parameters that is characterized by such distributions includes size and number of synapses[6–9]; size of post-synaptic currents[10–12]; diameter of axons[13]; density of neurons[14]; *in vivo* single-unit-activity (SUA) firing rates[15–17]; spike transmission probability[10,17]; pairwise correlations among spike trains[18]; and power of the local field potential (LFP),[19,20] electroencephalogram (EEG),[21–23] magnetoencephalogram (MEG),[22–24] and blood-oxygen-level-dependent (BOLD)[25] signals.

If a parameter follows such a distribution, it is implied that a large proportion of the data display small values that fall well below the mean. Conversely, extremely large values are more commonly observed than if they followed a narrower distribution such as the normal (or Gaussian), as is often implicitly assumed.[1,2] Thus, these distributions are characterized by high levels of inequality. We define such distributions as being "extreme."[26] It has been suggested that the extreme distribution of neural parameters might have several useful properties.[1,2,10,27] For instance, the log-normal distribution of synaptic sizes might promote the formation and propagation of neuronal sequences,[10,28] while at the same time optimizing storage capacity.[27] Moreover, the extreme distribution of firing rates might result in an environment with an optimal balance between a large amount of "specialist" neurons complemented by few "generalists." The first ones would only fire upon receiving a highly specific constellation of pre-synaptic inputs, and thereby have a spiking activity with unique and distinctive "interpretation" for post-synaptic partners. Conversely, generalist neurons would require less specific pre-synaptic inputs to generate a spike. This could allow such neurons to generalize over similar sensory stimuli and might therefore represent the brain's "best guess."[1,2] Overall, this organization is thought of producing a system that allows for concomitant specialization and flexibility, while limiting the number of energy-demanding high-firing-rate neurons.[10]

While it is widely accepted that the adult brain is an extreme environment, how this unfolds throughout development is still unclear. Two main competing hypotheses have been put forward. The "blank-slate model" posits that the developing brain is a *tabula rasa*, a blank slate that lacks a refined structure.[29] A corollary of this view is that structural and functional parameters in the developing brain should follow a narrow, thin-tailed distribution. Only upon developmental learning would the brain structure gradually become skewed, heavy tailed, and unequal, as reported for the adult brain. While this view is not often openly advocated for, it is often implied.[2,30,31] The competing theory is the "preconfigured brain hypothesis," which proposes that the developing brain is pre-packaged with non-random structure and already displays extreme distributions of structural and functional parameters. Consequently, this hypothesis implies that developmental learning should not fundamentally transform the brain architecture. Rather, learning is viewed as a matching process that associates pre-existing structure, which is

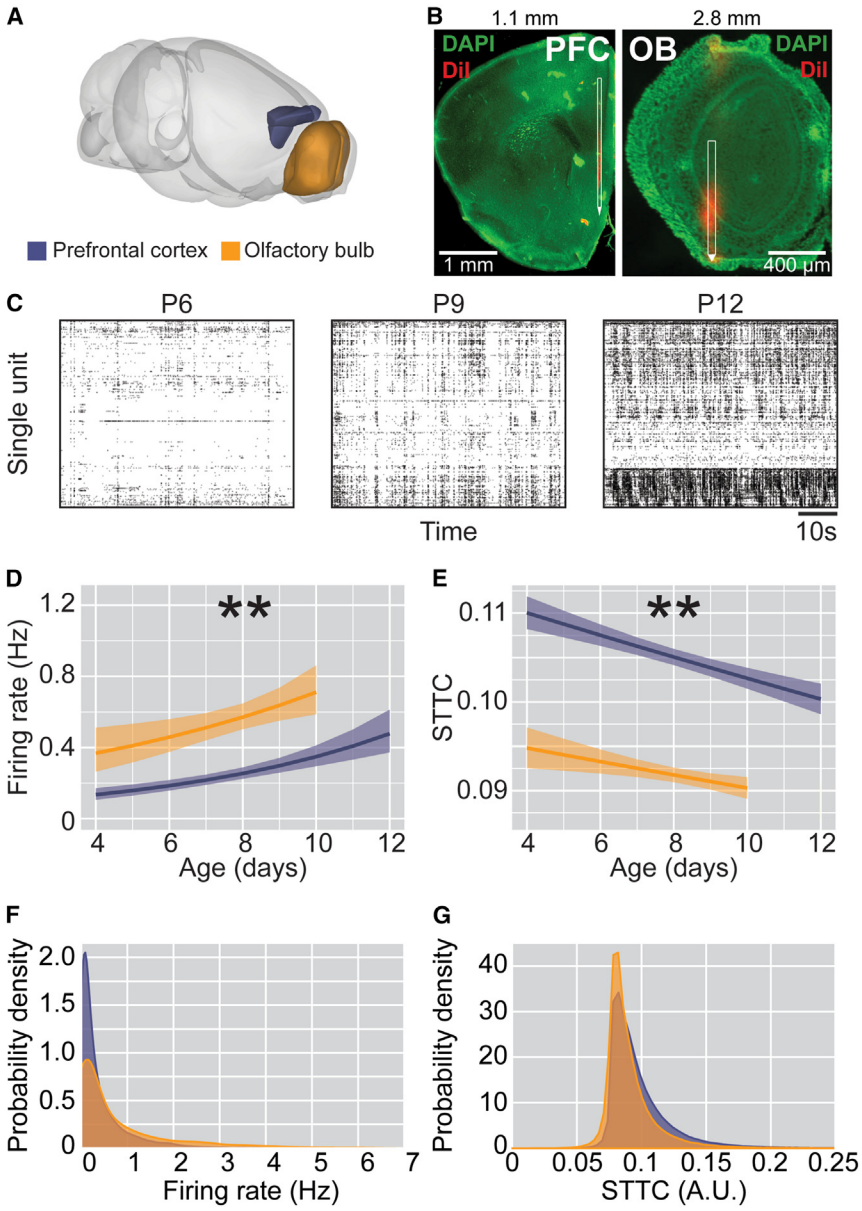

Figure 1. SUA firing statistics in the mouse PFC and OB across the first two postnatal weeks

(A) Schematic representation[46] of extracellular recordings in the PFC and OB of P4–12 mice.

(B) Digital reconstruction of the position of a DiI-labeled recording electrode in the PFC (left) and OB (right) with the antero-posterior distance from bregma (top) of a Nissl-stained coronal section (green) of a P9 and P10 mouse, respectively. Scale bar: 1 mm (left) and 400 μm (right).

(C) Representative raster plot of 1 min of SUA activity recorded in the PFC of a P6 (left), P9 (middle), and P12 (right) mouse.

(D) Line plot displaying the SUA firing rate of P4–12 mice (n = 278 mice and 14,357 single units). Color codes for brain region.

(E) Same as (D) for STTC (n = 278 mice and 654,335 spike train pairs).

(F) Probability density distribution for SUA firing rate in P4–12 mice. Color codes for brain region.

(G) Same as (F) for STTC. In (D) and (E) data are presented as mean and 95% confidence interval (CI). Asterisks in (D) and (E) indicate significant effect of age. **p < 0.01, generalized linear mixed-effect models.

initially devoid of meaning, with a behavioral output or a sensory sensation.[2,32–35]

To tease apart these two hypotheses, we investigated the *in vivo* development of brain activity in a large-scale dataset from unanesthetized postnatal day (P) 4–60 mice (n = 302 mice). The youngest mice in the dataset belong to a very immature developmental phase in which, even though neurons in the sensory systems are active, they mostly do not represent sensory information. An exception to this developmental dynamic is the olfactory system. From birth onward, rodents rely on olfaction for survival, as they actively employ olfactory cues to locate the dam's nipple.[36,37] Thus, in the present study, to control for the potential effect of developmental learning, we investigated the early developing olfactory bulb (OB) and the prefrontal cortex (PFC), the cortical region with the most protracted development.[38] We show that, in both brain regions, the skewness, tailedness, and inequality of the distributions of *in vivo* SUA firing rates and pairwise interactions among spike trains do not increase throughout development. Along the same lines, already midway through the first postnatal week, the PFC displays a non-random small-world topography. Moreover, in both brain regions, neurons in the right tail of the firing-rate distribution are overwhelmingly more likely to also be in the right tail of the pairwise interaction distribution and to exhibit hub-like properties. We refer to this organization as oligarchical, and we show that it gradually wanes throughout adulthood, concomitantly with a maturation of excitation-inhibition balance.

RESULTS

SUA firing rate exponentially increases over age, while spiking activity decorrelates

To assess the *in vivo* developmental firing dynamics, we analyzed a large-scale dataset of SUA (n = 278 mice, 14,357 units and 654,335 spike train pairs) recorded with Neuropixels as well as single- and multi-shank Neuronexus silicon probes from the PFC and the ventral OB of non-anesthetized P4-P12 mice (n = 278 mice) (Figures 1A–1C and S1A–S1C). Some of the data have been used in previously published studies.[39,40] We calculated the firing rate (first-order SUA statistics) and the

spike-time tiling coefficient (STTC; second-order SUA statistics, calculated at a 10-ms timescale), a measure of pairwise correlation among spike trains that is not biased by firing rate.[41] In line with previous reports,[39,40,42–45] using multivariate linear regression, we found that firing rate exponentially increased with age in both brain regions (age effect = 0.11, confidence interval [CI] [0.04; 0.18], p = 0.004, generalized linear mixed-effect model) (Figure 1D) and that the OB displayed a higher firing rate than the PFC (firing rate at P8 = 0.57 and 0.25 Hz, CI [0.50; 0.65] and [0.22; 0.29] for OB and PFC, respectively, $p < 10^{-16}$) (Figures 1D and S1D).

Concomitant with the increase of firing rate, and consistent with previously published data,[39,47,48] the STTC exponentially decreased with age (age effect = −0.008, CI [−0.014; −0.003], p = 0.003, linear mixed-effect model), indicating a developmental decorrelation of spiking activity (Figure 1E). When evaluating this effect on individual brain regions, we found that the OB displayed lower STTC values than the PFC (STTC value at P8 = 0.092 and 0.105, CI [0.091; 0.093] and [0.104; 0.106] for OB and PFC, respectively, $p < 10^{-16}$) (Figures 1E and S1E).

Lastly, when pooled across mice and brain regions, both firing rate and STTC already displayed a right-skewed and heavy-tailed distribution at these early developmental stages (Figures 1F and 1G).

These data indicate that, in both brain regions, SUA firing rates exponentially increase across the first two postnatal weeks while, at the same time, spiking activity decorrelates. Consistent with the early maturation of the OB and its high density of INs,[37] the OBs display higher firing rates and lower STTC values than the PFCs. Even at neonatal age, the two variables exhibit a right-skewed and heavy-tailed distribution in both brain areas.

The skewness, tailedness, and inequality of the SUA firing statistics do not increase over age

A corollary of the blank-slate model is that the distributions of functional parameters should become more extreme over development. To quantify the distribution shape for the first- and second-order SUA statistics, we computed their skewness, kurtosis, and Gini coefficient (Figures 2A–2C). Skewness and kurtosis are the third and fourth central moments of a variable, and they measure its asymmetry and tailedness, respectively. Negative values of skewness indicate a left-skewed distribution, positive values a right-skewed distribution, and null values a symmetrical distribution (Figure 2A). Kurtosis only takes positive values. Normal distributions have a kurtosis value of 3 and are referred to as mesokurtic distributions. Distributions with a kurtosis below 3 are platykurtic (thin tailed), whereas distribution with a kurtosis above 3 are leptokurtic (heavy tailed) (Figure 2B). The Gini coefficient measures the inequality of a distribution[49,50] and takes values ranging between 0 (representing total equality) and 1 (representing total inequality). It is calculated as the area between the line of equality and the Lorenz curve divided by the total area under the line of equality (Figure 2C). To increase the estimation accuracy of these three parameters, for this analysis we only considered mice with at least 20 simultaneously recorded single units (n = 195 out of 278 mice).

When combining data from the PFC and OB, contrary to the prediction of the blank-slate model, neither the skewness nor the kurtosis of firing rates (age coefficient = −0.06 and −0.02, CI [−0.19; 0.07] and [−0.05; 0.02], p = 0.39 and p = 0.45, for skewness and kurtosis, respectively, linear model) and STTC (age coefficient = 0.06 and 0.01, CI [−0.27; 0.39] and [−0.05; 0.07], p = 0.73 and p = 0.71, for skewness and kurtosis, respectively, linear model) exhibited an age-dependent trend (Figures 2D and 2E). Pooling together firing rate and STTC distributions, 100% of the distributions were right skewed (390 out of 390, skewness >0), and 94% were leptokurtic or heavy tailed (366 out of 390, kurtosis >3). Along the same lines, the Gini coefficient of firing rate did not significantly change over the first two postnatal weeks (age coefficient = −0.004, CI [−0.014; 0.007], p = 0.50, linear model), whereas the Gini coefficient of STTC even slightly decreased over age (age coefficient = −0.02, CI [−0.03; −0.002], p = 0.02, linear model) (Figure 2F). This dynamic was consistent across brain regions (Figures S2A–S2C) and robust to changes in the minimum number of single units used as cutoff for analysis (Figure S2D). Even analyzing the distributions of firing rate and STTC after pooling together units recorded in the same brain region and in mice of the same age did not lead to age dependency for any of the evaluated parameters (Figure S3).

These data indicate that, irrespective of brain region, the skewness, tailedness, and inequality of first- and second-order SUA statistics do not increase with age, as would be predicted by the blank-slate model. On the contrary, the only parameter to exhibit a significant age dependence is the Gini coefficient of STTC, which decreases with age. However, this effect is of modest size, and it is the only result that depends on the number of units used as cutoff for a mouse to be included in the analysis (Figure S3D). Further, almost the totality of these distributions is right skewed and heavy tailed. The fact that these results are largely brain region independent indicates that the different developmental speed of the early-maturating OB and the late-maturing PFC does not affect these dynamics. Considering the large size of the investigated datasets, it is also unlikely that we were unable to detect the presence of developmental trends due to a lack of statistical power.

Lastly, solely skewness and kurtosis of both firing rate and STTC robustly correlated with each other (r^2 = 0.9 and 0.88, respectively). Despite similar developmental trajectories, the other pairwise parameter combinations were poorly predictive of each other (median r^2 = 0.03) (Figure S4), indicating that they quantify distinct distributions that are largely independent of each other and, thus, not redundant.

Complex functional network properties of the PFC do not vary over development

Even if the skewness, tailedness, and inequality of firing rate and STTC are largely constant over age, we hypothesized that developmental changes might be detectable at a network level. To test this hypothesis, we resorted to complex network analysis[51] and investigated the functional network topology of the developing PFC *in vivo* (Figure 3A), similarly to what was previously done *in vitro*.[52] To minimize a potential estimation bias due to low number of single units, an inherent drawback of recordings in neonatal mice, we limited this analysis to mice having at least 20 single units (n = 108 out of 131 PFC recordings). We restricted

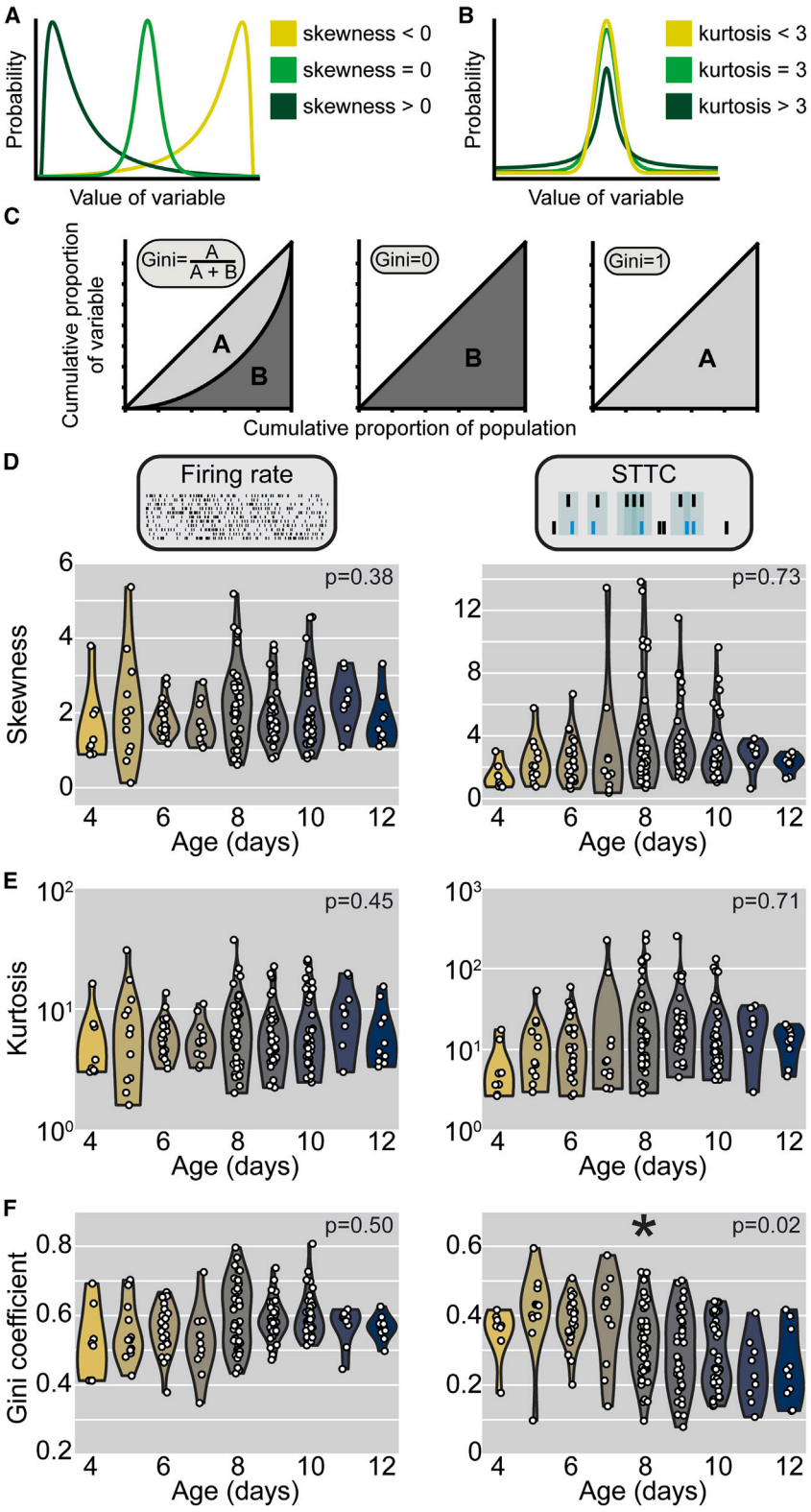

Figure 2. Skewness, kurtosis, and Gini coefficient of firing rate and STTC over the first two postnatal weeks

(A) Schematic representation of three distributions with different skewness values.

(B) Same as (A) for kurtosis.

(C) Lorenz curves for three distributions with different Gini coefficient values and schematic representation of how the Gini coefficient is calculated.

(D) Violin plot displaying the skewness of firing rate (left) and STTC (right) of P4–12 mice (n = 195 mice). Color codes for age with 1-day increments.

(E and F) Same as (D) for kurtosis (E) and Gini coefficient (F). White dots indicate individual mice, and the shaded area represents the probability density of the variable. Asterisk in (F) indicates a significant effect of age. *$p < 0.05$, linear model. p values in (D)–(F) refer to the effect of age, linear models.

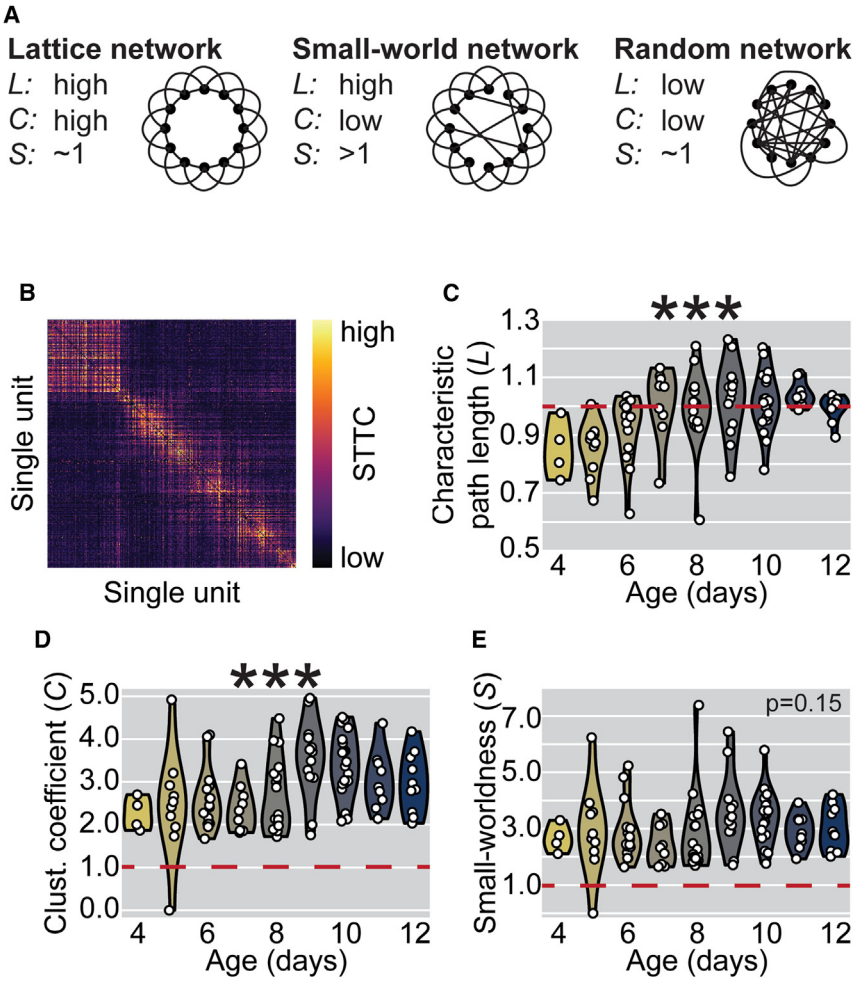

Figure 3. Complex network analysis in the PFC across the first two postnatal weeks

(A) Schematic representation of a lattice, small world, and random network and their respective values of characteristic path length (L), clustering coefficient (C), and small-worldness (S).

(B) Weighted adjacency STTC matrix of a representative P10 mouse. Color codes for STTC value. Units are sorted by recording depth.

(C) Violin plot displaying the characteristic path length as a function of age (n = 108 mice). The dashed red line indicates the value of the corresponding random network. Color codes for age with 1-day increments.

(D and E) Same as (C) for clustering coefficient (D) and small-worldness (E). In (C)–(E), white dots indicate individual mice and shaded area represents the probability density of the variable. Asterisks in (C) and (D) indicate a significant effect of age. ***$p < 0.001$, linear models. p value in (E) refers to the effect of age, linear model.

the investigation to the PFC because the network analysis for OB was biased by the low number of units and the level of recurrent connectivity.

The functional network analysis was carried out on symmetric STTC matrices computed on individual mice, where each node corresponds to a single unit (Figure 3B). These matrices were thresholded and binarized by a shuffling procedure that swapped the identity of the neurons while preserving the population firing rate (see STAR Methods for details). To evaluate the topology of the graphs, we computed their density and three main network properties: characteristic path length (L), clustering coefficient (C), and small-worldness (S) (Figure 3A). These last three parameters were normalized by dividing them with a corresponding null value extracted from random networks with the same density (the dashed red line in Figures 3C–3E indicates the value of the corresponding random network).

Similar to the parameters based on SUA statistics, the density of the graphs did not significantly vary over age (age coefficient = −0.003, CI [−0.009; 0.002], p = 0.23, linear model) (Figure S5A). While L values were similar to those computed on random networks (58 out of 108 = 54% networks with normalized L > 1) (Figure 3C), all but one network had larger C values than the corresponding random network (107 out of 108 = 99% networks with normalized C > 1) (Figure 3D). The graphs' transitivity, a parameter that is closely related to the clustering coefficient, was analogously higher than in random networks (107 out of 108 = 99% networks with normalized transitivity >1) (Figure S5B).

Low L and high C values are typical of so-called small-world networks, a category that includes many real-world networks, including the adult brain[53–55] (but see Hilgetag and Goulas[56]). Accordingly, the small-worldness of the developing PFC was robustly higher than its corresponding null value (107 out of 108 = 108 = 99% networks with normalized S > 1) (Figure 3E). The normalized L and C increased over age (age coefficient = 0.13 and 0.02, CI [0.06; 0.21] and [0.01; 0.03], $p < 10^{-4}$ and $p < 10^{-4}$, for normalized L and C, respectively, linear model) (Figures 3C and 3D). While this effect could be explained by an increase on the graph's size (the number of units per mouse),[57] more central for the aim of the project is the fact the normalized S did not vary with age (age coefficient = 0.07, CI [−0.02; 0.16], p = 0.15, linear model) (Figure 3E). Further, all these results were robust to changes in the minimum number of single units used as cutoff for analysis (Figure S5C).

Thus, complex network analysis revealed that, already during the first two postnatal weeks, the PFC displays a non-random and small-world functional network architecture that is similar to that described in the adult brain[53–55] and is stable over age.

The developing brain is in an oligarchical state

Next, we investigated whether the SUA statistics are not only extremely distributed but also correlated to each other. For this, we used multivariate linear regression with age as a covariate, and we evaluated the relationship between the log-transformed firing rate of a neuron and its log-transformed

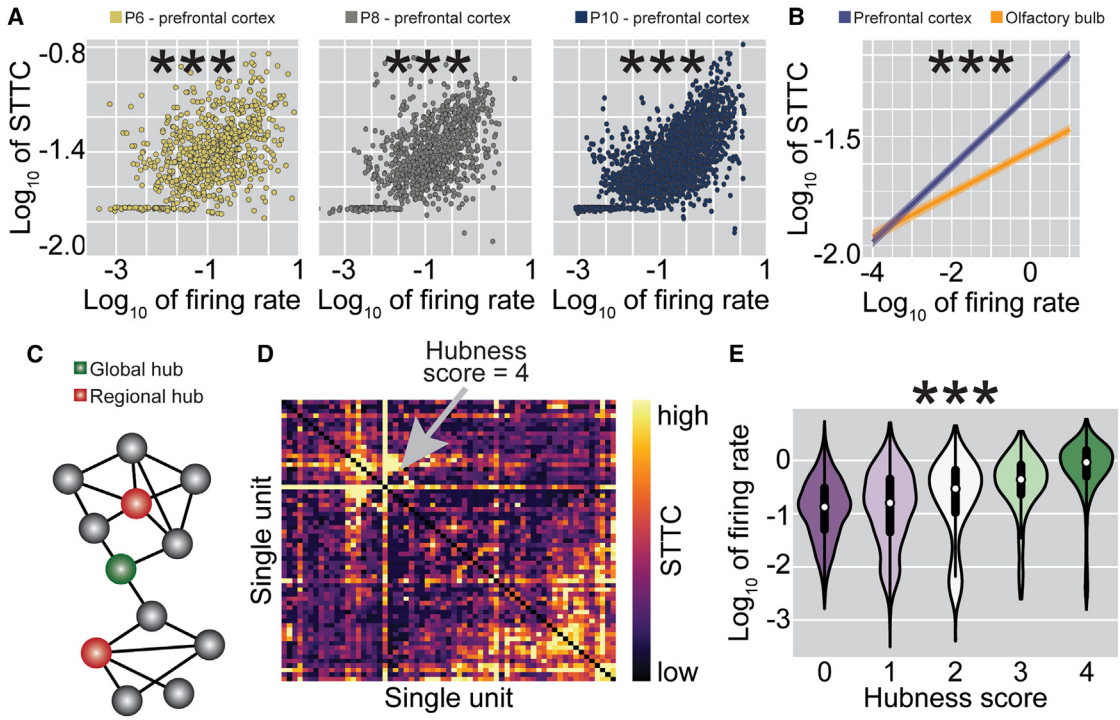

Figure 4. Firing rate correlates with average STTC and hubness score

(A) Scatterplot displaying the log-transformed average STTC of prefrontal neurons as a function of their log-transformed firing rate in all recorded P6 (left), P8 (center), and P10 (right) mice. Color codes for age.

(B) Line plot displaying the log-transformed average STTC as a function of log-transformed firing rate across brain regions (n = 259 mice and 14,043 single units). Color codes for brain region.

(C) Schematic representation of a network's graph in which regional (red) and global (green) hubs are highlighted.

(D) Weighted adjacency STTC matrix recorded from the PFC of a P10 mouse. The gray arrow indicates a neuron with high hubness score. Color codes for STTC value.

(E) Violin plot displaying the log-transformed firing rate of a neuron as a function of its hubness score. Color codes for hubness score. In (A), colored dots indicate individual neurons. In (E), data are presented as median, 25th percentile, 75th percentile, and interquartile range, and the shaded area represents the probability density of the variable. Asterisks in (A) and (B) indicate a significant effect of firing rate and in (E) of hubness score. ***$p < 0.001$, linear mixed-effect models.

average STTC. We found that, irrespective of brain region, the two variables robustly correlated with each other (firing rate coefficient = 0.08, CI [0.07; 0.08], $p < 10^{-70}$, linear mixed-effect model) (Figures 4A, 4B, and S5D). This correlation between firing rate and average STTC was lower in the OB than in the PFC (firing rate and brain area interaction coefficient = 0.06, CI [0.05; 0.06], $p < 10^{-84}$, linear mixed-effect model) (Figure 4B). Since the STTC lacks a firing rate bias,[41] this is indicative of a genuine correlation between the two variables. Consequently, neurons with high firing rates disproportionately contribute to network dynamics during development, a property reminiscent of hub neurons, as recently shown in the developing barrel cortex.[58] We define this state, in which extreme distributions are tightly correlated with each other, as being "oligarchical."

To investigate whether the firing rate of a neuron also correlates to its network-level features, we used the prefrontal STTC matrices described in the paragraph above and extracted four different regional and global "hubness" metrics for each individual node: degree (i.e., total number of connections), strength (i.e., sum of connection weights), betweenness centrality (the fraction of shortest paths containing a given node), and closeness centrality (the reciprocal of the average shortest path for a given node) (Figures 4C and 4D). For each of these measures, we then assigned a score of 0 or 1 to each node, depending on whether it exceeded the 75th percentile of that specific metric.[52] Summing the individual scores, we obtained a composite hubness score, with values ranging from 0 to 4. The majority of neurons (6,580 out of 10,512 = 63%) had a hubness score of 0, whereas a smaller proportion (1,471 out of 10,512 = 14%) of neurons received a hubness score of 4. As previously reported in 2D neuronal cultures,[52] the hubness score robustly correlated with firing rate (hubness score effect, $p < 10^{-70}$, linear mixed-effect model), with the median firing rate differing by almost an order of magnitude between neurons with hubness score 0 and 4 (Figure 5E).

These data indicate that the developing cortex is not only an environment characterized by stably extreme SUA statistics distributions but also that it exhibits a peculiar oligarchical state, in which the firing rate of a neuron robustly correlates with the strength of its pairwise interactions and its network-level properties.

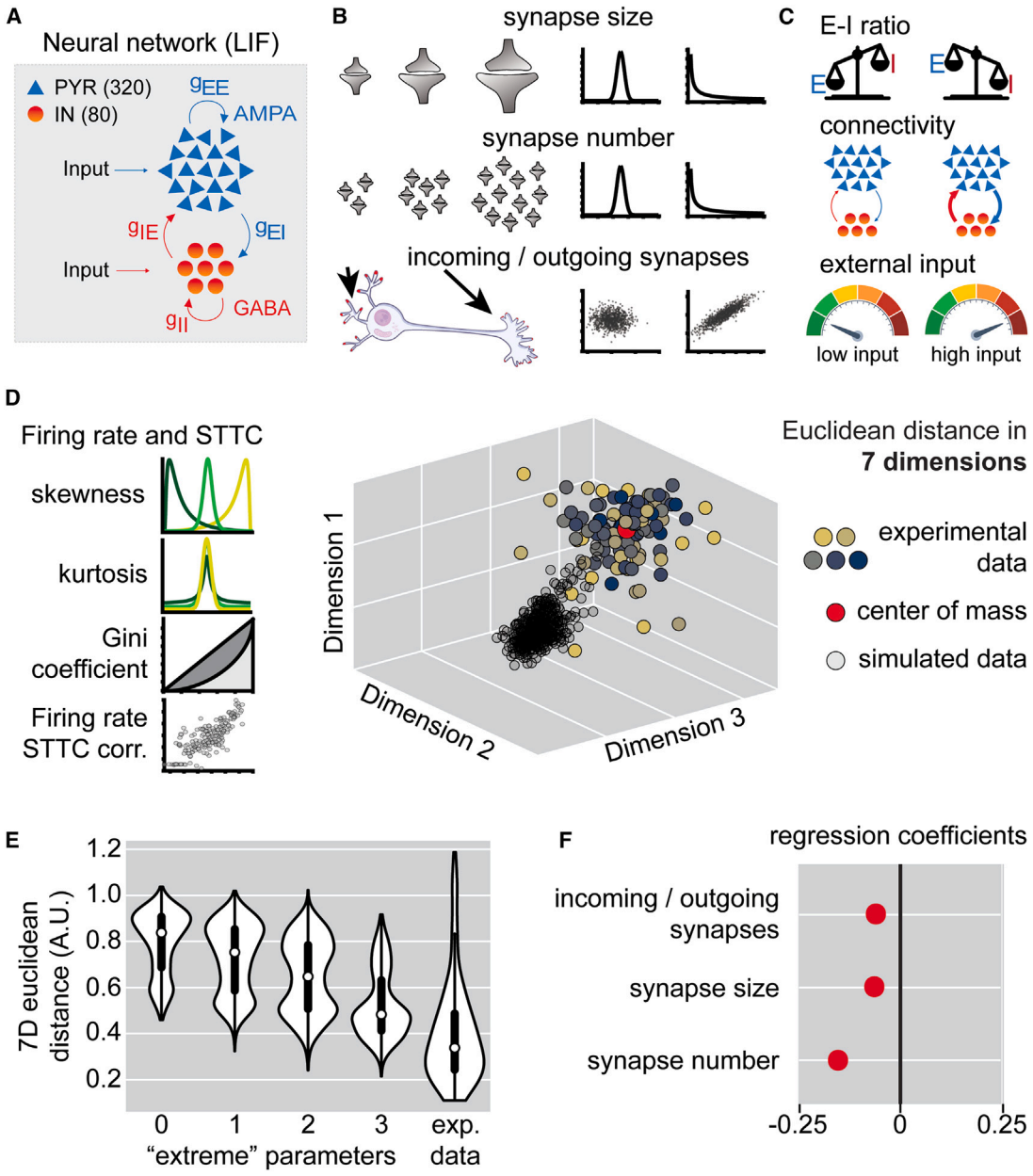

Figure 5. Spiking neural network modeling of the distribution shape of SUA statistics in the developing PFC

(A) Schematic representation of the neural network model.

(B and C) Same as (A) for the three synaptic parameters (B) and the simulation parameters that were treated as random variables (C).

(D) Schematic representation of the parameters that were used to evaluate the distribution shape of the experimental and simulated spiking data (left) and the approach that was used to evaluate the distance between experimental and simulated data (right). Note that the plot is for visualization purposes only. Even though only three dimensions are shown, the distance between simulated and experimental data were calculated in a seven-dimensional space. Color in the scatterplot codes for age.

(E) Violin plot displaying the distance between simulated data and the center of mass of experimental data as a function of the number of synaptic parameters set in their "extreme" configuration.

(F) Multivariate regression coefficients for the three synaptic parameters over the distance from the center of mass of experimental data. In (E), data are presented as median, 25th percentile, 75th percentile, and interquartile range, and the shaded area represents the probability density of the variable. In (F), regression coefficients are presented as mean and 95% CI.

Extreme synaptic distributions are necessary to recapitulate early PFC activity in a spiking neural network model

We hypothesized that, to generate such extreme distributions of the SUA statistics, analogously extremely distributed structural synaptic parameters are necessary. To explore this proposition, we simulated ~8,000 spiking neural networks of interconnected conductance-based leaky integrate-and-fire (LIF) neurons. The networks mimicked spontaneous activity: they did not receive any structured input and did not perform any task. The simulated networks had no spatial structure and consisted of 400 neurons, 80% of which were excitatory (PYRs) and 20% inhibitory (INs), in line with anatomical data for neocortical areas.[59,60] PYRs were simulated with outgoing excitatory AMPA synapses, while INs were equipped with outgoing inhibitory GABAergic synapses (Figure 5A). In these models, we investigated how the simulated firing statistics were affected by three structural (synaptic) parameters: (1) whether the size of synapses followed a normal or a log-normal distribution, (2) whether the number of synapses of individual neurons followed a normal or a log-normal distribution, and (3) whether the number of dendritic and axonic (incoming and outgoing) synapses were correlated or uncorrelated with each other (Figure 5B). This resulted in a total of 2^3 = 8 possible synaptic parameters combinations. To avoid choosing an arbitrary structural network architecture to test the effect of these three variables, a set of other parameters (average size of AMPA and GABA synapses, average connectivity, and the strength of the noisy input driving PYRs and INs) were randomly drawn from a range of biologically constrained values (see STAR Methods for details) (Figure 5C). Given that the general structural network architecture is inspired by the neocortical anatomical organization (e.g., average connectivity and proportion of PYRs and INs), the simulated data were compared to PFC recordings.

To evaluate how accurately the different structural network architectures recapitulated the SUA statistics of the developing PFC, we employed the same parameters that we used to describe the experimental data. For each simulation, we computed the simulated firing rates and STTC, and, for both variables, we extracted their skewness, kurtosis, Gini coefficient, and the correlation between log-transformed firing rates and average STTC. We then derived the coordinates of the center of mass of the experimental data in this seven-dimensional parameter space and calculated the Euclidian distance from every simulation (see simplified scheme in Figure 5D).

Using multivariate linear regression, we observed a decrease in the distance from the experimental data's center of mass as a function of the number of structural parameters set in its extreme configuration (log-normal distribution of synapse size and number, and correlated number of incoming and outgoing synapses) (Figure 5E). Further, the distance from the experimental center of mass decreased supra-linearly as a function of the number of extreme parameters (0–1 extreme parameters distance difference = 0.07, 1–2 extreme parameters distance difference = 0.09, 2–3 extreme parameters distance difference = 0.12, linear model) (Figure 5E). This effect is also visually appreciable when the seven dimensions in which we evaluated the model fit are reduced using t-distributed stochastic neighborhood embedding (tSNE) (Figure S6A). When few synaptic parameters are set to their extreme configuration, there is little to no overlap between experimental and simulated data. Conversely, when all three synaptic parameters are set to their extreme configuration, the areas of maximum density of the two distributions are overlapping (Figure S6A).

Taken individually, the structural parameter with the largest effect on the average distance from the experimental data's center of mass was the distribution of synapse number (regression coefficient = −0.16, linear model), followed by the distribution of synaptic weight (regression coefficient = −0.06, linear model) and by the proportionality of incoming and outgoing synapses (regression coefficient = −0.06, linear model) (Figure 5F). Next, we considered the effect of the three synaptic parameters on individual properties of the simulated SUA statistics (Figures S6B–S6H). We found that the distribution of the synapse number had the largest effect on (1 and 2) skewness of firing rate and STTC, (3) the kurtosis of STTC, (4) the Gini coefficient of firing rate and (5) the log-log correlation between firing rate and average STTC. The proportionality of incoming and outgoing synapses had the largest effect on (1) the kurtosis of firing rate and (2) the Gini coefficient of STTC. The distribution of synaptic weights did not have the largest effect on any of the seven parameters (Figures S6B–S6H). Lastly, we run a separate set of simulation varying network size and found that it only minimally affected the distance between simulated and experimental data (Figure S6J).

Taken together, these data indicate that, in spiking neural networks simulations, extreme distributions of synaptic parameters are required to stably recapitulate the SUA statistics that we observed in the developing PFC. The distribution of synapse number on individual neurons is the synaptic parameter with the largest influence on the model fit. However, all three synaptic parameters play a significant role and influence different aspects of the simulated data.

The shape of the SUA statistics distributions is stable throughout adulthood, while the oligarchy decreases with age

So far, we have shown that, already shortly after birth, the brain has a right-skewed, heavy-tailed, and unequal distribution of SUA statistics that largely does not vary during the first two postnatal weeks. Since similar properties have been previously reported for the adult brain, the question arises of whether and how the extremeness of these parameters varies throughout late development and into adulthood. To address this question, we chronically recorded from the PFC of head-fixed mice from P16 to P60 (n = 24 mice, 95 recordings, 2,498 single units, and 36,899 spike train pairs).

SUA firing rate and STTC did not vary with age (age coefficient = −0.003 and -10^{-4}, CI [−0.003; 0.001] and [-6×10^{-4}; 4×10^{-4}], p = 0.28 and p = 0.63, respectively, generalized linear mixed-effect model) (Figures S7A and S7B).

Analogously to the data for the neonatal brain, the skewness of the SUA statistics did not change also for the P16–60

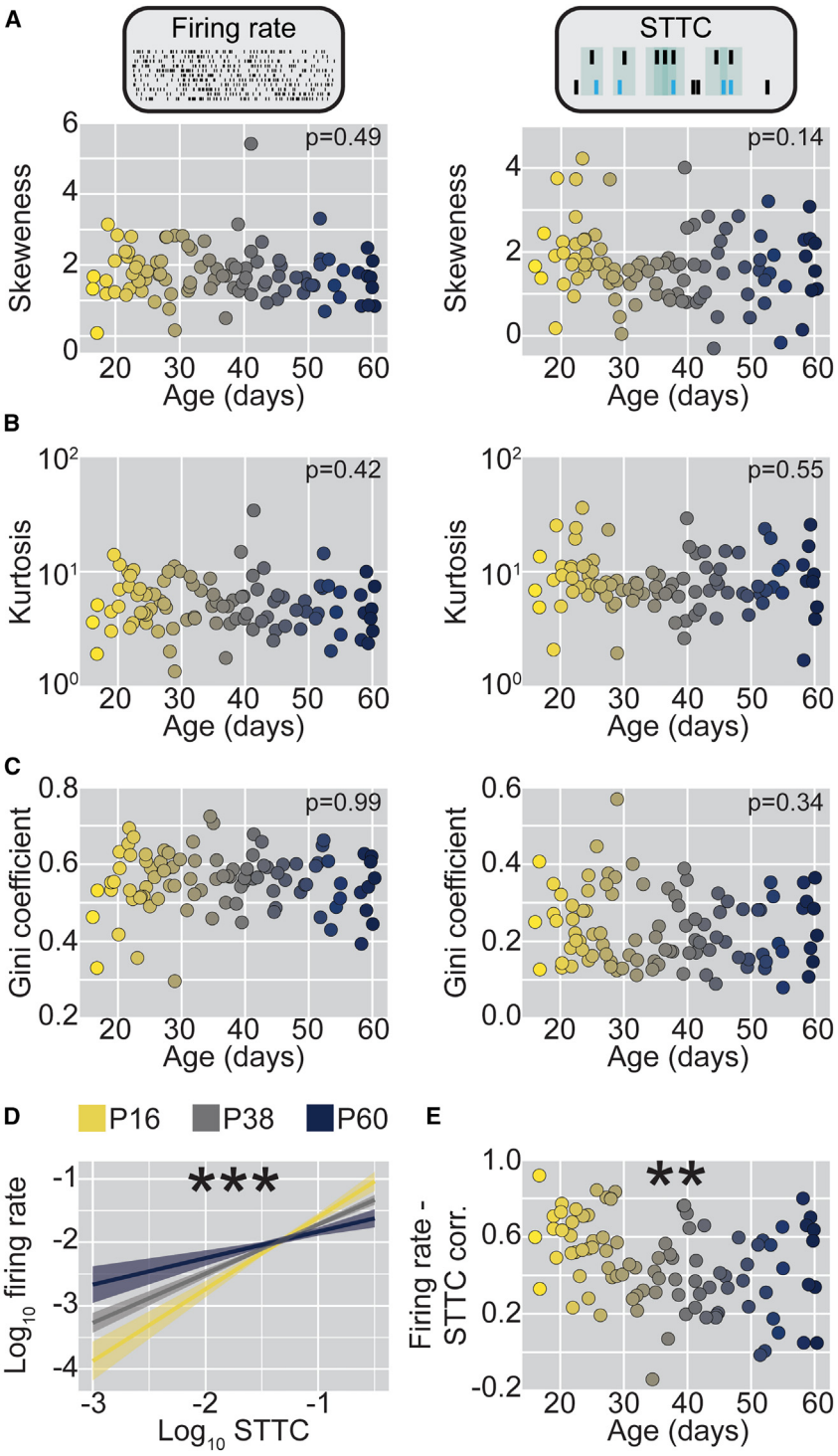

Figure 6. Skewness, kurtosis, Gini coefficient, and correlations of firing rate and STTC in P16–60 mice

(A) Scatterplot displaying the skewness of firing rate (left) and STTC (right) of P16–60 mice (n = 24 mice and 95 recordings). Color codes for age with 1-day increments.

(B and C) Same as (A) for kurtosis (B) and Gini coefficient (C).

(D) Line plot displaying the log-transformed average STTC as a function of log-transformed firing rate across ages (n = 24 mice and 2,498 single units). Color codes for age.

(E) Same as (A) for the Pearson correlation between log-transformed average STTC and log-transformed firing rate within individual mice. In (A–C) and (E), colored dots indicate individual recordings. In (D), data are presented as mean and 95% CI. Asterisks in (D) and (E) indicate a significant effect of age. ***$p < 0.001$, **$p < 0.01$, linear mixed-effect models. p values in (A)–(C) refer to the effect of age, linear mixed-effect models.

developmental time window (age coefficient = −0.004 and −0.01, CI [−0.02; 0.007] and [−0.02; 0.003], p = 0.49 and p = 0.14, for firing rate and STTC, respectively, linear mixed-effect model) (Figure 6A). Along the same line, also the kurtosis (age coefficient = −0.001 and −0.001, CI [−0.005; 0.002] and [−0.005; 0.002], p = 0.42 and p = 0.55, for firing rate and STTC, respectively, linear mixed-effect model) and the Gini coefficient (age coefficient = 10^{-5} and 7×10^{-4}, CI [−0.001; 0.001] and [−0.002; 8×10^{-4}], p = 0.99 and p = 0.34, for firing rate and STTC, respectively, linear mixed-effect model) of the two variables remained constant for the investigated time window (Figures 6B and 6C).

Similar to what reported for early development, also in the adult PFC the log-transformed firing rate of a neuron and its average STTC strongly correlated with each other (average STTC coefficient = 1.53, CI [1.34; 1.71], $p < 10^{-56}$, linear mixed-effect model) (Figure 6D). However, fitting a model that included an interaction of STTC with age revealed that the correlation strength between the two variables decreased over late development (age and average STTC interaction coefficient = −0.03, CI [−0.05; −0.02], $p < 10^{-5}$, linear mixed-effect model) (Figure 6D). Accordingly, the Pearson correlation between firing rate and average STTC on an individual-mouse basis robustly declined with age, from roughly ∼0.6 to ∼0.3 (age coefficient = −0.006, CI [−0.009; −0.002], p = 0.001, linear mixed-effect model) (Figure 6E).

Thus, in the mouse PFC, the extremeness of SUA statistics distributions does not significantly change between P16 and P60. However, the correlation between firing rate and STTC is roughly halved from P16 to P60, indicating that the oligarchical state in PFC is more pronounced during early development than at adulthood.

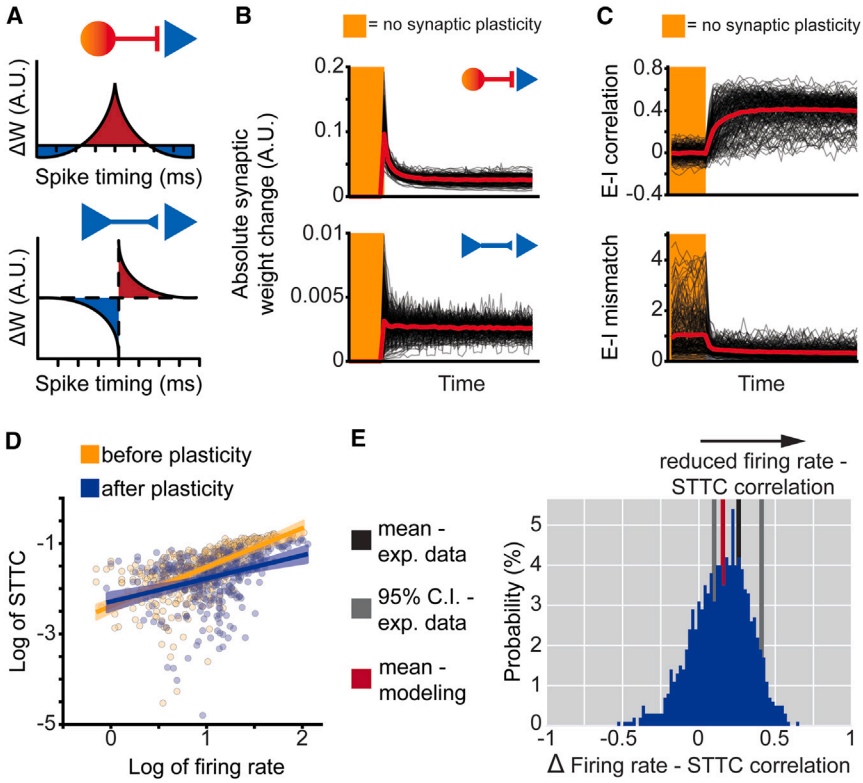

Figure 7. Spike-time-dependent inhibitory synaptic plasticity decreases the correlation between firing rate and STTC

(A) Schematic representation of the simulated inhibitory (top) and excitatory (bottom) synaptic plasticity rules.

(B) Line plot of the IN-PYR (top) and PYR-PYR (bottom) synaptic weight changes over time. The shaded area indicates the period without synaptic plasticity.

(C) Line plot of excitatory and inhibitory currents correlation (top) and absolute difference (bottom) over time. The shaded area indicates the period without synaptic plasticity.

(D) Scatter and line plot of a representative example of the correlation between simulated firing rate and average STTC before (yellow) and after (blue) synaptic plasticity.

(E) Histogram plot of the difference in simulated firing rate and average STTC correlation before and after synaptic plasticity. The black line indicates the mean of the experimental data, the two gray lines the 95% CI of the mean, and the red line the mean of the simulated data. In (B) and (C), individual black lines represent individual simulations and the red line represents the mean across simulations. For visualization purposes, only one-fifth of the individual simulations are shown. In (D), individual dots represent individual simulated neurons, and data are presented as mean and 95% CI.

Inhibitory synaptic plasticity parsimoniously explains the gradual disappearance of the oligarchy

Throughout the same developmental phase during which we observed a decrease in the correlation between the firing rate of a neuron and its average STTC, the cortex transitions into a state of detailed E-I balance,[61] a phenomenon that has been linked to inhibitory synaptic plasticity.[62] Given the critical role that E-I ratio plays in controlling correlations among neurons,[39] we hypothesized that this transition might explain the progressive decline of the correlation between firing rate and STTC.

To test this hypothesis, we resorted to spiking neural network modeling with an architecture analogous to the one used to model early cortical activity. After an initial period in which the networks were run with frozen synaptic sizes and all the synaptic parameters in their extreme configuration, we added symmetric spike-time-dependent inhibitory plasticity (ISTDP) on the synapses connecting INs to PYRs[62] (Equation 1) and classic asymmetric Hebbian plasticity (STDP) on PYR-PYR excitatory synapses[63] (Figure 7A). The original formulation of the ISTDP rule implemented a single target firing rate (α, Equation 1) for the entire population of PYRs. In this study, we instead decided to draw α from a log-normal distribution to better recapitulate the diversity of the experimentally observed firing rates (see STAR Methods for details):

$$\frac{dW}{dt} = \frac{\eta(pre * post - \alpha * pre)}{\tau_{STDP}} \quad \text{(Equation 1)}$$

where W is an IN-PYR synaptic weight, *pre* and *post* are the pre- and post-synaptic activity, α is the target rate for the post-synaptic PYR and is drawn from a log-normal distribution, τ_{STDP} is the decay time constant of the plasticity rule, and η is the learning rate.

Analogously to the approach that we previously described, also for this set of simulations, we treated several other structural parameters as random variables, and we systematically varied them within the same biologically constrained range of values that we employed for the former simulations. To evaluate the effect of synaptic plasticity, we compared the SUA statistics of the frozen synapses phase and those of the last fifth of the simulated data, a phase in which synaptic changes were stable (Figure 7B).

Analogously to previous results,[62] we observed that adding ISTDP resulted in a network with detailed E-I balance. ISTDP increased the correlation between incoming excitatory and inhibitory currents across neurons (Figure 7C, top) and reduced the temporal mismatch (i.e., the absolute value of the difference) between excitatory and inhibitory currents across time (computed in 5-s bins) within individual neurons (Figure 7C, bottom).

In line with our hypothesis, we found that adding ISTDP and STDP to the network also decreased the correlation between firing rate and average STTC, similarly to what we experimentally observed in P16–60 mice (mean decrease in firing rate – average STTC correlation in simulated data = 0.16, in experimental data = 0.26, CI [0.11; 0.41], Figures 7D and 7E). When we further evaluated the effects of synaptic plasticity, we found that it only

minimally affected the skewness, kurtosis, and Gini coefficient of firing rate and STTC, in line with the experimental data from the PFC of P16–60 mice (Figure S7). Of these six parameters, only the kurtosis and the Gini coefficient of firing rate were narrowly outside the 95% CI of the experimental values (Figures S7C–S7H).

To investigate the differential role of ISTDP and STDP in decreasing the correlation between firing rate and average STTC, we next run two sets of simulations with only one of the two synaptic plasticity rules. These simulations revealed that, while ISTDP-only networks displayed a decrease between firing rate and average STTC that was comparable to networks with both synaptic plasticity rules, the correlation between the two variables was unchanged in STDP-only networks (Figure S7I). However, ISTDP-only simulations provided an overall significantly worse fit to the experimental data than networks with both synaptic plasticity rules (Figure S7J). Thus, the two synaptic plasticity rules have different effects on the simulated spiking activity. ISTDP is mainly responsible for the decrease in the oligarchical organization, whereas STDP allows this to happen while only minimally affecting the skewness, kurtosis, and Gini coefficient of firing rate and STTC.

Taken together, these data indicate that adding ISTDP and STDP to a spiking neural network parsimoniously recapitulates the developmental decrease in the correlation between firing rate and STTC while only minimally affecting the distribution shape of the two variables, consistent with what we observed in the PFC of P16–60 mice.

DISCUSSION

A fascinating property of the adult brain is that a large number of parameters, ranging from the size of synapses to the power of extracellular currents,[1,3,4] follow extreme distributions. This organization has been suggested to have many desirable properties,[10,27] but how and when it arises is still a matter of debate. Here, we report that, in the PFC and OB, two brain regions exemplifying slow and fast maturational dynamics, in the first days of extrauterine life, the distributions of first- and second-order SUA statistics are already extreme: right skewed, heavy tailed, and highly unequal. While the central tendency of these distributions varies across development, their shape remains largely unchanged until adulthood. We also show that early brain activity is in an oligarchical state in which high-firing-rate neurons display hub-like properties and exert a disproportionate influence on their local network, a phenomenon that becomes less prominent as mice age. Leveraging spiking neural network modeling, we demonstrate that, to recapitulate these network properties, analogously extremely distributed synaptic parameters are needed. We conclude by showing that the progressive disappearance of the oligarchical state can be parsimoniously explained by introducing an inhibitory synaptic plasticity rule that establishes a detailed excitation-inhibition balance. This work suggests that the distribution shape of structural and functional neural parameters is not fundamentally altered by developmental processes but rather is preconfigured and experience independent.

In altricial animals such as rodents, the first postnatal week roughly corresponds to mid-late gestation in humans.[38] At this early stage, brain activity has several unique traits, such as discontinuity,[38] highly correlated spiking activity,[39,47,48] the presence of transient cell types and circuits,[64] extremely low firing rates,[39,65] low levels of inhibition,[39,66,67] and a loose temporal coordination of excitation and inhibition.[61,62] Importantly, sensory systems are still very underdeveloped. In rodents, the retina becomes light sensitive around P8–P9,[65,68] and eye opening only takes place around P14–P15, a few days after hearing onset occurs.[69] The whisking-related sensory system also follows a similar timeline. In the first postnatal week, ~90% of whisker movements do not induce increased firing rate in the somatosensory cortex, and ~90% of firing in the somatosensory cortex is unrelated to whisker movements.[70] Even after splitting whisker movements by size and only considering the few large ones that occur, the somatosensory cortex is active concomitantly with a whisker movement less than 50% of the time.[71] Whisker-elicited sensory responses are initially mainly the result of passive stimulations by the dam and the littermates, while robust active whisking only emerges around P10–P12.[72–74] Solely the olfactory system follows a distinct developmental dynamic and, even though it is also still developing,[75] it is already functional and behaviorally relevant in the first postnatal days.[36,37] Despite the paucity of sensory information that is therefore available in the first postnatal week, we find that the distribution of SUA statistics is already extreme and does not significantly vary from early development to adulthood. Corroborating the idea that experience does not play a significant role in this process, we find no differences between the OB, which is already "online," and the PFC, which is supposed to be one of the slowest-developing brain regions.[38] We further show that, already from P4 onwards, the PFC also displays a complex network topology that is reminiscent of small-world networks, a property that is typical of many real-world networks,[76] including the adult brain[53–55] (but see Hilgetag and Goulas[56]).

These results are difficult to reconcile with the hypothesis that brain structure is initially "diffuse" and only later acquires the structural organization that is typical of the adult brain.[30,31,77] Rather, they support several recent studies that have highlighted the importance of "nature over nurture"[78,79] in establishing neural circuits and the distributions of their parameters. For instance, in neuronal cultures, the variance of glutamatergic synaptic sizes does not differ between networks that are silenced from plating onwards and networks that are spontaneously active.[7] Similarly, cultures of dissociated neurons exhibit the ability to self-organize into a complex network topology with small-world properties that are characterized by extreme distributions of firing rates and connection weights.[52] Extreme distributions of firing rates and functional connectivity are also observed in human brain organoids,[80–82] which, despite not having access to sensory inputs, even display structured spiking "protosequences."[82] Along the same lines, *in vivo* blocking of synaptic transmission in the mouse hippocampus does not alter the distribution of spine sizes,[83] and "soloist" neurons (uncorrelated to the overall local firing) coexist with "choristers" (strongly correlated with local firing) already in the first postnatal week.[84] Even more surprisingly, completely abolishing all central nervous system

activity for the first 4 days of life of the larval zebrafish only minimally affects the tuning and functionality of neurons and the ability of the fish to learn a complex visuomotor task.[78] Intriguingly, similar concepts are beginning to percolate also in the field of artificial intelligence,[85] which has traditionally been dominated by a bottom-up and learning-based approach.

The relationship between the firing rate of a neuron and the strength of its pairwise interactions with other neurons is complex and still debated. A number of experimental and theoretical studies found a positive correlation between the two variables.[86–89] However, this relationship has also been reported to be absent or even negative.[90–93] Here we show that, in the PFC and OB of P4–12 mice, there is a strong positive correlation between firing rate and average pairwise interaction of a neuron, as measured by the STTC coefficient. Thus, neurons with extreme firing rates are also likely to have extreme average STTC values, an organization that we refer to as oligarchical. The correlation between firing rate and STTC weakens throughout development, but it is present also in adulthood. In the early PFC, firing rate also correlates with a neuron's hubness score, a composite metric that encompasses four different measures of local and global hubness. The topic of hub neurons, defined as a subclass of neurons that has an outsized influence on the network activity, has been the subject of extensive experimental and theoretical research in the developing brain.[58,94–96] In agreement with our results, hub neurons in the developing entorhinal[94,95] and barrel cortex[58] are also characterized by high firing rates and high functional connectivity, a prediction that is shared by theoretical work.[97] Previous work has also shown that hub neurons are generally INs, something that we could not investigate in the current study due to the difficulty of separating INs and PYRs based on their waveform properties in the early developing brain.[98] This work further shows that, in a neural network model, adding inhibitory synaptic plasticity results in detailed E-I balance and decreases the influence of high-firing-rate neurons on the network activity. Thus, we propose that the loose temporal E-I balance that is typical of the developing brain[61,62] might be a permissive mechanism for the role exerted by hub neurons on their surroundings. Whether the developmental shift of E-I ratio toward inhibition[39,66] also plays a role remains to be investigated.

Lastly, we show that there is a mechanistic link between the distribution of structural (synaptic) and functional (SUA statistics) parameters. In particular, we report that, in a spiking neural network model, three synaptic parameters have a strong influence on the extremeness of the simulated spiking activity: (1) whether the size of synapses follows a log-normal distribution, (2) whether the number of synapses of individual neurons follows a log-normal distribution, and (3) whether the number of dendritic and axonic (incoming and outgoing) synapses are correlated with each other. The three parameters have a synergistic effect on the model goodness of fit to the experimental data and a distinct impact on different properties (skewness, kurtosis, and Gini coefficient) of the simulated firing rate and STTC distributions. While a large body of evidence supports the notion that the size and number of synapses follow an extreme distribution,[1] to the best of our knowledge, whether the number of dendritic and axonic synapses are correlated with each other has not been explicitly investigated in mammals. However, a recent study found that, in the mouse PFC, the length of a neuron's dendrite and axon are positively correlated.[99] Further, in a full-brain *Drosophila melanogaster* reconstruction, the numbers of incoming and outgoing synapses are tightly correlated with each other (Person coefficient = 0.8).[100] The fact that extremely distributed synaptic parameters are required to faithfully reproduce the SUA statistics of the developing PFC suggests that the distribution of synaptic parameters is also experience independent.

In summary, we report that the extremeness with which functional and structural parameters are distributed is stable across a large portion of the lifespan, which suggests that the brain is in a preconfigured state and that experience-dependent processes do not fundamentally alter this aspect of its organization. Further elucidating the principles underlying the establishment of neural circuits might prove insightful for advancing the field of biological and artificial intelligence alike.

Limitations of the study

This study has several limitations. First, despite investigating mice from a very early developmental phase, and doing so also in the PFC, one of the slowest-developing brain regions, we cannot exclude that some experience-dependent processes have not already taken place. Second, we do not directly experimentally probe whether the distribution shape of synaptic parameters is stable across the first postnatal weeks. However, our modeling results generate a number of predictions that could be experimentally addressed: (1) synapse size and number on individual neurons follow extreme distributions already in the first postnatal week, (2) the shape of these distributions should be stable across development, and (3) the number of incoming and outgoing synapses should be tightly correlated. Third, while our results argue against a role of experience in shaping these processes, we do not provide an alternative mechanistic answer to the question. This topic has, however, already been the subject of a number of theoretical studies.[7,9,83,97] Further, we generated a large and detailed experimental open-access database that could be instrumental in benchmarking future research on this topic. An approach that we believe might be of particular interest is that of generative models.[101,102] Illustrating the promise of this approach, generative models solely based on spatiotemporal gradients of neuronal development[103] or homophily principles[81] can recapitulate important features of the complex topology of adult brains.

STAR★METHODS

Detailed methods are provided in the online version of this paper and include the following:

- KEY RESOURCES TABLE
- RESOURCE AVAILABILITY
  - Lead contact
  - Materials availability
  - Data and code availability
- EXPERIMENTAL MODEL AND STUDY PARTICIPANT DETAILS
- METHOD DETAILS
  - *In vivo* electrophysiology in P4-12 mice
  - *In vivo* electrophysiology in P16-60 mice

SUPPLEMENTAL INFORMATION

Supplemental information can be found online at https://doi.org/10.1016/j.celrep.2024.114267.

ACKNOWLEDGMENTS

We thank Sebastian Bitzenhofer and Irina Pochinok for valuable discussions and feedback on the manuscript and P. Putthoff, A. Marquardt, and A. Dahlmann for excellent technical assistance. This work was funded by grants from the European Research Council (ERC-2015-CoG 681577to I.L.H.-O.), Marie Curie Training Network euSNN (MSCA-ITN-H2020-860563 to I.L.H.-O.), Horizon2020 DEEPER 101016787, the German Research Foundation (437610067, 178316478, and 302153259 to I.L.H.-O.), and Landesforschungsförderung Hamburg (LFF76 and LFF73 to I.L.H.-O.).

AUTHOR CONTRIBUTIONS

M.C. and I.L.H.-O. designed the experiments and wrote the manuscript. M.C., J.K.K., M.H., and Y.-N.C. carried out the experiments. M.C. analyzed the experimental data and carried out neural network modeling. All authors interpreted the data and discussed and commented on the manuscript.

DECLARATION OF INTERESTS

The authors declare no competing interests.

Received: December 20, 2023
Revised: March 13, 2024
Accepted: May 8, 2024
Published: May 24, 2024

REFERENCES

1. Buzsáki, G., and Mizuseki, K. (2014). The log-dynamic brain: how skewed distributions affect network operations. Nat. Rev. Neurosci. *15*, 264–278.
2. Buzsaki, G., and Buzsaki, G. (2021). The Brain from Inside Out (Oxford University Press).
3. Levenstein, D., and Okun, M. (2023). Logarithmically scaled, gamma distributed neuronal spiking. J. Physiol. *601*, 3055–3069.
4. Wilting, J., and Priesemann, V. (2019). 25 years of criticality in neuroscience - established results, open controversies, novel concepts. Curr. Opin. Neurobiol. *58*, 105–111.
5. Barabasi, A.L., and Albert, R. (1999). Emergence of scaling in random networks. Science *286*, 509–512.
6. Song, S., Sjöström, P.J., Reigl, M., Nelson, S., and Chklovskii, D.B. (2005). Highly nonrandom features of synaptic connectivity in local cortical circuits. PLoS Biol. *3*, e68.
7. Hazan, L., and Ziv, N.E. (2020). Activity Dependent and Independent Determinants of Synaptic Size Diversity. J. Neurosci. *40*, 2828–2848.
8. Wittner, L., Henze, D.A., Záborszky, L., and Buzsáki, G. (2007). Three-dimensional reconstruction of the axon arbor of a CA3 pyramidal cell recorded and filled in vivo. Brain Struct. Funct. *212*, 75–83.
9. Loewenstein, Y., Kuras, A., and Rumpel, S. (2011). Multiplicative Dynamics Underlie the Emergence of the Log-Normal Distribution of Spine Sizes in the Neocortex In Vivo. J. Neurosci. *31*, 9481–9488.
10. Ikegaya, Y., Sasaki, T., Ishikawa, D., Honma, N., Tao, K., Takahashi, N., Minamisawa, G., Ujita, S., and Matsuki, N. (2013). Interpyramid spike transmission stabilizes the sparseness of recurrent network activity. Cereb. Cortex 1991 *23*, 293–304.
11. Keck, T., Keller, G.B., Jacobsen, R.I., Eysel, U.T., Bonhoeffer, T., and Hübener, M. (2013). Synaptic scaling and homeostatic plasticity in the mouse visual cortex in vivo. Neuron *80*, 327–334.
12. Cossell, L., Iacaruso, M.F., Muir, D.R., Houlton, R., Sader, E.N., Ko, H., Hofer, S.B., and Mrsic-Flogel, T.D. (2015). Functional organization of excitatory synaptic strength in primary visual cortex. Nature *518*, 399–403.
13. Wang, S.S.-H., Shultz, J.R., Burish, M.J., Harrison, K.H., Hof, P.R., Towns, L.C., Wagers, M.W., and Wyatt, K.D. (2008). Functional trade-offs in white matter axonal scaling. J. Neurosci. *28*, 4047–4056.
14. Morales-Gregorio, A., van Meegen, A., and van Albada, S.J. (2023). Ubiquitous lognormal distribution of neuron densities in mammalian cerebral cortex. Cereb. Cortex *33*, 9439–9449.
15. Fujisawa, S., Amarasingham, A., Harrison, M.T., and Buzsáki, G. (2008). Behavior-dependent short-term assembly dynamics in the medial prefrontal cortex. Nat. Neurosci. *11*, 823–833.
16. Hromádka, T., DeWeese, M.R., and Zador, A.M. (2008). Sparse Representation of Sounds in the Unanesthetized Auditory Cortex. PLoS Biol. *6*, e16.
17. Mizuseki, K., and Buzsáki, G. (2013). Preconfigured, skewed distribution of firing rates in the hippocampus and entorhinal cortex. Cell Rep. *4*, 1010–1021.
18. Mizuseki, K., and Buzsaki, G. (2014). Theta oscillations decrease spike synchrony in the hippocampus and entorhinal cortex. Philos. Trans. R. Soc. Lond. B Biol. Sci. *369*, 20120530.
19. Ponce-Alvarez, A., Jouary, A., Privat, M., Deco, G., and Sumbre, G. (2018). Whole-Brain Neuronal Activity Displays Crackling Noise Dynamics. Neuron *100*, 1446–1459.e6.
20. Petermann, T., Thiagarajan, T.C., Lebedev, M.A., Nicolelis, M.A.L., Chialvo, D.R., and Plenz, D. (2009). Spontaneous cortical activity in awake monkeys composed of neuronal avalanches. Proc. Natl. Acad. Sci. USA *106*, 15921–15926.
21. Iyer, K.K., Roberts, J.A., Hellström-Westas, L., Wikström, S., Hansen Pupp, I., Ley, D., Vanhatalo, S., and Breakspear, M. (2015). Cortical burst dynamics predict clinical outcome early in extremely preterm infants. Brain *138*, 2206–2218.
22. Linkenkaer-Hansen, K., Nikouline, V.V., Palva, J.M., and Ilmoniemi, R.J. (2001). Long-range temporal correlations and scaling behavior in human brain oscillations. J. Neurosci. *21*, 1370–1377.
23. Palva, J.M., Zhigalov, A., Hirvonen, J., Korhonen, O., Linkenkaer-Hansen, K., and Palva, S. (2013). Neuronal long-range temporal correlations and avalanche dynamics are correlated with behavioral scaling laws. Proc. Natl. Acad. Sci. USA *110*, 3585–3590.
24. Shriki, O., Alstott, J., Carver, F., Holroyd, T., Henson, R.N.A., Smith, M.L., Coppola, R., Bullmore, E., and Plenz, D. (2013). Neuronal Avalanches in the Resting MEG of the Human Brain. J. Neurosci. *33*, 7079–7090.
25. Tagliazucchi, E., Balenzuela, P., Fraiman, D., and Chialvo, D.R. (2012). Criticality in large-scale brain FMRI dynamics unveiled by a novel point process analysis. Front. Physiol. *3*, 15.
26. Taleb, N.N. (2007). The Black Swan: The Impact of the Highly Improbable (Random House).
27. Barbour, B., Brunel, N., Hakim, V., and Nadal, J.-P. (2007). What can we learn from synaptic weight distributions? Trends Neurosci. *30*, 622–629.
28. Riquelme, J.L., Hemberger, M., Laurent, G., and Gjorgjieva, J. (2023). Single spikes drive sequential propagation and routing of activity in a cortical network. Elife *12*, e79928.
29. Dragoi, G. (2023). The generative grammar of the brain: a critique of internally generated representations. Nat. Rev. Neurosci. *1–16*.
30. Katz, L.C., and Shatz, C.J. (1996). Synaptic Activity and the Construction of Cortical Circuits. Science *274*, 1133–1138.

31. Pan, Y., and Monje, M. (2020). Activity Shapes Neural Circuit Form and Function: A Historical Perspective. J. Neurosci. *40*, 944–954.

32. Huszár, R., Zhang, Y., Blockus, H., and Buzsáki, G. (2022). Preconfigured dynamics in the hippocampus are guided by embryonic birthdate and rate of neurogenesis. Nat. Neurosci. *25*, 1201–1212.

33. Farooq, U., and Dragoi, G. (2019). Emergence of preconfigured and plastic time-compressed sequences in early postnatal development. Science *363*, 168–173.

34. Dragoi, G., and Tonegawa, S. (2011). Preplay of future place cell sequences by hippocampal cellular assemblies. Nature *469*, 397–401.

35. Malvache, A., Reichinnek, S., Villette, V., Haimerl, C., and Cossart, R. (2016). Awake hippocampal reactivations project onto orthogonal neuronal assemblies. Science *353*, 1280–1283.

36. Logan, D.W., Brunet, L.J., Webb, W.R., Cutforth, T., Ngai, J., and Stowers, L. (2012). Learned recognition of maternal signature odors mediates the first suckling episode in mice. Curr. Biol. *22*, 1998–2007.

37. Kostka, J.K., and Bitzenhofer, S.H. (2022). How the sense of smell influences cognition throughout life. Neuroform *28*, 177–185.

38. Chini, M., and Hanganu-Opatz, I.L. (2021). Prefrontal Cortex Development in Health and Disease: Lessons from Rodents and Humans. Trends Neurosci. *44*, 227–240.

39. Chini, M., Pfeffer, T., and Hanganu-Opatz, I. (2022). An increase of inhibition drives the developmental decorrelation of neural activity. Elife *11*, e78811.

40. Kostka, J.K., and Hanganu-Opatz, I.L. (2023). Olfactory-driven beta band entrainment of limbic circuitry during neonatal development. J. Physiol. *601*, 3605–3630.

41. Cutts, C.S., and Eglen, S.J. (2014). Detecting pairwise correlations in spike trains: an objective comparison of methods and application to the study of retinal waves. J. Neurosci. *34*, 14288–14303.

42. Chini, M., Pöpplau, J.A., Lindemann, C., Carol-Perdiguer, L., Hnida, M., Oberländer, V., Xu, X., Ahlbeck, J., Bitzenhofer, S.H., Mulert, C., and Hanganu-Opatz, I.L. (2020). Resolving and Rescuing Developmental Miswiring in a Mouse Model of Cognitive Impairment. Neuron *105*, 60–74.e7.

43. Chini, M., Gretenkord, S., Kostka, J.K., Pöpplau, J.A., Cornelissen, L., Berde, C.B., Hanganu-Opatz, I.L., and Bitzenhofer, S.H. (2019). Neural Correlates of Anesthesia in Newborn Mice and Humans. Front. Neural Circuits *13*, 38.

44. Yu, Y., Burton, S.D., Tripathy, S.J., and Urban, N.N. (2015). Postnatal development attunes olfactory bulb mitral cells to high-frequency signaling. J. Neurophysiol. *114*, 2830–2842.

45. Tufo, C., Poopalasundaram, S., Dorrego-Rivas, A., Ford, M.C., Graham, A., and Grubb, M.S. (2022). Development of the mammalian main olfactory bulb. Dev. Camb. Engl. *149*, dev200210.

46. Claudi, F., Tyson, A.L., Petrucco, L., Margrie, T.W., Portugues, R., and Branco, T. (2021). Visualizing anatomically registered data with brainrender. Elife *10*, e65751.

47. Golshani, P., Gonçalves, J.T., Khoshkhoo, S., Mostany, R., Smirnakis, S., and Portera-Cailliau, C. (2009). Internally Mediated Developmental Desynchronization of Neocortical Network Activity. J. Neurosci. *29*, 10890–10899.

48. Rochefort, N.L., Garaschuk, O., Milos, R.I., Narushima, M., Marandi, N., Pichler, B., Kovalchuk, Y., and Konnerth, A. (2009). Sparsification of neuronal activity in the visual cortex at eye-opening. Proc. Natl. Acad. Sci. USA *106*, 15049–15054.

49. Graf, J., Rahmati, V., Majoros, M., Witte, O.W., Geis, C., Kiebel, S.J., Holthoff, K., and Kirmse, K. (2022). Network instability dynamics drive a transient bursting period in the developing hippocampus in vivo. Elife *11*, e82756.

50. Sitthiyot, T., and Holasut, K. (2020). A simple method for measuring inequality. Palgrave Commun. *6*, 112–119.

51. Rubinov, M., and Sporns, O. (2010). Complex network measures of brain connectivity: uses and interpretations. Neuroimage *52*, 1059–1069.

52. Antonello, P.C., Varley, T.F., Beggs, J., Porcionatto, M., Sporns, O., and Faber, J. (2022). Self-organization of in vitro neuronal assemblies drives to complex network topology. Elife *11*, e74921.

53. Bassett, D.S., and Bullmore, E.T. (2017). Small-World Brain Networks Revisited. Neuroscientist *23*, 499–516.

54. Barabási, D.L., Bianconi, G., Bullmore, E., Burgess, M., Chung, S., Eliassi-Rad, T., George, D., Kovács, I.A., Makse, H., Nichols, T.E., et al. (2023). Neuroscience Needs Network Science. J. Neurosci. *43*, 5989–5995.

55. Brynildsen, J.K., Rajan, K., Henderson, M.X., and Bassett, D.S. (2023). Network models to enhance the translational impact of cross-species studies. Nat. Rev. Neurosci. *24*, 575–588.

56. Hilgetag, C.C., and Goulas, A. (2016). Is the brain really a small-world network? Brain Struct. Funct. *221*, 2361–2366.

57. Vragović, I., Louis, E., and Díaz-Guilera, A. (2005). Efficiency of informational transfer in regular and complex networks. Phys. Rev. E *71*, 036122.

58. Bollmann, Y., Modol, L., Tressard, T., Vorobyev, A., Dard, R., Brustlein, S., Sims, R., Bendifallah, I., Leprince, E., de Sars, V., et al. (2023). Prominent in vivo influence of single interneurons in the developing barrel cortex. Nat. Neurosci. *26*, 1555–1565.

59. Markram, H., Toledo-Rodriguez, M., Wang, Y., Gupta, A., Silberberg, G., and Wu, C. (2004). Interneurons of the neocortical inhibitory system. Nat. Rev. Neurosci. *5*, 793–807.

60. Hendry, S.H., Schwark, H.D., Jones, E.G., and Yan, J. (1987). Numbers and proportions of GABA-immunoreactive neurons in different areas of monkey cerebral cortex. J. Neurosci. *7*, 1503–1519.

61. Dorrn, A.L., Yuan, K., Barker, A.J., Schreiner, C.E., and Froemke, R.C. (2010). Developmental sensory experience balances cortical excitation and inhibition. Nature *465*, 932–936.

62. Vogels, T.P., Sprekeler, H., Zenke, F., Clopath, C., and Gerstner, W. (2011). Inhibitory plasticity balances excitation and inhibition in sensory pathways and memory networks. Science *334*, 1569–1573.

63. Song, S., Miller, K.D., and Abbott, L.F. (2000). Competitive Hebbian learning through spike-timing-dependent synaptic plasticity. Nat. Neurosci. *3*, 919–926.

64. Marques-Smith, A., Lyngholm, D., Kaufmann, A.K., Stacey, J.A., Hoerder-Suabedissen, A., Becker, E.B.E., Wilson, M.C., Molnár, Z., and Butt, S.J.B. (2016). A Transient Translaminar GABAergic Interneuron Circuit Connects Thalamocortical Recipient Layers in Neonatal Somatosensory Cortex. Neuron *89*, 536–549.

65. Shen, J., and Colonnese, M.T. (2016). Development of Activity in the Mouse Visual Cortex. J. Neurosci. *36*, 12259–12275.

66. Zhang, Z., Jiao, Y.-Y., and Sun, Q.-Q. (2011). Developmental maturation of excitation and inhibition balance in principle neurons across four layers of somatosensory cortex. Neuroscience *174*, 10–25.

67. Murata, Y., and Colonnese, M.T. (2020). GABAergic interneurons excite neonatal hippocampus in vivo. Sci. Adv. *6*, eaba1430.

68. Colonnese, M.T., Kaminska, A., Minlebaev, M., Milh, M., Bloem, B., Lescure, S., Moriette, G., Chiron, C., Ben-Ari, Y., and Khazipov, R. (2010). A Conserved Switch in Sensory Processing Prepares Developing Neocortex for Vision. Neuron *67*, 480–498.

69. Sonntag, M., Englitz, B., Kopp-Scheinpflug, C., and Rübsamen, R. (2009). Early postnatal development of spontaneous and acoustically evoked discharge activity of principal cells of the medial nucleus of the trapezoid body: an in vivo study in mice. J. Neurosci. *29*, 9510–9520.

70. Mizuno, H., Ikezoe, K., Nakazawa, S., Sato, T., Kitamura, K., and Iwasato, T. (2018). Patchwork-Type Spontaneous Activity in Neonatal Barrel Cortex Layer 4 Transmitted via Thalamocortical Projections. Cell Rep. *22*, 123–135.

71. Dooley, J.C., Glanz, R.M., Sokoloff, G., and Blumberg, M.S. (2020). Self-Generated Whisker Movements Drive State-Dependent Sensory Input to Developing Barrel Cortex. Curr. Biol. *30*, 2404–2410.e4.

72. Arakawa, H., and Erzurumlu, R.S. (2015). Role of whiskers in sensorimotor development of C57BL/6 mice. Behav. Brain Res. *287*, 146–155.

73. Akhmetshina, D., Nasretdinov, A., Zakharov, A., Valeeva, G., and Khazipov, R. (2016). The Nature of the Sensory Input to the Neonatal Rat Barrel Cortex. J. Neurosci. *36*, 9922–9932.

74. Yang, J.-W., Kilb, W., Kirischuk, S., Unichenko, P., Stüttgen, M.C., and Luhmann, H.J. (2018). Development of the whisker-to-barrel cortex system. Curr. Opin. Neurobiol. *53*, 29–34.

75. Quast, K.B., Ung, K., Froudarakis, E., Huang, L., Herman, I., Addison, A.P., Ortiz-Guzman, J., Cordiner, K., Saggau, P., Tolias, A.S., and Arenkiel, B.R. (2017). Developmental broadening of inhibitory sensory maps. Nat. Neurosci. *20*, 189–199.

76. Telesford, Q.K., Joyce, K.E., Hayasaka, S., Burdette, J.H., and Laurienti, P.J. (2011). The Ubiquity of Small-World Networks. Brain Connect. *1*, 367–375.

77. Hübener, M., and Bonhoeffer, T. (2014). Neuronal plasticity: beyond the critical period. Cell *159*, 727–737.

78. Barabási, D.L., Schuhknecht, G.F.P., and Engert, F. (2024). Functional neuronal circuits emerge in the absence of developmental activity. Nat. Commun. *15*, 364.

79. Mitchell, K.J. (2020). Innate: How the Wiring of Our Brains Shapes Who We Are (Princeton University Press).

80. Sharf, T., van der Molen, T., Glasauer, S.M.K., Guzman, E., Buccino, A.P., Luna, G., Cheng, Z., Audouard, M., Ranasinghe, K.G., Kudo, K., et al. (2022). Functional neuronal circuitry and oscillatory dynamics in human brain organoids. Nat. Commun. *13*, 4403.

81. Akarca, D., Dunn, A.W.E., Hornauer, P.J., Ronchi, S., Fiscella, M., Wang, C., Terrigno, M., Jagasia, R., Vértes, P.E., Mierau, S.B., et al. (2022). Homophilic wiring principles underpin neuronal network topology in vitro. Preprint at bioRxiv. https://doi.org/10.1101/2022.03.09.483605.

82. van der Molen, T., Spaeth, A., Chini, M., Bartram, J., Dendukuri, A., Zhang, Z., Bhaskaran-Nair, K., Blauvelt, L.J., Petzold, L.R., Hansma, P.K., et al. (2023). Protosequences in human cortical organoids model intrinsic states in the developing cortex. Preprint at bioRxiv. https://doi.org/10.1101/2023.12.29.573646.

83. Rößler, N., Jungenitz, T., Sigler, A., Bird, A., Mittag, M., Rhee, J.S., Deller, T., Cuntz, H., Brose, N., Schwarzacher, S.W., and Jedlicka, P. (2023). Skewed distribution of spines is independent of presynaptic transmitter release and synaptic plasticity and emerges early during adult neurogenesis. Open Biol. *13*, 230063.

84. Colonnese, M.T., Shen, J., and Murata, Y. (2017). Uncorrelated Neural Firing in Mouse Visual Cortex during Spontaneous Retinal Waves. Front. Cell. Neurosci. *11*, 289.

85. Barabási, D.L., Beynon, T., Katona, Á., and Perez-Nieves, N. (2023). Complex computation from developmental priors. Nat. Commun. *14*, 2226.

86. Lin, I.-C., Okun, M., Carandini, M., and Harris, K.D. (2015). The Nature of Shared Cortical Variability. Neuron *87*, 644–656.

87. Schulz, D.P.A., Sahani, M., and Carandini, M. (2015). Five key factors determining pairwise correlations in visual cortex. J. Neurophysiol. *114*, 1022–1033.

88. de la Rocha, J., Doiron, B., Shea-Brown, E., Josić, K., and Reyes, A. (2007). Correlation between neural spike trains increases with firing rate. Nature *448*, 802–806.

89. Cohen, M.R., and Maunsell, J.H.R. (2009). Attention improves performance primarily by reducing interneuronal correlations. Nat. Neurosci. *12*, 1594–1600.

90. Kohn, A., and Smith, M.A. (2005). Stimulus Dependence of Neuronal Correlation in Primary Visual Cortex of the Macaque. J. Neurosci. *25*, 3661–3673.

91. Ecker, A.S., Berens, P., Keliris, G.A., Bethge, M., Logothetis, N.K., and Tolias, A.S. (2010). Decorrelated Neuronal Firing in Cortical Microcircuits. Science *327*, 584–587.

92. Barreiro, A.K., and Ly, C. (2018). Investigating the Correlation–Firing Rate Relationship in Heterogeneous Recurrent Networks. J. Math. Neurosci. *8*, 8.

93. Doiron, B., Litwin-Kumar, A., Rosenbaum, R., Ocker, G.K., and Josić, K. (2016). The mechanics of state-dependent neural correlations. Nat. Neurosci. *19*, 383–393.

94. Luccioli, S., Angulo-Garcia, D., Cossart, R., Malvache, A., Módol, L., Sousa, V.H., Bonifazi, P., and Torcini, A. (2018). Modeling driver cells in developing neuronal networks. PLoS Comput. Biol. *14*, e1006551.

95. Mòdol, L., Sousa, V.H., Malvache, A., Tressard, T., Baude, A., and Cossart, R. (2017). Spatial Embryonic Origin Delineates GABAergic Hub Neurons Driving Network Dynamics in the Developing Entorhinal Cortex. Cereb. Cortex N. Y. N *27*, 4649–4661.

96. Bonifazi, P., Goldin, M., Picardo, M.A., Jorquera, I., Cattani, A., Bianconi, G., Represa, A., Ben-Ari, Y., and Cossart, R. (2009). GABAergic hub neurons orchestrate synchrony in developing hippocampal networks. Science *326*, 1419–1424.

97. Kleberg, F.I., and Triesch, J. (2018). Neural oligarchy: how synaptic plasticity breeds neurons with extreme influence. Preprint at bioRxiv. https://doi.org/10.1101/361394.

98. Weir, K., Blanquie, O., Kilb, W., Luhmann, H.J., and Sinning, A. (2014). Comparison of spike parameters from optically identified GABAergic and glutamatergic neurons in sparse cortical cultures. Front. Cell. Neurosci. *8*, 460.

99. Gao, L., Liu, S., Wang, Y., Wu, Q., Gou, L., and Yan, J. (2023). Single-neuron analysis of dendrites and axons reveals the network organization in mouse prefrontal cortex. Nat. Neurosci. *26*, 1111–1126.

100. Dorkenwald, S., Matsliah, A., Sterling, A.R., Schlegel, P., Yu, S., McKellar, C.E., Lin, A., Costa, M., Eichler, K., Yin, Y., et al. (2023). Neuronal wiring diagram of an adult brain. Preprint at bioRxiv. https://doi.org/10.1101/2023.06.27.546656.

101. Astle, D.E., Johnson, M.H., and Akarca, D. (2023). Toward computational neuroconstructivism: a framework for developmental systems neuroscience. Trends Cogn. Sci *27*, 726–744.

102. Hiesinger, P.R. (2021). The Self-Assembling Brain (Princeton University Press).

103. Goulas, A., Betzel, R.F., and Hilgetag, C.C. (2019). Spatiotemporal ontogeny of brain wiring. Sci. Adv. *5*, eaav9694.

104. Juczewski, K., Koussa, J.A., Kesner, A.J., Lee, J.O., and Lovinger, D.M. (2020). Stress and behavioral correlates in the head-fixed method: stress measurements, habituation dynamics, locomotion, and motor-skill learning in mice. Sci. Rep. *10*, 12245.

105. Kislin, M., Mugantseva, E., Molotkov, D., Kulesskaya, N., Khirug, S., Kirilkin, I., Pryazhnikov, E., Kolikova, J., Toptunov, D., Yuryev, M., et al. (2014). Flat-floored air-lifted platform: a new method for combining behavior with microscopy or electrophysiology on awake freely moving rodents. J. Vis. Exp. *88*, e51869.

106. Steinmetz, N.A., Aydin, C., Lebedeva, A., Okun, M., Pachitariu, M., Bauza, M., Beau, M., Bhagat, J., Böhm, C., Broux, M., et al. (2021). Neuropixels 2.0: A miniaturized high-density probe for stable, long-term brain recordings. Science *372*, eabf4588.

107. Rossant, C., Kadir, S.N., Goodman, D.F.M., Schulman, J., Hunter, M.L.D., Saleem, A.B., Grosmark, A., Belluscio, M., Denfield, G.H., Ecker, A.S., et al. (2016). Spike sorting for large, dense electrode arrays. Nat. Neurosci. *19*, 634–641.

108. (2023). Gini Coefficient and the Lorentz Curve. https://de.mathworks.com/matlabcentral/fileexchange/28080-gini-coefficient-and-the-lorentz-curve.

109. Stimberg, M., Brette, R., and Goodman, D.F. (2019). Brian 2, an intuitive and efficient neural simulator. Elife *8*, e47314.

110. Trakoshis, S., Martínez-Cañada, P., Rocchi, F., Canella, C., You, W., Chakrabarti, B., Ruigrok, A.N., Bullmore, E.T., Suckling, J., Markicevic,

M., et al. (2020). Intrinsic excitation-inhibition imbalance affects medial prefrontal cortex differently in autistic men versus women. Elife *9*, e55684.

111. Bates, D., Mächler, M., Bolker, B., and Walker, S. (2014). Fitting Linear Mixed-Effects Models using lme4. Preprint at ArXiv14065823 Stat. https://doi.org/10.18637/jss.v067.i01.

112. Kuznetsova, A., Brockhoff, P.B., and Christensen, R.H.B. (2017). lmerTest Package: Tests in Linear Mixed Effects Models. J. Stat. Softw. *82*, 1–26.

113. Lüdecke, D., Ben-Shachar, M., Patil, I., Waggoner, P., and Makowski, D. (2021). performance: An R Package for Assessment, Comparison and Testing of Statistical Models. J. Open Source Softw. *6*, 3139.

114. Lüdecke, D. (2021). sjPlot: Data Visualization for Statistics in Social Science.

115. Lenth, R.V. (2020). Emmeans: Estimated Marginal Means, Aka Least-Squares Means.

STAR★METHODS

KEY RESOURCES TABLE

REAGENT or RESOURCE	SOURCE	IDENTIFIER
Deposited Data		
Raw Data	This paper	https://gin.g-node.org/mchini/Chini_et_al_Preconfigured
Experimental Models: Organisms/Strains		
Mouse: C57BL6/J	The Jackson Laboratory	Strain #: 000664
Software and Algorithms		
Original code	This paper	https://zenodo.org/doi/10.5281/zenodo.11091323
Python 3.11.3	Python Software Foundation	https://www.python.org/
MATLAB R2019b	Mathworks	https://ww2.mathworks.cn/
R 4.3.1	The R Foundation for Statistical Computing	https://www.r-project.org/
Other		
Phase 3B Neuropixels 1.0 silicon probes	IMEC, Belgium	www.neuropixels.org

RESOURCE AVAILABILITY

Lead contact

Further information and requests for resources and reagents should be directed to and will be fulfilled by the lead contact, Mattia Chini (mattia.chini@zmnh.uni-hamburg.de).

Materials availability

The study did not generate new unique reagents.

Data and code availability

- SUA data that was newly generated for this study is available at the following open-access repository: https://gin.g-node.org/mchini/Chini_et_al_Preconfigured
- Code, processed data and statistical analysis supporting the findings of this study are available at the following open-access repository: https://zenodo.org/doi/10.5281/zenodo.11091323
- Any additional information required to reanalyze the data reported in this work paper is available from the lead contact upon request.

EXPERIMENTAL MODEL AND STUDY PARTICIPANT DETAILS

All experiments were performed in compliance with the German laws and following the European Community guidelines regarding the research animal's use. All experiments were approved by the local ethical committee (G132/12, G17/015, N18/015, N19/121). Experiments were carried out on C57BL/6J mice of both sexes. Mice were housed in individual cages on a 12 h light/12 h dark cycle, and were given access to water and food *ad libitum*. P16-60 mice were housed with a minimum of two cage-mates after weaning. The mice had access to nesting material in the form of tissues and wooden gnawing material. The day of birth was considered P0. Details on the data acquisition and experimental setup of open-access datasets that were used in this project have been previously published.[39,40]

METHOD DETAILS

In vivo electrophysiology in P4-12 mice

Surgery. *In vivo* extracellular recordings were performed from the PFC and the ventral portion of the OB of non-anesthetized P4-P12 mice. The surgery and animal preparation were analogous for the two brain regions. Before starting with the surgical procedure, a local anesthetic was applied on the neck muscles (0.5% bupivacain/1% lidocaine). The surgery was performed under isoflurane anesthesia (induction: 5%; maintenance: 1–3%, lower for older pups, higher for younger pups). Neck muscles were severed to minimize muscle artifacts. A craniotomy over the PFC (0.5 mm anterior to bregma, 0.1–0.5 mm lateral to the midline) or the OB (0.5–0.8 mm anterior to frontonasal suture, 0.5 mm lateral to inter-nasal suture) was performed by carefully thinning the skull and then

removing it with the use of a motorized drill. Mice were head-fixed into a stereotactic frame and kept on a heated (37°) surface surrounded by cotton wool throughout the entire recording. To record from the PFC, a Neuropixels probe 1.0 phase 3B (Imec, Belgium) was slowly vertically inserted (angle 0°) into the frontal lobe (insertion time 20–30 min), at a depth varying between 2.6 and 4 mm depending on the age of the animal. Due to the small size of the brain, in younger animals, not all 384 recording channels were inserted in the brain. The tip of the probe was used as reference. To record from the OB, a single-shank silicon probe (NeuroNexus, MI, USA) with 16 recording sites and 50 μm inter-site spacing was vertically inserted (angle 0°) at a depth varying between 1.0 and 2.0 mm. A silver wire inserted in the cerebellum was used as reference. Both probe types were inserted using a micromanipulator. Before signal acquisition, mice were allowed to recover for ~45 min, to maximize the quality and stability of the recording as well as single units' yield.

Signal acquisition. For PFC recordings, signals from the bottom 384 channels were recorded at a 30 kHz using the Neuropixels head-stage 1.0 and Neuropixels 1.0 PXIe acquisition system (Imec, Belgium). The SUA signal was acquired through the OpenEphys interface and the Neuropixels plugin (AP gain = 500, AP Filter Cut = ON). For OB recordings, signals were band-pass filtered (0.1–9 kHz) and digitized (32 kHz) by a multichannel amplifier (Digital Lynx SX; Neuralynx, Bozeman, MO, USA) and acquired through the Cheetah acquisition software (Neuralynx, Bozeman, MO, USA).

Histology. Epifluorescence images of coronal brain sections were acquired postmortem to reconstruct the position of the DiI-stained recording electrode. Only mice in which the electrodes were placed in the correct position were kept for further analysis.

In vivo electrophysiology in P16-60 mice

Surgery. Acute *In vivo* extracellular recordings were performed from the PFC of awake, head-fixed mice of both sexes. Before starting with the surgical procedure to implant a metal head-plate (Neurotar, Helsinki, Finland) for head-fixation, buprenorphine (0.5 mg/kg bw) was injected subcutaneously. The surgery was performed under isoflurane anesthesia (induction: 5%; maintenance: 2.5%). Anesthesia depth was confirmed with the paw withdrawal reflex. Eyes were covered with an ointment (Vidisic, Bausch + Lomb, Berlin, Germany) to prevent them from drying out. After disinfection with Betasisodona, the scalp was removed from the top of the head and the edges treated for analgesia with application of a Lidocain/Bupivicain mixture (0.5% bupivacain/1% lidocaine). A craniotomy was performed to make the mPFC (0.5–2.0 mm anterior to bregma, 0.1–0.5 mm right to the midline) accessible for recordings. A synthetic window was fixed to the skull around the craniotomy to be able to protect the tissue with Kwik-Cast sealant (World Precision Instruments, Friedberg, Germany). A silver wire, serving as a ground and reference electrode, was inserted between the skull and cerebellum. The metal head-plate was attached to the skull with dental cement. For recovery from anesthesia, mice were placed in a cage on a heating mat and after being fully awake, they were put back into their home cage with their cage mates. For further analgesia, Metacam (0.5 mg/mL, Boehringer-Ingelheim, Germany) was mixed into soft food and provided for 48 h after the surgery.

Training and signal acquisition. After recovery from the surgery, mice were accustomed to the head-fixation system and trained to move the air-lifted carbon cage from the MobileHomeCage system (Neurotar, Helsinki, Finland). To perform electrophysiological recordings, the craniotomy was uncovered and an electrode (NeuroNexus, MI, USA) was stereotactically inserted into the mPFC (one-shank, A1x16-channel, 100 μm-spaced, 2.0 mm deep). The signal was acquired for 30–40 min. Extracellular signals were band-pass filtered (0.1–9000 Hz) and digitized (32 kHz) with a multichannel extracellular amplifier (Digital Lynx SX; Neuralynx, Bozeman, MO, USA). During the electrophysiological recordings, mice were head-fixed and able to move the air-lifted platform, mimicking free locomotion.[104,105] All mice showed a combination of voluntary movement and quiet wakefulness. To ensure that we analyzed data from a consistent behavioral state, we excluded movement periods from further analysis. For a subset of mice, we also recorded eye movement and pupil size, and did not detect any sleep epoch. We focused our analysis on periods of quiet wakefulness because these behavioral epochs were much more abundant and displayed a higher signal quality. Multiple electrophysiological recordings were performed in the same animal, with a minimal recovery period of two days in between the recordings. Between recording sessions, mice were housed in their standard housing conditions and did not perform any particular behavioral task.

Histology. Epifluorescence images of coronal brain sections were acquired postmortem to reconstruct the position of the recording electrode. To this aim, after the last recording, a DiI-coated electrode was inserted. Only mice in which the electrodes were placed in the correct position were kept for further analysis.

QUANTIFICATION AND STATISTICAL ANALYSIS

Spike sorting

P4-12 PFC recordings were spike-sorted with Kilosort 2.5[106] (fshigh = 500, minFR = 0.001, spkTh = −4, sig = 20, nblocks = 5). All other recordings were spike-sorted with Klusta.[107] Automatically-obtained clusters were manually curated using phy (https://github.com/cortex-lab/phy).

SUA firing statistics and shape distribution parameters

Firing rate. Firing rate (in Hz) was computed as the number of spikes divided by the total recording length in seconds.

Spike-Time Tiling Coefficient (STTC)

The STTC (timescale of 10 ms) was computed as follows[39,41]:

$$STTC = \frac{1}{2}\left(\frac{P_A - T_B}{1 - P_A T_B} + \frac{P_B - T_A}{1 - P_B T_A}\right) \quad \text{(Equation 2)}$$

where P_A is the proportion of spikes of spike train A that occurs within $\pm\Delta t$ of a spike train B spike. T_A is the proportion of time that occurs within (is "tiled" by) $\pm\Delta t$ from spikes of spike train A. The same applies for P_B and T_B. $\pm\Delta t$ is the lag parameter and was set at 10 ms.

Skewness

Skewness was computed using the homonymous MATLAB function *skewness* as:

$$skewness = E\left[\left(\frac{(X - \mu)}{\sigma}\right)^3\right] \quad \text{(Equation 3)}$$

Where X is the random variable of interest, μ is its mean, σ its standard deviation, and E is the expectation operator.

Kurtosis

Kurtosis was computed using the homonymous MATLAB function *kurtosis* as:

$$kurtosis = E\left[\left(\frac{(X - \mu)}{\sigma}\right)^4\right] \quad \text{(Equation 4)}$$

Where X is the random variable of interest, μ is its mean, σ its standard deviation, and E is the expectation operator.

Gini coefficient

The Gini coefficient was computed using the MATLAB function *gini*[108]. The Gini coefficient is calculated by taking the ratio of the area that lies between the line of equality and the Lorenz curve, over the total area under the line of equality.

Complex network properties

To calculate the network properties of the developing brain, we utilized symmetrical STTC matrices. The pre-processing consisted of thresholding and binarization. To threshold the data, we computed surrogate spiking data for each mouse individually. To account for the slow co-modulation of firing rates that is typical of the developing brain, we generated surrogate spiking data by leaving the timing of spikes unaffected and shuffling the identity of the neuron that emitted the spike. This pseudo-randomization thus generated surrogate spike vectors while preserving the population rate. Using these spike vectors, we then computed at least 1000 STTC values on shuffled data, and used the 90th percentile value to threshold and binarize the real-data STTC matrices. The binary and undirected matrices were then analyzed with the MATLAB Brain Connectivity Toolbox.[51]

The clustering coefficient and transitivity of the matrices were extracted with the *clustering_coef_bu* and *transitivity_bu* functions, respectively. To compute the characteristic path length, we first computed the distance matrix (*distance_bin*) and then computed the characteristic path length (*charpath*) without including distances on the main diagonal and infinite distances. All these values were normalized by dividing them with a corresponding "null" value that was computed by generating 100 synthetic random networks (*makerandCIJ_und*), extracting the same parameters for each iteration, and computing the average. Small-worldness was computed by dividing the normalized clustering coefficient by the normalized characteristic path length.

The four "hubness" parameters that we used to compute the composite "hubness score" were also extracted with the same MATLAB toolbox. For each node individually, we computed its total amount of edges (i.e., its degree, using *degrees_und*), its total amount of weights (*strengths_und*, this is the only parameter that was computed on weighted and not binary matrices), its betweenness centrality (*betweenness_bin*, after using *weight_conversion* and 'lengths') and its closeness centrality (the inverse of the node's average distance computed with *distance_bin*).

Neural network modeling

All simulations were performed using Brian2 for Python3.7.[109]

General structural neural network architecture

The architecture of the network[39,110] is schematically illustrated in Figures 6A–6C. The network was composed of 400 conductance-based leaky integrate-and-fire neurons, 80% of which were excitatory (PYRs) ($N = 320$) and 20% were inhibitory (INs) ($N = 80$). PYRs were simulated with outgoing excitatory synapses and INs with outgoing inhibitory synapses. Excitatory (PYR → PYR, PYR → IN) and inhibitory (IN → IN and IN → PYR) synapses were simulated as AMPA and GABA conductances, respectively. Due to the near-instantaneous rise times of AMPA- and GABA-mediated currents (both typically <0.5 ms), we opted to neglect these in the simulations. Synaptic transmission was assumed to be instantaneous (i.e., with zero delay).

The dynamics of each excitatory and inhibitory cell were governed by the following stochastic differential equation:

$$C_m\frac{dV_m}{dt} = -g_L(V_m - V_L) - g_{AMPA}(V_m - E_{AMPA}) - g_{GABA}(V_m - E_{GABA}) + \sigma\xi \quad \text{(Equation 5)}$$

with

$$\frac{dg_{AMPA}}{dt} = -\frac{g_{AMPA}}{\tau_{AMPA}} \quad \text{(Equation 6)}$$

and

$$\frac{dg_{GABA}}{dt} = -\frac{g_{GABA}}{\tau_{GABA}} \quad \text{(Equation 7)}$$

where V_m is the membrane potential, V_L is the leak membrane potential and E_{AMPA} and E_{GABA} denote the AMPA and GABA current reversal potentials, respectively. The synaptic conductance parameters and the corresponding decay time constants are denoted by g_{AMPA}, g_{GABA} and τ_{AMPA}, τ_{GABA}, respectively. $\sigma\xi$ is a noise term that is generated by an Ornstein-Uhlenbeck process with zero mean. The networks were simulated for a duration of 10 s (simulations without plasticity) or 50 s (simulations with plasticity). All simulations were performed with a time step (dt) of 0.1 ms and integrated with Euler's method. All parameter values/ranges used in the simulations are listed in Table S1.

Random variables

To avoid choosing an arbitrary structural neural network architecture, a number of parameters were treated as ''random variables'' and systematically varied across a biologically-constrained range. These parameters included: 1) the noisy input (Ornstein-Uhlenbeck process) that was used to independently drive PYRs and INs; 2) the mean probability with which neurons were connected, which was the same for all possible population combinations: i) PYR-PYR, ii) PYR-IN, iii) IN-PYR, iv) IN-IN; 3) the mean size of excitatory and inhibitory synaptic weights.

Synaptic parameters

In these networks, we studied the influence on the simulated SUA statistics exerted by three synaptic parameters: whether the size of synapses followed a normal or a log-normal distribution, whether the number of synapses of individual neurons followed a normal or a log-normal distribution, and whether the number of dendritic and axonic (incoming and outgoing) synapses were correlated or uncorrelated with each other. The 2 possible configurations for the 3 synaptic parameters resulted in $2^3 = 8$ different network types, of which we simulated 1000 each. These 3 synaptic parameters were simultaneously varied for the entire network and not in a neuronal population-specific manner.

Number of synapses and correlation between dendritic and axonic synapses

We first generated a normal (mean = 1, std = 1/4) or log-normal (mean of the underlying normal = 0, std of the underlying normal = 0.5) relative distribution of the number of connections that was normalized to have a sum = 1. To account for the different number of connections in different simulations (see previous paragraph *Random variables*), the relative distribution was then scaled by the total amount of connections between the pre- and post-synaptic population according to:

$$tot.\,connections = N_{pre} * N_{post} * mean\ connectivity \quad \text{(Equation 8)}$$

Where N_{pre} is the number of presynaptic neurons (PYRs or INs), N_{post} is the number of postsynaptic neurons (PYRs or INs) and *mean connectivity* is a parameter that is randomly varied between simulations. Please note that, due to the normalization, the fact that the two original distributions have a different mean is irrelevant. This process was repeated until the simulated number of connections had no negative values and no values exceeded the maximum amount of possible synaptic partners (N_{pre} or N_{post}). In the case of uncorrelated incoming and outgoing number of synapses, the same procedure was then repeated for the distribution of pre/post-synaptic partners. In simulations in which the number of incoming and outgoing synapses was correlated, the number of presynaptic connections was drawn using a random number generator (numpy function *rng.choice*), in which the maximum value (a, following the nomenclature of *rng.choice*) was set equal to the number of pre/post-synaptic neurons, the number of values to draw was equal to *tot. connections* (size, following the nomenclature of *rng.choice*) and the probabilities associated with each presynaptic neuron were equal to the number of outgoing connections of that neuron (p, following the nomenclature of *rng.choice*). This resulted in a Pearson correlation of the number of incoming and outgoing synapses ~0.85, in line with what has been described in Drosophila.[100] Finally, to generate a connectivity matrix in which each neuron had the desired amount of incoming and outgoing connections, we used the *directed_havel_hakimi_graph* function from the *networkx* python package.

Size of synapses

The distribution of synaptic sizes was simulated according to a normal (mean = $\sqrt[2]{e}$, std = 1/2) or log-normal (mean of the underlying normal = 0, std of the underlying normal = 1) distribution. Please note that it can be analytically shown that the two distributions have the same mean. These distributions were then scaled by different scalars (see Table S1) according to the specifics of the connected populations.

Synaptic plasticity

For simulations with synaptic plasticity, synaptic parameters were set to their extreme configuration (lognormal distribution of synaptic weights and number, and correlated amount of incoming and outgoing number of synapses). A set of other parameters controlling the structural network architecture was systematically varied across a biologically-constrained range, analogously to simulations without synaptic plasticity (see *Random variables*). In these networks, we first simulated 10s with frozen synaptic weights, and 40s with synaptic plasticity.

PYR-PYR excitatory synapses were plastic according to a classic asymmetric Hebbian plasticity rule[63] that can be summarized as follows:

$$\frac{dW}{dt} = \frac{\eta(pre * post)}{\tau_{STDP}} \quad \text{(Equation 9)}$$

Where W is a PYR-PYR synaptic weight, *pre* and *post* are the pre- and postsynaptic activity, η is the learning rate, and τ_{STDP} is the decay time constant of the plasticity rule.

In practice, synaptic weights from a pre-synaptic neuron i to a post-synaptic neuron j (W_{ij}) were updated at every pre- and post-synaptic event occurring at time t_i and t_j such that:

$$W_{ij} \rightarrow W_{ij} + \eta x_j \text{ for presynaptic spikes at time } t_i \quad \text{(Equation 10)}$$

$$W_{ij} \rightarrow W_{ij} + \eta x_i \text{ for postsynaptic spikes at time } t_j \quad \text{(Equation 11)}$$

Where x_i and x_j are the pre- and post-synaptic trace.

x_i was updated with each spike $x_i \rightarrow x_i + 0.01$ and decayed according to:

$$\frac{dx_i}{dt} = -\frac{x_i}{\tau_{STDP}} \quad \text{(Equation 12)}$$

x_j was updated with each spike $x_j \rightarrow x_j - 0.01$ and decayed according to:

$$\frac{dx_j}{dt} = -\frac{x_j}{\tau_{STDP}} \quad \text{(Equation 13)}$$

Synaptic weights were clipped within the 0–10 range.

IN-PYR inhibitory synapses were plastic according to a symmetric plasticity rule.[62] This rule can be summarized as follows:

$$\frac{dW}{dt} = \frac{\eta(pre * post - \alpha * pre)}{\tau_{STDP}} \quad \text{(Equation 14)}$$

Where W is an IN-PYR synaptic weight, *pre* and *post* are the pre- and postsynaptic activity, α is the target rate for the postsynaptic PYR, drawn from a log-normal distribution, η is the learning rate, and τ_{STDP} is the decay time constant of the plasticity rule.

Synaptic weights W_{ij} were updated at every pre- and post-synaptic event occurring at time t_j and t_i such that:

$$W_{ij} \rightarrow W_{ij} + \eta(x_i - \alpha) \text{ for presynaptic spikes at time } t_j \quad \text{(Equation 15)}$$

$$W_{ij} \rightarrow W_{ij} + \eta x_j \text{ for postsynaptic spikes at time } t_i \quad \text{(Equation 16)}$$

Where x_i and x_j are the pre- and post-synaptic trace that increased with each spike x $x \ x \rightarrow x + 1$ and decayed according to:

$$\frac{dx}{dt} = -\frac{x}{\tau_{STDP}} \quad \text{(Equation 17)}$$

Synaptic weights were clipped within the 0–100 range.

Simulated SUA statistics and quality of model fit

For each network, we extracted the simulated spike times and computed the same 7 parameters as for the experimental data (described in *SUA firing statistics and shape distribution parameters*): skewness, kurtosis and Gini coefficient of firing rate and STTC, and the correlation between the log-transformed firing rate and STTC. To compute the quality of the model fit, we extracted the median of these 7 parameters from the P4-12 PFC dataset. For each simulation, we then computed the Euclidian distance (MATLAB function *pdist*) between the median of the experimental data and the 7D coordinates of that specific simulation. To ensure that each metric contributed equally to the distance from the experimental data, kurtosis and skewness of firing rate and STTC were divided by their maximum value. This normalized them to a range comprised between 0 and 1, as the Gini coefficient.

Statistical modeling

Statistical modeling was carried out in the R environment. All the scripts and the processed data on which the analysis is based are available on the following github repository: https://zenodo.org/doi/10.5281/zenodo.11091323.

Nested data (Figures 1, 4, and 6) were analyzed with (generalized) linear mixed-effects models (*lmer* and *glmer* functions of the *lme4* R package[111]) with "mouse" as random effect. Non-nested data were analyzed with linear models (*lm* function). Regression on data that was better fit by an exponential curve (Figure 1) was carried out with a generalized linear mixed-effect models with the following parameters: family = Gamma, link = log. For ease of interpretability and consistency with the other distribution shape parameters, kurtosis of firing rate and STTC, which followed an approximately log-normal distribution, was instead log-transformed and analyzed with a linear model.

Statistical significance for linear mixed-effects models was computed with the *lmerTest* R package[112] and the *summary* (type III sums of squares) R function. Statistical significance for linear models was computed with the *summary* R function.

When possible, model selection was performed according to experimental design. When this was not possible, models were compared using the *compare_performance* function of the *performance* R package,[113] and model choice was based on an holistic comparison of AIC, BIC, RMSE and R2.

Model output was plotted with the *plot_model* (type = 'pred') function of the *sjPlot* R package.[114] 95% C.I. were computed using the *confint* R function.

Post hoc analysis was carried out using the *emmeans* and *emtrends* functions of the *emmeans* R package.[115]

3 | Discussion

3.1 Considerations on the methodology to dissect the architecture and function of developing brain networks

A constant pursuit in neuroscience is to understand the biological mechanisms underlying the function of neuronal networks. The intricate architecture of neuronal connection is the basis for a broad spectrum of brain functions, from sensory perception to higher-order cognition. Until recently, the impact of sensory modalities on cognitive processing along development represents an open question, mainly due to the technical challenges. For example, the neonatal stage is characterized by rapid and dynamic changes in the structure and function of the brain, therefore dissecting the developmental trajectory of the networks linking olfaction with cognition requires complex and longitudinal experimental designs.

During the last decade, cell-type specific manipulation approaches such as chemogenetics and optogenetics have become novel and powerful tools for dissecting brain circuits and identifying their functions, since they allow precise control of distinct neuronal populations (Deisseroth, 2015; Roth, 2016). Taking advantage of a transgenic Cre-recombinase mouse line in combination with Cre-dependent viral vectors, we expressed the AAVs carrying the gene for a receptor that can be activated solely by a synthetic ligand, or a light-sensitive opsin, into the OBs of Tbet-Cre mice to selectively target and manipulate the activity of M/TCs. The viral vector AAV9 used here brought adequate expression of chemogenetic and optogenetic actuators at similar time points in the present and previous studies, which enables the manipulation of specific neuronal populations during the neonatal period (Gretenkord et al., 2019; Xu et al., 2021; Chini et al., 2022; Kostka & Hanganu-Opatz, 2023). Expression of these tools can be also achieved with different strategies. Apart from injecting the viral tools encoding the desired receptor into

the brain region of interest, crossing a transgenic mouse line carrying the desired gene with another line with cre recombinase expressed in specific neuronal populations (Haddad et al., 2013; Graf et al., 2024), or prenatally transfecting the neuronal precursor cells by *in utero* electroporation (IUE) are implemented in practice of developmental neuroscience research to fully explore the *in vivo* applications of the tools. Though crossing transgenic mouse lines provides a possibility for cell type-specific expression without additional experimental operation, it is often costly and time-consuming to generate and maintain the required mouse lines. Also, crossbreeding mouse lines carries the risk of introducing genetic background effects which may impact the experimental outcomes (A. J. Song & Palmiter, 2018). On the other hand, IUE proves to successfully target the specific neuronal population with sufficient gene expression in cortical and sub-cortical areas such as PFC and HP shortly after birth, but there is a potential for off-target expression in other brain areas, i.e., not all cell populations can be targeted through the labeling with IUE. Furthermore, the *in utero* operation might be technically challenging particularly for those without expertise in embryonic manipulation techniques, and can cause negative stress on the mother mice. Hence, the cre-dependent AAV-driven viral expression we used to achieve region and cell-type specific manipulation offers relatively higher flexibility for the experimental designs and budgets.

Designer receptors exclusively activated by designer drugs (DREADDs) gradually became widely used for chemogenetical manipulation in neuroscience practice. Gi-DREADDs including hM4Di are found to be located on both neuronal soma and axons (Mahler et al., 2014). It has proved that hM4Di-mediated inhibition could successfully suppress the vesicle release of targeted neurons in neonatal mice (Graf et al., 2024), and acute hM4Di chemogenetics reduced network activity of neuronal networks in the developing brain (Kostka & Hanganu-Opatz, 2023; Pochinok et al., 2024). The behavioral assessment on P8 mice demonstrated in Chapter 2.2.1 (Y. Chen et al., 2023) verifies that the acute silencing of M/TC outputs with hM4Di is sufficient to diminish olfactory function at this age. Regarding applying this method repeatedly over a few days, one of the biggest technical challenges is that neonatal pups require regular interactions and feeding by their mother. Shortly after birth, rodents rely on their sense of smell for mother-infant interaction, which could be affected by the method chosen for inhibiting the olfactory inputs and further perturb their normal somatic development. As stated there, the daily manipulation procedure induced by acute C21 injections does not cause a full abolishment of olfactory function. In addition, it has been previously reported that the activity of hm4Di-expressing neurons recovered at 4 h after C21 injection (Goutaudier et al., 2020). Thus, as corroborated in Chapter 2.2.1, the subtle silencing of the M/TC outputs induced minor negative effects on the somatic growth or locomotion of neonatal mice.

Compared to chemogenetics, optogenetic approaches offer much more precise time control for exploring the roles of the brain circuits, including manipulating M/TCs with depolarizing or hyperpolarizing opsins (Gretenkord et al., 2019; Dalal & Haddad, 2022). To capitalize on its advantages of time resolution, we achieved the dual-transduction of light-sensitive ChR2 together with hM4Di on neonatal Tbet-cre^{+} mice and performed the asynchronous manipulations on the same population of targeted M/TCs, with results pointing to less responsiveness to stimuli within the OB-LEC-HP network. Besides, by evaluating the LFPs and spiking activity of the OB within millisecond-scale in response to blue light stimulations with different parameters, which is described in Chapter 2.2.2 (Y. Chen et al., 2024), we showed that the effects of *in vivo* activation ChR2-expressing neurons on network activity are highly dependent on intensities and frequencies of the rhythmic light pulses as well. These findings help the laying out of the experimental design for investigating functional brain development such as the olfactory-entorhinal-hippocampal system during neonatal stage. However, despite the cell-type specificity and temporal precision, it is almost infeasible to chronically use optogenetics for M/TC silencing, largely due to the implantation of stimulation devices required for repeated manipulation significantly interferes with normal maternal care and restricts both the somatic and brain development of the pups, and the OB location is extremely close to the nasal cavity with which the pups frequently use to localize and attach the feeding from their mother. Alongside that, how to combine the optogenetic manipulation with behavior in neonatal animals remains an open question until several technical difficulties can be solved.

3.2 Olfactory inputs as a key player in structural and functional brain maturation

Abundant research has identified the role of sensory inputs in the emergence of cortical topographies and fine-tuned sensory discrimination early in life (Fox, 2002; Fox & Wong, 2005; Zheng et al., 2014; Hu et al., 2022). However, much less is known about the early sensory influence on higher-order brain regions involved in cognitive processing along development. Even more strikingly, it is fully unknown, whether the M/TC activity that is present already at birth can influence the development and later function of the downstream networks. In Chapter 2.2.1, to address these issues, we set out to investigate the role of the coordinated activity in the OB during a defined developmental period, when olfaction is exceptionally functional, in the maturation of downstream cortical-hippocampal networks, with results identifying that:

i. The impact of neonatal olfactory inputs on entorhinal-hippocampal network activity.

The unchanged olfactory behavior and no effects on endogenous OB activity after 3-day chemogenetically suppression of M/TCs mediated by hM4Di confirm that it is a reversible manipulation; in contrast, the transient olfactory output silencing daily from P8 to P10 persistently led to a reduction in the network and spiking activity of the downstream areas LEC and hippocampal CA1, as well as the inter-regional communications in OB-LEC-CA1 network during both neonatal and pre-juvenile stages. It is worth noting that the strong reduction in the synchrony and directionality of the oscillatory activity is mainly in 1–10 Hz, which encompasses the RR and theta rhythm previously shown to reflect the entrainment of the cortical-hippocampal networks (Zelano et al., 2016; Gretenkord et al., 2019). The present findings indicate that the short-term absence of olfactory inputs disrupted the local neuronal interactions within LEC and subsequently hippocampal CA1, and further impaired the long-range synchrony and directionality within OB-LEC-HP network in a long-term manner. These complement previous studies showing the effects of early life events, such as maternal deprivation or neonatal handling, on the development of hippocampal formation and network coupling (Meaney et al., 1988; Reincke & Hanganu-Opatz, 2017). On the other hand, it has been shown that the topographical and functional development of other sensory systems is critically shaped by the corresponding sensory peripheries, such as visual cortex (Ackman et al., 2012; Hanganu et al., 2006), auditory cortex (E. F. Chang & Merzenich, 2003; Nakahara et al., 2004; Xue et al., 2022), and somatosensory cortex (L.-J. Lee et al., 2009; Sieben et al., 2015). Given that cross-modal plasticity might be able to compensate the missing sensory inputs (Xu et al., 2020; Ewall et al., 2021), we performed the same chemogenetical silencing of M/TC outputs from P13 to P15, a later developmental time window when eyelids and ear canals are opened, to test the specificity of the chosen age window (P8-10). The manipulation at this age did not affect OB-LEC-HP network activity later in life, suggesting that taking out olfactory inputs when both visual and auditory systems are functional has much less detrimental effects on the development of the hippocampal formation. This emphasizes the significance of olfactory inputs during early postnatal days for functional network maturation.

ii. The contribution of neonatal olfactory inputs to downstream neuronal morphology.

By using a set of neuroanatomical and molecular biological methods, including retrograde viral tracing, immunostaining and morphological investigation, we found that the transient olfactory output silencing from P8 to P10 compromised the dendritic complexity and spine densities of entorhinal pyramidal neurons which project to hippocampal CA1, and this sparsification persisted to pre-juvenile age. The decreased dendritic arborization was

confined to the apical dendrites that are responsible for receiving synaptic inputs from upstream areas. This morphological dysfunction lay at the same time point when the electrical activity and connectivity within LEC-HP network were altered, which offers a potential mechanism on the neuronal structural level contributing to the weakened LEC-HP coupling. It has been shown that the development of apical dendrites requires specific instruction from upstream innervating axons (Szczurkowska et al., 2020). Moreover, during the first two postnatal weeks, a substantial activity-dependent reorganization of dendritic arborization takes place in cortical areas and actively contributes to the maturation of activity pattern (Wayman et al., 2006; Bitzenhofer et al., 2021). Considering the anatomical basis of the LEC-HP neuronal projection, it is also likely that the morphological alterations are not restricted to pyramidal neurons but also affect DG-projecting fan cells located in LEC, which are known to receive strong olfactory inputs (Bitzenhofer et al., 2022) and important for association memory (Vandrey et al., 2020; J. Y. Lee et al., 2021).

iii. Long-term functional consequences of transient silencing of olfactory inputs during neonatal stage.

Since the chemogenetical manipulation confined to P8–P10 resulted in perturbations of neuronal structure and network activity which last to pre-juvenile age, it is worth asking if the impaired LEC-HP network activity ultimately leads to any impairments of learning and memory functions. Mice at pre-juvenile stage have been previously identified to get well-developed sensory and motor abilities required for the object recognition tests that are applied in the present study (Hartung et al., 2016b; Schepanski et al., 2022), which capitalizes on the preference of mice to explore a novel object and recognize when an object has been relocated. Both object recognition and association recognition memory rely strongly on the LEC and HP functions in a long lifespan (D. I. G. Wilson et al., 2013; Xu et al., 2021; Sun et al., 2019), as LEC mainly transfers non-spatial (contextual) information to HP (Hargreaves et al., 2005; Tsao et al., 2013). Interestingly, the behavioral performance in these tests later in life was impaired after transient M/TC output silencing during P8–P10, resembling the dampened entorhinal-hippocampal coupling, which is believed to facilitate the binding of information related to objects, places and contexts (Staresina et al., 2019; Fernández-Ruiz et al., 2021; X. Huang et al., 2023). On the other hand, as one of the most critical brain functions, spatial memory is highly dependent on intact HP and emerges in developing rodents from the 3rd postnatal week (Blair et al., 2013; Albani et al., 2014). The behavioral test on manipulated mice later in life also showed a poorer performance in the spatial working memory task, suggesting that temporal M/TC output silencing during P8–P10 is sufficient to prompt a long-lasting HP deficit which accounts for compromised spatial memory.

In summary, the work described in Chapter 2.2.1 extends the line of investigation on olfaction from simple sensory processing to the level of higher cognitive functions, and corroborates the critical role of neonatal olfactory inputs in the functional LEC-HP maturation and the development of associated cognitive functions. Nevertheless, there are still some limitations of the research. First, the i.p. injections of C21 used for chemogenetical manipulation allow general distribution of the compound including the whole brain. Given that PIR receives the densest and most direct inputs from M/TCs and is also important for olfactory processing, we cannot rule out the contributions of possibly inhibited PIR to dampening the OB-LEC-HP network after transient M/TC output silencing. To achieve projection-specific suppression of M/TC axonal terminals located in LEC and further test the consequences after solely manipulating OB→LEC inputs, applying the up-to-date tools for presynaptic transmission silencing (Mahn et al., 2021; Wietek et al., 2024) would be an available option in future studies. Another limitation comes to the property of the recording methods. The electrode (optrode) used in the current setup for *in vivo* electrophysiology allows 16-channel simultaneously being recorded for one region, which covers most of the cell layers in the target regions but acquires limited numbers of spiking units. For more specific analysis on single-unit spiking under spontaneous and manipulated conditions, one may consider combining higher-yield electrodes such as Neuropixels (Steinmetz et al., 2021) with optogenetic stimulation, which is currently being developed. Overall, the developmental interplay between the olfactory network and hippocampal formation found in this thesis provides deeper insights into how sensory information anatomically and functionally shapes the cognitive processing in the brain.

3.3 The olfactory network dysfunction as an early marker for neurodevelopmental disorders

In humans, the sense of smell is substantially overlooked, mainly because vision and hearing dominate the hierarchy of senses in daily life (Viberg, 2001, 2014; Roque et al., 2015). Although olfactory deficits often manifest already during the incubation stages of neurodevelopmental and neurodegenerative diseases by preceding or coexisting with the typical clinical symptoms, it remains poorly understood whether there are any common pathophysiological progressions along neuronal pathways originating from the olfactory system. Due to the pandemic of COVID-19 which is symptomized with prodromal and persistent anosmia (Spinato et al., 2020; Renaud et al., 2021), and the prevalent occurrence of lasting “brain fog” after recovery (Becker et al., 2021; Hampshire et al., 2024), the link between olfactory dysfunction and neurological disorders is attracting increasing attention

in both clinical and basic research. As what is summarized in Chapter 2.2.3 (Y. Chen & Kostka, 2024), olfactory deficits commonly precede the onset of abnormal cognitive performance in patients with neurodevelopmental and neurodegenerative diseases, and structural and functional dysfunction of the olfactory system especially the OB significantly reflects the progression of the diseases in the brain. These evidences highlight a pressing need to investigate the underlying mechanisms of olfactory impairments under disease conditions.

It has long been hypothesized that the pathophysiology of neurodevelopmental disorders initiates prior to the emergence of an appreciable symptomatology. A question that follows the key role of neonatal OB activity in the functional development of cortical-hippocampal networks is, whether there are any alternations in olfactory behavior and olfactory system in a mouse model of neuropsychiatric disorders which is identified with cortical-hippocampal impairments. We tried to answer this question in the subsequent Chapter 2.2.4 (Parbst et al., 2024) with a dual-hit GE mouse model of mental disorders during early development, in light of the converging evidence over the past few years showing the miswired communications in the HP-PFC as well as LEC-HP networks of it at the start of the 2nd postnatal week (Hartung et al., 2016b; Chini et al., 2020; Xu et al., 2021; L. Song et al., 2022). This GE mouse model mimics the etiology of neuropsychiatric disorders with a combination of two pathogenic factors: viral mimetic-induced MIA (Meyer & Feldon, 2012), and a heterozygous knockdown in the gene disrupted-in-schizophrenia 1 (Disc1$^{+/-}$) resulting in a truncated DISC1 protein (Kvajo et al., 2008). Through digging into the electrophysiological features of the developing olfactory-hippocampal-prefrontal network, we found that GE mice aged at P8-10 had weaker spontaneous activity in the OB for both oscillatory pattern and spiking activity. Correspondingly, the directionality from the OB to the downstream HP-PFC network was reduced. In contrast, the odor-evoked activity in the investigated network and odor detection were unaffected. However, the long-term memory for odor information was impaired in neonatal GE mice. Taken together, these data suggest that diminished endogenous OB activity by genetic mutation and environmental stressors for mental disorders leads to the impaired function of the neocortical-hippocampal network as well as deficits in odor-related memory.

Previous studies found that LEC, HP, and PFC are abnormally decoupled in GE mice during early postnatal development, which further contributes to the poor performance in cognitive tasks dependent on the functions of cortical-hippocampal networks later in life (Hartung et al., 2016b; Chini et al., 2020; Xu et al., 2021). These resemble the decreased activity and functional communications in the developing entorhinal-hippocampal networks following transient M/TC output silencing within the same time window

corroborated in Chapter 2.2.1, letting us question if the neurodevelopmental disorders are driven by the olfactory network dysfunction. It is worth noting that mice solely carrying the genetic mutation showed a similar reduction in endogenous OB activity as that in GE mice. Considering the existing evidence that the knockdown of Disc1 gene is not sufficient to disrupt neither the HP-PFC oscillatory activity and network coupling nor non-odor related behaviors (Oberlander et al., 2019; Xu et al., 2021), and DISC protein is highly expressed in M/TCs (Schurov et al., 2004), the reduced OB activity implies that olfactory network dysfunction occurs earlier than impaired neocortical-hippocampal communications and cognitive deficits in line with the clinical studies. At present, we can only speculate how our findings correlate with the altered olfactory system reported on patients with neuropsychiatric disorders. Nevertheless, emerging findings observed in neurodevelopmental diseases with similar olfactory/cognitive deficits are not far from our hypothesis: in animal models of ASD, reduced OB network activity and HP-PFC connectivity have been reported (Cheaha et al., 2015; Richter et al., 2019); the suppression of another susceptibility gene of SCZ and major depression have been shown to impair both oscillatory activity in the OB and attentional process mediated by HP-PFC synchrony (Tan et al., 2022). Moreover, for neurodegenerative diseases, early impairments in OB and LEC are found before the onset of cognitive decline in AD animal models, including early accumulated histological markers, neuronal death and functional disorders in LEC superficial layers (Braak & Braak, 1991; Kobro-Flatmoen et al., 2016; Goettemoeller et al., 2024), along with neuronal atrophy and altered network activity in the OB (Yao et al., 2017; S. Li et al., 2019; M. Chen et al., 2020), indicating OB and LEC are affected at the prodromal stage of AD pathology. Recently, it has been revealed that hippocampal-projecting neurons in LEC of neonatal GE mice have reduced dendritic complexity, which is aligned with a less entorhinal drive on HP-PFC network (Xu et al., 2021; Kringel et al., 2023) and the results presented in Chapter 2.2.1. These implicate a comparable disease progression from the olfactory regions to higher-order brain regions along the neuronal projections in neurological conditions, and emphasize the potential of olfactory network dysfunction to be an early indicator for neuropsychiatric disorders.

Last but not least, there are still several open options to advance our understanding of the olfactory deficits in neurological disorders in the “post-COVID” era. First of all, the reduced endogenous OB activity in neonatal GE mice might be related to the disruption of neuronal innervation from the olfactory periphery, such as the OE, which requires further histological measurements for OSN amounts or glomeruli synapses in future studies. Also, another question is raised whether a more region-specific gene manipulation in the OB could similarly cause a consequence to alter olfactory-hippocampal-prefrontal networks and behaviors, which would help identify the source of the disease progression.

3.4 Outlook and future challenges

With the identification of an early dysfunction in the olfactory network as a potential diagnostic indicator for neurodevelopmental and neurodegenerative diseases associated with cognitive impairments (Chapter 2.2.3; Chapter 2.2.4), monitoring olfactory network dysfunctions might be a helpful strategy for the diagnosis and intervention of neurological disorders in prodromal stages. It has been reported that the electrical stimulation in the olfactory system can ameliorate the memory deficits in an AD mouse model (Salimi et al., 2024) and depressive-like behavior in rats (Q. Li et al., 2023), suggesting the potential of manipulating the olfactory pathway for the treatment of neurocognitive deficits; however, the invasiveness of the surgical procedure might halt the methods on clinical application. Another promising possibility in treating neurological diseases through the olfactory system is nasal drug administration. Considering the direct access of the OE connecting to brain regions originating from the OB, the nasal route provides an advantageous and efficient pathway for the delivery of therapeutic agents to the brain which can bypass the blood-brain barrier. Recent studies have shown promising results using neuroprotective compounds through intranasal administration. In this aspect, injecting insulin intranasally was reported to improve cognitive function and slow down neurodegeneration in AD patients (Freiherr et al., 2013). Intranasal oxytocin treatment was shown to improve social abilities in children with ASD (Parker et al., 2017). Furthermore, gene therapy delivered intranasally is being investigated for its capacity to target and modify specific neuronal pathways associated with disease progression (Itokazu et al., 2021; Jaijyan et al., 2022; D. Zhang et al., 2024; Ryu et al., 2024), which need more detailed understanding for the underlying mechanisms. These offer hopes for interventions that could slow or even prevent disease progression directly at the preclinical stage.

The research in this thesis (Chapter 2.2.1) provides the first evidence for functional modulation of neonatal OB activity on the development of cognitive abilities dependent on LEC-HP network, which suggests that not only do olfactory outputs during a critical developmental time window shape the development of the olfactory system, but these effects are also essential for the hippocampal formation accounting for higher-order cognitive functions. Although we showed a preconfigured framework in Chapter 2.2.5 (Chini et al., 2024) with an extremely distributed neuronal spiking activity that is not dependent on the experience along development and applies to both early-maturating OB and the late-maturing PFC, the results are currently restricted on a single regional level. Experience-dependent processes especially complex behaviors might be more a proxy of the intricate architecture of inter-regional connection which gets constantly fine-tuned;

from a behavioral perspective, both human and animal studies have shown that interfering with environmental stimuli during early development dramatically influences brain functions in adulthood in either a positive or negative way, such the improved sensory perception and memory performance by environmental enrichment (Sale et al., 2009; Zheng et al., 2014; Clemenson & Stark, 2015), memory deficits by maternal separation (Molet et al., 2016; Reincke & Hanganu-Opatz, 2017), and sensory compensation across modalities for visual deprivation (Kupers et al., 2011; Zhou et al., 2017). Given the tight and efficient connections between the olfactory system and neocortical-hippocampal brain network already at birth, whether a simple odor cue during neonatal stage can powerfully mold the consolidation and retrieval of long-term involuntary memory, as the literary anecdote written by Marcel Proust in his novel "*In Search of Lost Time*", is a question worth further asking, which might call more attention on newborn care improvements in the regard of olfaction. Also, it would be interesting to explore if the early odor experience could have the capacity to ameliorate cognitive deficits in neuropsychiatric disorders in the future. How to implement interdisciplinary neuroscience approaches to address this concern longitudinally will be one of the thought-provoking topics.

3.5 Concluding remarks

In this thesis, I present several new findings for the physiological and pathological network development of the murine olfactory-hippocampal-prefrontal network. We confirm the hypothesis that OB activity early in life is a key modulator for the maturation of downstream neuronal networks. Importantly, silencing the olfactory network leads to profound consequences in cognitive deficits. This resembles the impairments of the olfactory-hippocampal-prefrontal network and associated cognitive abilities in a neuropsychiatric mouse model. It brings us new perspectives for advancing the knowledge about the link between olfaction and cognition in health and disease, which might provide an insightful reference to improve newborn care, predict the disease progression and further assess the clinical efficacy of treatments.

4 General Summary

4.1 Summary in English

How sensory perception interplays with higher-order cognitive functions is a fascinating topic in the field of neuroscience. Though the tight connections between the olfactory system and cortical-hippocampal network have been documented in the adult brain, the functional development of these anatomical architectures is still poorly understood. Being one of the first senses exceptionally functional at birth, olfaction might promote cognitive development, which requires reliable evidence on neurobiological level.

Rodents are altricial species compared to humans, and are thus already accessible for investigations at a neonatal stage that roughly corresponds to human mid- and late embryogenesis, with mature olfaction. Accumulating evidence in rodent studies has suggested that the development of sensory cortices during the neonatal stage, critically depends on the endogenously-generated electrical activity of the corresponding sensory systems, with much less known about the early sensory influence on higher-order brain regions especially those involved in cognitive abilities along development. Several recent research reveals that endogenous and odor-evoked activity in the olfactory bulb (OB) boosts the oscillatory entrainment of the lateral entorhinal cortex (LEC), hippocampus (HP) and prefrontal cortex (PFC) in neonatal mice——that are blind and deaf, do not whisker and have limited sensorimotor abilities until the 3rd postnatal week. However, whether the early olfactory processing especially the information inputs originating from the OB influences the functional formation of cognitive abilities, remains an open question.

In this thesis, I try to identify the role of neonatal olfactory afferent inputs in the functional development of the downstream entorhinal-hippocampal network, by silencing the synaptic outputs of the main olfactory output neurons——mitral/tufted cells (M/TCs)

in the OB, transiently from postnatal days 8 to 10 using chemogenetic tools. Applying a wide range of advanced neuroscience methods, including *in vivo* electrophysiological recording, optogenetics, morphological assessments and behavioral tests, I monitor the long-term consequences of this transient manipulation on the activity and communication within olfactory-cortical-hippocampal networks as well as the associated cognitive functions. The results show the lasting impact of neonatal OB activity on the coupling of entorhinal-hippocampal network activity and neuronal structure of HP-projecting neurons in LEC. Moreover, transient M/TC silencing during the neonatal stage profoundly leads to impairments in learning and memory dependent on entorhinal-hippocampal functions.

Taken together, the findings corroborate the neonatal olfactory inputs as a critical modulator in the functional maturation of cortical-hippocampal networks and higher-order cognitive development. In light of this, we further tested the olfactory network functions in a mouse model of neuropsychiatric disorders which has been identified with abnormal cortical-hippocampal wiring during neonatal stage. The reduced spontaneous activity in the OB and its coupling with HP-PFC network confirm the olfactory network deficits in this model, which echoes the early emerging olfactory dysfunctions in a broad spectrum of neurological diseases associated with later cognitive deficits.

In general, the work in this thesis unveils a modulating effect of the olfactory inputs especially the OB activity in early postnatal days on the structural and functional development of higher-order brain circuits accounting for cognitive abilities. This offers novel insights into olfaction beyond a primal sensory perception, and might help establish new principles in the discovery of therapeutic strategies for neurodevelopmental disorders.

4.2 Summary in German

Zusammenfassung

Wie die sensorische Wahrnehmung mit höheren kognitiven Funktionen interagiert, ist ein faszinierendes Thema in der Neurowissenschaft. Im erwachsenen Gehirn beeinflusst der Geruchssinn höhere kognitive Fähigkeiten. Obwohl im erwachsenen Gehirn enge anatomische Verbindungen zwischen dem olfaktorischen System und dem kortikal-hippocampalen Netzwerk beschrieben wurden, ist die funktionelle Entwicklung dieser Strukturen noch immer kaum verstanden. Da der Geruchssinn zu den ersten Sinnen gehört, die bei der Geburt funktionsfähig sind, könnte er die kognitive Entwicklung fördern. Diese Hypothese erfordert zuverlässige Beweise auf neurobiologischer Ebene.

Nagetiere sind im Vergleich zum Menschen altrisch und können daher bereits in einem neonatalen Stadium untersucht werden, das in etwa der mittleren und späten der menschlichen Embryogenese entspricht, wenn der Geruchssinn bereits funktionsfähig ist.

Zunehmende Evidenz aus Studien an Nagetieren hat gezeigt, dass die Entwicklung der sensorischen Kortexregionen während der neonatalen Phase entscheidend von der endogen generierten elektrischen Aktivität der jeweiligen sensorischen Systeme abhängt. Im Gegensatz dazu ist über den frühen sensorischen Einfluss auf Hirnregionen höherer Ordnung, insbesondere auf jene, die an den kognitiven Fähigkeiten im Laufe der Entwicklung beteiligt sind, viel weniger bekannt ist. Mehrere neuere Forschungsarbeiten zeigen, dass endogene und durch Geruch hervorgerufene Aktivität im Riechkolben (olfactory bulb, OB) von neugeborenen Mäusen die oszillatorische Synchronisation des lateralen entorhinalen Kortex (lateral entorhinal cortex, LEC), des Hippocampus (HP) und des präfrontalen Kortex (prefrontal cortex, PFC). Neugeborene Mäuse sind bis zur dritten postnatalen Woche blind und taub und haben nur begrenzte sensomotorische Fähigkeiten. Die Frage, ob die frühe Olfaktorische Wahrnehmung, insbesondere der vom OB verarbeitenden Information, die funktionelle Ausbildung kognitiver Fähigkeiten beeinflusst, bleibt jedoch offen.

In dieser Dissertation versuche ich, die Rolle neonatalen olfaktorischen afferenten Inputs für der funktionellen Entwicklung des nachgeschalteten entorhinal-hippocampalen Netzwerks zu identifizieren, indem ich die synaptischen Übertragung der wichtigsten olfaktorischen Ausgangsneuronen——der Mitral-/Tufted-Zellen (mitral/tufted cells, M/TCs) – vom 8. bis 10. postnatalen Tag mit Hilfe chemogenetischer Methoden ausschalte. Unter Anwendung einer breiten Palette fortschrittlicher neurowissenschaftlicher Methoden, darunter elektrophysiologische In-vivo-Aufzeichnungen, Optogenetik, morphologischen Beschreibung und Verhaltenstests, beobachte ich die langfristigen Folgen dieser vorübergehenden Manipulation auf die Aktivität und Kommunikation innerhalb der olfaktorisch-kortikalen-hippokampalen Netzwerke sowie die damit verbundenen kognitiven Funktionen. Die Ergebnisse zeigen eine dauerhafte Auswirkunge der neonatalen OB-Aktivität auf die Synchronisation der Aktivität des entorhinal-hippocampalen Netzwerks und die neuronale Struktur der HP-projizierenden Neuronen im LEC. Darüber hinaus führt eine vorübergehende Ausschaltung von M/TC während der Neugeborenenphase zu tiefgreifenden Beeinträchtigungen des Lernens und des Gedächtnisses, welche von entorhinal-hippocampalen Funktionen abhängen.

Zusammengefasst bestätigen die Ergebnisse, dass neonatale olfaktorische Inputs ein entscheidender Modulator für die funktionelle Entwicklung von kortikal-hippokampalen Netzwerken und daraus folgend der kognitive Entwicklung ist. Vor diesem Hintergrund haben wir die Funktionen des Geruchsnetzwerks in einem Mausmodell für neuropsychiatrische Störungen getestet, bei dem eine abnorme kortikal-hippokampale Vernetzung während des Neugeborenenstadiums festgestellt worden war. Die reduzierte Spontanaktivität im OB und seine Kopplung mit dem kortikal-hippocampalen Netzwerk

bestätigen Defizite im olfaktorischen Netzwerk in diesem Modell, was mit den früh auftretenden olfaktorischen Dysfunktionen in einem breiten Spektrum neurologischer Erkrankungen mit kognitiven Beeinträchtigungen übereinstimmt.

Insgesamt zeigt die Arbeit in dieser Dissertation einen modulierenden Effekt der olfaktorischen Inputs, insbesondere der OB-Aktivität, in den frühen postnatalen Tagen auf die strukturelle und funktionelle Entwicklung höherer Gehirnschaltkreise, die kognitiven Fähigkeiten zugrunde liegen. Dies bietet neue Einblicke in den Geruchssinn, die über die ursprüngliche Sinneswahrnehmung hinausgehen, und könnte dazu beitragen, neue Prinzipien für die Entwicklung von therapeutischen Strategien für neurologische Entwicklungsstörungen zu entwickeln.

5 | Bibliography

Ackman, J. B., Burbridge, T. J., & Crair, M. C. (2012). Retinal waves coordinate patterned activity throughout the developing visual system. *Nature*, *490*(7419), Article 7419. DOI: 10.1038/nature11529

Adams, W., Graham, J. N., Han, X., & Riecke, H. (2019). Top-down inputs drive neuronal network rewiring and context-enhanced sensory processing in olfaction. *PLoS Computational Biology*, *15*(1), e1006611. DOI: 10.1371/journal.pcbi.1006611

Adrian, E. D. (1942). Olfactory reactions in the brain of the hedgehog. *The Journal of Physiology*, *100*(4), 459–473. DOI: 10.1113/jphysiol.1942.sp003955

Agster, K. L., & Burwell, R. D. (2009). Cortical efferents of the perirhinal, postrhinal, and entorhinal cortices of the rat. *Hippocampus*, *19*(12), 1159–1186. DOI: 10.1002/hipo.20578

Ahlbeck, J., Song, L., Chini, M., Bitzenhofer, S. H., & Hanganu-Opatz, I. L. (2018). Glutamatergic drive along the septo-temporal axis of hippocampus boosts prelimbic oscillations in the neonatal mouse. *eLife*, *7*, e33158. DOI: 10.7554/eLife.33158

Akers, K. G., Martinez-Canabal, A., Restivo, L., Yiu, A. P., De Cristofaro, A., Hsiang, H.-L. (Liz), Wheeler, A. L., Guskjolen, A., Niibori, Y., Shoji, H., Ohira, K., Richards, B. A., Miyakawa, T., Josselyn, S. A., & Frankland, P. W. (2014). Hippocampal Neurogenesis Regulates Forgetting During Adulthood and Infancy. *Science*, *344*(6184), 598–602. DOI: 10.1126/science.1248903

Albani, S. H., McHail, D. G., & Dumas, T. C. (2014). Developmental studies of the hippocampus and hippocampal-dependent behaviors: Insights from interdisciplinary studies and tips for new investigators. *Neuroscience & Biobehavioral Reviews*, *43*, 183–190. DOI: 10.1016/j.neubiorev.2014.04.009

Albeanu, D. F., Provost, A. C., Agarwal, P., Soucy, E. R., Zak, J. D., & Murthy, V. N. (2018). Olfactory marker protein (OMP) regulates formation and refinement of the olfactory glomerular map. *Nature Communications*, *9*(1), 5073. DOI:

10.1038/s41467-018-07544-9

Amaral, D. G., & Witter, M. P. (1989). The three-dimensional organization of the hippocampal formation: A review of anatomical data. *Neuroscience*, *31*(3), 571–591. DOI: 10.1016/0306-4522(89)90424-7

Aoi, M. C., Mante, V., & Pillow, J. W. (2020). Prefrontal cortex exhibits multidimensional dynamic encoding during decision-making. *Nature Neuroscience*, *23*(11), 1410–1420. DOI: 10.1038/s41593-020-0696-5

Arshamian, A., Iravani, B., Majid, A., & Lundström, J. N. (2018). Respiration Modulates Olfactory Memory Consolidation in Humans. *The Journal of Neuroscience: The Official Journal of the Society for Neuroscience*, *38*(48), Article 48. DOI: 10.1523/JNEUROSCI.3360-17.2018

Attems, J., Walker, L., & Jellinger, K. A. (2014). Olfactory bulb involvement in neurodegenerative diseases. *Acta Neuropathologica*, *127*(4), 459–475. DOI: 10.1007/s00401-014-1261-7

Baccalá, L. A., & Sameshima, K. (2001). Partial directed coherence: A new concept in neural structure determination. *Biological Cybernetics*, *84*(6), 463–474. DOI: 10.1007/PL00007990

Ballard, C., Gauthier, S., Corbett, A., Brayne, C., Aarsland, D., & Jones, E. (2011). Alzheimer's disease. *The Lancet*, *377*(9770), 1019–1031. DOI: 10.1016/S0140-6736(10)61349-9

Bannerman, D. M., Sprengel, R., Sanderson, D. J., McHugh, S. B., Rawlins, J. N. P., Monyer, H., & Seeburg, P. H. (2014). Hippocampal synaptic plasticity, spatial memory and anxiety. *Nature Reviews Neuroscience*, *15*(3), 181–192. DOI: 10.1038/nrn3677

Barr, J. L., Bray, B., & Forster, G. L. (2018). The hippocampus as a neural link between negative affect and vulnerability for psychostimulant relapse. *The Hippocampus—Plasticity and Functions Ed. A. Stuchlik (London, UK: IntechOpen Limited)*, 127–167. DOI: 10.5772/intechopen.70854

Barraclough, D. J., Conroy, M. L., & Lee, D. (2004). Prefrontal cortex and decision making in a mixed-strategy game. *Nature Neuroscience*, *7*(4), 404–410. DOI: 10.1038/nn1209

Batista-Brito, R., Close, J., Machold, R., & Fishell, G. (2008). The distinct temporal origins of olfactory bulb interneuron subtypes. *The Journal of Neuroscience: The Official Journal of the Society for Neuroscience*, *28*(15), Article 15. DOI: 10.1523/JNEUROSCI.5625-07.2008

Becker, J. H., Lin, J. J., Doernberg, M., Stone, K., Navis, A., Festa, J. R., & Wisnivesky, J. P. (2021). Assessment of Cognitive Function in Patients After COVID-19 Infection. *JAMA Network Open*, *4*(10), e2130645. DOI: 10.1001/jamanetworkopen.2021.30645

Bennetto, L., Kuschner, E. S., & Hyman, S. L. (2007). Olfaction and Taste Processing in Autism. *Biological Psychiatry*, *62*(9), 1015–1021. DOI: 10.1016/j.biopsych.2007.04.019

Beshel, J., Kopell, N., & Kay, L. M. (2007). Olfactory Bulb Gamma Oscillations Are Enhanced with Task Demands. *Journal of Neuroscience*, *27*(31), 8358–8365. DOI: 10.1523/JNEUROSCI.1199-07.2007

Best, A. R., & Wilson, D. A. (2003). A postnatal sensitive period for plasticity of cortical afferents but not cortical association fibers in rat piriform cortex. *Brain Research*, *961*(1), 81–87. DOI: 10.1016/S0006-8993(02)03847-7

Bitzenhofer, S. H., Pöpplau, J. A., Chini, M., Marquardt, A., & Hanganu-Opatz, I. L. (2021). A transient developmental increase in prefrontal activity alters network maturation and causes cognitive dysfunction in adult mice. *Neuron*, *109*(8), 1350–1364. DOI: 10.1016/j.neuron.2021.02.011

Bitzenhofer, S. H., Pöpplau, J. A., & Hanganu-Opatz, I. (2020). Gamma activity accelerates during prefrontal development. *eLife*, *9*, e56795. DOI: 10.7554/eLife.56795

Bitzenhofer, S. H., Sieben, K., Siebert, K. D., Spehr, M., & Hanganu-Opatz, I. L. (2015). Oscillatory Activity in Developing Prefrontal Networks Results from Theta-Gamma-Modulated Synaptic Inputs. *Cell Reports*, *11*(3), 486–497. DOI: 10.1016/j.celrep.2015.03.031

Bitzenhofer, S. H., Westeinde, E. A., Zhang, H.-X. B., & Isaacson, J. S. (2022). Rapid odor processing by layer 2 subcircuits in lateral entorhinal cortex. *Elife*, *11*, e75065. DOI: 10.7554/eLife.75065

Blair, M. G., Nguyen, N. N.-Q., Albani, S. H., L'Etoile, M. M., Andrawis, M. M., Owen, L. M., Oliveira, R. F., Johnson, M. W., Purvis, D. L., Sanders, E. M., Stoneham, E. T., Xu, H., & Dumas, T. C. (2013). Developmental Changes in Structural and Functional Properties of Hippocampal AMPARs Parallels the Emergence of Deliberative Spatial Navigation in Juvenile Rats. *Journal of Neuroscience*, *33*(30), 12218–12228. DOI: 10.1523/JNEUROSCI.4827-12.2013

Bolding, K. A., Nagappan, S., Han, B.-X., Wang, F., & Franks, K. M. (2020). Recurrent circuitry is required to stabilize piriform cortex odor representations across brain states. *Elife*, *9*, e53125. DOI: 10.7554/eLife.53125

Borisovska, M., Bensen, A. L., Chong, G., & Westbrook, G. L. (2013). Distinct Modes of Dopamine and GABA Release in a Dual Transmitter Neuron. *Journal of Neuroscience*, *33*(5), 1790–1796. DOI: 10.1523/JNEUROSCI.4342-12.2013

Boyd, A. M., Sturgill, J. F., Poo, C., & Isaacson, J. S. (2012). Cortical feedback control of olfactory bulb circuits. *Neuron*, *76*(6), 1161–1174. DOI: 10.1016/j.neuron.2012.10.020

Braak, H., & Braak, E. (1991). Neuropathological stageing of Alzheimer-related changes. *Acta Neuropathologica*, *82*(4), 239–259. DOI: 10.1007/bf00308809

Braak, H., & Del Tredici, K. (2015). The preclinical phase of the pathological process underlying sporadic Alzheimer's disease. *Brain*, *138*(10), 2814–2833. DOI: 10.1093/brain/awv236

Brockmann, M. D., Pöschel, B., Cichon, N., & Hanganu-Opatz, I. L. (2011). Coupled Oscillations Mediate Directed Interactions between Prefrontal Cortex and Hippocampus of the Neonatal Rat. *Neuron*, *71*(2), 332–347. DOI: 10.1016/j.neuron.2011.05.041

Buzsáki, G., & Moser, E. I. (2013). Memory, navigation and theta rhythm in the hippocampal-entorhinal system. *Nature Neuroscience*, *16*(2), 130–138. DOI: 10.1038/nn.3304

Buzsáki, G., & Wang, X.-J. (2012). Mechanisms of Gamma Oscillations. *Annual Review of Neuroscience*, *35*, 203–225. DOI: 10.1146/annurev-neuro-062111-150444

Canto, C. B., Wouterlood, F. G., & Witter, M. P. (2008). What Does the Anatomical Organization of the Entorhinal Cortex Tell Us? *Neural Plasticity*, *2008*, e381243. DOI: 10.1155/2008/381243

Chang, E. F., & Merzenich, M. M. (2003). Environmental Noise Retards Auditory Cortical Development. *Science*, *300*(5618), 498–502. DOI: 10.1126/science.1082163

Chang, Y.-S., Owen, J. P., Desai, S. S., Hill, S. S., Arnett, A. B., Harris, J., Marco, E. J., & Mukherjee, P. (2014). Autism and Sensory Processing Disorders: Shared White Matter Disruption in Sensory Pathways but Divergent Connectivity in Social-Emotional Pathways. *PLOS ONE*, *9*(7), e103038. DOI: 10.1371/journal.pone.0103038

Chapuis, J., Cohen, Y., He, X., Zhang, Z., Jin, S., Xu, F., & Wilson, D. A. (2013). Lateral Entorhinal Modulation of Piriform Cortical Activity and Fine Odor Discrimination. *Journal of Neuroscience*, *33*(33), 13449–13459. DOI: 10.1523/JNEUROSCI.1387-13.2013

Cheaha, D., Bumrungsri, S., Chatpun, S., & Kumarnsit, E. (2015). Characterization of in

utero valproic acid mouse model of autism by local field potential in the hippocampus and the olfactory bulb. *Neuroscience Research*, *98*, 28–34. DOI: 10.1016/j.neures.2015.04.006

Chen, F., Liu, W., Liu, P., Wang, Z., Zhou, Y., Liu, X., & Li, A. (2021). α-Synuclein aggregation in the olfactory bulb induces olfactory deficits by perturbing granule cells and granular–mitral synaptic transmission. *Npj Parkinson's Disease*, *7*(1), 1–15. DOI: 10.1038/s41531-021-00259-7

Chen, M., Chen, Y., Huo, Q., Wang, L., Tan, S., Misrani, A., Jiang, J., Chen, J., Chen, S., Zhang, J., & others. (2020). Enhancing GABAergic signaling ameliorates aberrant gamma oscillations of olfactory bulb in AD mouse models. *Molecular Neurodegeneration*, *16*(1), 1–23. DOI: 10.1186/s13024-021-00434-7

Chen, Y., & Kostka, J. K. (2024). Beyond anosmia: Olfactory dysfunction as a common denominator in neurodegenerative and neurodevelopmental disorders. *Frontiers in Neuroscience*, *18*. DOI: 10.3389/fnins.2024.1502779

Chen, Y., Kostka, J. K., Bitzenhofer, S. H., & Hanganu-Opatz, I. L. (2023). Olfactory bulb activity shapes the development of entorhinal-hippocampal coupling and associated cognitive abilities. *Current Biology*, *33*(20), 4353-4366.e5. DOI: 10.1016/j.cub.2023.08.072

Chen, Y., Kostka, J. K., Bitzenhofer, S. H., & Hanganu-Opatz, I. L. (2024). Protocol for adeno-associated virus-mediated optogenetic activation of olfactory output neurons in neonatal mice. *STAR Protocols*, *5*(3), 103164. DOI: 10.1016/j.xpro.2024.103164

Chini, M., & Hanganu-Opatz, I. L. (2021). Prefrontal Cortex Development in Health and Disease: Lessons from Rodents and Humans. *Trends in Neurosciences*, *44*(3), 227–240. DOI: 10.1016/j.tins.2020.10.017

Chini, M., Hnida, M., Kostka, J. K., Chen, Y., & Hanganu-Opatz, I. L. (2024). Preconfigured architecture of the developing mouse brain. *Cell Reports*, *43*(6), 114267. DOI: 10.1016/j.celrep.2024.114267

Chini, M., Pfeffer, T., & Hanganu-Opatz, I. (2022). An increase of inhibition drives the developmental decorrelation of neural activity. *ELife*, *11*, e78811. DOI: 10.7554/eLife.78811

Chini, M., Pöpplau, J. A., Lindemann, C., Carol-Perdiguer, L., Hnida, M., Oberländer, V., Xu, X., Ahlbeck, J., Bitzenhofer, S. H., Mulert, C., & Hanganu-Opatz, I. L. (2020). Resolving and Rescuing Developmental Miswiring in a Mouse Model of Cognitive Impairment. *Neuron*, *105*(1), 60-74.e7. DOI: 10.1016/j.neuron.2019.09.042

Cleland, T. A., & Linster, C. (2003). Central Olfactory Structures. In *Handbook of*

Olfaction and Gustation (2nd ed.). CRC Press.

Clemenson, G. D., & Stark, C. E. L. (2015). Virtual Environmental Enrichment through Video Games Improves Hippocampal-Associated Memory. *Journal of Neuroscience*, *35*(49), 16116–16125. DOI: 10.1523/JNEUROSCI.2580-15.2015

Colgin, L. L., Denninger, T., Fyhn, M., Hafting, T., Bonnevie, T., Jensen, O., Moser, M.-B., & Moser, E. I. (2009). Frequency of gamma oscillations routes flow of information in the hippocampus. *Nature*, *462*(7271), 353–357. DOI: 10.1038/nature08573

Corcoran, C., Whitaker, A., Coleman, E., Fried, J., Feldman, J., Goudsmit, N., & Malaspina, D. (2005). Olfactory deficits, cognition and negative symptoms in early onset psychosis. *Schizophrenia Research*, *80*(2), 283–293. DOI: 10.1016/j.schres.2005.07.028

Courtiol, E., & Wilson, D. A. (2015). The olfactory thalamus: Unanswered questions about the role of the mediodorsal thalamic nucleus in olfaction. *Frontiers in Neural Circuits*, *9*. DOI: 10.3389/fncir.2015.00049

Cutts, C. S., & Eglen, S. J. (2014). Detecting Pairwise Correlations in Spike Trains: An Objective Comparison of Methods and Application to the Study of Retinal Waves. *Journal of Neuroscience*, *34*(43), 14288–14303. DOI: 10.1523/JNEUROSCI.2767-14.2014

Dalal, T., & Haddad, R. (2022). Upstream γ-synchronization enhances odor processing in downstream neurons. *Cell Reports*, *39*(3), 110693. DOI: 10.1016/j.celrep.2022.110693

David, F., Courtiol, E., Buonviso, N., & Fourcaud-Trocmé, N. (2015). Competing Mechanisms of Gamma and Beta Oscillations in the Olfactory Bulb Based on Multimodal Inhibition of Mitral Cells Over a Respiratory Cycle. *eNeuro*, *2*(6). DOI: 10.1523/ENEURO.0018-15.2015

Deisseroth, K. (2015). Optogenetics: 10 years of microbial opsins in neuroscience. *Nature Neuroscience*, *18*(9), 1213–1225. DOI: 10.1038/nn.4091

Dintica, C. S., Marseglia, A., Rizzuto, D., Wang, R., Seubert, J., Arfanakis, K., Bennett, D. A., & Xu, W. (2019). Impaired olfaction is associated with cognitive decline and neurodegeneration in the brain. *Neurology*, *92*(7), e700–e709. DOI: 10.1212/WNL.0000000000006919

Donato, F., Jacobsen, R. I., Moser, M.-B., & Moser, E. I. (2017). Stellate cells drive maturation of the entorhinal-hippocampal circuit. *Science*, *355*(6330). DOI: 10.1126/science.aai8178

Doty, R. L. (2012). Olfactory dysfunction in Parkinson disease. *Nature Reviews Neurology*, *8*(6), 329–339. DOI: 10.1038/nrneurol.2012.80

Doty, R. L. (2017). Olfactory dysfunction in neurodegenerative diseases: Is there a common pathological substrate? *The Lancet Neurology*, *16*(6), 478–488. DOI: 10.1016/S1474-4422(17)30123-0

Drapeau, E., Riad, M., Kajiwara, Y., & Buxbaum, J. D. (2018). Behavioral Phenotyping of an Improved Mouse Model of Phelan–McDermid Syndrome with a Complete Deletion of the Shank3 Gene. *eNeuro*, *5*(3). DOI: 10.1523/ENEURO.0046-18.2018

Dumas, T. C. (2004). Early eyelid opening enhances spontaneous alternation and accelerates the development of perforant path synaptic strength in the hippocampus of juvenile rats. *Developmental Psychobiology*, *45*(1), 1–9. DOI: 10.1002/dev.20011

Elston, T. W., & Wallis, J. D. (2025). Context-dependent decision-making in the primate hippocampal–prefrontal circuit. *Nature Neuroscience*, 1–9. DOI: 10.1038/s41593-024-01839-5

Ewall, G., Parkins, S., Lin, A., Jaoui, Y., & Lee, H.-K. (2021). Cortical and Subcortical Circuits for Cross-Modal Plasticity Induced by Loss of Vision. *Frontiers in Neural Circuits*, *15*. DOI: 10.3389/fncir.2021.665009

Fernández-Ruiz, A., Oliva, A., Soula, M., Rocha-Almeida, F., Nagy, G. A., Martin-Vazquez, G., & Buzsáki, G. (2021). Gamma rhythm communication between entorhinal cortex and dentate gyrus neuronal assemblies. *Science*, *372*(6537). DOI: 10.1126/science.abf3119

Fernandez-Ruiz, A., Sirota, A., Lopes-dos-Santos, V., & Dupret, D. (2023). Over and above frequency: Gamma oscillations as units of neural circuit operations. *Neuron*, *111*(7), 936–953. DOI: 10.1016/j.neuron.2023.02.026

Fontanini, A., Spano, P., & Bower, J. M. (2003). Ketamine-xylazine-induced slow (< 1.5 Hz) oscillations in the rat piriform (olfactory) cortex are functionally correlated with respiration. *The Journal of Neuroscience: The Official Journal of the Society for Neuroscience*, *23*(22), 7993–8001. DOI: 10.1523/JNEUROSCI.23-22-07993.2003

Fourcaud-Trocmé, N., Courtiol, E., & Buonviso, N. (2014). Two distinct olfactory bulb sublaminar networks involved in gamma and beta oscillation generation: A CSD study in the anesthetized rat. *Frontiers in Neural Circuits*, *8*. DOI: 10.3389/fncir.2014.00088

Fox, K. (2002). Anatomical pathways and molecular mechanisms for plasticity in the barrel cortex. *Neuroscience*, *111*(4), 799–814. DOI: 10.1016/S0306-4522(02)00027-1

Fox, K., & Wong, R. O. L. (2005). A comparison of experience-dependent plasticity in the

visual and somatosensory systems. *Neuron*, *48*(3), 465–477. DOI: 10.1016/j.neuron.2005.10.013

Franklin, T. B., Silva, B. A., Perova, Z., Marrone, L., Masferrer, M. E., Zhan, Y., Kaplan, A., Greetham, L., Verrechia, V., Halman, A., Pagella, S., Vyssotski, A. L., Illarionova, A., Grinevich, V., Branco, T., & Gross, C. T. (2017). Prefrontal cortical control of a brainstem social behavior circuit. *Nature Neuroscience*, *20*(2), 260–270. DOI: 10.1038/nn.4470

Franks, K. M., & Isaacson, J. S. (2005). Synapse-Specific Downregulation of NMDA Receptors by Early Experience: A Critical Period for Plasticity of Sensory Input to Olfactory Cortex. *Neuron*, *47*(1), 101–114. DOI: 10.1016/j.neuron.2005.05.024

Freiherr, J., Hallschmid, M., Frey, W. H., Brünner, Y. F., Chapman, C. D., Hölscher, C., Craft, S., De Felice, F. G., & Benedict, C. (2013). Intranasal Insulin as a Treatment for Alzheimer's Disease: A Review of Basic Research and Clinical Evidence. *CNS Drugs*, *27*(7), 505–514. DOI: 10.1007/s40263-013-0076-8

Fries, P. (2005). A mechanism for cognitive dynamics: Neuronal communication through neuronal coherence. *Trends in Cognitive Sciences*, *9*(10), 474–480. DOI: 10.1016/j.tics.2005.08.011

Fuster, J. M. (2002). Frontal lobe and cognitive development. *Journal of Neurocytology*, *31*(3), 373–385. DOI: 10.1023/A:1024190429920

Garaschuk, O., Linn, J., Eilers, J., & Konnerth, A. (2000). Large-scale oscillatory calcium waves in the immature cortex. *Nature Neuroscience*, *3*(5), 452–459. DOI: 10.1038/74823

Geng, C., Li, R., Li, S., Liu, P., Peng, Y., Liu, C., Wang, Z., Zhang, H., & Li, A. (2025). Noradrenergic inputs from the locus coeruleus to anterior piriform cortex and the olfactory bulb modulate olfactory outputs. *Nature Communications*, *16*(1), 260. DOI: 10.1038/s41467-024-55609-9

Goedert, M., & Spillantini, M. G. (2006). A Century of Alzheimer's Disease. *Science*, *314*(5800), 777–781. DOI: 10.1126/science.1132814

Goettemoeller, A. M., Banks, E., Kumar, P., Olah, V. J., McCann, K. E., South, K., Ramelow, C. C., Eaton, A., Duong, D. M., Seyfried, N. T., Weinshenker, D., Rangaraju, S., & Rowan, M. J. M. (2024). Entorhinal cortex vulnerability to human APP expression promotes hyperexcitability and tau pathology. *Nature Communications*, *15*(1), 7918. DOI: 10.1038/s41467-024-52297-3

Gogtay, N., Giedd, J. N., Lusk, L., Hayashi, K. M., Greenstein, D., Vaituzis, A. C., Nugent, T. F., Herman, D. H., Clasen, L. S., Toga, A. W., Rapoport, J. L., & Thompson, P.

M. (2004). Dynamic mapping of human cortical development during childhood through early adulthood. *Proceedings of the National Academy of Sciences*, *101*(21), 8174–8179. DOI: 10.1073/pnas.0402680101

Gourévitch, B., Kay, L. M., & Martin, C. (2010). Directional coupling from the olfactory bulb to the hippocampus during a go/no-go odor discrimination task. *Journal of Neurophysiology*, *103*(5), Article 5. DOI: 10.1152/jn.01075.2009

Goutaudier, R., Coizet, V., Carcenac, C., & Carnicella, S. (2020). Compound 21, a two-edged sword with both DREADD-selective and off-target outcomes in rats. *PLOS ONE*, *15*(9), e0238156. DOI: 10.1371/journal.pone.0238156

Graf, J., Samiee, A., Flossmann, T., Holthoff, K., & Kirmse, K. (2024). Chemogenetic silencing reveals presynaptic Gi/o protein-mediated inhibition of developing hippocampal synchrony in vivo. *iScience*, *27*(10). DOI: 10.1016/j.isci.2024.110997

Gretenkord, S., Kostka, J. K., Hartung, H., Watznauer, K., Fleck, D., Minier-Toribio, A., Spehr, M., & Hanganu-Opatz, I. L. (2019). Coordinated electrical activity in the olfactory bulb gates the oscillatory entrainment of entorhinal networks in neonatal mice. *PLoS Biology*, *17*(1), e2006994. DOI: 10.1371/journal.pbio.2006994

Guthman, M. S., Harvey, N. C., & Kling, A. (1979). Somato-social development in the rhesus monkey following olfactory bulbectomy. *Primates*, *20*(2), 211–219. DOI: 10.1007/BF02373374

Guthrie, K. M., & Gall, C. (2003). Anatomic mapping of neuronal odor responses in the developing rat olfactory bulb. *Journal of Comparative Neurology*, *455*(1), 56–71. DOI: 10.1002/cne.10452

Haddad, R., Lanjuin, A., Madisen, L., Zeng, H., Murthy, V. N., & Uchida, N. (2013). Olfactory cortical neurons read out a relative time code in the olfactory bulb. *Nature Neuroscience*, *16*(7), Article 7. DOI: 10.1038/nn.3407

Haehner, A., Boesveldt, S., Berendse, H. W., Mackay-Sim, A., Fleischmann, J., Silburn, P. A., Johnston, A. N., Mellick, G. D., Herting, B., Reichmann, H., & Hummel, T. (2009). Prevalence of smell loss in Parkinson's disease – A multicenter study. *Parkinsonism & Related Disorders*, *15*(7), 490–494. DOI: 10.1016/j.parkreldis.2008.12.005

Hahn, C.-G., Han, L.-Y., Rawson, N. E., Mirza, N., Borgmann-Winter, K., Lenox, R. H., & Arnold, S. E. (2005). In vivo and in vitro neurogenesis in human olfactory epithelium. *Journal of Comparative Neurology*, *483*(2), 154–163. DOI: 10.1002/cne.20424

Hampshire, A., Azor, A., Atchison, C., Trender, W., Hellyer, P. J., Giunchiglia, V., Husain,

M., Cooke, G. S., Cooper, E., Lound, A., Donnelly, C. A., Chadeau-Hyam, M., Ward, H., & Elliott, P. (2024). Cognition and Memory after Covid-19 in a Large Community Sample. *New England Journal of Medicine*, *390*(9), 806–818. DOI: 10.1056/NEJMoa2311330

Hanganu, I. L., Ben-Ari, Y., & Khazipov, R. (2006). Retinal Waves Trigger Spindle Bursts in the Neonatal Rat Visual Cortex. *Journal of Neuroscience*, *26*(25), 6728–6736. DOI: 10.1523/JNEUROSCI.0752-06.2006

Hanganu-Opatz, I. L., Butt, S. J. B., Hippenmeyer, S., García, N. V. D. M., Cardin, J. A., Voytek, B., & Muotri, A. R. (2021). The Logic of Developing Neocortical Circuits in Health and Disease. *Journal of Neuroscience*, *41*(5), 813–822. DOI: 10.1523/JNEUROSCI.1655-20.2020

Hargreaves, E. L., Rao, G., Lee, I., & Knierim, J. J. (2005). Major Dissociation Between Medial and Lateral Entorhinal Input to Dorsal Hippocampus. *Science*, *308*(5729), 1792–1794. DOI: 10.1126/science.1110449

Hartung, H., Brockmann, M. D., Pöschel, B., De Feo, V., & Hanganu-Opatz, I. L. (2016a). Thalamic and Entorhinal Network Activity Differently Modulates the Functional Development of Prefrontal–Hippocampal Interactions. *The Journal of Neuroscience*, *36*(13), Article 13. DOI: 10.1523/JNEUROSCI.3232-15.2016

Hartung, H., Cichon, N., De Feo, V., Riemann, S., Schildt, S., Lindemann, C., Mulert, C., Gogos, J. A., & Hanganu-Opatz, I. L. (2016b). From Shortage to Surge: A Developmental Switch in Hippocampal–Prefrontal Coupling in a Gene–Environment Model of Neuropsychiatric Disorders. *Cerebral Cortex*, *26*(11), 4265–4281. DOI: 10.1093/cercor/bhw274

Hofer, S. B., Mrsic-Flogel, T. D., Bonhoeffer, T., & Hübener, M. (2009). Experience leaves a lasting structural trace in cortical circuits. *Nature*, *457*(7227), Article 7227. DOI: 10.1038/nature07487

Hu, J., Shi, Y., Zhang, J., Huang, X., Wang, Q., Zhao, H., Shen, J., Chen, Z., Song, W., Zheng, P., & others. (2022). Melanopsin retinal ganglion cells mediate light-promoted brain development. *Cell*, *185*(17), 3124–3137. DOI: 10.1016/j.cell.2022.07.009

Huang, T.-N., Yen, T.-L., Qiu, L. R., Chuang, H.-C., Lerch, J. P., & Hsueh, Y.-P. (2019). Haploinsufficiency of autism causative gene Tbr1 impairs olfactory discrimination and neuronal activation of the olfactory system in mice. *Molecular Autism*, *10*(1), 5. DOI: 10.1186/s13229-019-0257-5

Huang, X., Schlesiger, M. I., Barriuso-Ortega, I., Leibold, C., MacLaren, D. A. A., Bieber,

N., & Monyer, H. (2023). Distinct spatial maps and multiple object codes in the lateral entorhinal cortex. *Neuron*, *111*(19), 3068-3083.e7. DOI: 10.1016/j.neuron.2023.06.020

Humphrey, T. (1940). The development of the olfactory and the accessory olfactory formations in human embryos and fetuses. *Journal of Comparative Neurology*, *73*(3), 431–468. DOI: 10.1002/cne.900730305

Igarashi, K. M., Ieki, N., An, M., Yamaguchi, Y., Nagayama, S., Kobayakawa, K., Kobayakawa, R., Tanifuji, M., Sakano, H., Chen, W. R., & others. (2012). Parallel mitral and tufted cell pathways route distinct odor information to different targets in the olfactory cortex. *Journal of Neuroscience*, *32*(23), 7970–7985. DOI: 10.1523/JNEUROSCI.0154-12.2012

Igarashi, K. M., Lu, L., Colgin, L. L., Moser, M.-B., & Moser, E. I. (2014). Coordination of entorhinal–hippocampal ensemble activity during associative learning. *Nature*, *510*(7503), Article 7503. DOI: 10.1038/nature13162

Illig, K. R. (2005). Projections from orbitofrontal cortex to anterior piriform cortex in the rat suggest a role in olfactory information processing. *Journal of Comparative Neurology*, *488*(2), 224–231. DOI: 10.1002/cne.20595

Illig, K. R. (2007). Developmental changes in odor-evoked activity in rat piriform cortex. *Neuroscience*, *145*(1), 370–376. DOI: 10.1016/j.neuroscience.2006.11.049

Inoue, N., Nishizumi, H., Ooyama, R., Mogi, K., Nishimori, K., Kikusui, T., & Sakano, H. (2021). The olfactory critical period is determined by activity-dependent Sema7A/PlxnC1 signaling within glomeruli. *eLife*, *10*, e65078. DOI: 10.7554/eLife.65078

Itokazu, Y., Fuchigami, T., Morgan, J. C., & Yu, R. K. (2021). Intranasal infusion of GD3 and GM1 gangliosides downregulates alpha-synuclein and controls tyrosine hydroxylase gene in a PD model mouse. *Molecular Therapy*, *29*(10), 3059–3071. DOI: 10.1016/j.ymthe.2021.06.005

Jaijyan, D. K., Selariu, A., Cruz-Cosme, R., Tong, M., Yang, S., Stefa, A., Kekich, D., Sadoshima, J., Herbig, U., Tang, Q., Church, G., Parrish, E. L., & Zhu, H. (2022). New intranasal and injectable gene therapy for healthy life extension. *Proceedings of the National Academy of Sciences*, *119*(20), e2121499119. DOI: 10.1073/pnas.2121499119

Janiesch, P. C., Krüger, H.-S., Pöschel, B., & Hanganu-Opatz, I. L. (2011). Cholinergic Control in Developing Prefrontal–Hippocampal Networks. *Journal of Neuroscience*, *31*(49), 17955–17970. DOI: 10.1523/JNEUROSCI.2644-11.2011

Jay, T. M., Glowinski, J., & Thierry, A.-M. (1989). Selectivity of the hippocampal projection to the prelimbic area of the prefrontal cortex in the rat. *Brain Research*, *505*(2), 337–340. DOI: 10.1016/0006-8993(89)91464-9

Jeffery, K. J. (2007). Integration of the sensory inputs to place cells: What, where, why, and how? *Hippocampus*, *17*(9), 775–785. DOI: 10.1002/hipo.20322

Jones, M. W., & Wilson, M. A. (2005). Theta Rhythms Coordinate Hippocampal–Prefrontal Interactions in a Spatial Memory Task. *PLOS Biology*, *3*(12), e402. DOI: 10.1371/journal.pbio.0030402

Kamath, V., Crawford, J., DuBois, S., Nucifora Jr., F. C., Nestadt, G., Sawa, A., & Schretlen, D. (2019). Contributions of olfactory and neuropsychological assessment to the diagnosis of first-episode schizophrenia. *Neuropsychology*, *33*(2), 203–211. DOI: 10.1037/neu0000502

Karalis, N., & Sirota, A. (2022). Breathing coordinates cortico-hippocampal dynamics in mice during offline states. *Nature Communications*, *13*(1), 1–20. DOI: 10.1038/s41467-022-28090-5

Karlsson, K. Æ., Mohns, E. J., di Prisco, G. V., & Blumberg, M. S. (2006). On the co-occurrence of startles and hippocampal sharp waves in newborn rats. *Hippocampus*, *16*(11), 959–965. DOI: 10.1002/hipo.20224

Katz, L. C., & Shatz, C. J. (1996). Synaptic Activity and the Construction of Cortical Circuits. *Science*, *274*(5290), 1133–1138. DOI: 10.1126/science.274.5290.1133

Kay, L. M., & Sherman, S. M. (2007). An argument for an olfactory thalamus. *Trends in Neurosciences*, *30*(2), 47–53. DOI: 10.1016/j.tins.2006.11.007

Kim, J., Joshi, A., Frank, L., & Ganguly, K. (2023). Cortical–hippocampal coupling during manifold exploration in motor cortex. *Nature*, *613*(7942), 103–110. DOI: 10.1038/s41586-022-05533-z

Kitamura, T., Ogawa, S. K., Roy, D. S., Okuyama, T., Morrissey, M. D., Smith, L. M., Redondo, R. L., & Tonegawa, S. (2017). Engrams and circuits crucial for systems consolidation of a memory. *Science*, *356*(6333), 73–78. DOI: 10.1126/science.aam6808

Kiyokage, E., Pan, Y.-Z., Shao, Z., Kobayashi, K., Szabo, G., Yanagawa, Y., Obata, K., Okano, H., Toida, K., Puche, A. C., & Shipley, M. T. (2010). Molecular Identity of Periglomerular and Short Axon Cells. *The Journal of Neuroscience*, *30*(3), 1185–1196. DOI: 10.1523/JNEUROSCI.3497-09.2010

Kobro-Flatmoen, A., Nagelhus, A., & Witter, M. P. (2016). Reelin-immunoreactive neurons in entorhinal cortex layer II selectively express intracellular amyloid in early

Alzheimer's disease. *Neurobiology of Disease*, *93*, 172–183. DOI: 10.1016/j.nbd.2016.05.012

Koehler, L., Fournel, A., Albertowski, K., Roessner, V., Gerber, J., Hummel, C., Hummel, T., & Bensafi, M. (2018). Impaired Odor Perception in Autism Spectrum Disorder Is Associated with Decreased Activity in Olfactory Cortex. *Chemical Senses*, *43*(8), 627–634. DOI: 10.1093/chemse/bjy051

Kostka, J. K., & Bitzenhofer, S. H. (2022). Postnatal Development of Centrifugal Inputs to the Olfactory Bulb. *Frontiers in Neuroscience*, *16*. DOI: 10.3389/fnins.2022.815282

Kostka, J. K., & Hanganu-Opatz, I. L. (2022). *Olfactory-driven beta band entrainment of limbic circuitry during neonatal development* (p. 2021.10.04.463041). bioRxiv. DOI: 10.1101/2021.10.04.463041

Kostka, J. K., & Hanganu-Opatz, I. L. (2023). Olfactory-driven beta band entrainment of limbic circuitry during neonatal development. *The Journal of Physiology*, *601*(16), 3605–3630. DOI: 10.1113/JP284401

Kringel, R., Song, L., Xu, X., Bitzenhofer, S. H., & Hanganu-Opatz, I. L. (2023). Layer-specific impairment in the developing lateral entorhinal cortex of immune-challenged Disc1+/− mice. *The Journal of Physiology*, *601*(4), 847–857. DOI: 10.1113/JP283896

Kupers, R., Beaulieu-Lefebvre, M., Schneider, F. C., Kassuba, T., Paulson, O. B., Siebner, H. R., & Ptito, M. (2011). Neural correlates of olfactory processing in congenital blindness. *Neuropsychologia*, *49*(7), 2037–2044. DOI: 10.1016/j.neuropsychologia.2011.03.033

Kvajo, M., McKellar, H., Arguello, P. A., Drew, L. J., Moore, H., MacDermott, A. B., Karayiorgou, M., & Gogos, J. A. (2008). A mutation in mouse Disc1 that models a schizophrenia risk allele leads to specific alterations in neuronal architecture and cognition. *Proceedings of the National Academy of Sciences*, *105*(19), 7076–7081. DOI: 10.1073/pnas.0802615105

LaRovere, K. L., Riggs, B. J., Poussaint, T. Y., Young, C. C., Newhams, M. M., Maamari, M., Walker, T. C., Singh, A. R., Dapul, H., Hobbs, C. V., McLaughlin, G. E., Son, M. B. F., Maddux, A. B., Clouser, K. N., Rowan, C. M., McGuire, J. K., Fitzgerald, J. C., Gertz, S. J., Shein, S. L., … Overcoming COVID-19 Investigators. (2021). Neurologic Involvement in Children and Adolescents Hospitalized in the United States for COVID-19 or Multisystem Inflammatory Syndrome. *JAMA Neurology*, *78*(5), 536–547. DOI: 10.1001/jamaneurol.2021.0504

Le Jeune, H., & Jourdan, F. (1991). Postnatal development of cholinergic markers in the

rat olfactory bulb: A histochemical and immunocytochemical study. *Journal of Comparative Neurology*, *314*(2), 383–395. DOI: 10.1002/cne.903140212

Lee, J. Y., Jun, H., Soma, S., Nakazono, T., Shiraiwa, K., Dasgupta, A., Nakagawa, T., Xie, J. L., Chavez, J., Romo, R., Yungblut, S., Hagihara, M., Murata, K., & Igarashi, K. M. (2021). Dopamine facilitates associative memory encoding in the entorhinal cortex. *Nature*, *598*(7880), Article 7880. DOI: 10.1038/s41586-021-03948-8

Lee, L.-J., Chen, W.-J., Chuang, Y.-W., & Wang, Y.-C. (2009). Neonatal whisker trimming causes long-lasting changes in structure and function of the somatosensory system. *Experimental Neurology*, *219*(2), 524–532. DOI: 10.1016/j.expneurol.2009.07.012

Leinekugel, X., Khazipov, R., Cannon, R., Hirase, H., Ben-Ari, Y., & Buzsáki, G. (2002). Correlated Bursts of Activity in the Neonatal Hippocampus in Vivo. *Science*, *296*(5575), 2049–2052. DOI: 10.1126/science.1071111

Leitner, F. C., Melzer, S., Lütcke, H., Pinna, R., Seeburg, P. H., Helmchen, F., & Monyer, H. (2016). Spatially segregated feedforward and feedback neurons support differential odor processing in the lateral entorhinal cortex. *Nature Neuroscience*, *19*(7), Article 7. DOI: 10.1038/nn.4303

Lepousez, G., & Lledo, P.-M. (2013). Odor discrimination requires proper olfactory fast oscillations in awake mice. *Neuron*, *80*(4), 1010–1024.

Leprince, E., Dard, R. F., Mortet, S., Filippi, C., Giorgi-Kurz, M., Bourboulou, R., Lenck-Santini, P.-P., Picardo, M. A., Bocchio, M., Baude, A., & Cossart, R. (2023). Extrinsic control of the early postnatal CA1 hippocampal circuits. *Neuron*, *111*(6), 888–902. DOI: 10.1016/j.neuron.2022.12.013

Li, A., Zhang, L., Liu, M., Gong, L., Liu, Q., & Xu, F. (2012). Effects of Different Anesthetics on Oscillations in the Rat Olfactory Bulb. *Journal of the American Association for Laboratory Animal Science : JAALAS*, *51*(4), 458–463.

Li, Q., Takeuchi, Y., Wang, J., Gellért, L., Barcsai, L., Pedraza, L. K., Nagy, A. J., Kozák, G., Nakai, S., Kato, S., Kobayashi, K., Ohsawa, M., Horváth, G., Kékesi, G., Lőrincz, M. L., Devinsky, O., Buzsáki, G., & Berényi, A. (2023). Reinstating olfactory bulb-derived limbic gamma oscillations alleviates depression-like behavioral deficits in rodents. *Neuron*, *111*(13), 2065-2075.e5. DOI: 10.1016/j.neuron.2023.04.013

Li, S., Li, W., Wu, X., Li, J., Yang, J., Tu, C., Ye, X., & Ling, S. (2019). Olfactory deficit is associated with mitral cell dysfunction in the olfactory bulb of P301S tau transgenic mice. *Brain Research Bulletin*, *148*, 34–45. DOI: 10.1016/j.brainresbull.2019.03.006

Li, W., Li, S., Shen, L., Wang, J., Wu, X., Li, J., Tu, C., Ye, X., & Ling, S. (2019).

Impairment of Dendrodendritic Inhibition in the Olfactory Bulb of APP/PS1 Mice. *Frontiers in Aging Neuroscience*, *11*. DOI: 10.3389/fnagi.2019.00002

Li, Y., Xu, J., Liu, Y., Zhu, J., Liu, N., Zeng, W., Huang, N., Rasch, M. J., Jiang, H., Gu, X., & others. (2017). A distinct entorhinal cortex to hippocampal CA1 direct circuit for olfactory associative learning. *Nature Neuroscience*, *20*(4), 559–570. DOI: 10.1038/nn.4517

Lisman, J., & Morris, R. (2001). Why is the cortex a slow learner? *Nature*, *411*(6835), 248–249. DOI: 10.1038/35077185

Liu, G., Froudarakis, E., Patel, J. M., Kochukov, M. Y., Pekarek, B., Hunt, P. J., Patel, M., Ung, K., Fu, C.-H., Jo, J., Lee, H.-K., Tolias, A. S., & Arenkiel, B. R. (2019). Target specific functions of EPL interneurons in olfactory circuits. *Nature Communications*, *10*(1), 3369. DOI: 10.1038/s41467-019-11354-y

Liu, P., Gao, C., Wu, J., Wu, T., Zhang, Y., Liu, C., Sun, C., & Li, A. (2023). Negative valence encoding in the lateral entorhinal cortex during aversive olfactory learning. *Cell Reports*, *42*(10), 113204. DOI: 10.1016/j.celrep.2023.113204

Livneh, Y., Adam, Y., & Mizrahi, A. (2014). Odor Processing by Adult-Born Neurons. *Neuron*, *81*(5), 1097–1110. DOI: 10.1016/j.neuron.2014.01.007

Lledo, P.-M., & Valley, M. (2016). Adult Olfactory Bulb Neurogenesis. *Cold Spring Harbor Perspectives in Biology*, *8*(8), Article 8. DOI: 10.1101/cshperspect.a018945

Logan, D. W., Brunet, L. J., Webb, W. R., Cutforth, T., Ngai, J., & Stowers, L. (2012). Learned Recognition of Maternal Signature Odors Mediates the First Suckling Episode in Mice. *Current Biology*, *22*(21), 1998–2007. DOI: 10.1016/j.cub.2012.08.041

Luo, W., Yun, D., Hu, Y., Tian, M., Yang, J., Xu, Y., Tang, Y., Zhan, Y., Xie, H., & Guan, J.-S. (2022). Acquiring new memories in neocortex of hippocampal-lesioned mice. *Nature Communications*, *13*(1), Article 1. DOI: 10.1038/s41467-022-29208-5

Mahler, S. V., Vazey, E. M., Beckley, J. T., Keistler, C. R., McGlinchey, E. M., Kaufling, J., Wilson, S. P., Deisseroth, K., Woodward, J. J., & Aston-Jones, G. (2014). Designer receptors show role for ventral pallidum input to ventral tegmental area in cocaine seeking. *Nature Neuroscience*, *17*(4), 577–585. DOI: 10.1038/nn.3664

Mahn, M., Saraf-Sinik, I., Patil, P., Pulin, M., Bitton, E., Karalis, N., Bruentgens, F., Palgi, S., Gat, A., Dine, J., Wietek, J., Davidi, I., Levy, R., Litvin, A., Zhou, F., Sauter, K., Soba, P., Schmitz, D., Lüthi, A., … Yizhar, O. (2021). Efficient optogenetic silencing of neurotransmitter release with a mosquito rhodopsin. *Neuron*, *109*(10), 1621-1635.e8. DOI: 10.1016/j.neuron.2021.03.013

Mair, R. G., & Gesteland, R. C. (1982). Response properties of mitral cells in the olfactory bulb of the neonatal rat. *Neuroscience*, *7*(12), 3117–3125. DOI: 10.1016/0306-4522(82)90234-2

Malik, R., Li, Y., Schamiloglu, S., & Sohal, V. S. (2022). Top-down control of hippocampal signal-to-noise by prefrontal long-range inhibition. *Cell*, *185*(9), 1602-1617.e17. DOI: 10.1016/j.cell.2022.04.001

Maren, S., & Holt, W. (2000). The hippocampus and contextual memory retrieval in Pavlovian conditioning. *Behavioural Brain Research*, *110*(1), 97–108. DOI: 10.1016/S0166-4328(99)00188-6

Marlier, L., Schaal, B., & Soussignan, R. (1998). Neonatal Responsiveness to the Odor of Amniotic and Lacteal Fluids: A Test of Perinatal Chemosensory Continuity. *Child Development*, *69*(3), 611–623. DOI: 10.1111/j.1467-8624.1998.tb06232.x

Martin-Lopez, E., Vidyadhara, D. J., Liberia, T., Meller, S. J., Harmon, L. E., Hsu, R. M., Spence, N., Brennan, B., Han, K., Yücel, B., Chandra, S. S., & Greer, C. A. (2023). α-Synuclein Pathology and Reduced Neurogenesis in the Olfactory System Affect Olfaction in a Mouse Model of Parkinson's Disease. *Journal of Neuroscience*, *43*(6), 1051–1071. DOI: 10.1523/JNEUROSCI.1526-22.2022

McLean, J. H., & Shipley, M. T. (1987). Serotonergic afferents to the rat olfactory bulb: II. Changes in fiber distribution during development. *Journal of Neuroscience*, *7*(10), 3029–3039. DOI: 10.1523/JNEUROSCI.07-10-03029.1987

McLean, J. H., & Shipley, M. T. (1991). Postnatal development of the noradrenergic projection from locus coeruleus to the olfactory bulb in the rat. *The Journal of Comparative Neurology*, *304*(3), 467–477. DOI: 10.1002/cne.903040310

Meaney, M. J., Aitken, D. H., van Berkel, C., Bhatnagar, S., & Sapolsky, R. M. (1988). Effect of Neonatal Handling on Age-Related Impairments Associated with the Hippocampus. *Science*, *239*(4841), 766–768. DOI: 10.1126/science.3340858

Medendorp, W. E., Bjorefeldt, A., Crespo, E. L., Prakash, M., Pal, A., Waddell, M. L., Moore, C. I., & Hochgeschwender, U. (2021). Selective postnatal excitation of neocortical pyramidal neurons results in distinctive behavioral and circuit deficits in adulthood. *iScience*, *24*(3), 102157. DOI: 10.1016/j.isci.2021.102157

Meissner-Bernard, C., Dembitskaya, Y., Venance, L., & Fleischmann, A. (2019). Encoding of Odor Fear Memories in the Mouse Olfactory Cortex. *Current Biology*, *29*(3), 367-380.e4. DOI: 10.1016/j.cub.2018.12.003

Mena, W., Baker, K., Rubin, A., Kohli, S., Yoo, Y., Ziv, Y., Razaei-Mazinani, C., & Fleischmann, A. (2023). *Differential encoding of odor and place in mouse piriform*

and entorhinal cortex (p. 2023.10.05.561119). bioRxiv. DOI: 10.1101/2023.10.05.561119

Méndez, R., Balanzá-Martínez, V., Luperdi, S. C., Estrada, I., Latorre, A., González-Jiménez, P., Bouzas, L., Yépez, K., Ferrando, A., Reyes, S., & Menéndez, R. (2022). Long-term neuropsychiatric outcomes in COVID-19 survivors: A 1-year longitudinal study. *Journal of Internal Medicine*, *291*(2), 247–251. DOI: 10.1111/joim.13389

Mennella, J. A., Jagnow, C. P., & Beauchamp, G. K. (2001). Prenatal and Postnatal Flavor Learning by Human Infants. *Pediatrics*, *107*(6), e88. DOI: 10.1542/peds.107.6.e88

Meyer, U., & Feldon, J. (2012). To poly(I:C) or not to poly(I:C): Advancing preclinical schizophrenia research through the use of prenatal immune activation models. *Neuropharmacology*, *62*(3), 1308–1321. DOI: 10.1016/j.neuropharm.2011.01.009

Mihalj, D., Borbelyova, V., Pirnik, Z., Bacova, Z., Ostatnikova, D., & Bakos, J. (2024). Shank3 Deficiency Results in a Reduction in GABAergic Postsynaptic Puncta in the Olfactory Brain Areas. *Neurochemical Research*, *49*(4), 1008–1016. DOI: 10.1007/s11064-023-04097-2

Miller, S. S., & Spear, N. E. (2008). Olfactory learning in the rat neonate soon after birth. *Developmental Psychobiology*, *50*(6), 554–565. DOI: 10.1002/dev.20318

Miyamichi, K., Shlomai-Fuchs, Y., Shu, M., Weissbourd, B. C., Luo, L., & Mizrahi, A. (2013). Dissecting local circuits: Parvalbumin interneurons underlie broad feedback control of olfactory bulb output. *Neuron*, *80*(5), 1232–1245. DOI: 10.1016/j.neuron.2013.08.027

Moberly, A. H., Schreck, M., Bhattarai, J. P., Zweifel, L. S., Luo, W., & Ma, M. (2018). Olfactory inputs modulate respiration-related rhythmic activity in the prefrontal cortex and freezing behavior. *Nature Communications*, *9*(1), 1528. DOI: 10.1038/s41467-018-03988-1

Mochizuki-Kawai, H., Ichitani, Y., Ayabe-Kanamura, S., & Yamada, K. (2022). Odors associated with neonatal experiences with the dam have enhanced anxiolytic effects in rat. *Chemical Senses*, *47*, bjac019. DOI: 10.1093/chemse/bjac019

Molet, J., Maras, P. M., Kinney-Lang, E., Harris, N. G., Rashid, F., Ivy, A. S., Solodkin, A., Obenaus, A., & Baram, T. Z. (2016). MRI uncovers disrupted hippocampal microstructure that underlies memory impairments after early-life adversity. *Hippocampus*, *26*(12), 1618–1632. DOI: 10.1002/hipo.22661

Mori, K., Manabe, H., Narikiyo, K., & Onisawa, N. (2013). Olfactory consciousness and gamma oscillation couplings across the olfactory bulb, olfactory cortex, and

orbitofrontal cortex. *Frontiers in Psychology*, *4*, 743. DOI: 10.3389/fpsyg.2013.00743

Mori, K., & Sakano, H. (2011). How Is the Olfactory Map Formed and Interpreted in the Mammalian Brain? *Annual Review of Neuroscience*, *34*(Volume 34, 2011), 467–499. DOI: 10.1146/annurev-neuro-112210-112917

Moser, M. B., Moser, E. I., Forrest, E., Andersen, P., & Morris, R. G. (1995). Spatial learning with a minislab in the dorsal hippocampus. *Proceedings of the National Academy of Sciences*, *92*(21), 9697–9701. DOI: 10.1073/pnas.92.21.9697

Muller, T. H., Butler, J. L., Veselic, S., Miranda, B., Wallis, J. D., Dayan, P., Behrens, T. E. J., Kurth-Nelson, Z., & Kennerley, S. W. (2024). Distributional reinforcement learning in prefrontal cortex. *Nature Neuroscience*, *27*(3), 403–408. DOI: 10.1038/s41593-023-01535-w

Murphy, C. (2019). Olfactory and other sensory impairments in Alzheimer disease. *Nature Reviews Neurology*, *15*(1), Article 1. DOI: 10.1038/s41582-018-0097-5

Nadarajah, B., & Parnavelas, J. G. (2002). Modes of neuronal migration in the developing cerebral cortex. *Nature Reviews Neuroscience*, *3*(6), 423–432. DOI: 10.1038/nrn845

Nakahara, H., Zhang, L. I., & Merzenich, M. M. (2004). Specialization of primary auditory cortex processing by sound exposure in the "critical period." *Proceedings of the National Academy of Sciences*, *101*(18), 7170–7174. DOI: 10.1073/pnas.0401196101

Nakamura, N. H., Fukunaga, M., & Oku, Y. (2018). Respiratory modulation of cognitive performance during the retrieval process. *PLOS ONE*, *13*(9), Article 9. DOI: 10.1371/journal.pone.0204021

Nakashima, A., Ihara, N., Shigeta, M., Kiyonari, H., Ikegaya, Y., & Takeuchi, H. (2019). Structured spike series specify gene expression patterns for olfactory circuit formation. *Science*, *365*(6448), eaaw5030. DOI: 10.1126/science.aaw5030

Nardin, M., Kaefer, K., Stella, F., & Csicsvari, J. (2023). Theta oscillations as a substrate for medial prefrontal-hippocampal assembly interactions. *Cell Reports*, *42*(9), 113015. DOI: 10.1016/j.celrep.2023.113015

Neville, K. R., & Haberly, L. B. (2003). Beta and Gamma Oscillations in the Olfactory System of the Urethane-Anesthetized Rat. *Journal of Neurophysiology*, *90*(6), 3921–3930. DOI: 10.1152/jn.00475.2003

Neville, K. R., & Haberly, L. B. (2004). Olfactory Cortex. In G. M. Shepherd (Ed.), *The Synaptic Organization of the Brain* (p. 0). Oxford University Press. DOI: 10.1093/acprof:oso/9780195159561.003.0010

Nguyen, A. D., Pelavin, P. E., Shenton, M. E., Chilakamarri, P., McCarley, R. W., Nestor, P. G., & Levitt, J. J. (2011). Olfactory sulcal depth and olfactory bulb volume in patients with schizophrenia: An MRI study. *Brain Imaging and Behavior*, *5*(4), 252–261. DOI: 10.1007/s11682-011-9129-0

Nishizumi, H., Miyashita, A., Inoue, N., Inokuchi, K., Aoki, M., & Sakano, H. (2019). Primary dendrites of mitral cells synapse unto neighboring glomeruli independent of their odorant receptor identity. *Communications Biology*, *2*(1), 1–12. DOI: 10.1038/s42003-018-0252-y

Nolte, G., Bai, O., Wheaton, L., Mari, Z., Vorbach, S., & Hallett, M. (2004). Identifying true brain interaction from EEG data using the imaginary part of coherency. *Clinical Neurophysiology*, *115*(10), 2292–2307. DOI: 10.1016/j.clinph.2004.04.029

Nouraeinejad, A. (2023). The functional and structural changes in the hippocampus of COVID-19 patients. *Acta Neurologica Belgica*, *123*(4), 1247–1256. DOI: 10.1007/s13760-023-02291-1

Oberlander, V. C., Xu, X., Chini, M., & Hanganu-Opatz, I. L. (2019). Developmental dysfunction of prefrontal–hippocampal networks in mouse models of mental illness. *European Journal of Neuroscience*, *50*(6), 3072–3084. DOI: 10.1111/ejn.14436

O'Keefe, J. (1978). *The hippocampus as a cognitive map*. Oxford University Press.

Padilla-Coreano, N., Bolkan, S. S., Pierce, G. M., Blackman, D. R., Hardin, W. D., Garcia-Garcia, A. L., Spellman, T. J., & Gordon, J. A. (2016). Direct Ventral Hippocampal-Prefrontal Input Is Required for Anxiety-Related Neural Activity and Behavior. *Neuron*, *89*(4), 857–866. DOI: 10.1016/j.neuron.2016.01.011

Padmanabhan, K., Osakada, F., Tarabrina, A., Kizer, E., Callaway, E. M., Gage, F. H., & Sejnowski, T. J. (2019). Centrifugal Inputs to the Main Olfactory Bulb Revealed Through Whole Brain Circuit-Mapping. *Frontiers in Neuroanatomy*, *12*. DOI: 10.3389/fnana.2018.00115

Parbst, F., Kostka, J. K., Günther, A., Chen, Y., Hanganu-Opatz, I. L., & Bitzenhofer, S. H. (2024). *Developmental olfactory dysfunction and abnormal odor memory in immune-challenged Disc1+/- mice* (p. 2024.05.17.594663). bioRxiv. DOI: 10.1101/2024.05.17.594663

Parker, K. J., Oztan, O., Libove, R. A., Sumiyoshi, R. D., Jackson, L. P., Karhson, D. S., Summers, J. E., Hinman, K. E., Motonaga, K. S., Phillips, J. M., Carson, D. S., Garner, J. P., & Hardan, A. Y. (2017). Intranasal oxytocin treatment for social deficits and biomarkers of response in children with autism. *Proceedings of the National Academy of Sciences*, *114*(30), 8119–8124. DOI:

10.1073/pnas.1705521114

Peng, S., Yang, X., Meng, S., Liu, F., Lv, Y., Yang, H., Kong, Y., Xie, W., & Li, M. (2024). Dual circuits originating from the ventral hippocampus independently facilitate affective empathy. *Cell Reports*, *43*(6). DOI: 10.1016/j.celrep.2024.114277

Persson, B. M., Ambrozova, V., Duncan, S., Wood, E. R., O'Connor, A. R., & Ainge, J. A. (2022). Lateral entorhinal cortex lesions impair odor-context associative memory in male rats. *Journal of Neuroscience Research*, *100*(4), 1030–1046. DOI: 10.1002/jnr.25027

Piekarski, D. J., Boivin, J. R., & Wilbrecht, L. (2017). Ovarian Hormones Organize the Maturation of Inhibitory Neurotransmission in the Frontal Cortex at Puberty Onset in Female Mice. *Current Biology*, *27*(12), 1735-1745.e3. DOI: 10.1016/j.cub.2017.05.027

Pochinok, I., Stöber, T. M., Triesch, J., Chini, M., & Hanganu-Opatz, I. L. (2024). A developmental increase of inhibition promotes the emergence of hippocampal ripples. *Nature Communications*, *15*(1), 738. DOI: 10.1038/s41467-024-44983-z

Poo, C., & Isaacson, J. S. (2007). An Early Critical Period for Long-Term Plasticity and Structural Modification of Sensory Synapses in Olfactory Cortex. *Journal of Neuroscience*, *27*(28), 7553–7558. DOI: 10.1523/JNEUROSCI.1786-07.2007

Pöpplau, J. A., Schwarze, T., Dorofeikova, M., Pochinok, I., Günther, A., Marquardt, A., & Hanganu-Opatz, I. L. (2024). Reorganization of adolescent prefrontal cortex circuitry is required for mouse cognitive maturation. *Neuron*, *112*(3), 421-440.e7. DOI: 10.1016/j.neuron.2023.10.024

Price, D. J., Ferrer, J. M., Blakemore, C., & Kato, N. (1994). Postnatal development and plasticity of corticocortical projections from area 17 to area 18 in the cat's visual cortex. *Journal of Neuroscience*, *14*(5), 2747–2762. DOI: 10.1523/JNEUROSCI.14-05-02747.1994

Price, J. L. (1985). Beyond the primary olfactory cortex: Olfactory-related areas in the neocortex, thalamus and hypothalamus. *Chemical Senses*, *10*(2), 239–258. DOI: 10.1093/chemse/10.2.239

Rajasethupathy, P., Sankaran, S., Marshel, J. H., Kim, C. K., Ferenczi, E., Lee, S. Y., Berndt, A., Ramakrishnan, C., Jaffe, A., Lo, M., Liston, C., & Deisseroth, K. (2015). Projections from neocortex mediate top-down control of memory retrieval. *Nature*, *526*(7575), 653–659. DOI: 10.1038/nature15389

Rangel, L. M., Rueckemann, J. W., Riviere, P. D., Keefe, K. R., Porter, B. S., Heimbuch, I. S., Budlong, C. H., & Eichenbaum, H. (2016). Rhythmic coordination of

hippocampal neurons during associative memory processing. *eLife*, *5*, e09849. DOI: 10.7554/eLife.09849

Ray, J. P., & Price, J. L. (1992). The organization of the thalamocortical connections of the mediodorsal thalamic nucleus in the rat, related to the ventral forebrain–prefrontal cortex topography. *Journal of Comparative Neurology*, *323*(2), 167–197. DOI: 10.1002/cne.903230204

Reincke, S. A. J., & Hanganu-Opatz, I. L. (2017). Early-life stress impairs recognition memory and perturbs the functional maturation of prefrontal-hippocampal-perirhinal networks. *Scientific Reports*, *7*(1), 42042. DOI: 10.1038/srep42042

Renaud, M., Thibault, C., Le Normand, F., Mcdonald, E. G., Gallix, B., Debry, C., & Venkatasamy, A. (2021). Clinical Outcomes for Patients With Anosmia 1 Year After COVID-19 Diagnosis. *JAMA Network Open*, *4*(6), e2115352. DOI: 10.1001/jamanetworkopen.2021.15352

Rexrode, L. E., Hartley, J., Showmaker, K. C., Challagundla, L., Vandewege, M. W., Martin, B. E., Blair, E., Bollavarapu, R., Antonyraj, R. B., Hilton, K., Gardiner, A., Valeri, J., Gisabella, B., Garrett, M. R., Theoharides, T. C., & Pantazopoulos, H. (2024). Molecular profiling of the hippocampus of children with autism spectrum disorder. *Molecular Psychiatry*, *29*(7), 1968–1979. DOI: 10.1038/s41380-024-02441-8

Richter, M., Murtaza, N., Scharrenberg, R., White, S. H., Johanns, O., Walker, S., Yuen, R. K. C., Schwanke, B., Bedürftig, B., Henis, M., Scharf, S., Kraus, V., Dörk, R., Hellmann, J., Lindenmaier, Z., Ellegood, J., Hartung, H., Kwan, V., Sedlacik, J., … Calderon de Anda, F. (2019). Altered TAOK2 activity causes autism-related neurodevelopmental and cognitive abnormalities through RhoA signaling. *Molecular Psychiatry*, *24*(9), 1329–1350. DOI: 10.1038/s41380-018-0025-5

Roque, L. S., Kendrick, K. H., Norcliffe, E., Brown, P., Defina, R., Dingemanse, M., Dirksmeyer, T., Enfield, N. J., Floyd, S., Hammond, J., Rossi, G., Tufvesson, S., Putten, S. van, & Majid, A. (2015). Vision Verbs Dominate in Conversation Across Cultures, but the Ranking of Non-Visual Verbs Varies. *Cognitive Linguistics*, *26*(1), 31–60. DOI: 10.1515/cog-2014-0089

Ross, G. W., Petrovitch, H., Abbott, R. D., Tanner, C. M., Popper, J., Masaki, K., Launer, L., & White, L. R. (2008). Association of olfactory dysfunction with risk for future Parkinson's disease. *Annals of Neurology*, *63*(2), 167–173. DOI: 10.1002/ana.21291

Roth, B. L. (2016). DREADDs for Neuroscientists. *Neuron*, *89*(4), 683–694. DOI: 10.1016/j.neuron.2016.01.040

Roy, D. S., Arons, A., Mitchell, T. I., Pignatelli, M., Ryan, T. J., & Tonegawa, S. (2016). Memory retrieval by activating engram cells in mouse models of early Alzheimer's disease. *Nature*, *531*(7595), 508–512. DOI: 10.1038/nature17172

Ryndych, D., Sebold, A., Strassburg, A., Li, Y., Ramos, R. L., & Otazu, G. H. (2023). Haploinsufficiency of Shank3 in Mice Selectively Impairs Target Odor Recognition in Novel Background Odors. *Journal of Neuroscience*, *43*(46), 7799–7811. DOI: 10.1523/JNEUROSCI.0255-23.2023

Ryu, J.-Y., Cerecedo-Lopez, C., Yang, H., Ryu, I., & Du, R. (2024). Brain-targeted intranasal delivery of protein-based gene therapy for treatment of ischemic stroke. *Theranostics*, *14*(12), 4773–4786. DOI: 10.7150/thno.98088

Sakamoto, M., Ieki, N., Miyoshi, G., Mochimaru, D., Miyachi, H., Imura, T., Yamaguchi, M., Fishell, G., Mori, K., Kageyama, R., & others. (2014). Continuous postnatal neurogenesis contributes to formation of the olfactory bulb neural circuits and flexible olfactory associative learning. *Journal of Neuroscience*, *34*(17), 5788–5799. DOI: 10.1523/JNEUROSCI.0674-14.2014

Sakano, H. (2010). Neural Map Formation in the Mouse Olfactory System. *Neuron*, *67*(4), 530–542. DOI: 10.1016/j.neuron.2010.07.003

Sale, A., Berardi, N., & Maffei, L. (2009). Enrich the environment to empower the brain. *Trends in Neurosciences*, *32*(4), 233–239. DOI: 10.1016/j.tins.2008.12.004

Salimi, M., Ghazvineh, S., Zare, M., Parsazadegan, T., Dehdar, K., Nazari, M., Mirnajafi-Zadeh, J., Jamaati, H., & Raoufy, M. R. (2019). Distraction of olfactory bulb-medial prefrontal cortex circuit may induce anxiety-like behavior in allergic rhinitis. *PLOS ONE*, *14*(9), e0221978. DOI: 10.1371/journal.pone.0221978

Salimi, M., Nazari, M., Shahsavar, P., Dehghan, S., Javan, M., Mirnajafi-Zadeh, J., & Raoufy, M. R. (2024). Olfactory bulb stimulation mitigates Alzheimer's-like disease progression. *CNS Neuroscience & Therapeutics*, *30*(10), e70056. DOI: 10.1111/cns.70056

Salimi, M., Tabasi, F., Abdolsamadi, M., Dehghan, S., Dehdar, K., Nazari, M., Javan, M., Mirnajafi-Zadeh, J., & Raoufy, M. R. (2022). Disrupted connectivity in the olfactory bulb-entorhinal cortex-dorsal hippocampus circuit is associated with recognition memory deficit in Alzheimer's disease model. *Scientific Reports*, *12*(1), Article 1. DOI: 10.1038/s41598-022-08528-y

Salimi, M., Tabasi, F., Nazari, M., Ghazvineh, S., Salimi, A., Jamaati, H., & Raoufy, M. R. (2021). The olfactory bulb modulates entorhinal cortex oscillations during spatial working memory. *The Journal of Physiological Sciences*, *71*(1), 1–9. DOI:

10.1186/s12576-021-00805-1

Schaal, B., Saxton, T. K., Loos, H., Soussignan, R., & Durand, K. (2020). Olfaction scaffolds the developing human from neonate to adolescent and beyond. *Philosophical Transactions of the Royal Society B: Biological Sciences*, *375*(1800), 20190261. DOI: 10.1098/rstb.2019.0261

Schalbetter, S. M., von Arx, A. S., Cruz-Ochoa, N., Dawson, K., Ivanov, A., Mueller, F. S., Lin, H.-Y., Amport, R., Mildenberger, W., Mattei, D., Beule, D., Földy, C., Greter, M., Notter, T., & Meyer, U. (2022). Adolescence is a sensitive period for prefrontal microglia to act on cognitive development. *Science Advances*, *8*(9), eabi6672. DOI: 10.1126/sciadv.abi6672

Schechter, I., Butler, P. D., Silipo, G., Zemon, V., & Javitt, D. C. (2003). Magnocellular and parvocellular contributions to backward masking dysfunction in schizophrenia. *Schizophrenia Research*, *64*(2), 91–101. DOI: 10.1016/S0920-9964(03)00008-2

Schepanski, S., Chini, M., Sternemann, V., Urbschat, C., Thiele, K., Sun, T., Zhao, Y., Poburski, M., Woestemeier, A., Thieme, M.-T., & others. (2022). Pregnancy-induced maternal microchimerism shapes neurodevelopment and behavior in mice. *Nature Communications*, *13*(1), 1–14. DOI: 10.1038/s41467-022-32230-2

Schurov, I. L., Handford, E. J., Brandon, N. J., & Whiting, P. J. (2004). Expression of disrupted in schizophrenia 1 (DISC1) protein in the adult and developing mouse brain indicates its role in neurodevelopment. *Molecular Psychiatry*, *9*(12), 1100–1110. DOI: 10.1038/sj.mp.4001574

Sevelinges, Y., Sullivan, R. M., Messaoudi, B., & Mouly, A.-M. (2008). Neonatal odor-shock conditioning alters the neural network involved in odor fear learning at adulthood. *Learning & Memory*, *15*(9), 649–656. DOI: 10.1101/lm.998508

Sheriff, A., Zhou, G., Sagar, V., Morgenthaler, J. B., Cyr, C., Hauner, K. K., Omidbeigi, M., Rosenow, J. M., Schuele, S. U., Lane, G., & Zelano, C. (2024). Breathing orchestrates synchronization of sleep oscillations in the human hippocampus. *Proceedings of the National Academy of Sciences*, *121*(52), e2405395121. DOI: 10.1073/pnas.2405395121

Shimshek, D. R., Bus, T., Kim, J., Mihaljevic, A., Mack, V., Seeburg, P. H., Sprengel, R., & Schaefer, A. T. (2005). Enhanced odor discrimination and impaired olfactory memory by spatially controlled switch of AMPA receptors. *PLoS Biology*, *3*(11), e354. DOI: 10.1371/journal.pbio.0030354

Shin, J. D., & Jadhav, S. P. (2024). Prefrontal cortical ripples mediate top-down suppression of hippocampal reactivation during sleep memory consolidation.

Current Biology, *34*(13), 2801-2811.e9. DOI: 10.1016/j.cub.2024.05.018

Shipkov, D., Nasretdinov, A., Khazipov, R., & Valeeva, G. (2024). Synchronous excitation in the superficial and deep layers of the medial entorhinal cortex precedes early sharp waves in the neonatal rat hippocampus. *Frontiers in Cellular Neuroscience*, *18*. DOI: 10.3389/fncel.2024.1403073

Sieben K., Bieler M., Röder B., & Hanganu-Opatz I. L. (2015). Neonatal Restriction of Tactile Inputs Leads to Long-Lasting Impairments of Cross-Modal Processing. *PLOS Biology*, *13*(11), e1002304. DOI: 10.1371/journal.pbio.1002304

Sigurdsson, T., Stark, K. L., Karayiorgou, M., Gogos, J. A., & Gordon, J. A. (2010). Impaired hippocampal–prefrontal synchrony in a genetic mouse model of schizophrenia. *Nature*, *464*(7289), 763–767. DOI: 10.1038/nature08855

Siper, P. M., Rowe, M. A., Guillory, S. B., Rouhandeh, A. A., George-Jones, J. L., Tavassoli, T., Lurie, S., Zweifach, J., Weissman, J., Foss-Feig, J., Halpern, D., Trelles, M. P., Mulhern, M. S., Brittenham, C., Gordon, J., Zemon, V., Buxbaum, J. D., & Kolevzon, A. (2022). Visual Evoked Potential Abnormalities in Phelan-McDermid Syndrome. *Journal of the American Academy of Child & Adolescent Psychiatry*, *61*(4), 565-574.e1. DOI: 10.1016/j.jaac.2021.07.006

Song, A. J., & Palmiter, R. D. (2018). Detecting and Avoiding Problems When Using the Cre/lox System. *Trends in Genetics : TIG*, *34*(5), 333–340. DOI: 10.1016/j.tig.2017.12.008

Song, L., Xu, X., Putthoff, P., Fleck, D., Spehr, M., & Hanganu-Opatz, I. L. (2022). Sparser and Less Efficient Hippocampal-Prefrontal Projections account for Developmental Network Dysfunction in a Model of Psychiatric Risk Mediated by Gene-Environment Interaction. *Journal of Neuroscience*, *42*(4), 601–618. DOI: 10.1523/JNEUROSCI.1203-21.2021

Sosulski, D. L., Bloom, M. L., Cutforth, T., Axel, R., & Datta, S. R. (2011). Distinct representations of olfactory information in different cortical centres. *Nature*, *472*(7342), Article 7342. DOI: 10.1038/nature09868

Spinato, G., Fabbris, C., Polesel, J., Cazzador, D., Borsetto, D., Hopkins, C., & Boscolo-Rizzo, P. (2020). Alterations in Smell or Taste in Mildly Symptomatic Outpatients With SARS-CoV-2 Infection. *JAMA*, *323*(20), 2089–2090. DOI: 10.1001/jama.2020.6771

Staresina, B. P., Niediek, J., Borger, V., Surges, R., & Mormann, F. (2023). How coupled slow oscillations, spindles and ripples coordinate neuronal processing and communication during human sleep. *Nature Neuroscience*, *26*(8), 1429–1437. DOI:

10.1038/s41593-023-01381-w

Staresina, B. P., Reber, T. P., Niediek, J., Boström, J., Elger, C. E., & Mormann, F. (2019). Recollection in the human hippocampal-entorhinal cell circuitry. *Nature Communications*, *10*(1), Article 1. DOI: 10.1038/s41467-019-09558-3

Steinbart, D., Yaakub, S. N., Steinbrenner, M., Guldin, L. S., Holtkamp, M., Keller, S. S., Weber, B., Rüber, T., Heckemann, R. A., Ilyas-Feldmann, M., Hammers, A., & Initiative, for the A. D. N. (2023). Automatic and manual segmentation of the piriform cortex: Method development and validation in patients with temporal lobe epilepsy and Alzheimer's disease. *Human Brain Mapping*, *44*(8), 3196–3209. DOI: 10.1002/hbm.26274

Steinmetz, N. A., Aydin, C., Lebedeva, A., Okun, M., Pachitariu, M., Bauza, M., Beau, M., Bhagat, J., Böhm, C., Broux, M., Chen, S., Colonell, J., Gardner, R. J., Karsh, B., Kloosterman, F., Kostadinov, D., Mora-Lopez, C., O'Callaghan, J., Park, J., … Harris, T. D. (2021). Neuropixels 2.0: A miniaturized high-density probe for stable, long-term brain recordings. *Science*, *372*(6539), eabf4588. DOI: 10.1126/science.abf4588

Strange, B. A., Witter, M. P., Lein, E. S., & Moser, E. I. (2014). Functional organization of the hippocampal longitudinal axis. *Nature Reviews Neuroscience*, *15*(10), Article 10. DOI: 10.1038/nrn3785

Suh, J., Rivest, A. J., Nakashiba, T., Tominaga, T., & Tonegawa, S. (2011). Entorhinal Cortex Layer III Input to the Hippocampus Is Crucial for Temporal Association Memory. *Science*, *334*(6061), 1415–1420. DOI: 10.1126/science.1210125

Sullivan, R. M., Landers, M., Yeaman, B., & Wilson, D. A. (2000). Good memories of bad events in infancy. *Nature*, *407*(6800), Article 6800. DOI: 10.1038/35024156

Sultan, S., Rey, N., Sacquet, J., Mandairon, N., & Didier, A. (2011). Newborn Neurons in the Olfactory Bulb Selected for Long-Term Survival through Olfactory Learning Are Prematurely Suppressed When the Olfactory Memory Is Erased. *Journal of Neuroscience*, *31*(42), 14893–14898. DOI: 10.1523/JNEUROSCI.3677-11.2011

Sun, Y., Jin, S., Lin, X., Chen, L., Qiao, X., Jiang, L., Zhou, P., Johnston, K. G., Golshani, P., Nie, Q., & others. (2019). CA1-projecting subiculum neurons facilitate object–place learning. *Nature Neuroscience*, *22*(11), 1857–1870. DOI: 10.1038/s41593-019-0496-y

Symanski, C. A., Bladon, J. H., Kullberg, E. T., Miller, P., & Jadhav, S. P. (2022). Rhythmic coordination and ensemble dynamics in the hippocampal-prefrontal network during odor-place associative memory and decision making. *eLife*, *11*,

e79545. DOI: 10.7554/eLife.79545

Szczurkowska, J., Lee, S.-I., Guo, A., Cwetsch, A. W., Khan, T., Rao, S., Walz, G., Huber, T. B., Cancedda, L., Pautot, S., & Shelly, M. (2020). A Localized Scaffold for cGMP Increase Is Required for Apical Dendrite Development. *Cell Reports*, *31*(2), 107519. DOI: 10.1016/j.celrep.2020.03.083

Tamura, M., Spellman, T. J., Rosen, A. M., Gogos, J. A., & Gordon, J. A. (2017). Hippocampal-prefrontal theta-gamma coupling during performance of a spatial working memory task. *Nature Communications*, *8*(1), 2182. DOI: 10.1038/s41467-017-02108-9

Tan, Z., Liu, Z., Liu, Y., Liu, F., Robinson, H., Lin, T. W., Xiong, W.-C., & Mei, L. (2022). An ErbB4-Positive Neuronal Network in the Olfactory Bulb for Olfaction. *Journal of Neuroscience*, *42*(34), 6518–6535. DOI: 10.1523/JNEUROSCI.0131-22.2022

Teyler, T. J., & Rudy, J. W. (2007). The hippocampal indexing theory and episodic memory: Updating the index. *Hippocampus*, *17*(12), 1158–1169. DOI: 10.1002/hipo.20350

Thomann, P. A., Dos Santos, V., Seidl, U., Toro, P., Essig, M., & Schröder, J. (2009a). MRI-Derived Atrophy of the Olfactory Bulb and Tract in Mild Cognitive Impairment and Alzheimer's Disease. *Journal of Alzheimer's Disease*, *17*(1), 213–221. DOI: 10.3233/JAD-2009-1036

Thomann, P. A., Dos Santos, V., Toro, P., Schönknecht, P., Essig, M., & Schröder, J. (2009b). Reduced olfactory bulb and tract volume in early Alzheimer's disease—A MRI study. *Neurobiology of Aging*, *30*(5), 838–841. DOI: 10.1016/j.neurobiolaging.2007.08.001

Tort, A. B. L., Ponsel, S., Jessberger, J., Yanovsky, Y., Brankačk, J., & Draguhn, A. (2018). Parallel detection of theta and respiration-coupled oscillations throughout the mouse brain. *Scientific Reports*, *8*(1), 6432. DOI: 10.1038/s41598-018-24629-z

Tozzi, F., Guglielmo, S., Paraciani, C., van den Oever, M. C., Mainardi, M., Cattaneo, A., & Origlia, N. (2024). Involvement of a lateral entorhinal cortex engram in episodic-like memory recall. *Cell Reports*, *43*(10), 114795. DOI: 10.1016/j.celrep.2024.114795

Trejo, D. H., Ciuparu, A., Silva, P. G. da, Velasquez, C. M., Rebouillat, B., Gross, M. D., Davis, M. B., Muresan, R. C., & Albeanu, D. F. (2023). *Fast updating feedback from piriform cortex to the olfactory bulb relays multimodal reward contingency signals during rule-reversal* (p. 2023.09.12.557267). bioRxiv. DOI: 10.1101/2023.09.12.557267

Tsai, L., & Barnea, G. (2014). A Critical Period Defined by Axon-Targeting Mechanisms

in the Murine Olfactory Bulb. *Science*, *344*(6180), 197–200. DOI: 10.1126/science.1248806

Tsao, A., Moser, M.-B., & Moser, E. I. (2013). Traces of Experience in the Lateral Entorhinal Cortex. *Current Biology*, *23*(5), 399–405. DOI: 10.1016/j.cub.2013.01.036

Turetsky, B. I., Moberg, P. J., Yousem, D. M., Doty, R. L., Arnold, S. E., & Gur, R. E. (2000). Reduced Olfactory Bulb Volume in Patients With Schizophrenia. *American Journal of Psychiatry*, *157*(5), 828–830. DOI: 10.1176/appi.ajp.157.5.828

Vaaga, C. E., Yorgason, J. T., Williams, J. T., & Westbrook, G. L. (2017). Presynaptic gain control by endogenous cotransmission of dopamine and GABA in the olfactory bulb. *Journal of Neurophysiology*, *117*(3), 1163–1170. DOI: 10.1152/jn.00694.2016

Valeeva, G., Janackova, S., Nasretdinov, A., Rychkova, V., Makarov, R., Holmes, G. L., Khazipov, R., & Lenck-Santini, P.-P. (2019). Emergence of Coordinated Activity in the Developing Entorhinal–Hippocampal Network. *Cerebral Cortex*, *29*(2), 906–920. DOI: 10.1093/cercor/bhy309

Vandrey, B., Garden, D. L., Ambrozova, V., McClure, C., Nolan, M. F., & Ainge, J. A. (2020). Fan cells in layer 2 of the lateral entorhinal cortex are critical for episodic-like memory. *Current Biology*, *30*(1), 169–175. DOI: 10.1016/j.cub.2019.11.027

Verhagen, J. V., Wesson, D. W., Netoff, T. I., White, J. A., & Wachowiak, M. (2007). Sniffing controls an adaptive filter of sensory input to the olfactory bulb. *Nature Neuroscience*, *10*(5), 631–639. DOI: 10.1038/nn1892

Vertes, R. P. (2004). Differential projections of the infralimbic and prelimbic cortex in the rat. *Synapse*, *51*(1), 32–58. DOI: 10.1002/syn.10279

Viberg, Å. (2001). *The verbs of perception* (Vol. 2, pp. 1294–1309). De Gruyter, Berlin. https://urn.kb.se/resolve?urn=urn:nbn:se:uu:diva-40595

Viberg, Å. (2014). The verbs of perception: A typological study. In B. Butterworth, B. Comrie, & Ö. Dahl (Eds.), *Explanations for Language Universals* (pp. 123–162). De Gruyter Mouton. DOI: 10.1515/9783110868555.123

Volman, I., Roelofs, K., Koch, S., Verhagen, L., & Toni, I. (2011). Anterior Prefrontal Cortex Inhibition Impairs Control over Social Emotional Actions. *Current Biology*, *21*(20), 1766–1770. DOI: 10.1016/j.cub.2011.08.050

Wagner, S., Issanchou, S., Chabanet, C., Lange, C., Schaal, B., & Monnery-Patris, S. (2019). Weanling Infants Prefer the Odors of Green Vegetables, Cheese, and Fish When Their Mothers Consumed These Foods During Pregnancy and/or Lactation. *Chemical Senses*, *44*(4), 257–265. DOI: 10.1093/chemse/bjz011

Walz, A., Omura, M., & Mombaerts, P. (2006). Development and topography of the lateral olfactory tract in the mouse: Imaging by genetically encoded and injected fluorescent markers. *Journal of Neurobiology*, *66*(8), 835–846. DOI: 10.1002/neu.20266

Wang, D., Wu, J., Liu, P., Li, X., Li, J., He, M., & Li, A. (2022). VIP interneurons regulate olfactory bulb output and contribute to odor detection and discrimination. *Cell Reports*, *38*(7), 110383. DOI: 10.1016/j.celrep.2022.110383

Wang, H., Li, F., Zheng, X., Meng, L., Chen, M., Hui, Y., Li, Y., Xie, K., Zhang, J., & Guo, G. (2022). Social defeat drives hyperexcitation of the piriform cortex to induce learning and memory impairment but not mood-related disorders in mice. *Translational Psychiatry*, *12*(1), 1–14. DOI: 10.1038/s41398-022-02151-1

Wang, J. X., Kurth-Nelson, Z., Kumaran, D., Tirumala, D., Soyer, H., Leibo, J. Z., Hassabis, D., & Botvinick, M. (2018). Prefrontal cortex as a meta-reinforcement learning system. *Nature Neuroscience*, *21*(6), 860–868. DOI: 10.1038/s41593-018-0147-8

Wang, S.-S., Mao, X.-F., Cai, Z.-S., Lin, W., Liu, X.-X., Luo, B., Chen, X., Yue, Y., Fan, H.-Y., Sasaki, T., Fukunaga, K., Zhang, W.-B., Lu, Y.-M., & Han, F. (2024). Distinct Olfactory Bulb-Cortex Neural Circuits Coordinate Cognitive Function in Parkinson's Disease. *Research*, *7*, 0484. DOI: 10.34133/research.0484

Wang, Z., Singh, B., Zhou, X., & Constantinidis, C. (2022). Strong Gamma Frequency Oscillations in the Adolescent Prefrontal Cortex. *Journal of Neuroscience*, *42*(14), 2917–2929. DOI: 10.1523/JNEUROSCI.1604-21.2022

Wayman, G. A., Impey, S., Marks, D., Saneyoshi, T., Grant, W. F., Derkach, V., & Soderling, T. R. (2006). Activity-Dependent Dendritic Arborization Mediated by CaM-Kinase I Activation and Enhanced CREB-Dependent Transcription of Wnt-2. *Neuron*, *50*(6), 897–909. DOI: 10.1016/j.neuron.2006.05.008

Wesson, D. W., Borkowski, A. H., Landreth, G. E., Nixon, R. A., Levy, E., & Wilson, D. A. (2011). Sensory Network Dysfunction, Behavioral Impairments, and Their Reversibility in an Alzheimer's β-Amyloidosis Mouse Model. *Journal of Neuroscience*, *31*(44), 15962–15971. DOI: 10.1523/JNEUROSCI.2085-11.2011

Wietek, J., Nozownik, A., Pulin, M., Saraf-Sinik, I., Matosevich, N., Gowrishankar, R., Gat, A., Malan, D., Brown, B. J., Dine, J., Imambocus, B. N., Levy, R., Sauter, K., Litvin, A., Regev, N., Subramaniam, S., Abrera, K., Summarli, D., Goren, E. M., … Yizhar, O. (2024). A bistable inhibitory optoGPCR for multiplexed optogenetic control of neural circuits. *Nature Methods*, *21*(7), 1275–1287. DOI: 10.1038/s41592-024-02285-8

Wilson, D. I. G., Watanabe, S., Milner, H., & Ainge, J. A. (2013). Lateral entorhinal cortex

is necessary for associative but not nonassociative recognition memory. *Hippocampus*, *23*(12), 1280–1290. DOI: 10.1002/hipo.22165

Wilson, M. A., Varela, C., & Remondes, M. (2015). Phase organization of network computations. *Current Opinion in Neurobiology*, *31*, 250–253. DOI: 10.1016/j.conb.2014.12.011

Wirt, R. A., & Hyman, J. M. (2019). ACC Theta Improves Hippocampal Contextual Processing during Remote Recall. *Cell Reports*, *27*(8), 2313-2327.e4. DOI: 10.1016/j.celrep.2019.04.080

Witter, M. P., Wouterlood, F. G., Naber, P. A., & Van Haeften, T. (2000). Anatomical Organization of the Parahippocampal-Hippocampal Network. *Annals of the New York Academy of Sciences*, *911*(1), 1–24. DOI: 10.1111/j.1749-6632.2000.tb06716.x

Wouterlood, F. G., & Nederlof, J. (1983). Terminations of olfactory afferents on layer II and III neurons in the entorhinal area: Degeneration-golgi-electron microscopic study in the rat. *Neuroscience Letters*, *36*(2), 105–110. DOI: 10.1016/0304-3940(83)90250-1

Xu, X., Hanganu-Opatz, I. L., & Bieler, M. (2020). Cross-Talk of Low-Level Sensory and High-Level Cognitive Processing: Development, Mechanisms, and Relevance for Cross-Modal Abilities of the Brain. *Frontiers in Neurorobotics*, *14*. DOI: 10.3389/fnbot.2020.00007

Xu, X., Song, L., Kringel, R., & Hanganu-Opatz, I. L. (2021). Developmental decrease of entorhinal-hippocampal communication in immune-challenged DISC1 knockdown mice. *Nature Communications*, *12*(1), 1–17. DOI: 10.1038/s41467-021-27114-w

Xue, B., Meng, X., Xu, Y., Kao, J. P. Y., & Kanold, P. O. (2022). Transient Coupling between Infragranular and Subplate Layers to Layer 1 Neurons Before Ear Opening and throughout the Critical Period Depends on Peripheral Activity. *Journal of Neuroscience*, *42*(9), 1702–1718. DOI: 10.1523/JNEUROSCI.2505-20.2021

Yang, K., Hasegawa, Y., Bhattarai, J. P., Hua, J., Dower, M., Etyemez, S., Prasad, N., Duvall, L., Paez, A., Smith, A., Wang, Y., Zhang, Y.-F., Lane, A. P., Ishizuka, K., Kamath, V., Ma, M., Kamiya, A., & Sawa, A. (2024). Inflammation-related pathology in the olfactory epithelium: Its impact on the olfactory system in psychotic disorders. *Molecular Psychiatry*, *29*(5), 1453–1464. DOI: 10.1038/s41380-024-02425-8

Yang, K., Hua, J., Etyemez, S., Paez, A., Prasad, N., Ishizuka, K., Sawa, A., & Kamath, V. (2021). Volumetric alteration of olfactory bulb and immune-related molecular changes in olfactory epithelium in first episode psychosis patients. *Schizophrenia*

Research, *235*, 9–11. DOI: 10.1016/j.schres.2021.07.016

Yang, Q., Zhou, G., Noto, T., Templer, J. W., Schuele, S. U., Rosenow, J. M., Lane, G., & Zelano, C. (2022). Smell-induced gamma oscillations in human olfactory cortex are required for accurate perception of odor identity. *PLoS Biology*, *20*(1), e3001509. DOI: 10.1371/journal.pbio.3001509

Yao, Z.-G., Hua, F., Zhang, H.-Z., Li, Y.-Y., & Qin, Y.-J. (2017). Olfactory dysfunction in the APP/PS1 transgenic mouse model of Alzheimer's disease: Morphological evaluations from the nose to the brain. *Neuropathology*, *37*(6), 485–494. DOI: 10.1111/neup.12391

Yarmohammadi-Samani, P., Taghipourbibalan, H., & Vatanparast, J. (2022). Long-lasting Postnatal Sensory Deprivation Alters Dendritic Morphology of Pyramidal Neurons in the Rat Hippocampus: Behavioral Correlates. *Neuroscience*, *480*, 79–96. DOI: 10.1016/j.neuroscience.2021.11.011

Yu, C. R., Power, J., Barnea, G., O'Donnell, S., Brown, H. E. V., Osborne, J., Axel, R., & Gogos, J. A. (2004). Spontaneous Neural Activity Is Required for the Establishment and Maintenance of the Olfactory Sensory Map. *Neuron*, *42*(4), 553–566. DOI: 10.1016/S0896-6273(04)00224-7

Yu, W., Wu, X., Chen, Y., Liang, Z., Jiang, J., Misrani, A., Su, Y., Peng, Y., Chen, J., Tang, B., Sun, M., Long, C., Shen, J., & Yang, L. (2021). Pelvic Pain Alters Functional Connectivity Between Anterior Cingulate Cortex and Hippocampus in Both Humans and a Rat Model. *Frontiers in Systems Neuroscience*, *15*. DOI: 10.3389/fnsys.2021.642349

Yuan, D., Cheng, A., Kawahata, I., Izumi, H., Xu, J., & Fukunaga, K. (2021). Single Administration of the T-Type Calcium Channel Enhancer SAK3 Reduces Oxidative Stress and Improves Cognition in Olfactory Bulbectomized Mice. *International Journal of Molecular Sciences*, *22*(2), Article 2. DOI: 10.3390/ijms22020741

Zelano, C., Jiang, H., Zhou, G., Arora, N., Schuele, S., Rosenow, J., & Gottfried, J. A. (2016). Nasal Respiration Entrains Human Limbic Oscillations and Modulates Cognitive Function. *Journal of Neuroscience*, *36*(49), 12448–12467. DOI: 10.1523/JNEUROSCI.2586-16.2016

Zhang, D., Zhang, W., Ming, C., Gao, X., Yuan, H., Lin, X., Mao, X., Wang, C., Guo, X., Du, Y., Shao, L., Yang, R., Lin, Z., Wu, X., Huang, T. Y., Wang, Z., Zhang, Y., Xu, H., & Zhao, Y. (2024). P-tau217 correlates with neurodegeneration in Alzheimer's disease, and targeting p-tau217 with immunotherapy ameliorates murine tauopathy. *Neuron*, *112*(10), 1676-1693.e12. DOI: 10.1016/j.neuron.2024.02.017

Zhang, J., Hao, C., Jiang, J., Feng, Y., Chen, X., Zheng, Y., Liu, J., Zhang, Z., Long, C., & Yang, L. (2018). The mechanisms underlying olfactory deficits in apolipoprotein E–deficient mice: Focus on olfactory epithelium and olfactory bulb. *Neurobiology of Aging*, *62*, 20–33. DOI: 10.1016/j.neurobiolaging.2017.09.036

Zhang, Y., Zhu, M., Sun, Y., Tang, B., Zhang, G., An, P., Cheng, Y., Shan, Y., Merzenich, M. M., & Zhou, X. (2021). Environmental noise degrades hippocampus-related learning and memory. *Proceedings of the National Academy of Sciences*, *118*(1), e2017841117. DOI: 10.1073/pnas.2017841117

Zhang, Z., Collins, D. C., & Maier, J. X. (2021). Network Dynamics in the Developing Piriform Cortex of Unanesthetized Rats. *Cerebral Cortex*, *31*(2), 1334–1346. DOI: 10.1093/cercor/bhaa300

Zhao, H., & Reed, R. R. (2001). X Inactivation of the *OCNC1* Channel Gene Reveals a Role for Activity-Dependent Competition in the Olfactory System. *Cell*, *104*(5), 651–660. DOI: 10.1016/S0092-8674(01)00262-8

Zhao, S., Shibata, K., Hellyer, P. J., Trender, W., Manohar, S., Hampshire, A., & Husain, M. (2022). Rapid vigilance and episodic memory decrements in COVID-19 survivors. *Brain Communications*, *4*(1), fcab295. DOI: 10.1093/braincomms/fcab295

Zheng, J.-J., Li, S.-J., Zhang, X.-D., Miao, W.-Y., Zhang, D., Yao, H., & Yu, X. (2014). Oxytocin mediates early experience–dependent cross-modal plasticity in the sensory cortices. *Nature Neuroscience*, *17*(3), Article 3. DOI: 10.1038/nn.3634

Zhou, Y., Fang, F.-H., Pan, P., Liu, Z.-R., & Ji, Y.-H. (2017). Visual deprivation induce cross-modal enhancement of olfactory perception. *Biochemical and Biophysical Research Communications*, *486*(3), 833–838. DOI: 10.1016/j.bbrc.2017.03.140

Ziegler-Waldkirch, S., Friesen, M., Loreth, D., Sauer, J.-F., Kemna, S., Hilse, A., Erny, D., Helm, C., Prinz, M., Bartos, M., & others. (2022). Seed-induced Aβ deposition alters neuronal function and impairs olfaction in a mouse model of Alzheimer's disease. *Molecular Psychiatry*, 1–11. DOI: 10.1038/s41380-022-01686-5

Zutshi, I., & Buzsáki, G. (2023). Hippocampal sharp-wave ripples and their spike assembly content are regulated by the medial entorhinal cortex. *Current Biology*, *33*(17), 3648-3659.e4. DOI: 10.1016/j.cub.2023.07.039

6 | Appendix

6.1 List of abbreviations

Abbreviation	Full name
2D	two demension
AAV	adeno-associated virus
ACC	anterior cingulate cortex
AD	Alzheimer’s disease
AMPA	α-amino-3-hydroxy-5-methyl-4-isoxazolepropionic acid
AON	anterior olfactory nucleus
APP	amyloid precursor protein
ASD	autism spectrum disorder
Aβ	β-amyloid plaque
a.u.	arbitrary unit
BCI	brain-computer interface
BOLD	bloodoxygen-level-dependent
BSA	bovine serum albumin
C21	compound 21
CA	cornu ammonis
COVID-19	Coronavirus disease 2019
ChR2	channelrhodopsin
CI	confidence interval

COA	cortical amygdaloid nucleus
CSD	current-source density
DA	dopaminergic
DG	dentate gyrus
Disc	gene disrupted-in-schizophrenia
DNA	deoxyribonucleic acid
DREADD	designer receptor exclusively activated by designer drug
E	embryonic day
EC	entorhinal cortex
EEG	electroencephalogram
EF1a	elongation factor 1-alpha 1
EPL	external plexiform layer
eSPW	early sharp wave
EYFP	enhanced yellow fluorescent protein
FFT	fast Fourier transformation
g	gram
GABA	gamma aminobutyric acid
GC	granule cell
GE	gene-environment
GFP	green fluorescent protein
GL	glomerular layer
gPDC	generalized partial directed coherence
h	hour
hM4Di	human Gαi-coupled M4 muscarinic receptor
HP	hippocampus
Hz	hertz
i.p.	itraperitoneal
IN	interneuron
IUE	*in utero* electroporation

L	liter
LEC	lateral entorhinal cortex
LFP	local field potential
LIF	leaky integrate-and-fire
LMEM	linear mixed-effects model
LOT	lateral olfactory tract
m	meter
M/TCs	mitral and tufted cells
MBI	mild behavior impairment
MCL	mitral cell layer
MEC	medial entorhinal cortex
MIA	maternal immune activation
min	minute
MRI	magnetic resonance imaging
MS	medial septum
MUA	multi-unit activity
NMDA	N-methyl-D-aspartic acid
NOR	novel object recognition
OB	olfactory bulb
OE	olfactory epithelium
OFC	orbitalfrontal cortex
OLP	object location preference
OSN	olfactory sensory neuron
P	postnatal day
PAC	phase-amplitude coupling
PCR	polymerase chain reaction
PBS	phosphate-buffered saline
PD	Parkinson’s disease
PFA	paraformaldehyde

PFC	prefrontal cortex
PGC	periglomerular cell
PIR	piriform cortex
poly(I:C)	polyinosinic:polycytidylic acid
PSD	power spectral density
P-tau	phosphorylated tau
PYR	pyramidal neuron
RR	respiration rhythm
s	second
SCZ	schizophrenia
STDP	spike-timing-dependent plasticity
STTC	Spike time tiling coefficient
SUA	single-unit activity
SVZ	subventricular zone
tSNE	t-distributed stochastic neighborhood embedding
TTL	transistor-to-transistor logic
USV	ultrasonic vocalization
µ	micro
V	volt
V1	primary visual cortex
W	watt
WT	wild-type

6.2 Supplementary materials

a) Reprint of supplementary information for Chapter 2.2.1:

Olfactory Bulb Activity Shapes the Development of Entorhinal-Hippocampal Coupling and Associated Cognitive Abilities

Chen *et al*., *Current Biology* 2023

Figures S1

Figures S2

Figures S3

Figures S4

Figures S5

Table S1

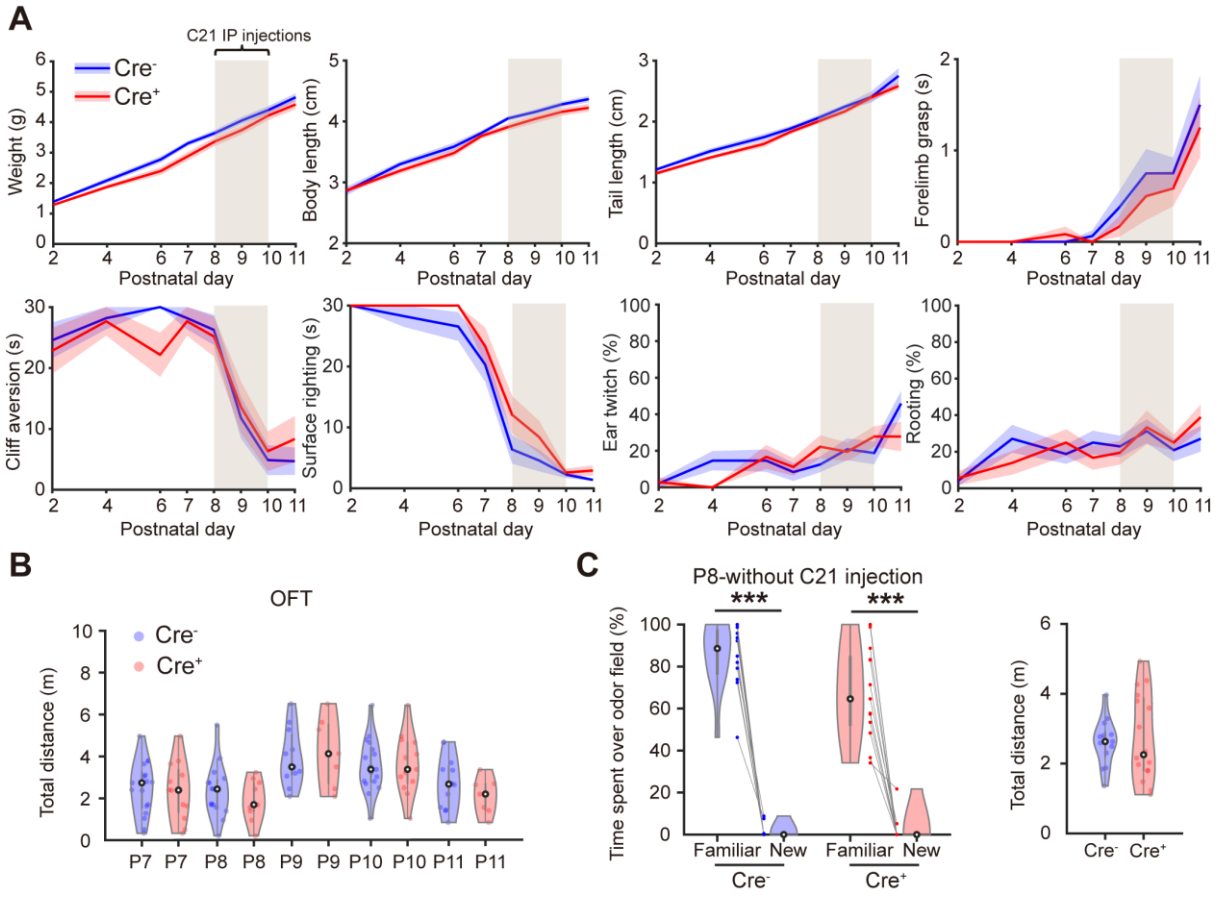

Figure S1. Effect of transient M/TC output silencing on somatic development, reflexes and locomotion of neonatal mice. Related to Figure 1.

(A) Averaged curves of age-dependent developmental milestones for neonatal Cre$^-$ (blue) and Cre$^+$ (red) mice from P2 to P11. **(B)** Violin plots displaying the distance traveled in OFT by P7-11 Cre$^-$ and Cre$^+$ mice. **(C)** Left: Violin plots displaying the relative time spent by P8 Cre$^-$ and Cre$^+$ mice over each odor field with no C21 injections (Cre$^-$: n=12, Cre$^+$: n=13; p=0.296 for interaction of genotype and odor, p<0.0001 for Cre$^-$-familiar vs Cre$^-$-new, p<0.0001 for Cre$^+$-familiar vs Cre$^+$-new, p=0.907 for Cre$^-$-new vs Cre$^+$-new, nonparametric multiple comparisons with Bonferroni's post-hoc test). Right: Violin plots displaying the total distance in the odor preference testing arena of P8 Cre$^-$ and Cre$^+$ mice with no C21 injections. For line plots data are presented as median ±standard error of the median. For violin plots data are presented as individual data points, median and interquartile range. ***p<0.001.

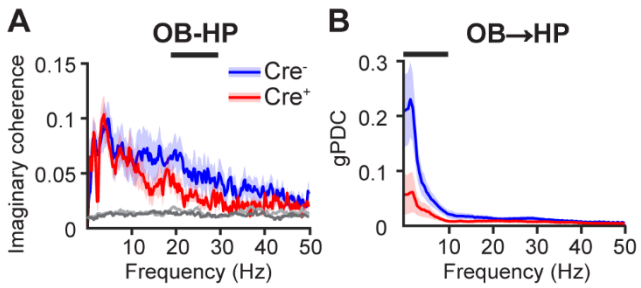

Figure S2. Effects of transient M/TC output silencing on long-range communication between OB and HP for P11 mice. Related to Figure 3.

(A) Averaged imaginary coherence for oscillatory activity simultaneously recorded in the OB and HP for P11 Cre^- (blue) and Cre^+ (red) mice (Cre^-: n=12, Cre^+: n=11; p=0.035 for interaction of genotype and frequency). The gray lines at the bottom correspond to the imaginary coherence calculated for shuffled LFPs (light gray for Cre^-, dark gray for Cre^+). **(B)** Information flow quantified by gPDC for oscillatory activity simultaneously recorded from OB and HP for P11 Cre^- and Cre^+ mice (Cre^-: n=12, Cre^+: n=11; p=0.0086 for interaction of genotype and frequency). Data are presented as median ±standard error of the median.

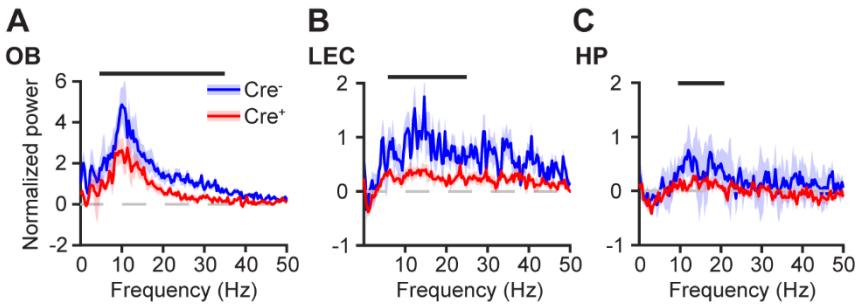

Figure S3. Effects of transient M/TC output silencing on odor-evoked activity in OB, LEC, and HP of P11 mice with another neutral odor. Related to Figure 4.

(A) Averaged power during odor stimulation with 1% vanillin normalized to the power before stimulation in OB of P11 Cre^- (blue) and Cre^+ (red) mice (Cre^-: n=12, Cre^+: n=8; p=0.0238 for interaction of genotype and frequency, LMEM). **(B)** Same as (A) for LEC (Cre^-: n=7, Cre^+: n=7; p=0.0388 for interaction of genotype and frequency, LMEM). **(C)** Same as (A) for HP (Cre^-: n=10, Cre^+: n=8; p=0.00622 for interaction of genotype and frequency, LMEM). Data are presented as median ±standard error of the median. Horizontal black lines indicate p<0.05.

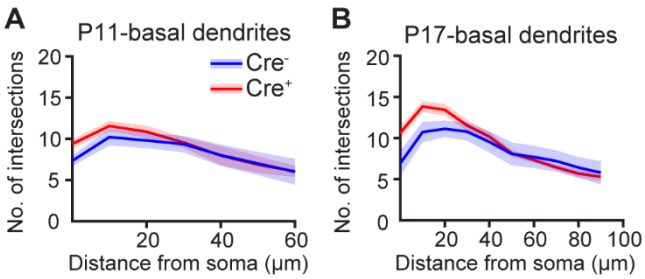

Figure S4. Complexity of basal dendrites of HP-projecting neurons in LEC after transient M/TC output silencing. Related to Figure 5.

(A) Averaged number of dendritic intersections from the soma center of labeled pyramidal neurons in LEC of P11 Cre^- (blue) and Cre^+ (red) mice for basal dendrites. **(B)** Same as (A) for P17 mice. Data are presented as median ±standard error of the median. Data are presented as median ±standard error of the median.

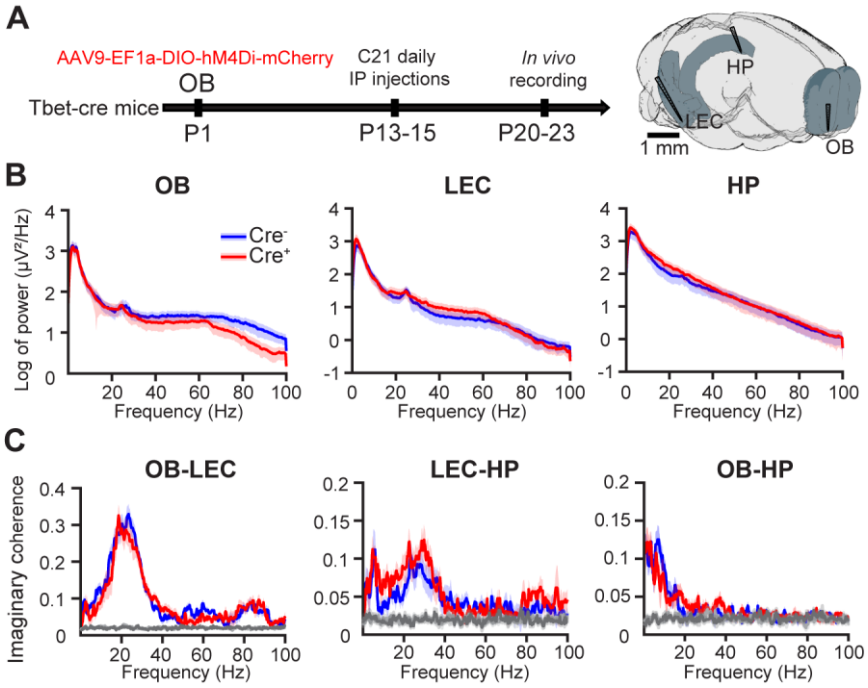

Figure S5. Effects of transient M/TC output silencing during P13-15 on neuronal and network activity in the OB-LEC-HP network of mice later in life. Related to Figure 6.

(A) (i) Experimental timeline of the chemogenetic inhibition of M/TC outputs during P13-15 followed by *in vivo* multi-site extracellular recordings of OB, LEC, and HP at P20-23. **(ii)** 3D schematic of the recording sites in OB, LEC and HP of P20-23. **(B)** Averaged power spectra of oscillatory activity recorded from Cre^- (blue) and Cre^+ (red) mice during P20-23 in OB (Cre^-: n=11, Cre^+: n=10; p=0.250 for genotype, LMEM), LEC (Cre^-: n=9, Cre^+: n=7; p=0.180 for genotype, LMEM) and HP (Cre^-: n=8, Cre^+: n=10; p=0.718 for genotype, LMEM). **(C)** Averaged imaginary coherence for simultaneous oscillatory activity recorded in OB and LEC (Cre^-: n=9, Cre^+: n=7; p=0.994 for interaction of genotype and frequency, LMEM), LEC and HP (Cre^-: n=7, Cre^+: n=7; p=0.182 for interaction of genotype and frequency, LMEM) as well as OB and HP (Cre^-: n=8, Cre^+: n=10; p=0.544 for interaction of genotype and frequency, LMEM) from Cre^- and Cre^+ mice during P20-23. The gray lines at the bottom correspond to the imaginary coherence calculated for shuffled LFPs of both groups respectively (light gray for Cre^-, dark gray for Cre^+). Data are presented as median ±standard error of the median.

Table S1. Detailed statistical information

Figure/Pannel	Groups	n (for mice if not specified)	Condition	Test	*p*-value
Fig 1C	Cre^- Cre^+	22 17	genotype x odor (interaction)	Nonparametric multiple comparisons	7.36e-05
Fig 1D	Cre^- Cre^+	22 17	genotype x odor (interaction)	Nonparametric multiple comparisons	0.216
Fig 2D (top)	Cre^- Cre^+	16 15	genotype	Linear mixed effect model	0.8102
Fig 2D (middle)	Cre^- Cre^+	12 12	genotype	Linear mixed effect model	0.00104
Fig 2D (down)	Cre^- Cre^+	12 11	genotype	Linear mixed effect model	0.0411
Fig 2E (top)	Cre^- Cre^+	126 units 190 units	genotype	Nonparametric ranksum test	0.5685
Fig 2E (middle)	Cre^- Cre^+	113 units 135 units	genotype	Nonparametric ranksum test	0.0775
Fig 2E (down)	Cre^- Cre^+	114 units 91 units	genotype	Nonparametric ranksum test	0.114
Fig 2F (top)	Cre^- Cre^+	2496 pairs 2216 pairs	genotype	Nonparametric ranksum test	0.36
Fig 2F (middle)	Cre^- Cre^+	976 pairs 1152 pairs	genotype	Nonparametric ranksum test	4.24e-05
Fig 2F (down)	Cre^- Cre^+	1716 pairs 1180 pairs	genotype	Nonparametric ranksum test	6.55e-06
Fig 3A	Cre^- Cre^+	1362 pairs 1235 pairs	genotype	Nonparametric ranksum test	5.72e-05
Fig 3D	Cre^- Cre^+	1426 pairs 820 pairs	genotype	Nonparametric ranksum test	3.40e-11
Fig 3B	Cre^- Cre^+	12 12	genotype x frequency (interaction)	Linear mixed effect model	0.00212
Fig 3E	Cre^- Cre^+	9 9	genotype x frequency (interaction)	Linear mixed effect model	0.0043
Fig 3C	Cre^- Cre^+	12 12	genotype x frequency (interaction)	Linear mixed effect model	0.0126
Fig 3F	Cre^- Cre^+	9 9	genotype x frequency (interaction)	Linear mixed effect model	0.0129

Fig 4B	Cre^- Cre^+	12 8	genotype x frequency (interaction)	Linear mixed effect model	0.0219
Fig S3A	Cre^- Cre^+	12 8	genotype x frequency (interaction)	Linear mixed effect model	0.0238
Fig 4C	Cre^- Cre^+	7 7	genotype x frequency (interaction)	Linear mixed effect model	0.0308
Fig S3B	Cre^- Cre^+	7 7	genotype x frequency (interaction)	Linear mixed effect model	0.0388
Fig 4D	Cre^- Cre^+	10 8	genotype x frequency (interaction)	Linear mixed effect model	0.0163
Fig S3C	Cre^- Cre^+	10 8	genotype x frequency (interaction)	Linear mixed effect model	0.00622
Fig 4F	Cre^+-saline Cre^+-C21	10 12	genotype	Nonparametric ranksum test	0.0161
Fig 4G	Cre^+-saline Cre^+-C21	63 units 81 units	genotype	Nonparametric ranksum test	0.000378
Fig 4H	Cre^+-saline Cre^+-C21	6 7	genotype	Nonparametric ranksum test	0.0293
Fig 4I	Cre^+-saline Cre^+-C21	32 units 48 units	genotype	Nonparametric ranksum test	0.0149
Fig 4J	Cre^+-saline Cre^+-C21	8 10	genotype	Nonparametric ranksum test	0.00555
Fig 4K	Cre^+-saline Cre^+-C21	17 units 39 units	genotype	Nonparametric ranksum test	0.0144
Fig 5E	Cre^- Cre^+	13 neurons 14 neurons	genotype	Nonparametric ranksum test	0.161
Fig 5F	Cre^- Cre^+	13 neurons 14 neurons	genotype x distance (interaction)	Linear mixed effect model	0.000395
Fig 5G	Cre^- Cre^+	13 neurons 14 neurons	genotype	Nonparametric ranksum test	0.0404
Fig 5J	Cre^- Cre^+	21 neurons 21 neurons	genotype	Nonparametric ranksum test	0.425
Fig 5K	Cre^- Cre^+	21 neurons 21 neurons	genotype x distance (interaction)	Linear mixed effect model	3.091e-11
Fig 5L	Cre^- Cre^+	21 neurons 21 neurons	genotype	Nonparametric ranksum test	0.0221

Fig 6B (left)	Cre^- Cre^+	16 15	genotype	Linear mixed effect model	0.296
Fig 6B (middle)	Cre^- Cre^+	10 12	genotype	Linear mixed effect model	0.00883
Fig 6B (right)	Cre^- Cre^+	11 13	genotype	Linear mixed effect model	0.0472
Fig 6C (left)	Cre^- Cre^+	3517 pairs 2419 pairs	genotype	Nonparametric ranksum test	0.000583
Fig 6C (middle)	Cre^- Cre^+	3103 pairs 1933 pairs	genotype	Nonparametric ranksum test	3.51e-13
Fig 6C (right)	Cre^- Cre^+	1500 pairs 1765 pairs	genotype	Nonparametric ranksum test	0.000604
Fig 6D (left)	Cre^- Cre^+	10 12	genotype x frequency (interaction)	Linear mixed effect model	0.0248
Fig 6D (middle)	Cre^- Cre^+	10 12	genotype x frequency (interaction)	Linear mixed effect model	0.0493
Fig 6D (right)	Cre^- Cre^+	11 13	genotype x frequency (interaction)	Linear mixed effect model	0.000577
Fig 6E (left)	Cre^- Cre^+	3754 pairs 2134 pairs	genotype	Nonparametric ranksum test	1.818e-26
Fig 6E (middle)	Cre^- Cre^+	1915 pairs 2016 pairs	genotype	Nonparametric ranksum test	1.204e-74
Fig 6E (right)	Cre^- Cre^+	1557 pairs 2357 pairs	genotype	Nonparametric ranksum test	0.282
Fig 7A	Cre^- Cre^+	26 18	genotype x trail (interaction)	Nonparametric multiple comparisons	0.0141
Fig 7B	Cre^- Cre^+	27 23	genotype x trail (interaction)	Nonparametric multiple comparisons	0.0122
Fig 7C(middle)	Cre^- Cre^+	37 25	genotype	Nonparametric ranksum test	0.511
Fig 7C (right)	Cre^- Cre^+	37 25	genotype	Nonparametric ranksum test	0.0355

b) Reprint of supplementary information for Chapter 2.2.5:

Preconfigured Architecture of the Developing Mouse Brain

Chini *et al*., *Cell Reports* 2024

Figures S1

Figures S2

Figures S3

Figures S4

Figures S5

Figures S6

Figures S7

Table S1

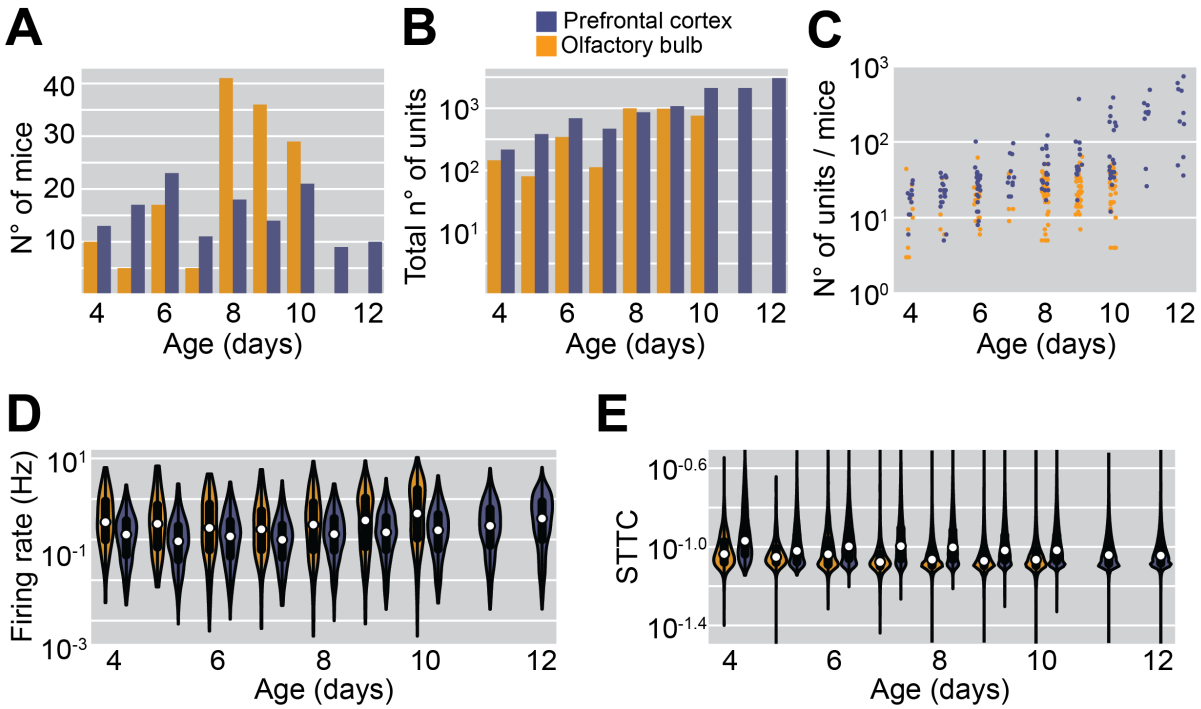

Figure S1. Descriptive statistics of the experimental dataset. Related to Figure 1. (**A**) Bar plot displaying the number of recorded mice across age and brain region (n=278 mice). Color codes for brain region. (**B**) Same as A for recorded single units (n=14357 single units). (**C**) Scatter plot displaying the number of recorded units per individual mice over age and brain regions (n=278 mice). (**D**) Violin plot displaying firing rate over age. Color codes for brain region. (**E**) same as (**D**) for STTC. In (**C**) dots indicate individual mice. In (**D-E**) data is presented as median, 25th, 75th percentile, and interquartile range, and the shaded area represents the probability density of the variable.

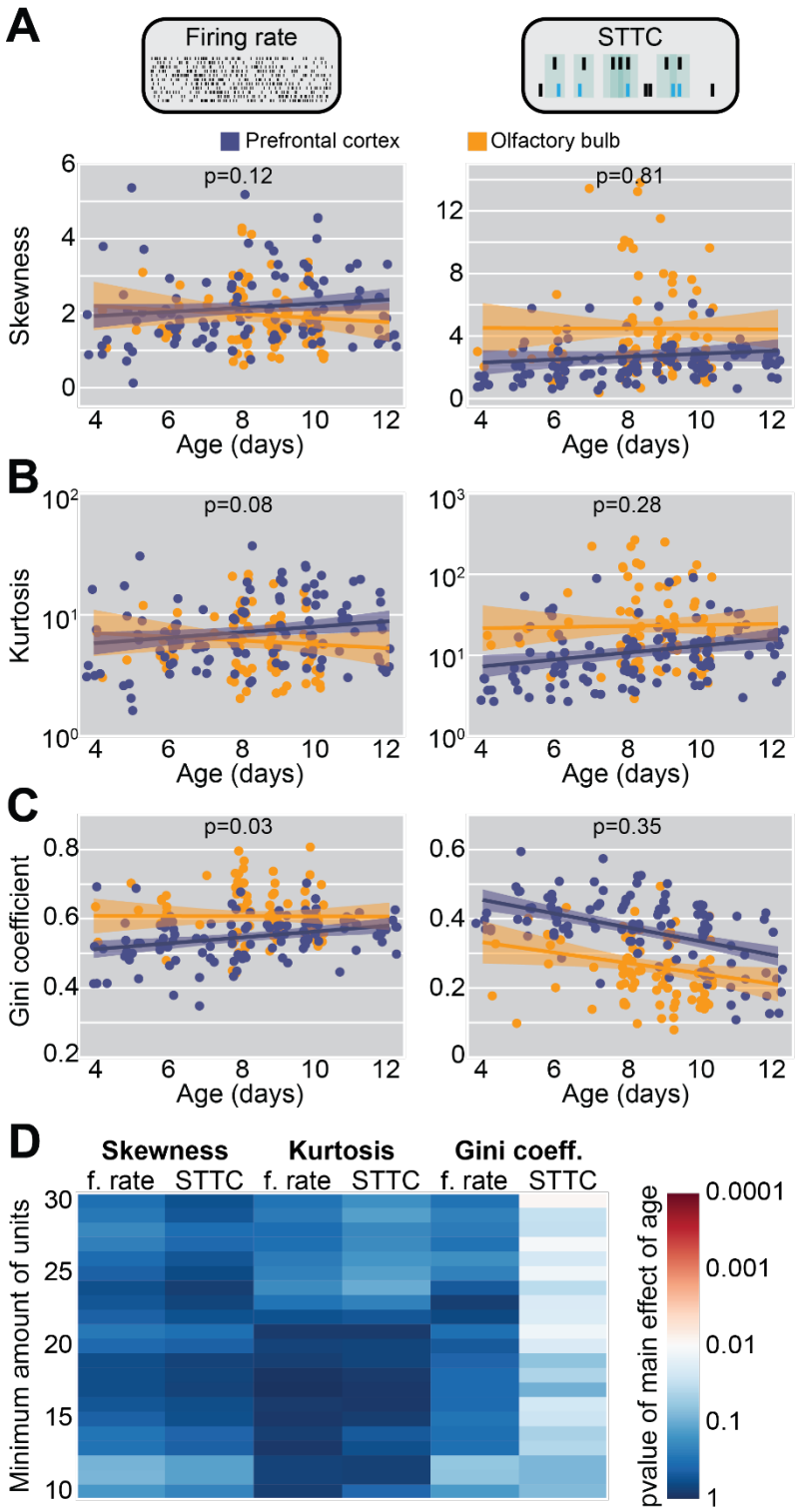

Figure S2. Skewness, kurtosis and Gini coefficient of firing rate and STTC across brain regions in the first two postnatal weeks. Related to Figure 2. (**A**) Scatter and line plot displaying the skewness of firing rate (left) and STTC (right) of P4-12 mice (n=238 mice). Color codes for brain region. (**B-C**) Same as (A) for kurtosis and Gini coefficient. (**D**) Heatmap displaying the p-value for the main effect of age as a function of the minimum number of units used as a cutoff to be included in the analysis. In (**A-C**) colored dots indicate individual mice, and data is presented as mean and 95% C.I.. P-values refer to the interaction between age and brain region.

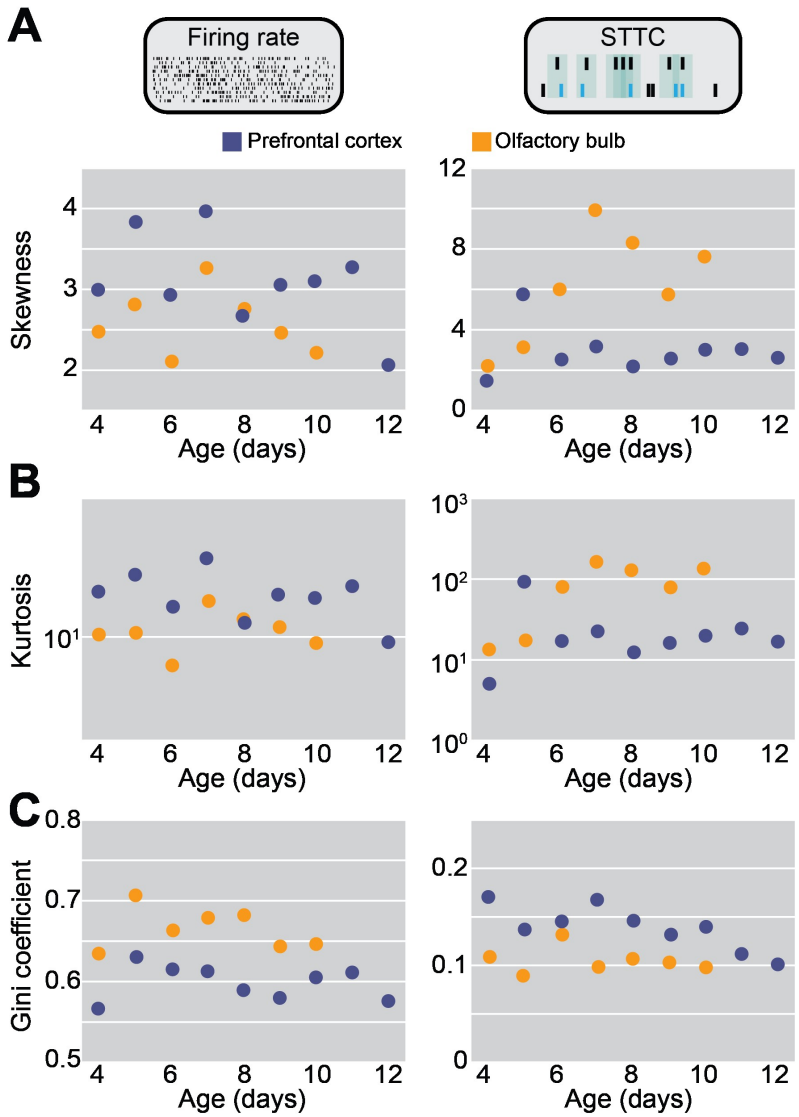

Figure S3. Skewness, kurtosis and Gini coefficient of firing rate and STTC pooled across mice over the first two postnatal weeks. Related to Figure 2. (**A**) Scatter plot displaying the skewness of firing rate (left) and STTC (right) of P4-12 mice. Color codes for brain region. (**B-C**) Same as (**A**) for kurtosis and Gini coefficient. In (**A-C**) dots indicate a single parameter estimation on data pooled across mice of the same age recorded from the same brain region.

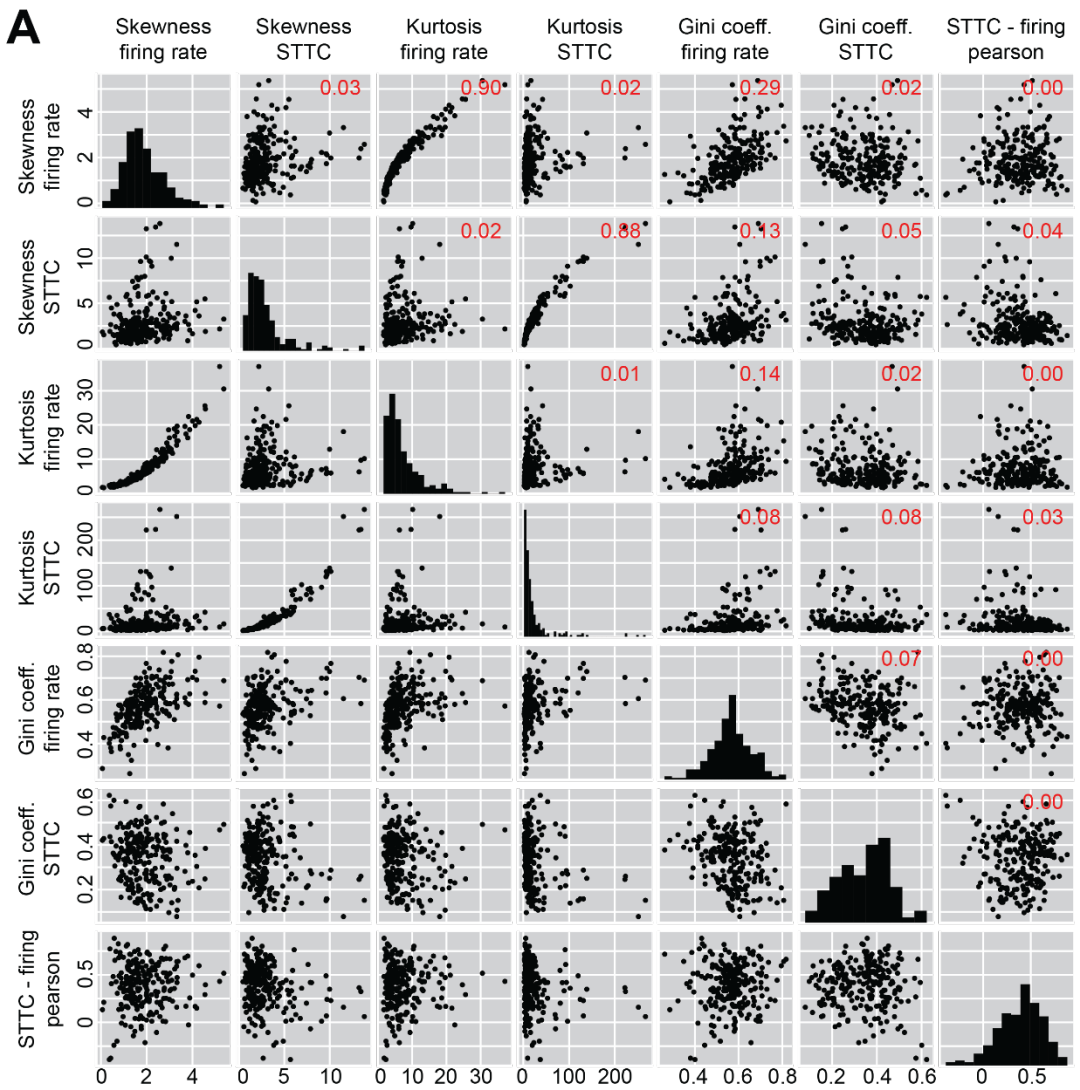

Figure S4. Distribution and pairwise correlations of skewness, kurtosis and Gini coefficient of firing rate and STTC. Related to Figure 2. (**A**) Pair plot of the 7 parameters used to describe the shape of the firing rate and STTC distributions. The plots on the main diagonal displays histograms of the distributions of each individual parameter across the entire dataset (n=238 mice). The off-diagonal plots display the pairwise correlations among the 7 parameters. The numbers in red indicate the Pearson r2 for that specific pairwise parameter combination. Black dots represent individual mice.

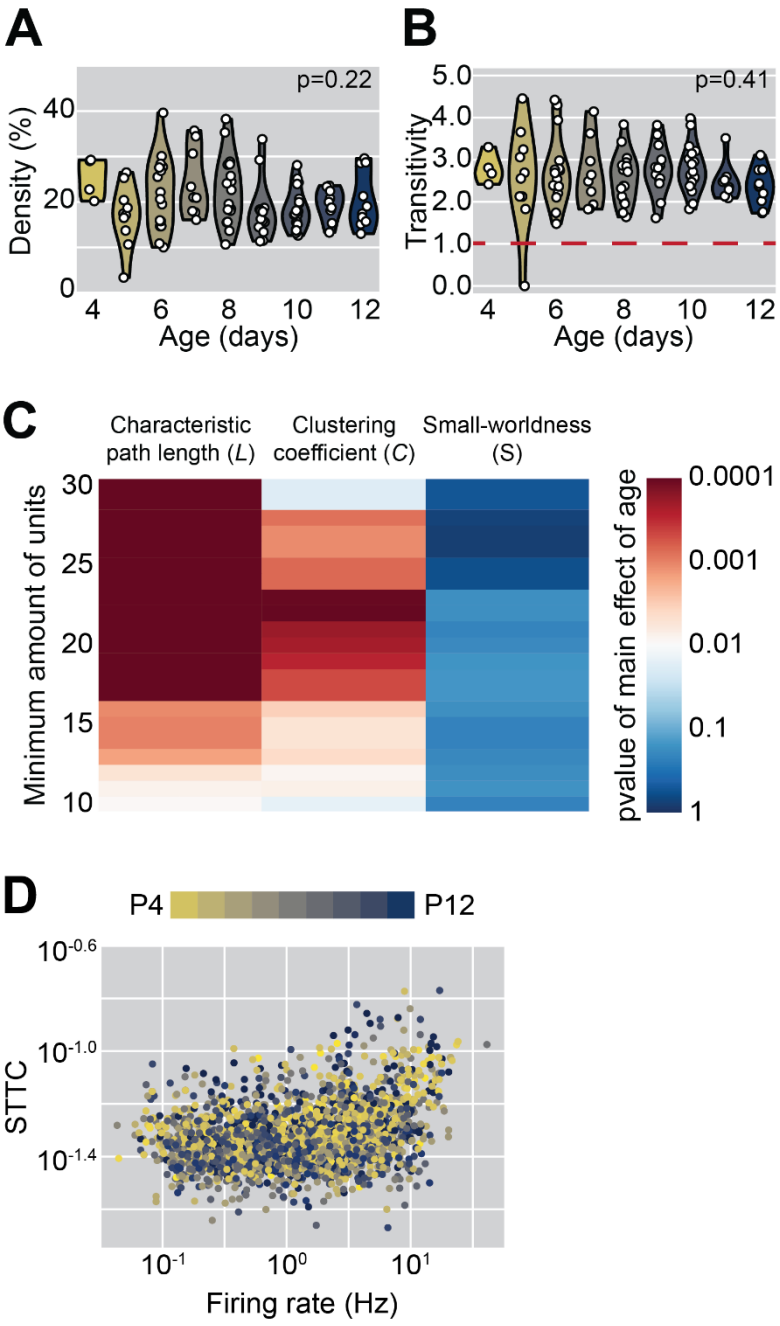

Figure S5. Network properties and the correlation between firing rate and average STTC across the first two postnatal weeks. Related to Figures 3 and 4. (**A**) Violin plot displaying the graph density of P4-12 mice (n=108 mice). Color codes for age with 1-day increments. (**B**) Same as (**A**) for transitivity. The dashed red line indicates the value of the corresponding random network. (**C**) Heatmap displaying the p-value for the main effect of age as a function of the minimum number of units used as a cutoff to be included in the analysis. (**D**) Scatter plot displaying the log-transformed average STTC of all recorded units as a function of their log-transformed firing rate. Color codes for age. In (**A-B**) white dots indicate individual mice, in (**D**) individual units. In (**A-B**) the shaded area represents the probability density of the variable.

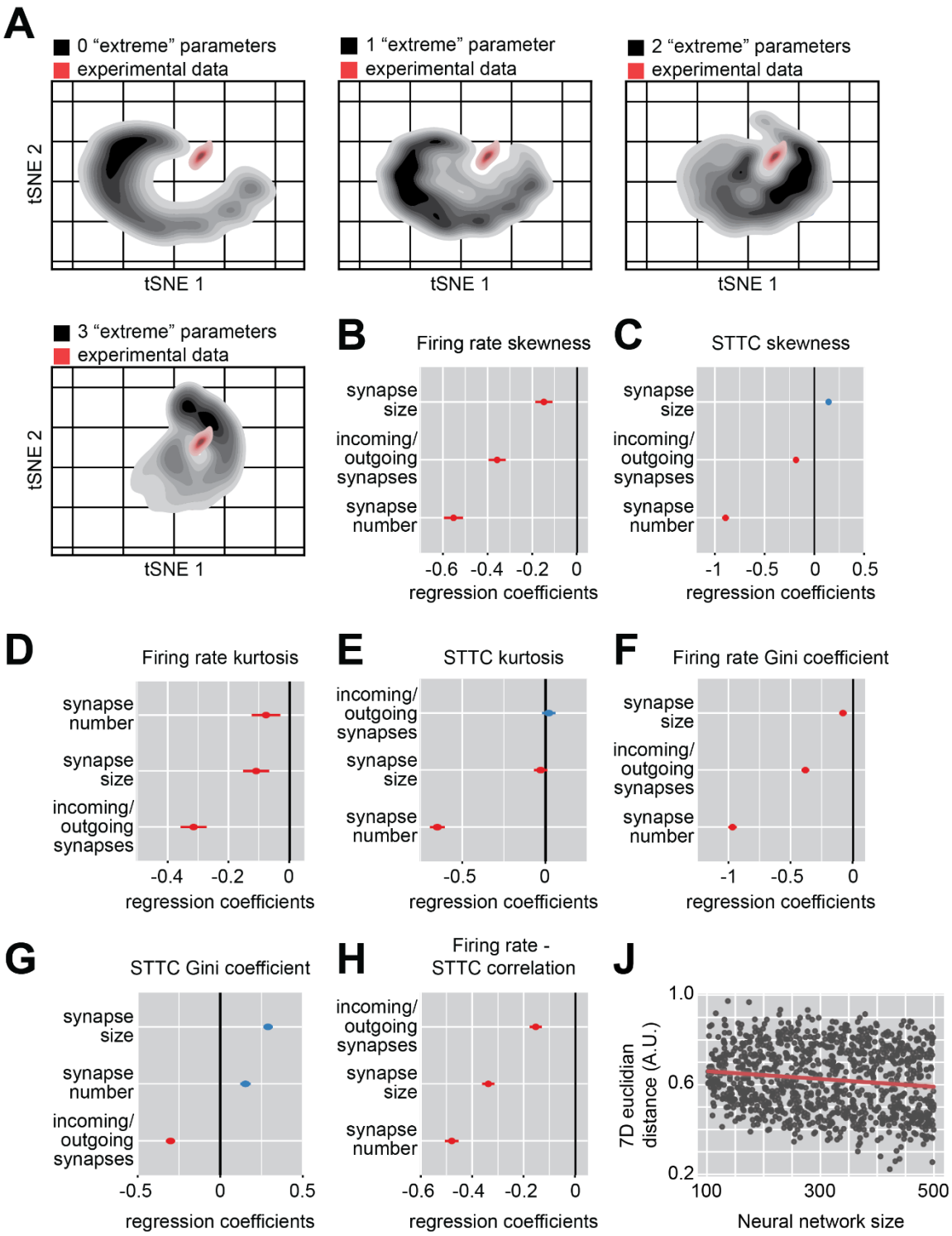

Figure S6. Spiking neural network modeling of the distribution shape of SUA statistics in the developing PFC. Related to Figure 5. (**A**) tSNE-embedded space occupied by experimental (red) and simulated (black) data in the 7-dimensional parameter space used to evaluate model fit, as a function of the number of synaptic parameters set in their “extreme” configuration. Color intensity codes for probability. (**B**) Multivariate regression coefficients for the 3 synaptic parameters over the distance from the median firing rate skewness of experimental data. (**C-H**) Same as (**B**) for STTC skewness (**C**), firing rate kurtosis (**D**), STTC kurtosis (**E**), firing rate Gini coefficient (**F**), STTC Gini coefficient (**G**) and firing rate – STTC correlation (**H**). (**J**) Scatter plot displaying the distance between simulated data and the center

of mass of experimental data as a function of network size. Dots represent individual simulations. In (**B-H**) regression coefficients are presented as mean and 95% C.I.. In (**J**) the regression is presented as mean and 95% C.I..

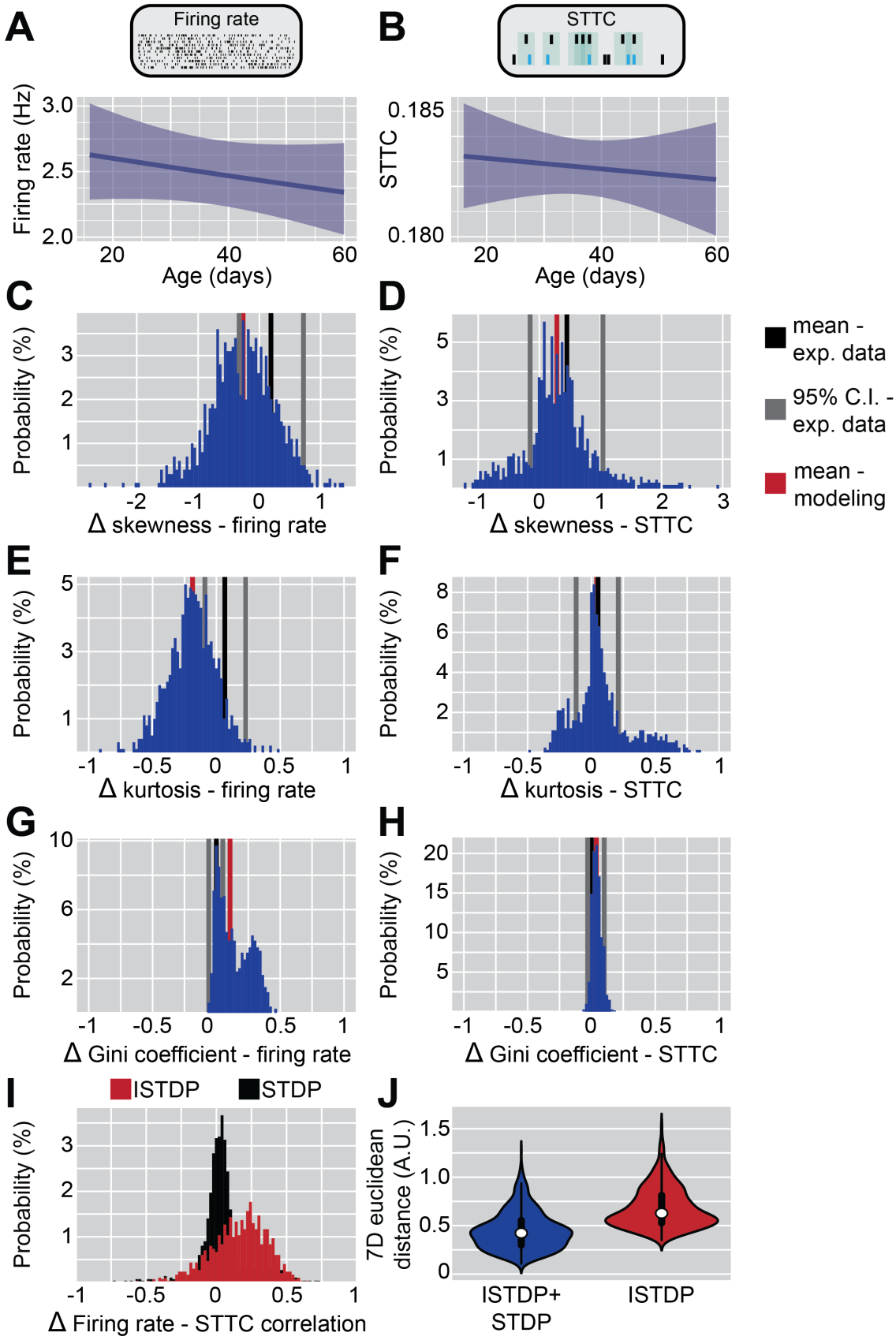

Figure S7. Prefrontal SUA firing statistics in P16-60 mice and simulated network effects of synaptic plasticity rules. Related to Figures 6 and 7. (**A**) Line plot displaying the SUA firing rate of P16-60 mice (n=24 mice, 95 recordings and 2498 single units) as a function of age. (**B**) Same as (**A**) for STTC (n=24 mice, 95 recordings and 36899 spike train pairs). (**C**) Histogram plot of the difference in simulated skewness of firing rate before and after synaptic

plasticity. The black line indicates the mean of the experimental data, the two grey lines the 95% C.I. of the mean and the red line the mean of the simulated data. (**D-H**) Same as (**C**) for the skewness of STTC (**D**), kurtosis of firing rate (**E**) and STTC (**F**) and Gini coefficient of firing rate (**G**) and STTC **(H**). (**I**) Histogram plot of the difference in the simulated firing rate and average STTC correlation before and after synaptic plasticity in ISTDP- (red) and STDP-only networks. (**J**). Violin plot displaying the 7-dimensional distance between simulated data of ISTDP+STDP (blue) and ISTDP-only (red) networks and the center of mass of the experimental data. In (**A)** and (**B**) data is presented as mean and 95% C.I..

Neuron model			
Parameter	*Description*	*Excitatory cells*	*Inhibitory cells*
V_L	Leak membrane potential	-70 mV	-70 mV
V_{Thr}	Spike threshold potential	-52 mV	-52 mV
V_{Res}	Reset potential	-59 mV	-59 mV
τ_{Ref}	Refractory period	2 ms	1 ms
C_m	Membrane capacitance	500 pF	200 pF
g_L	Membrane leak conductance	25 nS	20 nS
τ_m	Membrane time constant	20 ms	10 ms
$\sigma\xi$	Noisy input #	**normal**(15, 1)	**normal**(12.5, 1)
Synapse model			
Parameter	*Description*	*Excitatory cells*	*Inhibitory cells*
E_{AMPA}	Reversal potential (AMPA)	0 mV	0 mV
E_{GABA}	Reversal potential (GABA)	-80 mV	-80 mV
τ_{AMPA}	Time constant of AMPA decay	2 ms	1 ms
τ_{GABA}	Time constant of GABA decay	8 ms	8 ms
mean connectivity	mean connectivity of the network	**normal**(0.25, 0.25/4)	**normal**(0.25, 0.25/4)
g_{AMPA}	Conductance (AMPA) #	[**lognormal**(0, 1) or **normal**($\sqrt{e}$, 0.5)] / 25 * $AMPA_{mod}$ * nS	[**lognormal**(0, 1) or **normal**($\sqrt{e}$, 0.5)] / 25 * $AMPA_{mod}$ * nS
g_{GABA}	Conductance (GABA) #	[**lognormal**(0, 1) or **normal**($\sqrt{e}$, 0.5)] / 6 * $GABA_{mod}$ * nS	[**lognormal**(0, 1) or **normal**($\sqrt{e}$, 0.5)] / 30 * $GABA_{mod}$ * nS
$AMPA_{mod}$	Multiplier of AMPA conductance #	**normal**(0.7, 0.7/4)	**normal**(0.7, 0.7/4)
$GABA_{mod}$	Multiplier of GABA conductance #	**normal** *(2*, 0.5)	**normal** *(2*, 0.5)
Excitatory synaptic plasticity model			
τ_{STDP}	Time constant of synaptic plasticity	20 ms	Not applicable
g_{min}	Minimum synaptic weight	0	Not applicable
g_{max}	Maximum synaptic weight	10	Not applicable

XXX	Learning rate	0.01	Not applicable
Inhibitory synaptic plasticity model			
τ_{STDP}	Time constant of synaptic plasticity	Not applicable	20 ms
g_{min}	Minimum synaptic weight	Not applicable	0
g_{max}	Maximum synaptic weight	Not applicable	100
aaa	Learning rate	Not applicable	0.01
α	Target firing rate	**lognormal**(-0.5, 1)	Not applicable

Table S1. Parameters of the leaky integrate-and-fire network. Related to STAR Methods. "Normal" and "lognormal" refer to values of variables that are randomly drawn from a normal or lognormal distribution, respectively. The two values in parenthesis refer to, respectively, the mean and the standard deviation of the (underlying) normal distribution. [#]Note that the two distributions have the same mean (i.e. the mean of lognormal(0, 1) is $\sqrt{e}$).

7 | Acknowledgments

Finally I am here! Countless memories along the journey come into my mind.

First and foremost, I would like to express my deepest thanks to my supervisor Prof. Dr. Ileana Hanganu-Opatz for her continuous supervision, support, encouragement, and sometimes criticism, all of which enabled me to explore my research interests and empowered me to make my way for career development.

I am especially grateful to Dr. Johanna Kostka, who tutored me patiently in my early PhD days with constructive discussions and is always available to help like translating the "General Summary" here into German. I would like to specially thank Dr. Sebastian Bitzenhofer, who shared valuable knowledge with me and gave me critical comments on my research topics.

I would like to thank my former colleagues, specifically, Dr. Lingzhen Song for selflessly providing inspiring suggestions for histology, and Dr. Mattia Chini for kindly sharing great insights into statistics.

I would like to thank all the current and former labmates of the Hanganu-Opatz lab, for the animated discussions in both scientific and non-scientific aspects, in particular, Xiaxia, Marilena, Irina, Anne, Tony, Karo, Fiona, Ann Marlene. Working with people from different backgrounds has broadened my knowledge a lot.

Further, I would like to thank Peggy, Achim, Annette, and numerous “Hiwis” in the lab for their outstanding technical assistance on experiments over the past few years; as well as Thorsten and Fritz from ZMNH workshop for helpfully making some of my “wild” thoughts on experimental setups into nicely hand-made items.

I would also like to thank my football team with whom I share many thrilling moments and are very tolerant of my occasional absence for the training because of science.

I would like to thank my best friends from far away, who still kept strong bonds with me during the COVID pandemic and helped me overcome the hard times through remote but warm communications.

Most of all, I thank my parents for the unconditional boundless backup in my life. None of my work would come out without their support and trust.

8 | Curriculum Vitae

Lebenslauf aus datenschutzrechtlichen Gründen nicht enthalten.

Lebenslauf aus datenschutzrechtlichen Gründen nicht enthalten.

9 | Eidesstattliche Versicherung

Ich versichere ausdrücklich, dass ich die Arbeit selbständig und ohne fremde Hilfe, insbesondere ohne entgeltliche Hilfe von Vermittlungs- und Beratungsdiensten, verfasst, andere als die von mir angegebenen Quellen und Hilfsmittel nicht benutzt und die aus den benutzten Werken wörtlich oder inhaltlich entnommenen Stellen einzeln nach Ausgabe (Auflage und Jahr des Erscheinens), Band und Seite des benutzten Werkes kenntlich gemacht habe. Das gilt insbesondere auch für alle Informationen aus Internetquellen.
Soweit beim Verfassen der Dissertation KI-basierte Tools („Chatbots“) verwendet wurden, versichere ich ausdrücklich, den daraus generierten Anteil deutlich kenntlich gemacht zu haben. Die „Stellungnahme des Präsidiums der Deutschen Forschungsgemeinschaft (DFG) zum Einfluss generativer Modelle für die Text- und Bilderstellung auf die Wissenschaften und das Förderhandeln der DFG“ aus September 2023 wurde dabei beachtet.
Ferner versichere ich, dass ich die Dissertation bisher nicht einem Fachvertreter an einer anderen Hochschule zur Überprüfung vorgelegt oder mich anderweitig um Zulassung zur Promotion beworben habe.
Ich erkläre mich damit einverstanden, dass meine Dissertation vom Dekanat der Medizinischen Fakultät mit einer gängigen Software zur Erkennung von Plagiaten überprüft werden kann.

Datum: _____

Unterschrift: _____